

ANALYSES OF PROPERTY-GRADED STAINLESS STEEL 316L BULK  
STRUCTURES PROCESSED BY SELECTIVE LASER MELTING

A Dissertation

by

YASH BHARATBHUSHAN PARIKH

Submitted to the Office of Graduate and Professional Studies of  
Texas A&M University  
in partial fulfillment of the requirements for the degree of

DOCTOR OF PHILOSOPHY

Chair of Committee,	Hong Liang
Co-Chair of Committee,	Mathew Kuttolamadom
Committee Members,	ChaBum Lee
	Li-Jung Tai
	Angie H. Price
Head of Department,	Bryan Rasmussen

May 2021

Major Subject: Mechanical Engineering

Copyright 2021 Yash Bharatbhushan Parikh



## ABSTRACT

The overarching goal of this research is to investigate the processing, structure, properties, and performance of (mechanical) property-graded bulk structures made from a single metallic alloy via a laser powder bed fusion (LPBF) process. With a vision to realize repeatable/reproducible functionally-graded additively manufactured (FGAM) bulk structures, this study aims to elucidate the underlying causes of the variations in macro- and microstructures in relation to process conditions, the resulting physical and mechanical property distributions, and its local and global mechanical performance. For this purpose, a systematic design of experiments that spanned the volumetric energy density (VED)-related process parameter design space was utilized to investigate the range of functionally-acceptable physical/mechanical properties achievable in stainless steel 316L via a pulsed selective laser melting (SLM) process. Results demonstrated the significant, but functionally-usable variations attainable in hardness, relative density, and modulus. Property variations resulted from a combination of porosity types/amounts, martensitic phase fractions, and grain sizes. Based on these, select process parameters were utilized for fabricating ASTM standard tensile/bending specimens with intended property differentials within its gauge volumes. Analyses of structure and property variations were performed, coupled with metallography, microscopy, and spectroscopy. Digital image correlation (DIC) was used to examine the evolution of spatial and temporal strains, especially at zonal interfaces. Altogether, this work helped lay the foundation for tailoring the structure, properties and performance of FGAM bulk parts.

## DEDICATION

To my father...

## ACKNOWLEDGMENTS

I would like to express my deepest gratitude to Dr. Mathew Kuttolamadom for his continuous guidance and support throughout my Ph.D. studies. I am grateful to have had an opportunity to learn from a dedicated, patient, and curious individual, which has built up and shaped my research aptitude and attitude.

Besides my advisor, I want to thank Dr. Hong Liang for her invaluable guidance, valuable suggestions, and constant support for being my committee chair. I would also like to express my sincere thanks to the members of my doctoral committee: Dr. Bruce Tai, Dr. ChaBum Lee, and Dr. Angie Hill Price. Their insights from wider perspectives have only broader my research understandings.

I am grateful to all the research scientists, staff, and student colleagues at the Oak Ridge National Laboratory (ORNL) - Manufacturing Demonstration Facility (MDF) for their support and help, especially Dr. Ryan Dehoff, Dr. Suresh Babu, Dr. Peeyush Nandwana, Sarah Graham, Tom Geer, Kevin Sisco, Sabina Kumar, Serena Beauchamp, Caitlin Hensley, Sujana Chandrasekar, and Amy Godfrey.

Thanks to all my colleagues across different research groups at Texas A&M University for their assistance, fruitful discussion, and experimental assistance.

Finally, thanks to my spouse for her encouragement, patient, love, and other members of my family and extended family members for their support.

## CONTRIBUTORS AND FUNDING SOURCES

I would like to thank all the contributors and funding agencies for their generous support. In particular, this research was in part supported by the Advanced Short-Term Research Opportunity (ASTRO) Program at the Oak Ridge National Laboratory (ORNL), Manufacturing Demonstration Facility (MDF), Knoxville, Tennessee, sponsored by the U.S. Department of Energy and administered by the Oak Ridge Institute for Science and Education (ORISE).

### **Contributors**

This work was supervised by a dissertation committee comprising Professor Hong Liang [advisor], Professor ChaBum Lee, Professor Li-Jung Tai of the Department of Mechanical Engineering, and Professor Mathew Kuttolamadom [co-advisor], and Professor Angie Hill Price of the Department of Engineering Technology and Industrial Distribution.

Dr. Romaine Issacs provided the EBSD data analyzed for Chapter 4 from Carl Zeiss Industrial Metrology, LLC. The as-received SS 316L powder Particle Size Distribution (PSD) was conducted by Mr. Binyam Abraham, Mr. James Stanfill, Mr. Zachary Gray, and Dr. Devendra Verma from Nanoscience instruments and will be published in 2021.

Thermal conductivity analysis in Appendix was provided by Dr. Ankur Jain and Dr. Darshan Ravoori from the University of Texas at Arlington and will be published in 2021.

All other work conducted for the dissertation was completed by Mr. Yash Bharatbhushan Parikh independently.

### **Funding Sources**

Graduate study was supported by graduate assistantships from Engineering Technology & Industrial Distribution (ETID) department alongside several other fellowships and scholarships from Texas A&M University. Special thanks to the Office of Scholarship and Financial Aid (SFAID) and the Association of Former Students for their continued generous support throughout my graduate studies.

This work was also made possible in part by the National Science Foundation (NSF) under Grant Number 1659856. Its contents are solely the responsibility of the authors and do not necessarily represent the official views of the NSF.

## ABBREVIATIONS

2D	Two Dimensional
3D	Three Dimensional
3DP	Three-Dimensional Printing
.stl	Standard Triangulated Language
AI	Artificial Intelligence
AISI	American Iron and Steel Institute
AM	Additive Manufacturing
As-printed	No Post-Processing Done to Specimen (after manufacturing)
ASTM	American Society for Testing and Materials
BCC	Body-Centered Cubic
BCT	Body-Centered Tetragonal
BD	Building Direction
BJ	Binder Jetting
C	Carbon
CAD	Computer Aided Design
CAM	Computer Aided Manufacturing
Cr	Chromium
CT	Computed Tomography
CW	Continuous Wave
DED	Directed Energy Deposition

DIC	Digital Image Correlation
DMD	Direct Metal Deposition
DMLD	Direct Metal Laser Deposition
DMLS	Direct Metal Laser Sintering
DOE	Design of Experiment
EBM	Electron Beam Melting
EB-PBF	Electron Beam Powder Bed Fusion
EBS	Electron Backscatter Diffraction
EDM	Electric Discharge Machining
EDS	Energy Dispersive X-Ray Spectroscopy
FCC	Face-Centered Cubic
Fe	Iron
FGM	Functionally Graded Materials
FGAM	Functionally Graded Additively Manufactured
FPB	Four Point Bending
GA	Gas Atomized
GMA	Gas Metal Arc
HAZ	Heat Affected Zone
HB	Hardness Brinell
HIP	Hot Isostatic Pressing
HT	Heat Treatment
HV	Hardness Vickers

IPF	Inverse Pole Figure
K	Kelvin
L-PBF	Laser Powder Bed Fusion
LENS	Laser Engineered Net Shaping
LOF	Lack of Fusion
ME	Material Extrusion
MIM	Metal Injection Molding
MJ	Material Jetting
ML	Machine Learning
Mn	Manganese
Mo	Molybdenum
N	Nitrogen
ND	Normal Direction
Nd:YAG	Neodymium-doped Yttrium Aluminium Garnet
Ni	Nickel
OM	Optical Microscope
PBF	Powder Bed Fusion
PF	Pole Figure
PM	Powder Metallurgy
PREP	Plasma Rotating Electrode Processed
PSD	Powder Size Distribution
PSPP	Processing-Structure-Properties-Performance



ROI	Region Of Interest
R&R	Repeatable & Reproducible
RQ	Research Question
Si	Silicon
SD	Scanning Direction
SEM	Scanning Electron Microscopy
SLA	Stereolithography
SLM	Selective Laser Melting
SLMed SS316L	Selective Laser Melting Prepared SS316L
SLS	Selective Laser Sintering
SS	Stainless Steel
SS 316L	Stainless Steel 316L (a stainless-steel alloy)
STL	Stereo Lithography
TD	Transverse Direction
TEM	Transmission Electron Microscope
UTS	Ultimate Tensile Strength
VED	Volumetric Energy Density
WA	Water Atomized
WD	Working Distance
WT%	Weight Percent
XCT	X-ray Computed Tomography
XRD	X-ray Diffraction

YFL	Ytterbium Fiber Laser
YS	Yield Strength
%EL	Percentage Elongation

## NOMENCLATURES

$\nu$	Poisson's ratio
$\rho$	Density [g/cm <sup>3</sup> ]
$\sigma$	Stress [MPa]
$\epsilon$	Strain [mm/mm]
$\lambda$	Cell spacing [ $\mu\text{m}$ ]
$E$	Young's modulus [GPa]
$E_v$	Volumetric energy density [J/mm <sup>3</sup> ]
$h$	Hatch distance [ $\mu\text{m}$ ]
$k$	Thermal conductivity [W/mK]
$L_T$	Layer thickness [ $\mu\text{m}$ ]
$P$	Nominal laser power [W]
$T$	Cooling rate [K/s]
$t$	Exposure time [ $\mu\text{s}$ ]
$V$	Scan speed [mm/s]

## TABLE OF CONTENTS

	Page
ABSTRACT.....	ii
DEDICATION.....	iii
ACKNOWLEDGMENTS .....	iv
CONTRIBUTORS AND FUNDING SOURCES .....	v
ABBREVIATIONS .....	vii
NOMENCLATURES .....	xii
TABLE OF CONTENTS.....	xiii
LIST OF FIGURES .....	xvi
LIST OF TABLES.....	xxvi
1. INTRODUCTION .....	1
1.1 Aim and Objectives .....	1
1.2 Motivations .....	2
1.3 Research Methodology .....	6
1.4 Expected Original Contributions .....	8
1.5 Dissertation Structure .....	9
2. BACKGROUND & LITERATURE REVIEW .....	11
2.1 Additive Manufacturing.....	11
2.2 Selective Laser Melting (SLM) .....	16
2.2.1 General Process Overview .....	17
2.2.2 Ongoing Research Themes in SLM .....	18
2.2.3 Influence of Powder Feedstock.....	21
2.2.4 Laser-Powder Interactions .....	22
2.2.5 Influence of SLM Process Parameters .....	23
2.2.6 SLM Processing Effects on Structure and Properties .....	26
2.2.7 Post Processing .....	32
2.3 Stainless Steels.....	36

2.3.1	Stainless Steel 316L .....	39
2.3.2	Common Microstructures of Stainless Steel 316L .....	40
2.4	SLM of SS 316L .....	42
2.4.1	General Overview .....	42
2.4.2	Solidification Fundamentals .....	44
2.4.3	Microstructural Development .....	47
2.5	Previous Related Work in SLM.....	50
2.6	Functionally-Graded Materials (FGMs) .....	52
2.6.1	Classifications of FGMs.....	55
2.6.2	Manufacturing Techniques for FGMs.....	56
2.6.3	Functionally Graded Additively Manufactured (FGAM) Materials.....	58
2.7	Knowledge Gaps.....	61
3.	RESEARCH METHODOLOGY.....	64
4.	MATERIALS & METHODS .....	68
4.1	SLM Machine Specifications.....	69
4.1.1	Relevant Details of the Laser .....	70
4.1.2	Laser Scan Strategy.....	72
4.1.3	Build Chamber Conditions.....	74
4.2	Feedstock Material.....	75
4.3	Testing and Measurement.....	81
4.3.1	Bulk Density and Porosity Measurements .....	81
4.3.2	Hardness Measurements .....	82
4.3.3	Nanoindentation Measurements.....	83
4.3.4	Tensile Testing with Digital Image Correlation .....	85
4.3.5	Four Point Bending Test with Digital Image Correlation.....	89
4.4	Microstructural Characterization .....	90
5.	MAPPING PROCESS PARAMETER BOUNDS AGAINST STRUCTURE & PROPERTY TRENDS (RQ-1).....	94
5.1	Mapping SLM Process Parameters Design Space .....	94
5.2	Properties and Characterization .....	98
5.2.1	Results of Physical and Mechanical Properties .....	99
5.3	Down-selection of Five Process Parameter Combinations.....	105
5.4	Observations and Deductions .....	111
6.	INFLUENCE OF PROCESSING AND MICROSTRUCTURE ON PROPERTIES (RQ-2).....	117
6.1	Macro-scale Observations.....	118
6.2	Micro-scale Observations .....	126
6.3	Defects Characterizations .....	130

6.4 Phase Identification Analysis.....	143
6.4.1 Major Phases & Grain Size.....	143
6.4.2 XRD Analysis .....	148
6.4.3 EBSD/EDS Analysis.....	150
6.5 Resolution Study.....	156
6.6 Observations and Deductions .....	168
7. STRAIN BEHAVIOR OF GRADED FGAM BULK STRUCTURES (RQ-3).....	171
7.1 Sample Fabrication and Performance Tests.....	171
7.1.1 Tensile Tests .....	172
7.1.2 Fractography .....	180
7.2 Graded Structures Fabrication and Performance .....	190
7.2.1 Tensile Samples (Normal Stresses).....	190
7.2.2 Bending Test with DIC .....	207
7.3 Interfaces.....	213
7.4 Observations and Deductions .....	215
8. CONCLUSIONS AND FUTURE WORK .....	217
REFERENCES .....	223
PUBLICATIONS.....	260
APPENDIX A .....	264
APPENDIX B .....	273

## LIST OF FIGURES

	Page
Figure 1. Schematic of multi-material (density) distributions within the part [19].	3
Figure 2. Optical micrograph of multi-material FGAM sample exhibiting a large interlayer fracture at the transition region [21].	4
Figure 3. Framework implemented for this research work.	6
Figure 4. AM literature snapshot for the span of the last 20 years.	12
Figure 5. Multi-scale applications of different AM processes [13].	13
Figure 6. Seven families of AM processes according to ASTM F2792 standards.	14
Figure 7. Classification of metal AM processes [13].	15
Figure 8. Comparison amongst various primary manufacturing processes [33].	16
Figure 9. Schematic representation of the SLM process [40].	17
Figure 10. Obtaining “Picture-to-Part” via SLM [36].	18
Figure 11. Ongoing research avenues for the SLM.	19
Figure 12. Current processability of alloys for the SLM [70].	20
Figure 13. SEM images of stainless steel 316L powder particles processed via the a) GA and b) WA techniques [82].	21
Figure 14. Schematic of cross-sectional view of laser-powder interactions [84].	22
Figure 15. Laser path and powder interactions during SLM [86].	23
Figure 16. Classification of SLM process parameters [88].	24
Figure 17. Schematic of the energy density contour for the SLM process.	27
Figure 18. 30 Single tracks of SS 316L for various VED combinations [124].	29
Figure 19. Schematic of multi-scale, multi-physics phenomena in the SLM [130].	30
Figure 20. Schematic of the SLM melt pool with expected defects [132].	31

Figure 21. Post build powder removal [Courtesy: APWORKS]. .....	33
Figure 22. Before and after surface finishing of SS test part [Courtesy: Fintek]. .....	34
Figure 23. Illustration of steps involved in a typical SLM process [149].....	35
Figure 24. General classification of steels [152]. .....	37
Figure 25. Fe-C equilibrium phase diagram: Amount of wt% C is crucial in determining the solidification path [153]. .....	38
Figure 26. Properties of conventional SS 316L [157]. .....	40
Figure 27. OM of steel phases a) Austenite b) Ferrite and c) Martensite [158]. .....	41
Figure 28. Variation of solidification modes for different G and R conditions [182]. ....	44
Figure 29. Possible growth mechanisms and effects on the grain structure [185]. .....	45
Figure 30 (a-c). Different solidification microstructures are obtained via varying energy input. Figure re-created from reference [186]. .....	46
Figure 31. SS 316L microstructures processed by traditional vs. SLM process [193]....	47
Figure 32. 316L microstructures processed by a Renishaw showing columnar grain growth across the melt pool boundaries (as seen in a). Rod-like cells in melt pool envelop in both transverse (b) and along the longitudinal (c) sections of the sample. [197].....	48
Figure 33. The microstructure of SLM processed Inconel 718 cube of 2mm <sup>3</sup> when processed by laser power of a) 950 W and b) 250 W [202]. .....	49
Figure 34. Steps to development of FGMs [208]. .....	53
Figure 35. Possible property variations achievable in conventional vs. FGMs [211]. ....	53
Figure 36. Schematic of property variations due to grain size in bulk FGM [214]. .....	54
Figure 37. Schematic of three types of FGM Gradient [211]. .....	55
Figure 38. Classification of types of gradient [216]. .....	56
Figure 39. Types of FGM fabrication methods [218]. .....	57



Figure 40. Temperature gradients and cooling observed during solidification for SS316 parts using different AM methods. Oval shapes represent the ranges of various studies included [234].	59
Figure 41. Procedural steps for manufacture and characterization of samples.	68
Figure 42. The Renishaw AM 400 SLM platform [237].	69
Figure 43. Illustration of the types of laser exposure mechanisms for a) pulsed wave (Q-switched) laser systems and b) continuous wave (CW) laser systems.	71
Figure 44. Illustration of various Gaussian beam profile modes [238].	71
Figure 45. Meander scanning strategy utilized for irradiation in SLM for the fabrication of SS 316L samples.	72
Figure 46. Meander scanning strategy within a single slice of a part geometry [239].	73
Figure 47. Key elements inside build chamber of RENISHAW AM 400.	74
Figure 48. Morphology of virgin SS 316L powder particles employed in the experiments, and aspect ratio as well as roundness for the powder particles.	76
Figure 49. EDS maps for virgin SS 316L powder showing high concentration of Cr, Ni, and Fe.	77
Figure 50. Particle Size Distribution (PSD) of as received SS 316L powder based on (a) average particle count and (b) particle volume in $\mu\text{m}^3$ .	78
Figure 51. Diffractograph for SS 316L precursor powder showing FCC austenitic diffraction peaks.	79
Figure 52. SEM micrograph of loose impure SS 316L powder particles. Highlighted with yellow circles are non-spherical, partially sintered powder particles.	80
Figure 53. EDS maps for impure SS 316L powder showing high concentration of Cr, Ni, and Fe.	81
Figure 54. Density test setup based on Archimedes method.	82
Figure 55. Beuhler Wilson VH1102 microhardness tester.	83
Figure 56. Hysitron TI 950 Triboindenter nanomechanical test setup.	84
Figure 57. MTS Insight tensile testing setup.	85

Figure 58. Overview of the 2D DIC experimental setup. ....	86
Figure 59. Various types of speckle patterns used in DIC analysis. ....	87
Figure 60. Speckle pattern generation with white and black spray paint. ....	88
Figure 61. Vic-2D window showing overview of correlation in progress and results. ...	88
Figure 62. Four-point bending test setup on MTS Exceed test frame. ....	89
Figure 63. Four-point bending test setup with DIC. ....	90
Figure 64. Allied TechCut 5 precision saw to section specimens. ....	91
Figure 65. Buehler SimpliMet 4000 mounting press. ....	91
Figure 66. Sectioned and mounted samples in bakelite. ....	92
Figure 67. ZEISS EVO LS 15 SEM platform. ....	92
Figure 68. Electrochemical etching setup. ....	93
Figure 69. PV map implemented for processing 28 SS 316L samples. ....	96
Figure 70. Layout of 28 samples (as circled) arranged using QuantAM software. ....	96
Figure 71. Samples being processed inside the SLM build chamber. ....	97
Figure 72. As-built samples on the build plate with the support structures. Sample numbers are also indicated. Observe that sample #28 exhibited curling due to higher energy input. ....	97
Figure 73. Samples were cut using wire-EDM from the middle region. Each sample is 7 mm long, 5 mm thick, and 5 mm wide. ....	98
Figure 74. Vickers hardness indents on the lowest density sample #1 (90.78%). Visible are hatch patterns and pores (pores were due to incomplete melting of the powder). ....	99
Figure 75. Vickers hardness indents on a higher density sample #12 (98.21%). Note the significantly less pores in comparison to Figure 74. ....	100
Figure 76. Vickers hardness of 28 samples showing the effects of VED. Highlighted circles show five selections of hardness values incorporate for fabricating gradient samples. ....	103

Figure 77. Relative density graph for the SLM-built SS316L samples with varying process parameters. The average density data represented was measured by the Archimedes method. Notice the five circled values chosen for the gradient sample fabrication. ....	104
Figure 78. Light optical images of five-selected samples which will be used for fabricating graded bulk structures. ....	106
Figure 79. Comparison of densities: the red square markers are data points from the Archimedes method, whereas the black circle markers represent data points of the optical method (Image J).....	107
Figure 80. Nanoindentation measurements of Modulus of Elasticity (GPa) for selected five SLM-built SS316L samples. ....	108
Figure 81. VED-based bounds indicating different regions of defects.....	111
Figure 82. Archimedes density for all 28 samples. Highlighted is monotonic change in density with a single power.....	112
Figure 83. Archimedes density for all 28 samples. Highlighted in black circles are the five selected samples for graded bulk structure fabrication. ....	113
Figure 84. Single parameter control of relative density is achievable at constant laser power of 150 W.....	113
Figure 85. Optical density for all 28 samples across both XY/XZ planes. A second order equation for lower densities (~90-99%) and a linear fit for higher densities (~99% +).....	114
Figure 86. Hardness for all 28 samples. Highlighted is monotonic change in hardness with a single power.....	115
Figure 87. Monotonic change in hardness is achievable at constant laser power of 175 W. ....	116
Figure 88. DoE of the process parameters design space for SLM of SS 316L samples. Representative optical micrographs of the etched top build surfaces show over-melted, well-melted, and porous regions highlighted with different colors as per the color bar on the right. ....	118
Figure 89. Optical images showing hatch overlapped regions and laser scan tracks and half-cylindrical contours of melting pools and layer thickness in transverse (XY) and longitudinal (XZ) sections, respectively. ....	123

Figure 90. SEM images of SLM processed SS 316L sample 2 in (a) XY plane showing the laser scan tracks and hatch overlapped regions, and (b) XZ plane showing the half-cylindrical melt pools and layer thickness.....	124
Figure 91. SEM images showing the laser scan tracks, melting pools morphology, and defects (for instance, un-melted powder particles, voids, Lack-of-fusion voids) in transverse (XY) and longitudinal (XZ) sections for sample 4 ( $\rho = 90.78\%$ ) and sample 3 ( $\rho = 98.21\%$ ). .....	125
Figure 92. SEM micrographs of sample 3; (a) the transverse (XY) plane illustrated with the white arrows, and (b) the longitudinal (XZ) plane fusion line between the two melt pools is seen with grain refinements of cell structure illustrated with the white arrows. ....	127
Figure 93. SEM images showing the defects in XY plane of the sample. A) Melt tracks with lack-of-fusion defect, B) Solidification defect due to incomplete binding is visible, C) and D) Cellular cells inside a melt pool.....	128
Figure 94. SEM micrographs showing the defects in (XZ plane of the sample. A) Lack-of-fusion pore and unmelted powder particle, B) Zoom-in region of fusion line between the two melt pools along with spherical gas pores, C) Higher magnification of fusion line region depicting side-branching of cell structure.....	128
Figure 95. SLM processing regimes showing different defect regions. ....	130
Figure 96. Optical image of etched surface showing the LOF and gas pore. ....	131
Figure 97. SEM image showing the void and spherical gas pore.....	131
Figure 98. Defect analysis of (Top) XY plane and (Bottom) XZ plane for sample 1. ...	132
Figure 99. Defect analysis of (Top) XY plane and (Bottom) XZ plane for sample 2. ...	133
Figure 100. Defect analysis of (Top) XY plane and (Bottom) XZ plane for sample 3. ...	134
Figure 101. Defect analysis of (Top) XY plane and (Bottom) XZ plane for sample 4. ...	135
Figure 102. Defect analysis of (Top) XY plane and (Bottom) XZ plane for sample 5. ...	136
Figure 103. Sphericity analysis by XCT for sample 5.....	137
Figure 104. Optical density in both planes for select five samples against VED.....	138
Figure 105. Mean circularity in both planes for select five samples against VED.....	139

Figure 106. Mean pore radius in both planes for select five samples against VED. ....	139
Figure 107. Mean circularity in both planes for all samples against VED. ....	140
Figure 108. Mean pore radius in both planes for all samples against VED. ....	140
Figure 109. Optical density in both planes for all samples against VED. ....	141
Figure 110. Optical defects in both planes for all samples against VED. ....	141
Figure 111. Representative optical images of sample #2 ( $E_v = 39.77 \text{ J/mm}^3$ ; $\rho = 96.35\%$ ), #3 ( $E_v = 48.48 \text{ J/mm}^3$ ; $\rho = 98.21\%$ ), and #5 ( $E_v = 52.10 \text{ J/mm}^3$ ; $\rho = 97.50\%$ ) showing phases of ferrite, austenite, and martensite [264]. ....	144
Figure 112. XRD diffractogram of SLM-fabricated SS 316L on two different surface planes for sample 3 showing the prominent diffraction peaks of phases. Black color represents the transverse (XY) plane or top surface, whereas the red color represents the longitudinal (XZ) plane or side surface pattern. ....	148
Figure 113. (A) EBSD (2D) maps of the as-built SS 316L sample in a transverse (XY) plane. Pole figures and inverse pole figures are also shown. (B) EDS mapping of the sub-structure with selected region's elemental distributions with corresponding Fe, Cr, Ni, Mo, C elemental maps. ....	151
Figure 114. (A) EBSD (2D) maps of the as-built SS 316L sample in a longitudinal (XZ) plane. Pole figures and inverse pole figures are also shown. (B) EDS mapping of the sub-structure with selected region's elemental distributions with corresponding Fe, Cr, Ni, Mo, C elemental maps. ....	152
Figure 115. EDS spectrum of SLM fabricated SS 316L for, a) selected top surface area for sample 5, b) point analysis chosen over an unmelted powder particle. ....	154
Figure 116. Resolution study DOE with 1-layer, 2-layers, 4-layers and 8-layers configurations. Each layer is $50 \mu\text{m}$ in thickness. Layers shown in purple color are processed using standard process parameters. ....	157
Figure 117. Resolution study (pyramids) samples arranged on the build plate. ....	157
Figure 118. Mounted and polished resolution study samples. ....	158
Figure 119. 1-layer grid arrangements for nanoindentations. Each layer has three indents at $20 \mu\text{m} \times 20 \mu\text{m}$ grid with indents starting from lower left (1) to top-right corner (51). ....	159
Figure 120. Force-Displacement plots for 51 indents for 1-layer sample. ....	159

Figure 121. Average hardness for 1-layer sample. ....	160
Figure 122. Average modulus for 1-layer configuration sample. ....	161
Figure 123. Light optical overview of polished surfaces of 1-layer and 2-layers samples. ....	162
Figure 124. Light optical overview of polished surfaces of 4-layers and 8-layers samples. ....	163
Figure 125. Comparisons of average hardness of all four sample configurations. ....	164
Figure 126. Comparisons of average modulus of all four sample configurations. ....	165
Figure 127. Light optical images of etched 2-layers sample configuration. ....	166
Figure 128. SEM images of etched 2-layers sample configuration. ....	166
Figure 129. EDS analysis of on melt-pool overlap region for 2-layers sample. ....	167
Figure 130. Summary of phases in both planes for all 28 samples. ....	168
Figure 131. PV map for defects across all samples. ....	170
Figure 132. Dimensions of tensile specimen based on ASTM E8 [248]. ....	172
Figure 133. Build plate layout showing sample arrangements. ....	174
Figure 134. SLM printed SS 316L tensile, bending, fatigue, and resolution samples. ...	174
Figure 135. Stress-strain plot for 209_F sample. ....	175
Figure 136. Stress-strain plot for all 18 samples. ....	176
Figure 137. Side by side comparison of fracture location in the gauge section of front tensile samples. ....	181
Figure 138. Fracture surfaces (top & bottom) mounted for six front tensile samples. ...	181
Figure 139. Dimensions of medium size (50%) tensile specimen in mm based on ASTM E8 [285]. Notice the five different zones having monotonic changes in hardness along its gauge length. Also shown is the picture of the post-build base plate and other relevant details. ....	190

Figure 140. Pre-and post-tensile hardness measurements were taken at the transitional regions (common boundaries between two zones) as highlighted with arrowhead. ....	191
Figure 141. Comparison of microhardness: the square markers show target, whereas the red circle markers represent data points of the gradient sample for medium size graded sample. ....	192
Figure 142. Comparison of microhardness: the red square markers show target, whereas the green circle markers represent data points from post-tensile measurements for medium size graded sample. ....	193
Figure 143. Location and properties (HV, $E_v$ , $\rho$ ) of different zones highlighted on large samples. ....	194
Figure 144. Stress-strain curve of graded large sample #2. ....	195
Figure 145. Stress-strain curve of graded large sample #1. ....	196
Figure 146. Stress-strain curve of graded medium sample #1. ....	197
Figure 147. Stress-strain curve of graded medium sample #2. ....	198
Figure 148. DIC images of longitudinal strains across the graded gauge length of sample1 and sample 2 are shown. Highlighted marks showed the similar behavior of maximum strain regions. ....	199
Figure 149. Stress strain curve for graded large sample 2 with highlighted points indicating maximum localized strains captured via DIC during the test. ....	199
Figure 150. Successive DIC images of longitudinal strains in % of the large sample of highlighted points on the stress-strain curve. ....	200
Figure 151. Temporal strain evolution induced in each zone (shown as pixels) during the tensile test until 26% global strain. ....	200
Figure 152. Zone-wise temporal strain evolution induced in each of the five zones. Highlighted regions in green color showed shifts in strains during the test. ....	201
Figure 153. Temporal strain evolution (jumping around) across the five zones during the elastic regime of tensile testing. ....	202
Figure 154. Zone-2 induced the maximum strain at the end of tensile test. ....	203
Figure 155. Size comparison post-tensile test amongst different sample sizes. Notice the fracture location highlighted by the pink arrowheads. ....	206

Figure 156. Fracture morphologies of large tensile sample tested along build direction (a-b) low magnification and (c) high magnification views on the fracture surfaces. River marks are visible along with pores. ....	206
Figure 157. Dimensions of FPB samples as per the ASTM C1161-18 [251].....	207
Figure 158. Schematic representation of the FPB test. Regions denoted with a and b were graded with select process parameters.....	208
Figure 159. As-printed homogeneous and graded FPB specimens. Notice the outer and inner regions with different properties. ....	208
Figure 160. Load-deflection curves for FPB sample 4T2.....	209
Figure 161. DIC image of sample 4T2 from (a) during the test (b) bands of different colors shows the strains in $E_{xx}$ direction during FPB test. Note the transition from tension (red color) to compression (blue color) at the bottom and top of the beam, respectively. ....	210
Figure 162. Line analysis and strain distributions of sample 4T2 in (Top) $E_{xx}$ direction and, (Bottom) $E_{yy}$ direction during FPB test. Note the lines were symmetrical with respect to the neutral axis. ....	211
Figure 163. Point analysis of sample 4T2 in $E_{xx}$ direction during FPB test. The curves represent strains at select points in $E_{xx}$ . Note the lines passing through the middle point showed very little deflection due to vicinity to the neutral axis. ....	212
Figure 164. Interface region within the gauge length of medium tensile sample. Note 2_3 represents region between zone 2 ( $P = 200$ W; $E_v = 39.77$ J/mm <sup>3</sup> ; $\rho = 96.35\%$ ) and zone 3 ( $P = 200$ W; $E_v = 48.48$ J/mm <sup>3</sup> ; $\rho = 98.21\%$ ). ....	213
Figure 165. A portion of the interface reconstructed from a set of optical micrographs in different planes. The features are marked on two different planes along with the interface. Pore defects on the surface of zone 2 are visible, whereas relatively denser surface is seen for zone 3.....	214
Figure 166. Summary of process parameter bounds on PV map highlighting processing-structure-property relationships for all samples.....	219
Figure 167. Difference in thermal conductivity amongst samples with varying porosity.....	273



## LIST OF TABLES

	Page
Table 1. Recommended process parameters by the manufacturer.....	70
Table 2. Nominal chemical composition (in wt %) of SS 316L powder (as supplied) [241] and the ASTM A240 [242] specified composition range of SS 316L....	76
Table 3. Results from SS 316L PSD analysis.....	77
Table 4. Summary of selected 2D DIC parameters. ....	86
Table 5. VED-based process parameters used for experiments.....	95
Table 6. Average hardness and density results. ....	101
Table 7. Selected five process parameter configurations.....	105
Table 8. Summary of physical and mechanical properties of selected five samples. ....	110
Table 9. Summary of optical micrographs in both XY and XZ plane of five samples.	120
Table 10. Summary of XCT parameters used in analysis of 3D defects for sample 5. .	137
Table 11. Summary of defects in both XY and XZ plane of select five samples. ....	138
Table 12. Summary of directional defects for all samples. Highlighted in grey color are select five samples.....	142
Table 13. Summary of identified phases for all samples. Highlighted in grey color are select five samples.....	146
Table 14. Summary of five samples with processing conditions, and test results.....	147
Table 15. Composition (wt %) distributions of before and after SLM processing. ....	155
Table 16. Tensile specimen nomenclatures with hardness and density values.....	173
Table 17. Tensile properties for 209_F sample. ....	177
Table 18. Tensile performance for six variants across three sample positions.....	178
Table 19. SLM tensile performance when compared to traditionally made samples. ....	179

Table 20. Fractography observations for front 6 samples.....	183
Table 21. Fractography observations for reference wrought SS 316 L. ....	189
Table 22. Post-tensile hardness for each zone and interfaces for medium sample. ....	193
Table 23. Graded sample tensile performance.....	196
Table 24. Results from SS 316L PSD analysis.....	264
Table 25. Results from spherical SS particle examples.....	265
Table 26. Results from agglomerates SS particle examples.....	268
Table 27. Results from satellite SS particle examples.....	271

# 1. INTRODUCTION

## 1.1 Aim and Objectives

The overarching goal of this research was to systematically investigate the causalities within the processing-structure-properties-performance (PSPP) framework for the SLM of SS 316L FGAM bulk structures. Specifically, this study aims to elucidate the relationships between AM process conditions and variations in macro- and microstructures and how such physicochemical traits affect the resulting property distributions. To achieve this goal, the following objectives were coined:

- Investigate the VED-based process parameters to identify the processing bounds for obtaining specific macro/microstructures and functionally usable properties
- Elucidate processing-structure links at micro/macro scales to identify root causes of physical/mechanical property variations
- Investigate the FGAM bulk structure strain performance under various loadings and ascertain the role of zonal interfaces
- Develop guidelines for a single alloy graded bulk structure fabrication on a pulsed laser-based SLM platform for repeatable part production

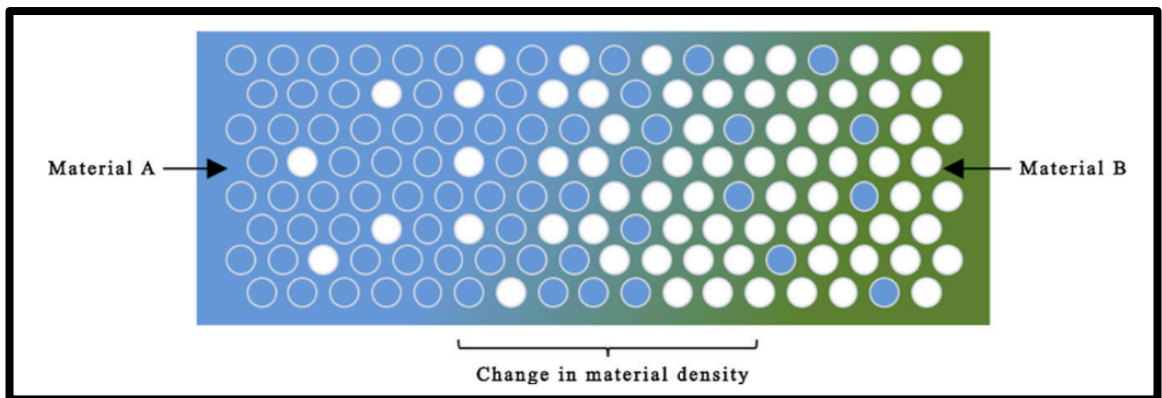
## 1.2 Motivations

With a growing need for the development of application-specific materials in aerospace, automotive, biomedical, and consumer products, conventional monolithic materials are limited in their capability to be tailored to the application. Functionally graded materials (FGMs) are a special class of composite materials that combine multiple materials, compositions, or geometries in gradually varying fashions, in one or more directions, from one end-surface to another, resulting in spatial variations of material properties [1]. FGMs offer abilities to gradually transition microstructure and compositions within a single component to meet local and bulk performance requirements of the component for end-use applications [2, 3]. FGMs are often characterized by their spatial variations of the constituent materials or macro/microstructure (*e.g.*, porosity, phase, texture, grain size, etc.) thereby, changing the corresponding material properties in line with the functional requirements [4, 5]. FGMs can also eliminate the sharp material type/property interfaces responsible for initiating failures and replace them with a smooth transition from one material to another [6, 7].

Additive manufacturing (AM), also known as three-dimensional (3D) printing, is a unique technique that allows the fabrication of three-dimensional near-net-shape parts by layer-wise addition of material [8-10]. This transformative process provides a high degree of design customization and efficient stock material usage with minimal waste [11-13]. AM has gained worldwide popularity across almost all sectors due to its

offering an enhanced alternative to many conventional manufacturing processes [14-17]. As per the recent Wohlers Report, the AM industry will see significant growth and may well exceed the total market presence of over \$40.8 billion by 2024 [18].

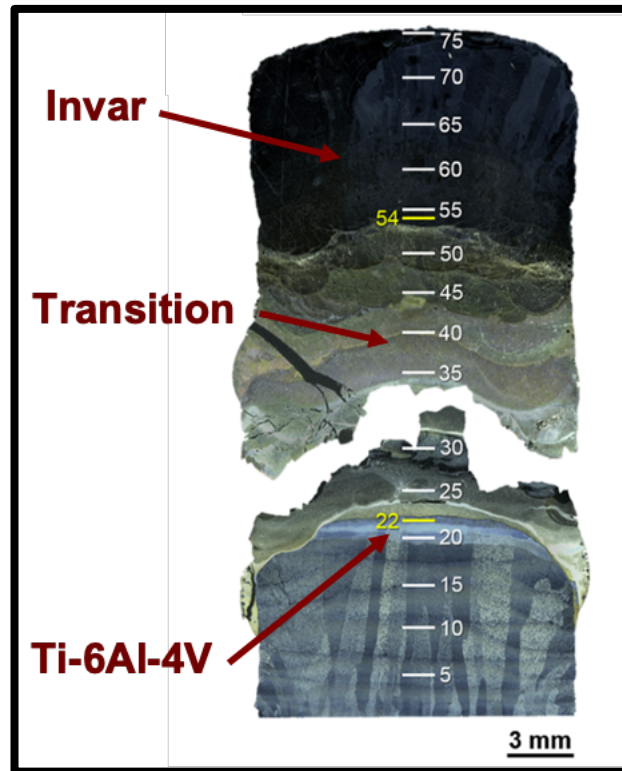
AM techniques enable a paradigm shift in FGM processing by allowing the directional control and spatial gradation of printed structures, hence coining a new term, Functionally Graded Additive Manufacturing (FGAM) [19]. Multi-material materials can well surpass monolithic materials' mechanical and microstructural limitations due to their unique capabilities of having heterogeneous properties [20]. Figure 1 illustrates two materials, when spatially graded, exhibit uniquely irreconcilable properties compared to that when processed individually.



**Figure 1. Schematic of multi-material (density) distributions within the part [19].**

However, multi-material structures present several challenges in terms of uncertainty at manufacturing and processing and performance and service life due to the heterogeneous nature of graded interfaces, different mechanical behaviors under stress,

thermal expansions, corruptions, amongst others. Figure 2 illustrates a multi-material sample that exhibited a large crack at the interface due to the different coefficients of thermal expansions amongst them.



**Figure 2. Optical micrograph of multi-material FGAM sample exhibiting a large interlayer fracture at the transition region [21].**

Single material FGAM processing via SLM is a novel research quest to overcome challenges and complex multi-material compatibility issues. Currently, with limited studies investigating the guidelines for design, fabrication, and performance, single material gradation offers the following advantages:

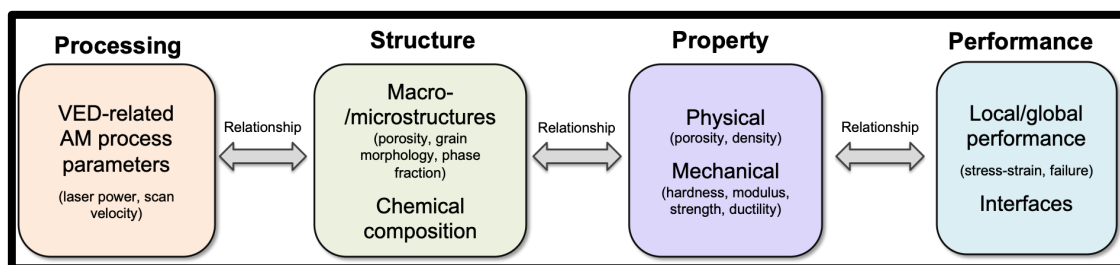
- Avoids sharp property interfaces, most common in multi-material parts, and limits restrictions and vulnerabilities of extraneous welds and joints
- Multi-material parts (manufactured via AM/other) can commonly display ‘incompatibility’ by sharply differing thermal coefficients and/or stress discontinuities leading to part failure. Further, certain material combinations in close contact can promote corrosion or other degradation mechanisms. Instead, when restricted to common chemical composition, the potential for such ‘material incompatibility’ is minimized.
- Currently, SLM machines are restricted to a single hopper (one powder feedstock), so investigating the repeatable property variations is worthwhile for tuning thermomechanical responses.
- Finally, the ability to tune spatial physical/mechanical property distributions allows for parts to be designed/optimized for minimizing weight, deflection, etc. For instance, stiffer (higher elastic modulus) layers could be imparted as top/bottom layers in bending beams to control deflection, and outer surface layers could be made to have higher hardness for abrasive wear resistance, failure paths or zones could be intentionally designed, etc.

In light of this, SLM offers tailoring of component macro/microstructure for efficient geometry/weight in specific thermo-mechanical applications while using a single alloy.

Alongside the ability to produce singular, low-volume components, SLM offers a single-step process to achieve multi-functionality in the as-built part, *e.g.*, harder surface layers, which, conventionally, would require post-processing. SLM manufacturers have a single powder hopper (currently but changing), which further warrants an investigation into achievable property variations for a given metal or alloy. Thus, the full potential of the SLM processing of FGAM has yet to be realized.

### 1.3 Research Methodology

In this work, a systematic investigation was carried out to demonstrate the fabrication of property-graded 316L bulk structures via SLM. Here, we provide a better understanding of the processing-structure-properties-performance (PSPP) framework for the SLM of FGAM bulk structures, as illustrated in Figure 3.



**Figure 3. Framework implemented for this research work.**

A brief overview of the research objectives and goals for each of the core pillars, *i.e.*, processing/structure/properties/performance, are explained.



The processing research area of SLM involves an extensively complex phenomenon at different spectrums of the processing steps. Even for a slight modification or minor adjustments in the feedstock material, component orientation or geometry, process parameters, or post-processing steps could result in drastically different properties in printed components. For this, the relationships between VED-related process parameters, such as laser power and scan speed/exposure time, were investigated to identify functionally acceptable processing bounds.

Structurally, the SLM process produces uniquely nonhomogeneous macro- and microstructures. Due to rapid solidification processing, detailed examinations have been made to elucidate the relationships between SLM process conditions and variations in macro- and microstructures and how such physicochemical traits affect the resulting property distributions.

Properties of SLMed materials or parts have been shown to supplant conventionally processed materials (hardness, tensile, fatigue, corrosion, etc.). Physical and mechanical responses have been investigated for structures fabricated using different SLM process conditions and are further linked to length-scale-dependent microstructures.

Performance of graded bulk structures (tailored for various thermo-mechanical responses) has been undertaken to investigate the effects of zonal variations in local/global strain evolution (spatial/temporal) and their roles in failure. The role of interfaces has also been explained in detail.

## 1.4 Expected Original Contributions

The outcomes of this research will add to the knowledgebase of the PSPP chain for SLM of metals from the perspective of designing and fabricating FGAM parts. Specifically, mechanical property-graded bulk structures can be realized from a single metallic alloy (SS 316L) and tailored for thermo-mechanical performance and failure. The following original contributions are expected from this research work:

- A mapping of the relevant process parameter subset design space that details the physical/mechanical property trends in relation to the VED-based process conditions – will define the processing bounds for functionally acceptable property ranges and will enable one to select a process parameter combination that intentionally yields a different (but repeatable) property value for SS 316L
- Scientifically linking the processing-structure-property chain of the SLM of SS 316L by correlating the processing-related causes with the variations in macro- and microstructures, and hence the resulting (intended) physical/mechanical property distributions – the focus will be on elucidating the underlying principles behind each cause-effect pair and their implications
- Local and global strain evolution (spatial/temporal) and failure in bulk FGAM structures under different loading/stress states
- Quantification of the spatial property resolutions that are repeatably achievable
- Role of zonal interfaces under strain evolution and for failure

Altogether, these findings could be used to control and alter the spatial macro- and microstructures of FGAM structures and further lay the foundation for understanding and tailoring the local and global mechanical properties and performance of FGAM bulk parts as well as the role of interfacial zone morphology.

## **1.5 Dissertation Structure**

The dissertation is arranged in the following order: Chapter 1 reported objectives, motivations (including a brief review on AM, FGM, and FGAM), research methodology along with intellectual merits and original contributions from this research endeavor. Chapter 2 provides an in-depth review of the state-of-the-art multi-disciplinary literature review. Firstly, a general summary of additive manufacturing processes is presented. Next, a detailed overview of the selective laser melting process is presented, along with process-specific parameters and post-processing techniques. Current knowledge of stainless steel is presented, followed by SLM processed SS 316L and their mechanical/physical properties and microstructures. Lastly, the chapter highlights the research in the functionally graded material field and summarizes identified knowledge gaps. Chapter 3 introduces the research methodology framework implemented during this study, including the research questions, tasks, and outcomes. Chapter 4 discusses the materials and equipment used in spectroscopy, microscopy along with the details about the experimental procedures for physical/mechanical testing. Chapter 5 focuses on the research's main theme, *i.e.*, performing experiments to

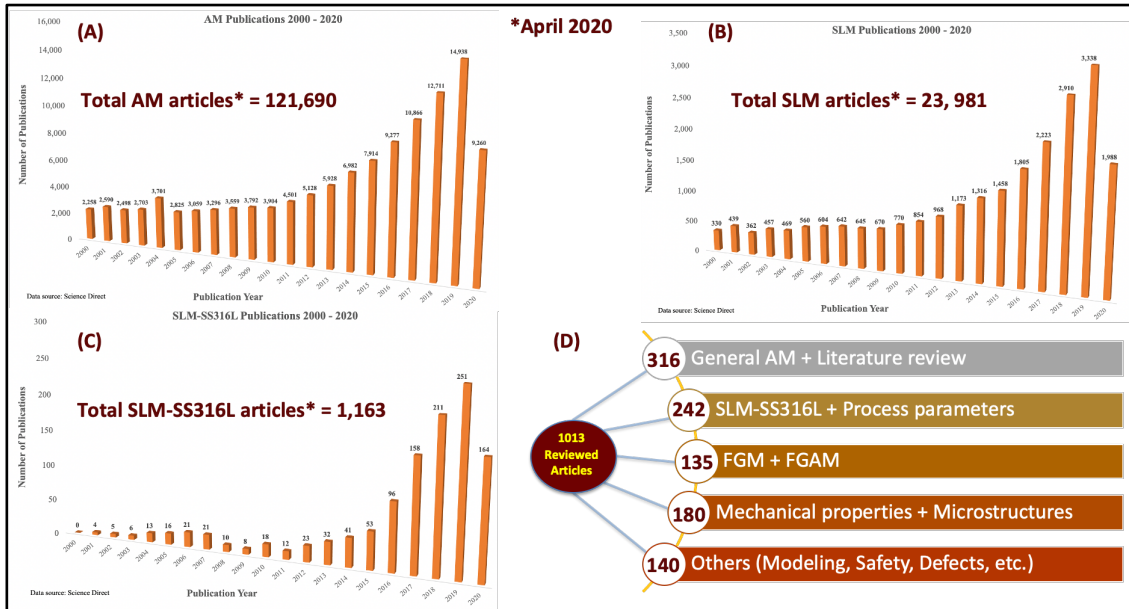
obtain usable property range for SS 316L when processed on a pulsed system. The remainder of the chapter examines the relationship of VED-related process parameters to dependent physical/mechanical properties. The purpose of Chapter 6 is to study the causation of mechanical property variations by investigating the microstructure at different length scales (micro, meso, and macro). This chapter also presents an in-depth analysis of microstructures and physical phenomena at each scale to showcase the causalities within the PSPP framework. Chapter 7 summarizes the remaining parts of the study, including manufacturing of property graded structures to be tested under various loading modes. Next, the effects of interfaces on local/global performance are presented. Chapter 8 discusses a summary of the main conclusions obtained from this research and briefly discusses the future work.

## 2. BACKGROUND & LITERATURE REVIEW

The literature review presented is an amalgamation of multi-disciplinary fields ranging from material science and metallography to mechanical engineering and manufacturing. The state-of-the-art in selective laser melting (SLM) especially pertaining to SS 316L, is presented, and literature reviews of stainless steels and functionally graded materials (FGMs). Finally, current knowledge of SLM related to FGMs is also explored to identify knowledge gaps.

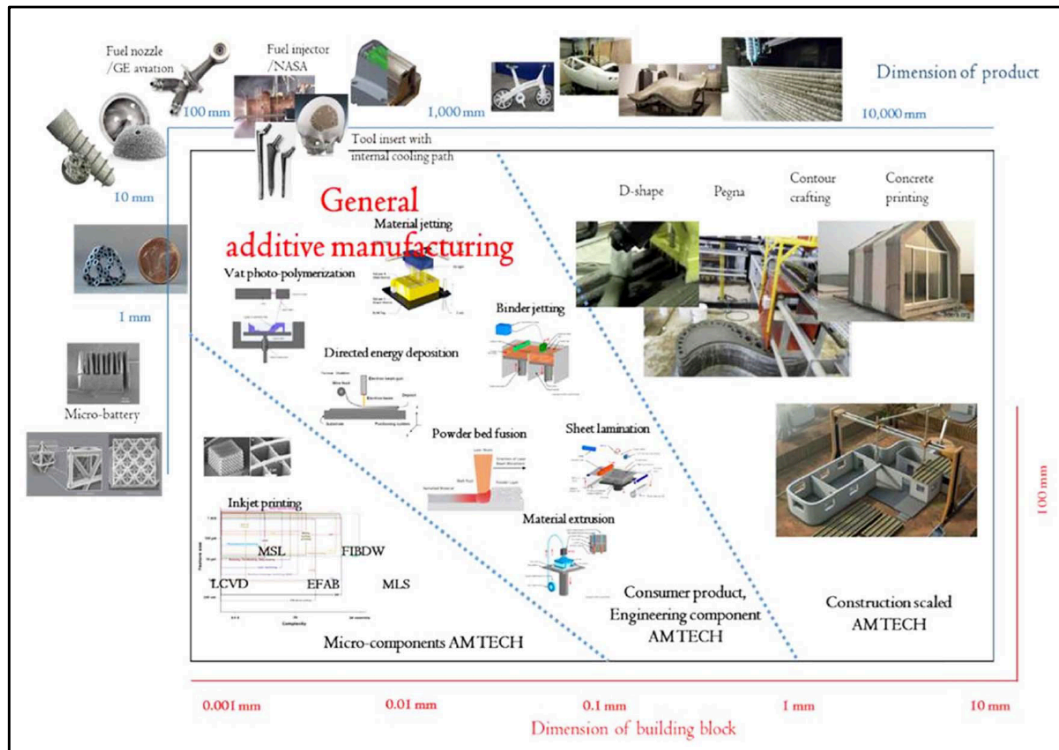
### **2.1 Additive Manufacturing**

Additive Manufacturing (AM), a.k.a. 3D printing, is a process for producing three-dimensional parts by layer-wise addition of material [22-25]. It is an umbrella term for a set of technologies and processes that have gained maturity over the last three decades. Considering AM, an understanding of layered fabrication dates back to 1920 when Baker [26] (U.S. patent, 1,533,300) used an electric arc and metal electrode to form decorative articles using the layer-wise material addition. Furthermore, Blather [27] discovered methods for topography and photosculpture in 1892. The field of AM is continuously evolving, and this report reviews a most recent subset of articles published in Science Direct, as seen from Figure 4.



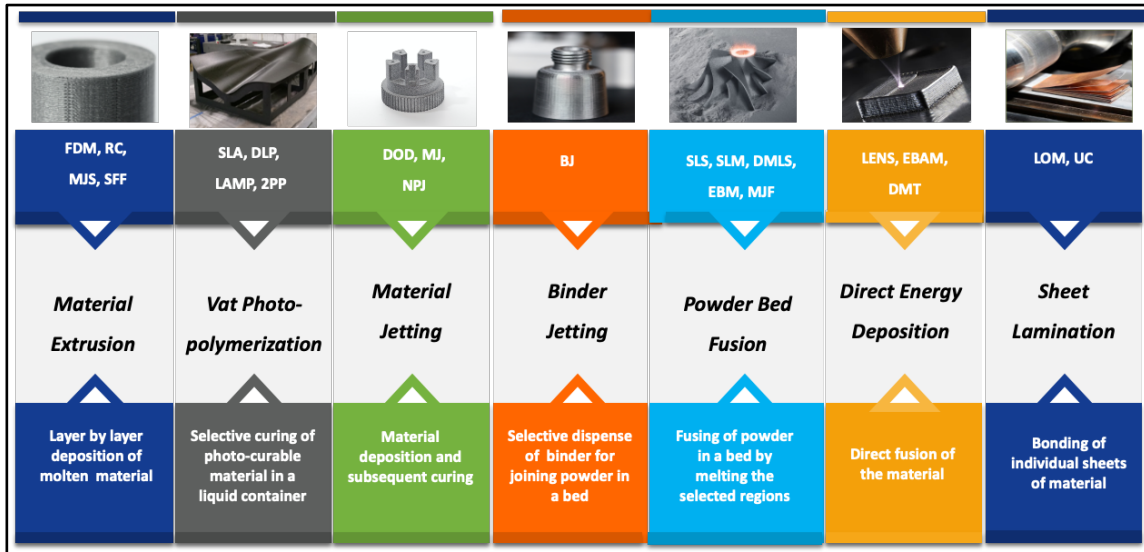
**Figure 4. AM literature snapshot for the span of the last 20 years.**

The American Society for Testing of Materials (ASTM) F2792-10 defined AM as "the process of joining materials to make objects from 3D model data, usually layer upon layer, as opposed to subtractive manufacturing methodologies" [28]. Figure 5 provides a multi-scale overview of AM applications in different sectors that have reached a maturity level to be adapted for commercial usages.



**Figure 5. Multi-scale applications of different AM processes [13].**

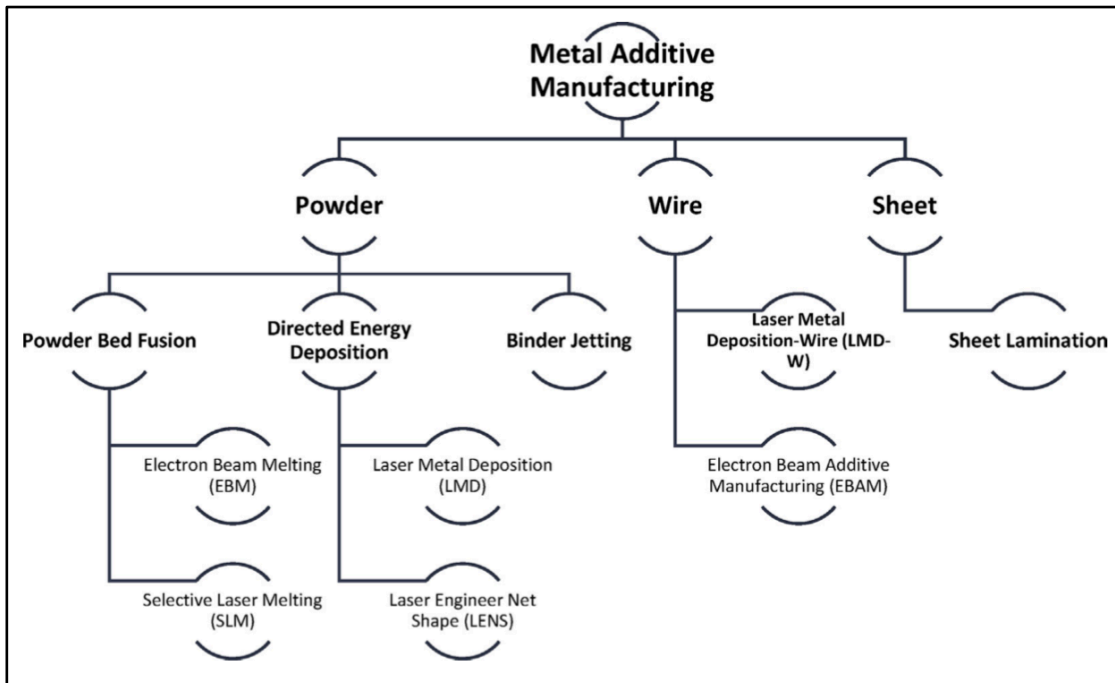
Figure 6 provides a broad classification of different AM processes based on the ASTM F2792 standards. They are primarily classified into seven types; namely, material jetting (MJ), binder jetting (BJ), directed energy deposition (DED), material extrusion (ME), powder bed fusion (PBF), vat polymerization, and sheet lamination. Further, hybrid manufacturing approaches could combine aspects of the above seven process type or combine additive and subtractive manufacturing processes on a single platform.



**Figure 6. Seven families of AM processes according to ASTM F2792 standards.**

Furthermore, the metal AM processes have gained special attention from researchers across industries and academia alike. As per the recent Wohlers Report 2020, the global AM market will see a significant growth of 14.4% and may well be exceeding the total market presence of over USD 26.68 billion by 2027 [18]. Advancements in metal 3D printing will be projected around USD 10 billion by 2027. This overwhelming popularity is not surprising because it aligns well with technologies such as scanning and reverse engineering that primarily drive component customization [29]. Figure 7 illustrates the classification of metal AM processes.

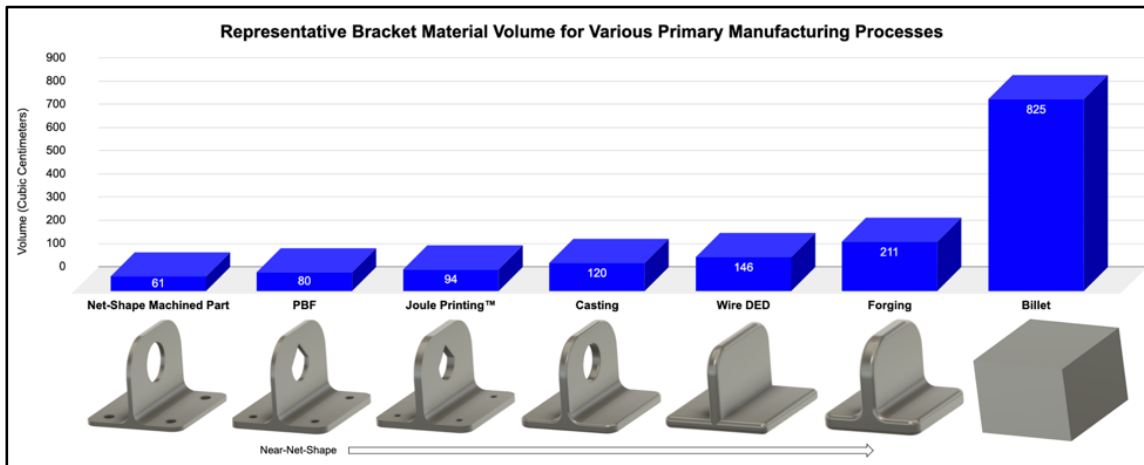




**Figure 7. Classification of metal AM processes [13].**

In a nutshell, AM is a unique manufacturing technique that is based on the common principle of slicing a solid 3D CAD model into multiple 2D layers, where each layer is built at a time and can be customized with a choice of processing conditions, thus providing design freedom to build complex part geometries to near-net-shape [30]. Furthermore, manufacturing parts via this approach eliminate part-specific tooling requirements, saves materials, and reduces machine downtime, leading to an increase in equipment readiness [31, 32].

Figure 8 illustrates a comparison between primary manufacturing processes, including subtractive and additive manufacturing processes, in terms of material volume (in cubic centimeters) consumed for obtaining a representative bracket.



**Figure 8. Comparison amongst various primary manufacturing processes [33].**

For this thesis’s purpose, we will be focusing on selective laser melting (SLM) technology. The following sections aim to introduce and explain the SLM working principles, laser processing parameters (particularly VED-related process parameters), and melting and solidification phenomenon.

## 2.2 Selective Laser Melting (SLM)

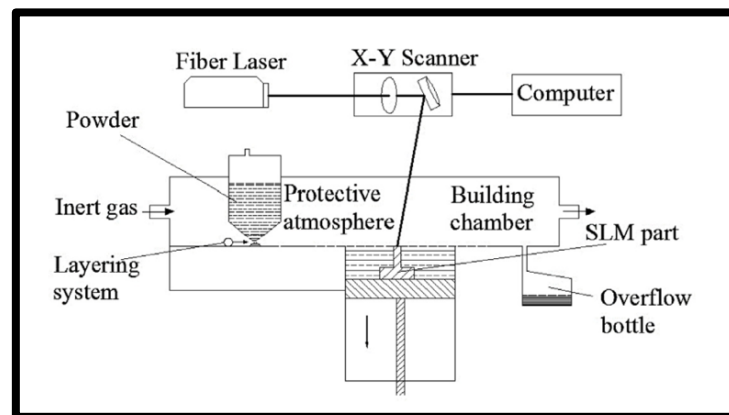
The laser powder bed fusion process (L-PBF) is one of the most versatile, well-researched, and important metal AM techniques that belong to a sub-class of powder-bed fusion (PBF) as per the terminology devised by ASTM International [28]. The L-PBF process is also sub-divided into Selective Laser Sintering (SLS) and Selective laser melting (SLM) [34]. SLS has been predominantly used in the manufacturing of plastic

parts, whereas SLM is for metal. SLM is also known as Direct Metal Laser Sintering (DMLS).

The following sub-sections explain the general framework of the SLM process, working principles, process physics, and current and future state of the art and trends.

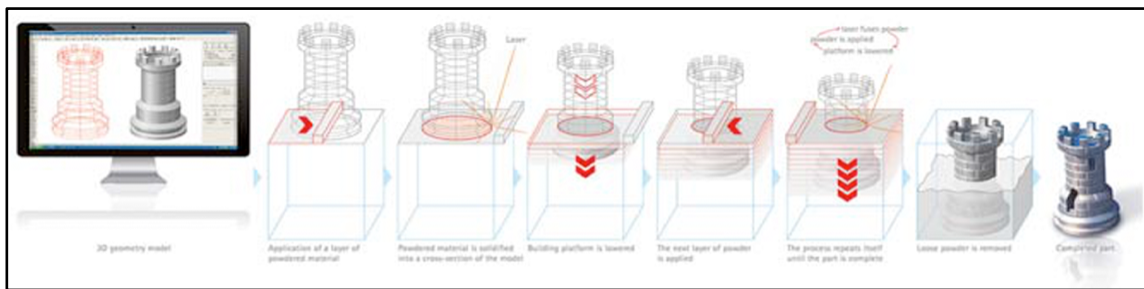
### 2.2.1 General Process Overview

SLM has been at the forefront of AM for the last two decades and has successfully realized a wide array of functional metal components, giving many design choices to improve and optimize the part functionality and usable life [35]. More recently, SLM manufacturers are coming up with next-generation SLM platforms with state-of-the-art updates such as multiple high-performance lasers, increased build volumes, configurable lasers/optics, no materials restrictions, open-source control software, amongst other capabilities that will further enhance the SLM technology [36-39].



**Figure 9. Schematic representation of the SLM process [40].**

As shown in Figure 9, the SLM process utilizes a bed of powder metal, which is selectively melted with the aid of a high-energy laser beam, focused at a defined area where the powder is spread uniformly [41, 42]. Selected locations of the powder bed are exposed to the laser beam at a controlled speed, which in turn fuses the powder, creating a solid 3D part layer-wise in an inert gas environment [43]. The SLM process involves repeated heating and cooling cycles, and hence thermal gyrations. This process repeats until the desired part geometry is achieved, as seen from Figure 10 [44-47].



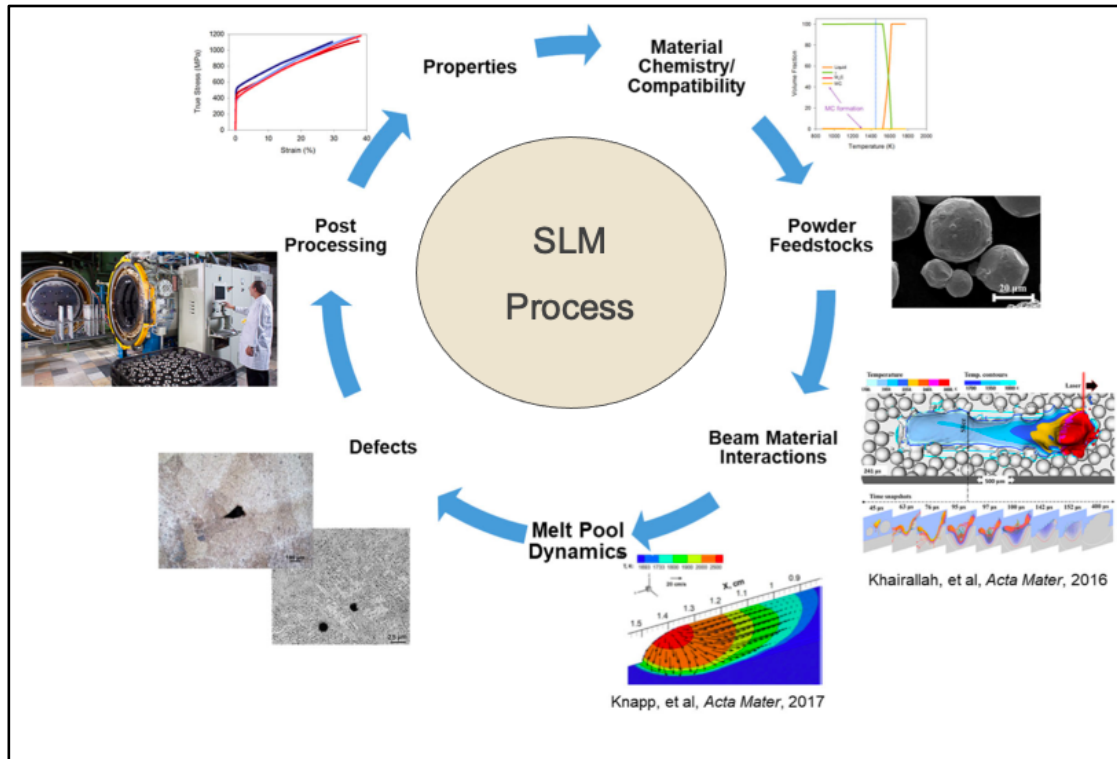
**Figure 10. Obtaining “Picture-to-Part” via SLM [36].**

### 2.2.2 Ongoing Research Themes in SLM

Early research on SLM was credited to Schleifenbaum and coworkers for demonstrating the tool-free manufacturing of complex part geometries [48]. Kruth et al. [49] have studied SLM of iron-based powder and characterized the parts by their microstructure, density, and mechanical properties. Kamath et al. [50] have reported that L-PBF has over 100 significant process parameters requiring process planning and control to ensure repeatable parts of desired geometry and material properties.

Assessment of these vital factors helps to understand the SLM process and how to obtain high-performance, defects-free, mission-critical parts with desired design optimization, mechanical properties, and near-full density [51-53].

To contribute to a greater understanding of the SLM process and further improve the part quality and reliability, substantial research efforts are underway, as seen from Figure 11.

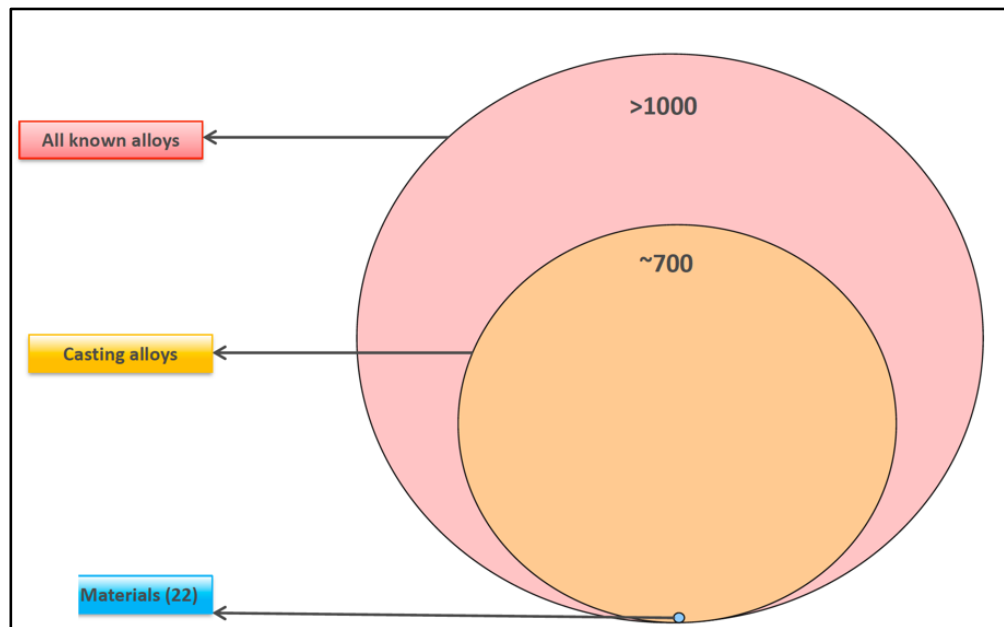


**Figure 11. Ongoing research avenues for the SLM.**

Researchers have reviewed recent developments of SLM literature with studies that have provided the status of this technology ever since it was first commercially

emerged in 1987. Initially, it was limited to mere a rapid prototype manufacturing up until early 2000, from where the SLM has been on a path to become a mature technology [54-56]. Scientific, technological, and economic challenges have currently been addressed for SLM processed parts [57-62].

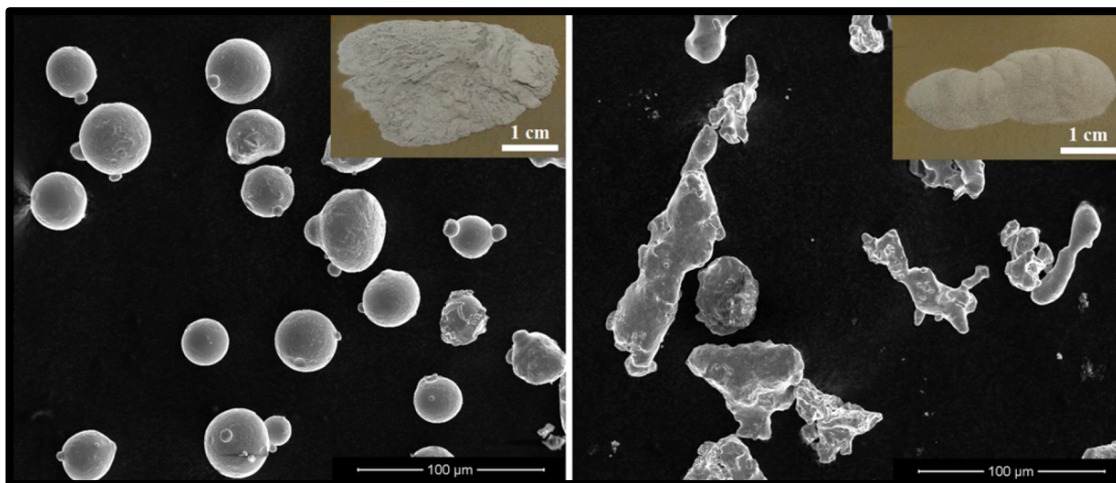
As of today, only conventional materials are fabricated using SLM [63]. SLM can only process over 20 different metallic alloys ranging from Inconel 625, Inconel 718, Ti-6Al-4V, Ti-6Al-7Nb, Ti-24Nb-4Zr-8Sn, Cobalt-based super-alloys, tantalum, AlSi10Mg, Al6061, Maraging Steels, H-13 Tool Steels, Stainless Steel (SS) 316L, 304, AISI 420, 17-4PH, 155PH, amongst several other [64-69]. As illustrated in Figure 12, designing next-generation alloys will be a critical technological gap for the current SLM landscape.



**Figure 12. Current processability of alloys for the SLM [70].**

### 2.2.3 Influence of Powder Feedstock

Powder morphology (for instance, shape, size, chemical composition) plays a crucial role in achieving the desired part performance. Researchers have paid attention to obtain revised powder manufacturing methods that suites AM industry needs in contrast to regular powder metallurgy (PM) and metal injection molding (MIM) sectors [71-80]. There are several powder processing techniques to produce metallic powders used in SLM, including gas atomization (GA), water atomization (WA), rotary atomization (RA), and plasma rotating electrode processing (PREP) [81]. Spherical-shaped particles have been preferred during SLM, which are commonly processed by the GA process. Powder particles exhibit irregular and sharp profiles when processed via the WA technique. Figure 13 illustrates SEM micrographs of stainless steel 316L powder particles processed by two different processing techniques.



**Figure 13. SEM images of stainless steel 316L powder particles processed via the a) GA and b) WA techniques [82].**

#### 2.2.4 Laser-Powder Interactions

After the powder is spread on the build plate or top of the already solidified layer, it is imperative to have a correct amount of laser exposure for successful melting and subsequent processing. The amount of energy imparted on the powder bed determines the melt pool shape, size, and ultimately solidification phenomenon [83]. The surface roughness, quality, and mechanical properties of the printed parts will be an amalgamation of the powder bed's thermal mapping and heat transfer phenomenon. Figure 14 illustrates a cross-sectional view of laser and powder bed interactions when the laser beam strikes the powder particles.

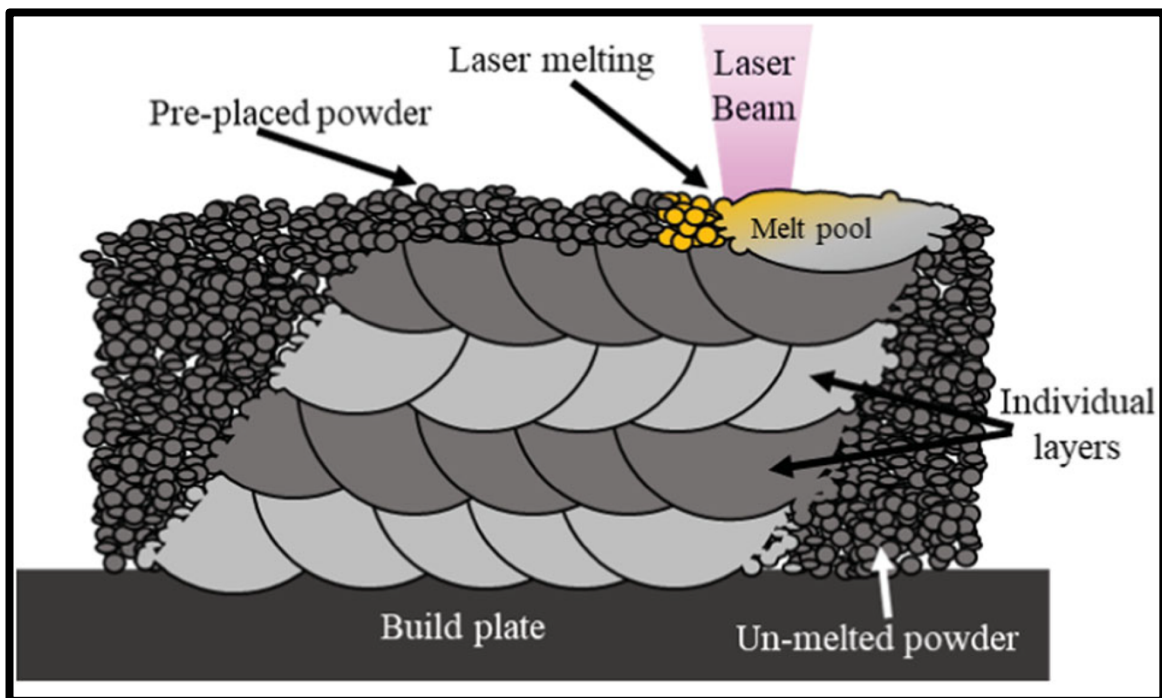
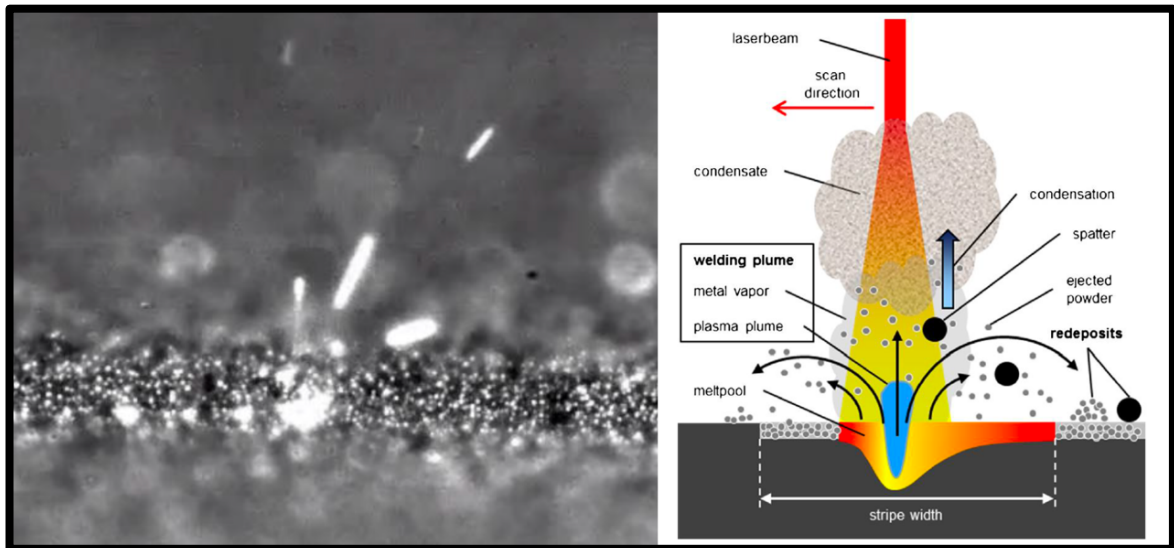


Figure 14. Schematic of cross-sectional view of laser-powder interactions [84].



Suppose the laser source moves too fast or too slow. In that case, the temperature distributions on the powder bed will be nonhomogeneous, experiencing phenomena such as Marangoni flow and conduction, convection, as well as radiation [85]. In case of too rapid and localized exposure of high-energy laser beam could induce defects such as residual stresses, material vaporization, elemental segregation, keyholing, spattering, and inclusions as seen from Figure 15 [86].



**Figure 15. Laser path and powder interactions during SLM [86].**

### *2.2.5 Influence of SLM Process Parameters*

The right combinations of process parameters are of paramount importance in obtaining printed parts with the desired mechanical/physical properties. With SLM technology progressing robustly, several current limitations about the building part's size have also been overcome to manufacture large-scale complex parts [87].

As illustrated in Figure 16, Malekipour et al. [88] studied the framework of the SLM process parameters and organized it into pre-process, controllable, and post-processing operations and represented the true interlinkage amongst them.

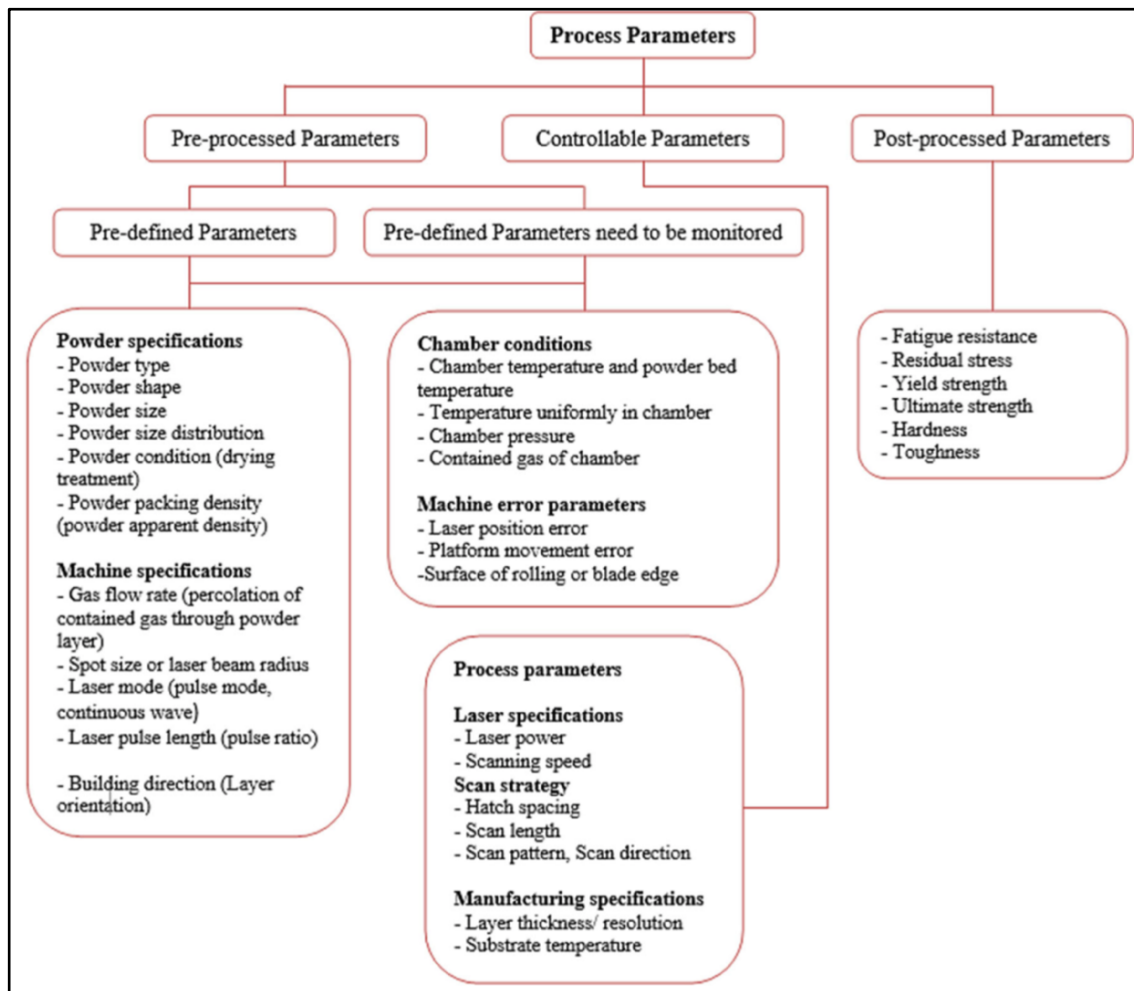


Figure 16. Classification of SLM process parameters [88].

Pre-process parameters are usually fixed parameters such as powder type, powder size distribution, powder packing density, inert gas flow rate, laser spot size,

laser pulse wavelength, and others that typically remain unchanged during the SLM process. Controllable process parameters include laser power, laser scan speed, scan pattern, hatch distance, layer thickness, amongst several others. Finally, separate post-processing (such as surface modifications, heat treatment, etc.) of parts is conducted to improve mechanical properties. Equipment manufacturers usually provide their “recommended” set of process parameters to their users to print defects free parts.

Key SLM process parameters and their effects on properties/performance are summarized:

- Laser-related parameters (laser power, laser spot size, laser intensity, laser pulse duration, laser mode, etc.) have the most significant influence on microstructure, phase formation, density, hardness, tensile strength, fatigue strength, amongst other factors [89, 90]; Laser power (too much or too little) alters melt pool geometry (too deep or too shallow) as well as temperature distribution across the build plate, which determines the final microstructure, phases, texture, residual stresses, and defects, amongst others [91];
- Temperature-related parameters (powder bed temperature, base plate preheating, build chamber temperature) affects heating of powder particles on the powder bed, leading to differences in sintering and packing of powder particles and hence different thermal gradients [92];
- Scan-related parameters (scan speed, scan pattern) has a significant influence on microstructure, mechanical behavior, surface finish, defects, etc. [93, 94];

- Hatch distance or hatch spacing determines the overlapping conditions between adjacent laser scan tracks. It is recommended to have 25 to 33% overlap between adjoining scan tracks to ensure defects free parts [95];
- Build direction, geometry, and part orientation on build plate affects cooling and heating cycles with noticeable differences in microstructure, mechanical properties, surface roughness, crack growth [96, 97];
- Powder-related parameters (powder morphology, processing techniques, packing density, reuse) determines the part quality as well as underlying defects such as balling, porosity, denudation (or clearing of powder around a laser-track), spatter, etc. [98];
- Inert gas (type, flow direction, flow rate) in the build chamber prevents part oxidation, reduces spatter and other unwanted by-products such as metal vapor and plasma plumes [99, 100].

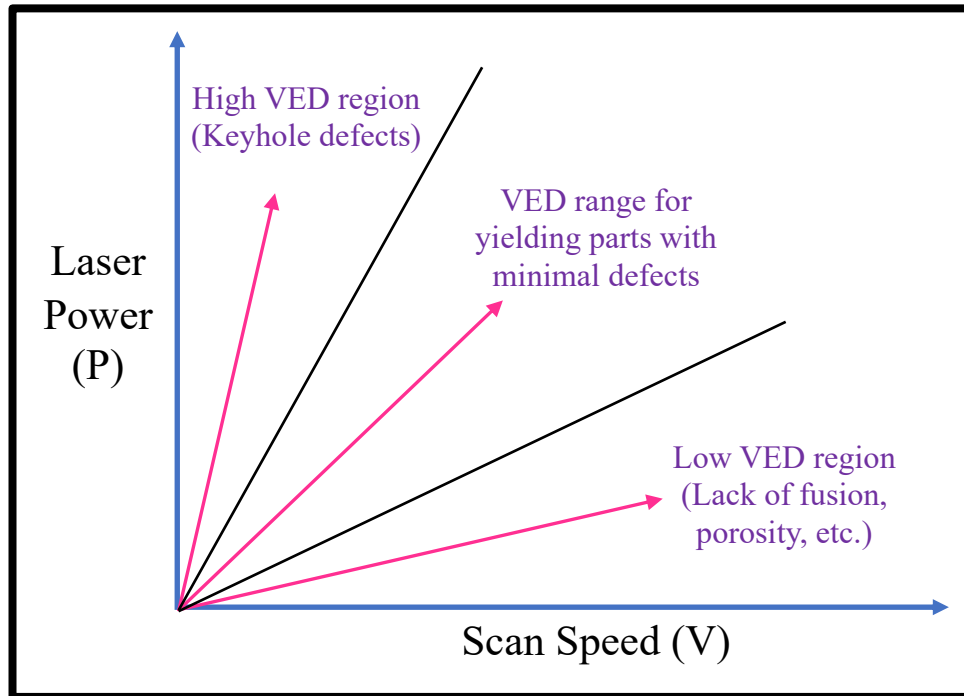
#### *2.2.6 SLM Processing Effects on Structure and Properties*

A consensus in the literature is that measuring energy density supplied to the powder bed is one of the significant factors affecting SLM part density [101-107]. Energy density is a composite parameter that helps to understand the melt pool behavior during the SLM process, an extensively complex phenomenon that has been best defined in literature with terms such as linear energy density (LED), area energy density (AED), and volumetric energy density (VED) [108]. LED (J/mm) relates essentially two parameters, laser power ( $P$ ) and scan speed ( $V$ ).

Considering the hatch spacing ( $h$ ) along with LED gives AED ( $\text{J}/\text{mm}^2$ ). Adding layer thickness ( $t$ ) to AED provides VED ( $\text{J}/\text{mm}^3$ ). The VED is a composite parameter that relates laser power ( $P$ ), scan speed ( $V$ ), layer thickness ( $t$ ), and hatch spacing ( $h$ ). The energy density ( $E_v$ ), or total energy input per unit volume or VED, is given by equation (1) [109]:

$$E_v = \frac{P}{V \cdot h \cdot t} \quad (1)$$

In SLM, porosity can be mostly controlled by optimizing specific process parameters, *i.e.*, laser power ( $P$ ) and scanning velocity ( $V$ ), as shown in Figure 17.

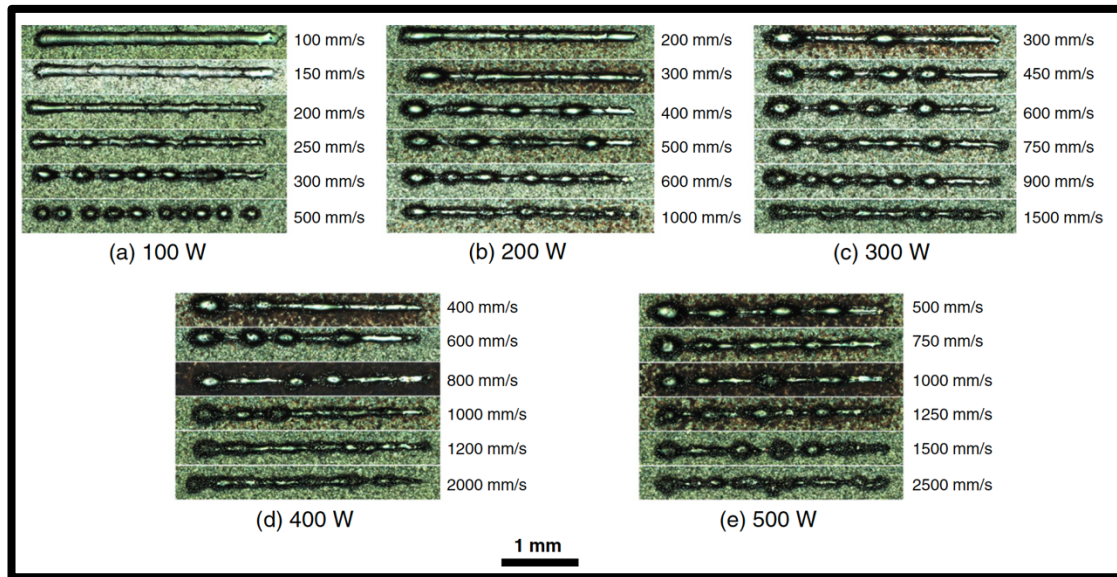


**Figure 17. Schematic of the energy density contour for the SLM process.**

These two parameters have a significant impact on the quality of SLM parts. For example, having higher  $P$  and lower  $V$  imparts a higher VED on the powder layer leading to a deeper melt pool wherein the already solidified layer could be re-melted and may lead to keyhole defects [110-112]. Similarly, having lower  $P$  and higher  $V$  imparts lower VED leading to a shallow/smaller melt pool and hence lack-of-fusion defects [113-115]. Donik et al. [116] reported different mechanical properties for SLMed SS 316L samples processed with the same VED. Moreover, both  $P$  and  $V$ 's combined effects result in complex thermal histories inside the melt pool, which affects the solidification microstructure of the material and, thereby, the resulting mechanical properties [117]. Furthermore, studies have shown VED also significantly affects the grain size, texture, and orientation [118-120]. According to Wang et al. [121], with an increase in VED, the primary dendrite arm spacing was significantly increased. They concluded that this was due to the non-equilibrium thermal gradient inside the melt pool at higher VED.

These energy-related parameters have reportedly shown a significant impact on the formation of defects in SLM components [122, 123]. For example, having higher  $P$  and low  $v$  imparts an excessive energy density on the powder layer leading to a deeper melt pool wherein the already solidified layer could be re-melted and may lead to keyhole defects [110-112]. Similarly, having lower  $P$  and higher  $V$  imparts low energy density leading to a shallow/smaller melt pool and exhibiting lack-of-fusion defects [113-115]. Moreover, both  $P$  and  $V$ 's combined effects result in complex thermal histories inside the melt pool, which affects the solidification microstructure of the

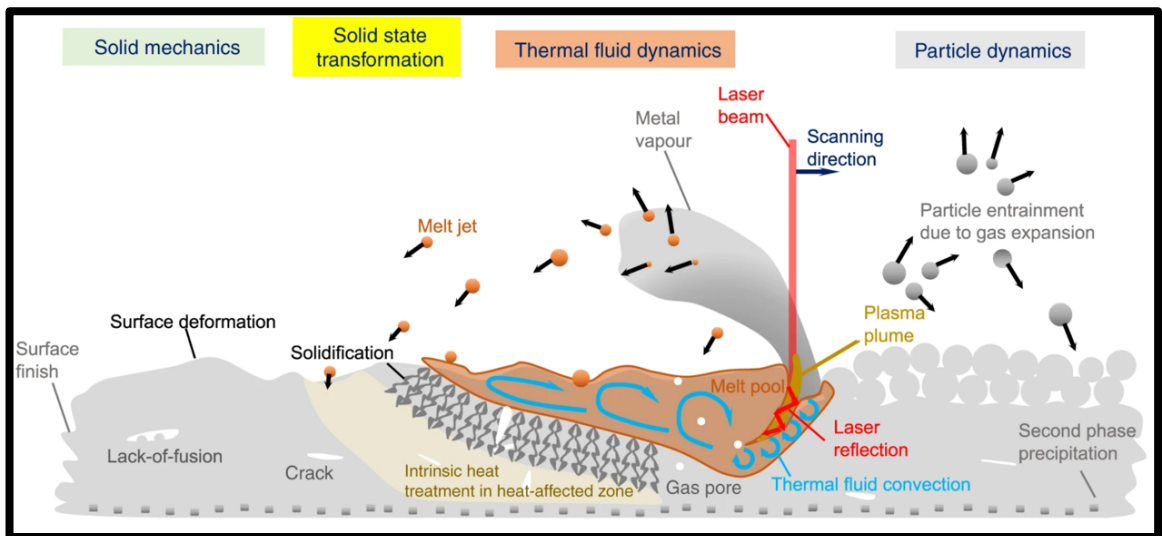
material and, thereby, the resulting mechanical properties [117]. The changes in energy density also significantly affect the grain size, as reported in the previous studies [119, 120].



**Figure 18.30** Single tracks of SS 316L for various VED combinations [124].

Figure 18 illustrates 30 single deposited tracks of SS 316L processed for different  $P$  and  $V$  combinations while keeping the  $L_T$  constant [124]. As mentioned earlier, when VED is relatively low, the track has shown irregularities in shape with unevenness and non-homogeneous melting. At sufficiently higher VED, track morphologies have been smooth with evenness and continuation. Therefore, it becomes vital to select a suitable VED range that will yield defects free parts.

Increasing the energy density reduces the temperature gradient and affects the grain size and shape [125]. The Marangoni effect due to the gradient in temperature inside the melt pool further affects the solidification microstructure, creating multi-directional grain orientation textures [126, 127]. Researchers have opted for modeling, simulations, and finite element analyses to obtain an extensive understanding of SLM process dynamics, multi-scale/physical across the length and time scales, as illustrated in Figure 19 [128-130].



**Figure 19. Schematic of multi-scale, multi-physics phenomena in the SLM [130].**

SLM parts have showcased defects at several length scales. These defects typically involve porosity, lack of fusion, inclusions, unconsolidated powder, trapped powder, entrapped gas, keyhole pore, voids, and residual stresses [131]. Figure 20 illustrates the SLM melt pool with various expected defects [132].



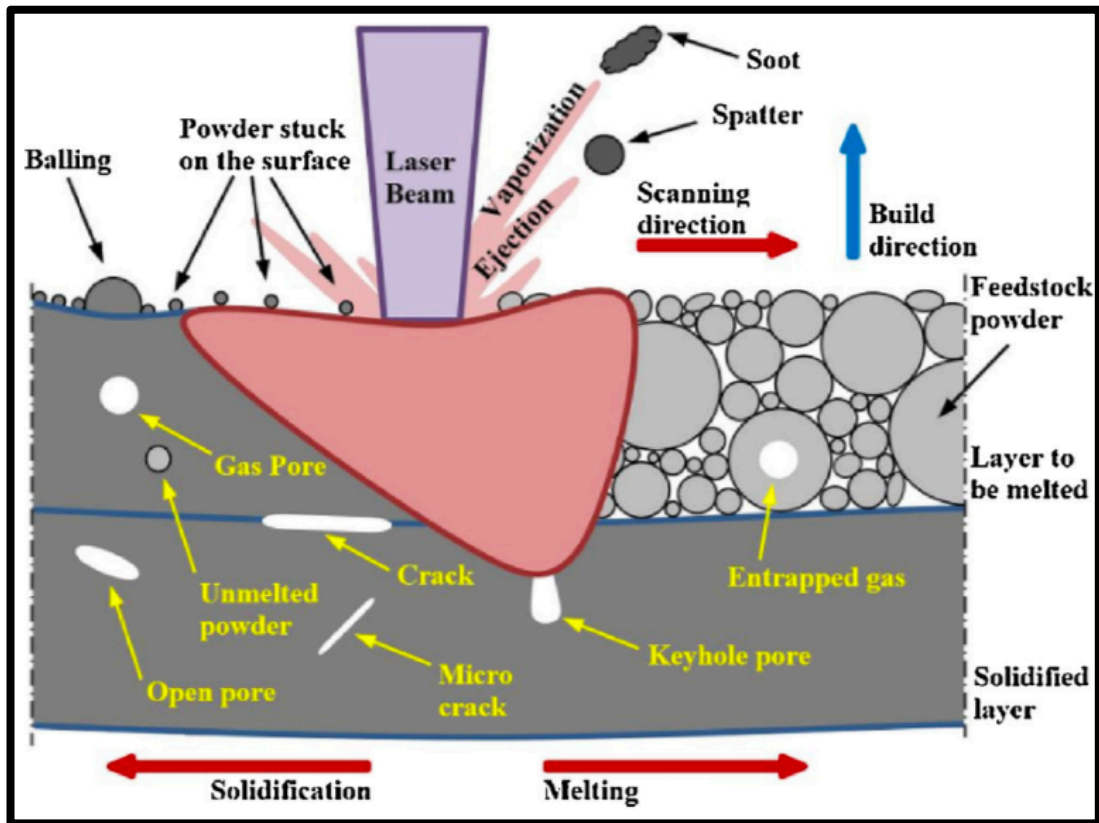


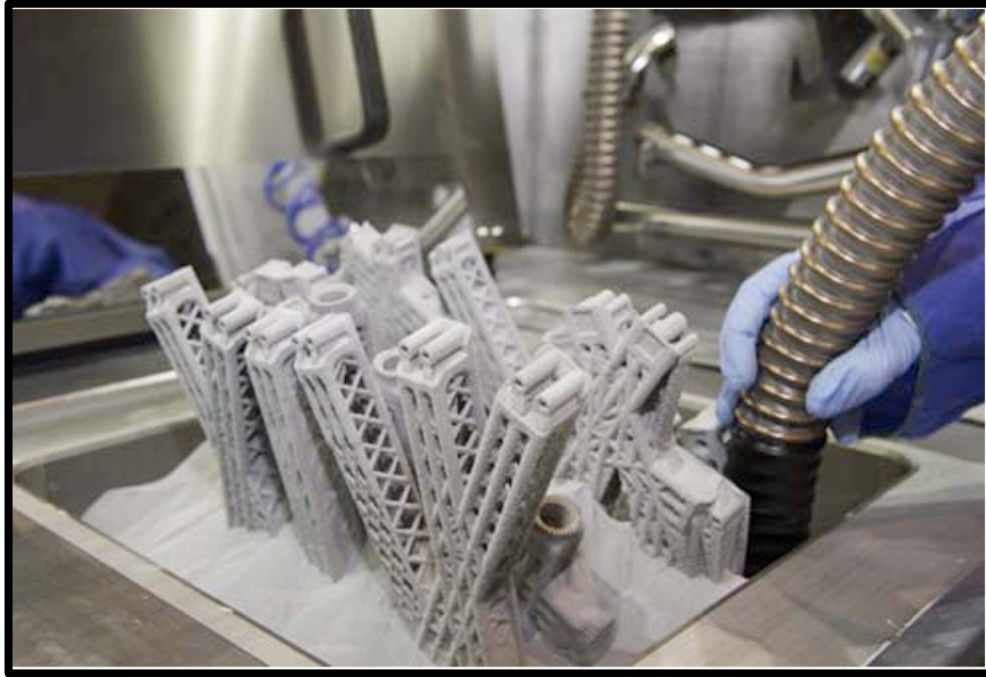
Figure 20. Schematic of the SLM melt pool with expected defects [132].

The presence of one defect type can trigger the next one. For example, having low VED may lead to under melting, which may lead to un-consolidated powder. While continued explorations regarding making the SLM more robust and viable manufacturing techniques are in full swing, several mechanisms require careful investigations. Notably, the need for a specific approach towards process parameter optimization, understanding melt pool dynamics, and flaws formation, resulting in mechanical properties and post-processing techniques amongst continuous and pulsed SLM platforms that can lead to R&R production of mission-critical parts.

More recently, the introduction of artificial intelligence (AI) and machine learning (ML) tools in metal AM space has further broadened the research horizons [133, 134]. Real-time, closed-loop control of SLM systems has now been possible with built-in monitoring systems that can measure the ongoing parts' thermal signatures from the build plate and adjust the scan speed and laser power accordingly [135, 136]. Moreover, in-situ process monitoring with high-speed imaging techniques has proved to be a useful tool in further establishing universal understanding amongst process specifications, laser-powder interactions, melt-pool dynamics, and defects formation with an ultimate goal of bettering part quality [137-139]. Therefore, it is expected to propose modifications in existing SLM platforms to accommodate high-resolution tomography, optical metrology, closed-loop process feedback, and monitoring techniques to improve process stability [140, 141].

### *2.2.7 Post Processing*

Once the parts are built, several post-processing steps are taken before using the parts for their intended use - the first one is removing the unconsolidated powder surrounding the printed parts, as seen from Figure 21.



**Figure 21. Post build powder removal [Courtesy: APWORKS].**

More often, several other post-processing steps are taken based on the end requirements. These include machining, polishing, electro-polishing, grinding, sandblasting, shot peening, and vibratory finishing, amongst several others [142].

Moreover, several studies have reportedly investigated SLM parts identical in appearance yet not conforming to strict technical expectations [143, 144]. It is estimated that surface finishing can cost up to roughly 60% of the total cost for a given SLM component. Figure 22 illustrates a comparison between as-printed and post-processed SLM fabricated SS parts.



**Figure 22. Before and after surface finishing of SS test part [Courtesy: Fintek].**

To eliminate the property variations to certain extents, several researchers have looked at the post-processed or performance enhancement techniques such as surface finishing, heat treatment (HT), hot isostatic pressing (HIP), and HIP+HT that have effects on the final part's properties, including hardness, toughness, yield strength, residual stresses, density, ultimate strength and fatigue resistance [34, 145, 146]. In a recent study, Tascioglu et al. [147] have studied the effects of different heat treatment temperatures on SS 316L samples to establish a substantial correlation between heat treatment and mechanical performance (microhardness, wear, etc.). They concluded that an increase in heat treatment temperature severely degrades the microhardness due to the release of residual stresses in SLM parts. To further understand the flaws formation in L-PBF, Snow et al. [148] provided a systematic review of each type of flaw and

categorized them into systematic and stochastic. Figure 23 represents the overall process steps involved from the ‘Picture-to-Part’ journey for the SLM process.



Figure 23. Illustration of steps involved in a typical SLM process [149].

## 2.3 Stainless Steels

According to the American Iron and Steel Institute (AISI), stainless steel (SS) typically falls into several major groups:

- Austenitic grades (identifying numbers of either 200 or 300).
- Ferritic steels (identified as the 400 series).
- Martensitic grades (also has some 400 series designation).
- Precipitation-hardened grades [150].

Steel is still the most common engineering material, especially stainless steel. The word ‘steel’ refers that iron represents the bulk of the material and ‘stainless’ denotes the absence of staining, rusting, or corroding in hostile environments where ‘normal’ steels are susceptible [151]. ‘Stainlessness’ in the steel comes from adding chromium (Cr), at least 11 wt%. Higher Cr can be added to guard in harsh environments (for instance, moist or polluted environments) that may trigger rusting or pitting. Molybdenum (Mo) is added for improving the resistance against pitting, Silicon (Si) provides better oxidation resistance at elevated temperatures, whereas Nickel (Ni) is added to obtain austenite. Figure 24 illustrates the general classification system used for steels [152].

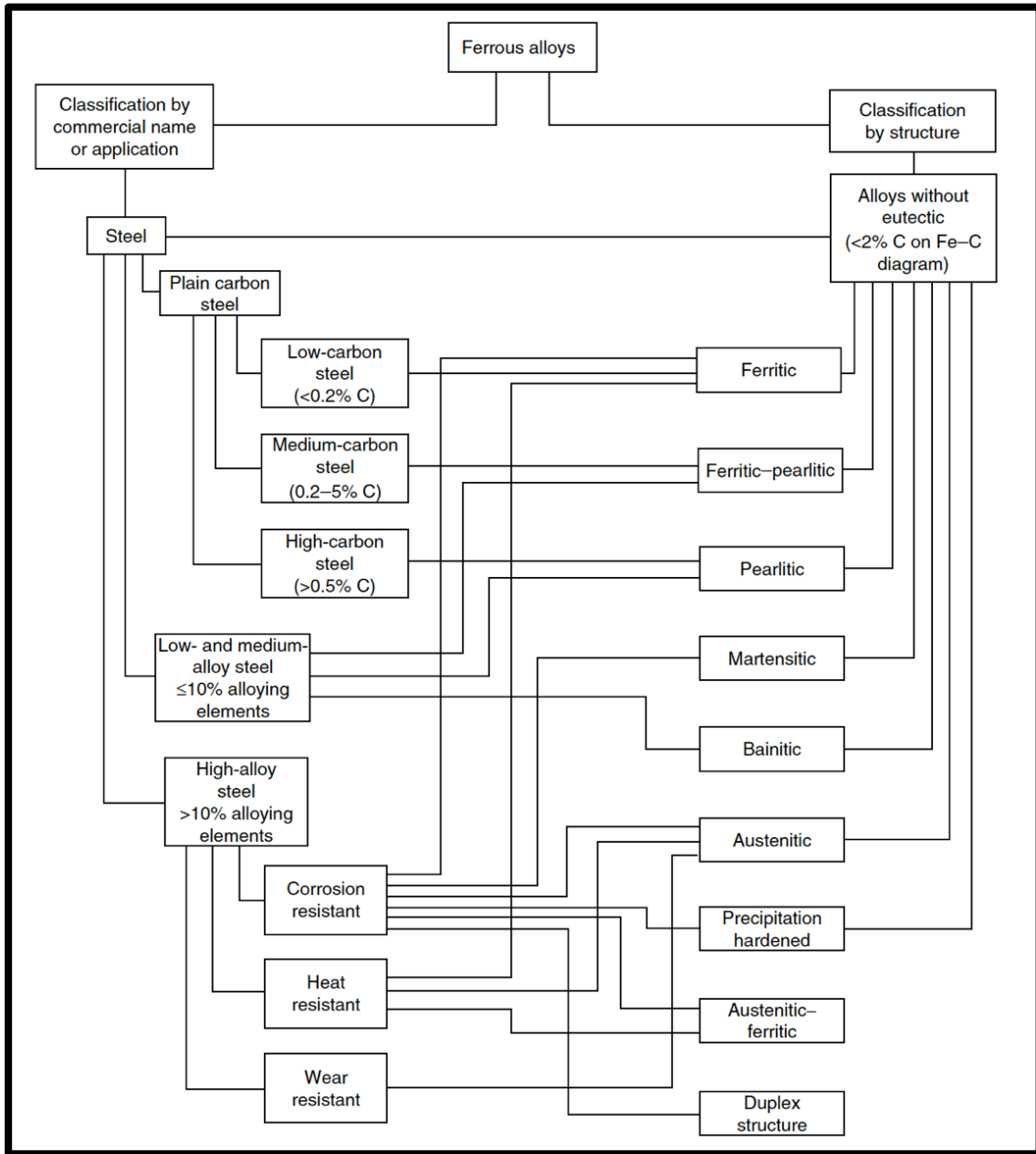
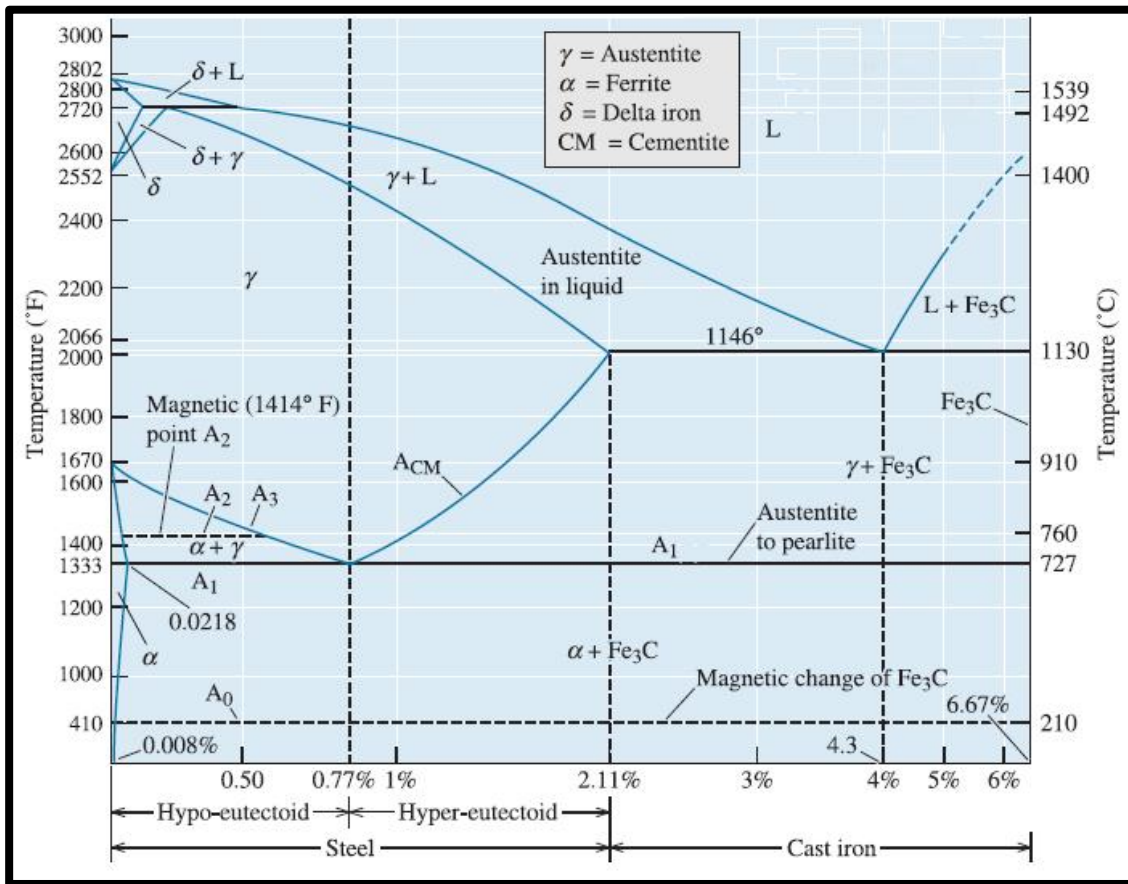


Figure 24. General classification of steels [152].





**Figure 25. Fe-C equilibrium phase diagram: Amount of wt% C is crucial in determining the solidification path [153].**

Figure 25 illustrates Iron-Carbon (Fe-C) equilibrium phase diagram that shows the relationships amongst temperature and wt% C while keeping the pressure constant at 1 atm. The microstructure of steels consists of various phases that are spatially arranged. Final mechanical and physical properties (including hardness, ductility, creep, and impact resistance) for any steel largely depend on the shape, size, crystal structure, and composition of phases. In most steels, iron exhibits two allotropes in body-centered cubic (BCC) ferrite and face-centered cubic (FCC) austenite. Iron melts above 2800 °F



(1538 °C) and is in a liquid state. Upon iron solidification, the BCC lattice phase starts to form stable from 2541 to 2800 °F (1394 to 1538 °C). The FCC phase is formed when the temperature drops below 2541 °F (1394 °C). On the other hand, some microstructures are far from equilibrium. One such phase is body-centered tetragonal (BCT) martensite. BCT martensite has supersaturated carbon and is farthest from equilibrium. By adding different alloying elements and selecting optimum heat treatment routes, researchers have regularly controlled the steel microstructures [150].

### *2.3.1 Stainless Steel 316L*

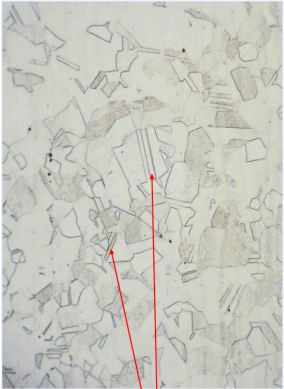
Stainless steel belongs to a group of Fe-Cr, Fe-Cr-C, and Fe-Cr-Ni systems derived from Fe-C-X steels (wherein X represents alloying elements present). Stainless steel 316L (SS 316L) is a widely popular alloy due to its combination of excellent machinability, good wear resistance, superior elevated temperature, and corrosive environment use along with low costs. SS 316L is an austenitic series of high-alloyed steel that is ideal for operating in elevated temperature and highly corrosive environments [154]. As explained earlier, SS 316L exhibits these properties due to Mo and Ni's presence, along with a lower carbon presence (less than 0.03 wt%), making it suitable for welding applications [151, 155, 156]. Figure 26 summarizes physical, mechanical, electrical, and thermal properties for conventionally processed SS 316L.

Physical Properties	Metric	English	Comments
Density	8 g/cc	0.289 lb/in <sup>3</sup>	
<b>Mechanical Properties</b>			
Hardness, Brinell	149	149	
Hardness, Rockwell B	80	80	
Hardness, Vickers	155	155	
Tensile Strength, Ultimate	515 MPa	74700 psi	
Tensile Strength, Yield	205 MPa	29700 psi	
Elongation at Break	60 %	60 %	in 50 mm
Modulus of Elasticity	193 GPa	28000 ksi	
Charpy Impact	103 J	76 ft-lb	V-notch, 30°C
Izod Impact	150 J	111 ft-lb	21°C
<b>Electrical Properties</b>			
Electrical Resistivity	7.4e-005 ohm-cm	7.4e-005 ohm-cm	at 20°C
Magnetic Permeability	1.008	1.008	at RT
<b>Thermal Properties</b>			
Specific Heat Capacity	0.5 J/g-°C	0.12 BTU/lb-°F	from 0-100°C (32-212°F)
Melting Point	1375 - 1400 °C	2510 - 2550 °F	
Solidus	1375 °C	2510 °F	
Liquidus	1400 °C	2550 °F	
Maximum Service Temperature, Air	870 °C	1600 °F	Intermittent Service
Maximum Service Temperature, Air	925 °C	1700 °F	Continuous Service

**Figure 26. Properties of conventional SS 316L [157].**

### 2.3.2 Common Microstructures of Stainless Steel 316L

The microstructure of stainless steel 316L consists of common phases such as austenite (FCC), ferrite (BCC), and martensite (BCT), and which are the most relevant to this study as seen from Figure 27.

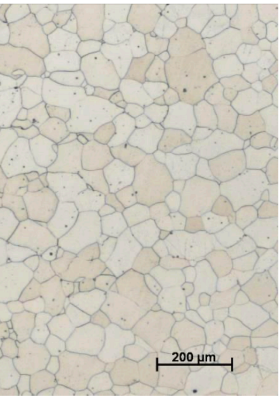


## Austenite

- $\gamma$ -iron
- face centered cubic structure
- non magnetic
- angular grain boundaries
- twins
- soft
- HB 100 – 400
- not stable at room temperature
- named after English professor Sir W. Chandler Roberts-Austen

Twin line

ASM INTERNATIONAL Education Frauke Hogue

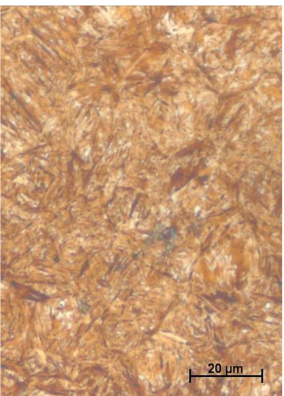


## Ferrite

- $\alpha$ -iron
- body centered cubic structure
- 0.008% C max.
- no twins
- magnetic
- soft
- rounded grain boundaries
- name derived from Latin word for iron: ferrum
- HB 100 - 250

100x

ASM INTERNATIONAL Education Frauke Hogue



## Martensite

- needle like
- hard
- body centered tetragonal structure
- forms generally with rapid cooling
- hardness depends on C content
  - .10% C – HRC 38
  - .65% C – HRC 65
- named after German professor Adolph Martens

1000x

ASM INTERNATIONAL Education Frauke Hogue

Figure 27. OM of steel phases a) Austenite b) Ferrite and c) Martensite [158].

SS 316L is an austenitic steel with a primary FCC austenite phase. The austenite phase has angular grain boundaries with an average hardness ranging between 100-400 HB. On the other hand, the ferrite phase has rounded grain boundaries and a softer average hardness of 100-250 HB. Martensite phases have a needle-like (acicular) structure, both brittle and hard, with an average hardness of 200-700 HB.

Phase formations and transformations that occur in steel can be understood from a simple Fe-C equilibrium phase diagram (cf. Figure 25). Typically, during the liquid state solidification, the first phase that forms is high-temperature  $\delta$ -ferrite (BCC) [52]. Moreover, with the modification in the cooling rate, the high-temperature  $\delta$ -ferrite can be decomposed to a high-temperature austenite phase (FCC) which can then decomposed to a low-temperature  $\alpha$ -ferrite (BCC) [152]. In addition, a hard martensite microstructure (BCT) can be obtained from austenite by a further increase in the cooling rate.

## **2.4 SLM of SS 316L**

### *2.4.1 General Overview*

By controlling the SLM processing conditions, SS 316L parts have been printed at near full density [159-161]. Further, corrosion and cavitation erosion resistance and other material properties of SLM-produced SS 316L parts have been investigated recently [162-164]. Li et al. [165] have confirmed the effects of the process parameters (varying laser power, scan speed, hatch spacing, and layer thickness) on the porosity and, thereby, on the density of the parts produced. They reported the densification

mechanisms at differing scan speeds (100 mm/s, 200 mm/s, 300 mm/s) while keeping other parameters constant and concluded that at higher scan speed, there was a linear increase in the number of irregular pores. Kurzynowski et al. [166] evaluated process parameter impacts on the microstructure and texture of parts by changing laser power (100–200 W), scanning speed (0.2–0.22 m/s), energy density (81–150 J/mm<sup>3</sup>), and scanning strategies. More recently, high-speed X-ray imaging has also been used in understanding changes to the melt pool solidification by *in-situ* sample analysis [167].

Furthermore, other studies have focused on the corrosion and material characterization of SLM processed SS 316L [168]. Zhong and coworkers [169] have investigated the occurrence of a cellular microstructure during SLM of SS 316L and attributed it to compositional fluctuations and the constitutional supercooling theory and stressed that more undercooling favored a dendrite mode of solidification. Krell et al. used SLM to produce hierarchical microstructures with several grains at a macro scale, a cellular subgrain at the microscale, and precipitants at the nanoscale within the cellular structure [170].

Moreover, Liverani et al. reported optimum process parameter windows for the SLM manufacture of SS 316L [29]. Other studies have documented a significant spread in the variations of mechanical/physical properties with process parameters for SLM processed SS 316L [171-174], including the effects of laser power and scanning speed on the mechanical properties as reported by Ahmadi et al. [175]. Studies have also focused on investigating the performance of SLM fabricated parts in tension, fatigue, bending, and tribological conditions [176-179].

### 2.4.2 Solidification Fundamentals

In SLM, the solidification dynamics and resulting microstructure are governed by the local temperature gradient,  $G$ , and the solidification velocity,  $R$  and are often represented by the solidification maps, as shown in Figure 28 [180].

$G$  and  $R$ 's combined effects lead to morphological changes, crystal growth, crystallographic orientation texture development, and solidification mode (for instance, planar, cellular, columnar, or equiaxed). For example, low  $G$  and high  $R$  lead to equiaxed grains, whereas a planar grain shape is formed at high  $G$  and low  $R$ . Typically, each SLM deposited layer exhibits an 'epitaxial grain growth mechanism'; however, the growth orientation of cells changes depending on the thermal gradient direction [181].

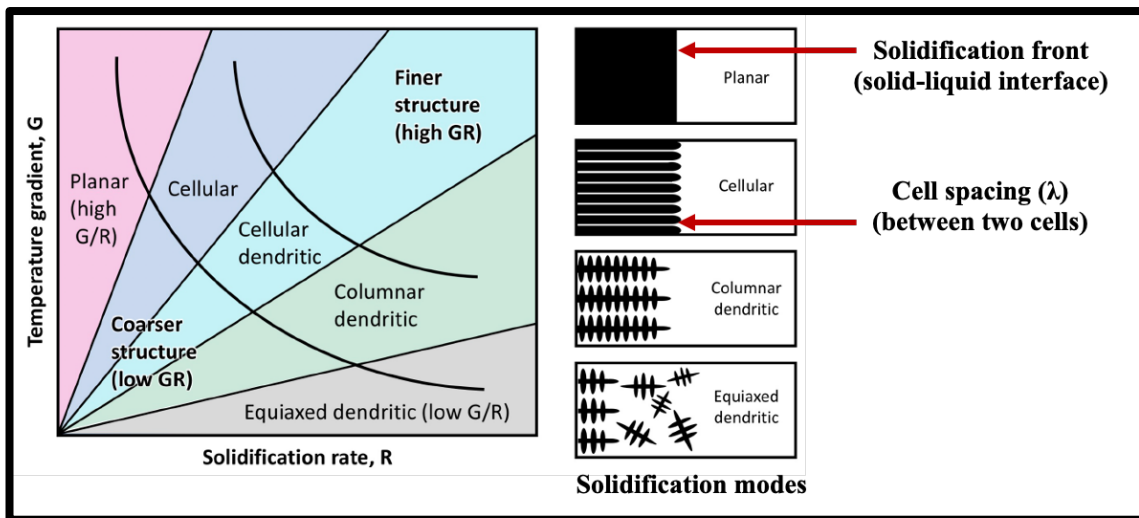


Figure 28. Variation of solidification modes for different  $G$  and  $R$  conditions [182].

Epitaxial grain growth is seen when re-melting of the already solidified layer occurs, providing a preferred crystallographic orientation and growth direction for the newly deposited layer.

Chen and coworkers [183] studied the grain growth observed during the SLM process and suggested the absence of planar solidification. It was due to extremely high laser scan speed ( $V = 200\text{-}2500$  mm/s) used in SLM which favors non-planar growth compared to conventional welding process ( $V = 2\text{-}15$  mm/s). At lower G/R ratios, solidification mode changes to cellular, cellular-dendritic, or dendritic, depending upon the constitutional undercooling ahead of the advancing solidification front (the moving solid/liquid interface). Constitutional undercooling is referred to as microsegregation due to thermal and compositional fluctuations near the solid/liquid interface, thereby lowering the freezing temperature [184]. Figure 29 shows possible nucleation and growth mechanisms and grain structure effects during the melt pool solidification [185].

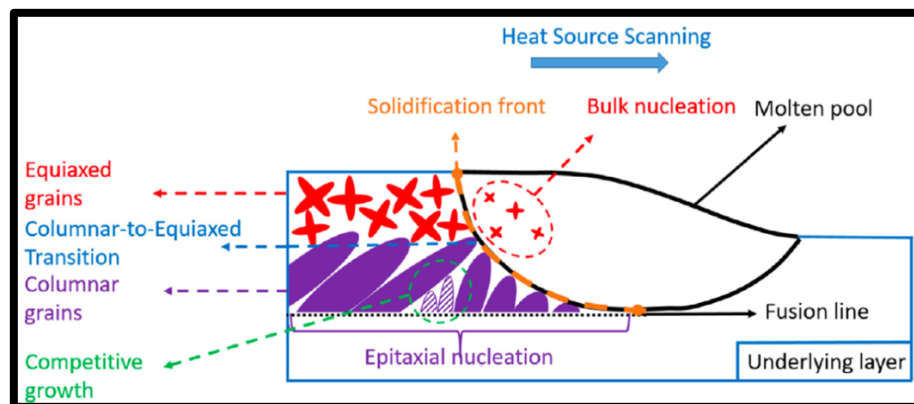
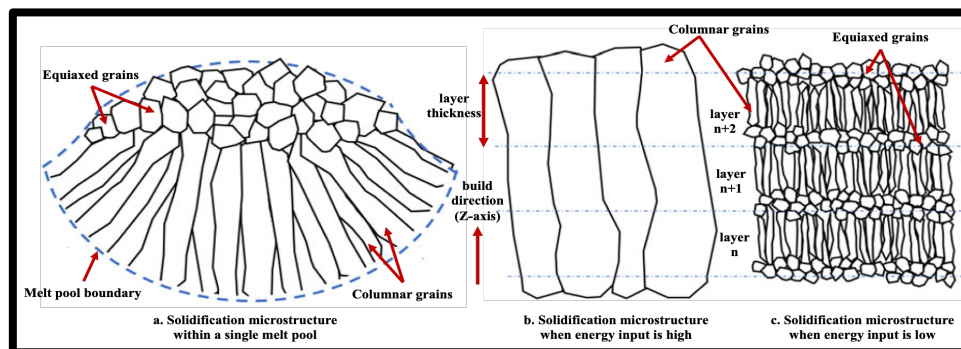


Figure 29. Possible growth mechanisms and effects on the grain structure [185].

During the build, melt pools are stacked on top of each other in the vertical orientation; thereby,  $G$  remains vertical at the center and does not alter towards the top of the melt pool. However,  $G$  changes significantly sideways, altering the heat flux and hence the direction of cell growth. Furthermore, the product of  $G \times R$  depicts the scale of the solidification microstructure. Higher the cooling rate, the smaller the cell spacing and the finer (smaller) the grain size. To obtain highly isotropic properties, it is desirable to have an equiaxed solidification. This diagram is often utilized in casting and welding as well [182]. Kim et al. [186] have recently revised the conventional solidification maps and tailored them to AM by including energy density and laser scan speed.

SLM involves simultaneous melting of a powder layer and the partial re-melting of the previously solidified layer underneath, which affects the grain size and morphology, phases, and induces pores, cracks, and residual stresses as noted in [187-189]. As seen from Figure 30, different solidification microstructures have been obtained by varying the energy input [186].



**Figure 30 (a-c). Different solidification microstructures are obtained via varying energy input. Figure re-created from reference [186].**



The cell spacing  $\lambda$  ( $\mu\text{m}$ ), for austenitic stainless steel, can be calculated from [190, 191]:

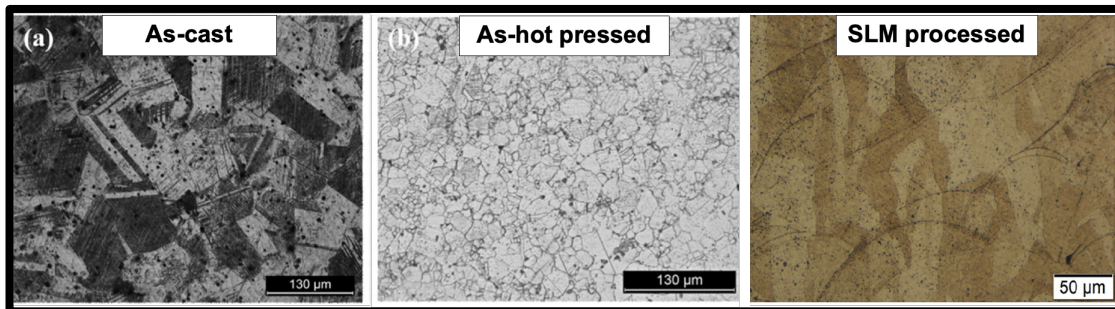
$$\lambda = 80 \cdot T^{-0.33} \quad (2)$$

where  $\lambda$  is the cell spacing in ( $\mu\text{m}$ ), and  $T$  is the cooling rate (K/s).

Different dominant phenomena impact the SLM process, including but not limited to laser absorption and reflection, mass and heat transfer, fluid flow due to surface tension variations, phase transformation, chemical reactions, and motion of liquid-solid interface (solidification mode) within the melt pool.

#### 2.4.3 Microstructural Development

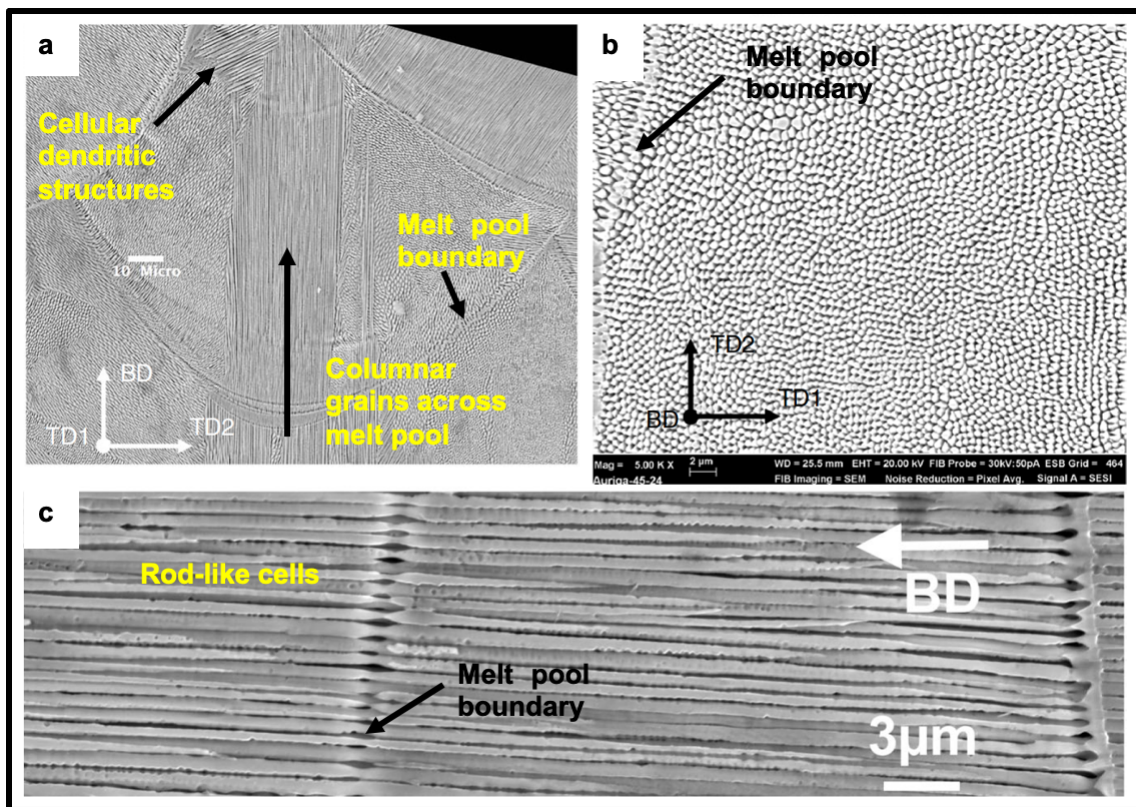
Figure 31 shows SS 316L microstructure comparisons when parts are fabricated conventionally, such as casting and hot pressing with the SLM [192].



**Figure 31. SS 316L microstructures processed by traditional vs. SLM process [193].**

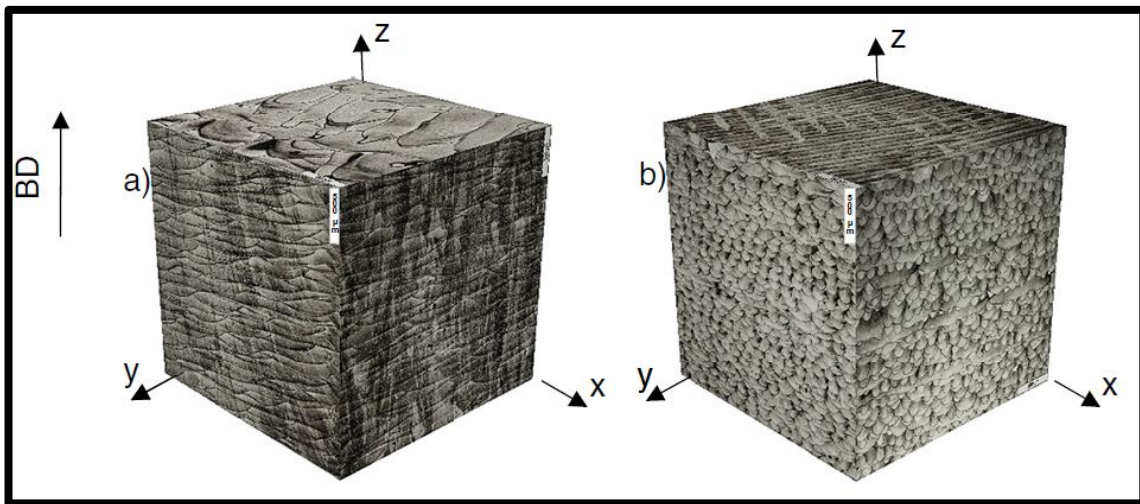
Casting process has the cooling rate of 0.5 K/s, which creates rectangular grains with an average size of  $91 \pm 17 \mu\text{m}$ . In contrast, hot pressing has a cooling rate of 3 K/s

leading to an average grain size of  $25 \pm 4 \mu\text{m}$ . The SLM process experiences an extremely high thermal gradient of about  $10^6 \text{ (K/m)}$  [194]. SLM forms very fine, metastable microstructures of an average grain size of  $13 \pm 4 \mu\text{m}$ . The observed microstructural change can be attributed to thermal cycles of rapid heating and cooling associated with the SLM process [195, 196]. Figure 32 shows an SEM micrograph of SS 316L processed by a Renishaw showing various cells in a melt pool of 316L along with transverse and longitudinal sections and related features [197].



**Figure 32.** 316L microstructures processed by a Renishaw showing columnar grain growth across the melt pool boundaries (as seen in a). Rod-like cells in melt pool envelop in both transverse (b) and along the longitudinal (c) sections of the sample. [197].

Past work has shown the average cellular spacing of about  $1.5 \pm 0.5 \mu\text{m}$  for a laser power of 380 W, and  $0.75 \pm 0.5 \mu\text{m}$  for the laser power of 200 W, leading to an average cooling rate of about  $1.7 \times 10^5$  to  $1.4 \times 10^6$  K/s, respectively [198]. Sun et al. [199] reported the average cell spacing of about  $1 \mu\text{m}$  for a cooling rate of about  $5.8 \times 10^5$  K/s. Saeidi et al. [200] reported the cell spacing of about  $0.5 \mu\text{m}$  for a cooling rate of about  $4.8 \times 10^6$  K/s. These studies show a wide variety of cooling rates and resulting cell sizes. It is known that the finer grain size often leads to higher hardness and high strength [201].



**Figure 33. The microstructure of SLM processed Inconel 718 cube of  $2\text{mm}^3$  when processed by laser power of a) 950 W and b) 250 W [202].**

Figure 33 depicts two cubes, both of size  $2 \text{mm}^3$  fabricated by SLM via implementing two different laser intensity profiles (Gaussian and Flat-top) at different laser powers (250 W and 950 W) in a study conducted by Popovich et al. [202]. They

found a sharp transition from fine to coarse grains with corresponding hardness changes (~20% reduced hardness for coarse-grained regions). Also, sections perpendicular to build directions showed distinct microstructures. More recently, Pham et al. [197], if the printed part contains porosity, then the cooling rates are significantly reduced (up to two orders of magnitude), thereby altering the local thermal gradient by acting as thermal insulation. This, in turn, changes both G and R in the regions above pores. Yadollahi et al. [203] reported that rapid solidification and the presence of Cr, Mo, and Si (conductive to ferrite formation) result in an increased percentage of ferrite at the cell boundaries. At the same time, the interiors of grain remain mostly in the austenite phase, thus affecting mechanical properties. It is recommended to carry out solution annealing and homogenizing post-processing to alleviate the elemental segregation.

In summary, previous studies conclude that SLM process parameters play a vital role in changing the thermal history, which affects the solidification microstructure and material properties of SS 316L. An in-depth understanding is necessary to relate the resulting macro- and microstructure to the VED-related process parameters to obtain usable and repeatable properties.

## **2.5 Previous Related Work in SLM**

Structures (at various scales) are significant contributors to the overall characteristics of how metals and alloys exhibit their mechanical and physical properties. Classically processed alloys via casting or forging will yield fairly standardize and homogenized macro- and microstructures [118]. Limited property

variations are thus attainable in finished parts due to several processing constraints. However, to obtain the controlled variations in physical and mechanical performances within the same part via tuning structure manipulations becomes expensive and difficult to accomplish by such processing techniques.

AM with unique layer-by-layer processing presents an unrivaled design freedom to manipulate site-specific, on-demand properties and shorter lead times. A usable property (functionally valid) range must be explored for various physical and mechanical properties such as density, hardness, modulus, fatigue, amongst several others. Engineering applications that specifically demand multipurpose parts are suitable avenues where these functional ranges can have inherent advantages. Thus far, minimal processing windows and resulting property ranges have been reported for alloys processed via DED and PBF processes. For instance, relative density between 90-99% still be a structurally valid range for non-critical, multipurpose parts and can very well fulfill the industrial application requirements. With the highest industrial relevance at the moment, SLM thus becomes an ideal processing technique to explore further and examine the available ranges of different alloys and fabricate parts that are both sustainable and cost-effective. SLM capabilities to perform gradation has been tested via different approaches, including but not limited to assimilating various alloys, altering laser-related process parameters, and using different scanning strategies [204].

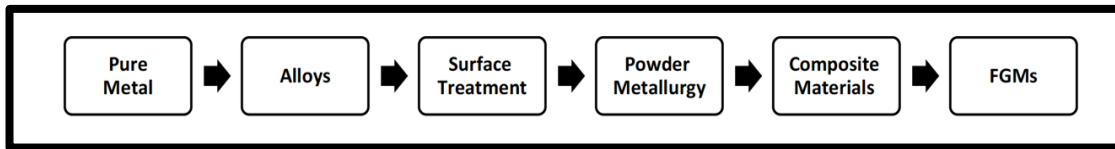
Only a handful of studies in the literature show the SLM processing capabilities towards the single alloy gradations. The early work of Mumtaz and Hopkinson [205] used SLM to fabricate bi-material specimens with Zirconia and Waspaloy using a high-

power Nd:YAG laser. The experimental work by Niendorf [206] demonstrated the use of SLM to produce a step-change SS 316L structure by using two different laser powers (400 and 1000 W) along with powder layer thickness (50 and 150  $\mu\text{m}$ ) while keeping the VED constant. They found columnar coarse-grains for regions processed with 1000 W and fine-grains for 400 W and showcased a local difference in mechanical properties by employing hardness and tensile tests. Popovich et al. [202] examined a step change of Inconel 718 by using two different laser intensity profiles (Gaussian and Flat-top) at laser powers (250 W and 950 W) and found a sharp transition from fine to coarse grains with corresponding changes in hardness ( $\sim 20\%$  reduced hardness for coarse-grained regions). Holzweissig et al. [20] fabricated a material transition between tool steel H13 and SS 316L by utilizing a reconfigured recoater design for SLM to accommodate two different materials. More recently, Attard et al. [207] have exhibited microstructural control for SLMed IN718 via altering the thermal history by tweaking process parameters (scan strategies, hatch spacing, laser power). They obtained two different microstructures (highly columnar and quasi-equiaxed) and concluded the preheat level from the previous layer to be the critical factor in forming the ultimate microstructure.

## **2.6 Functionally-Graded Materials (FGMs)**

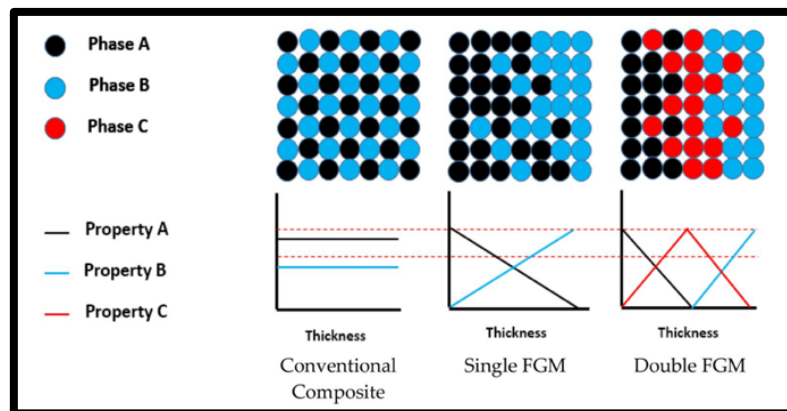
With the growing need to develop application-specific materials in aerospace, automotive, and biomedical industries, conventional monolithic materials have found limited usage due to their homogeneous properties. Tailored materials can well surpass

monolithic materials' mechanical and microstructural limitations due to their unique capabilities of having heterogeneous properties [20]. Figure 34 summarizes the aspects of material development towards FGM [208].



**Figure 34. Steps to development of FGMs [208].**

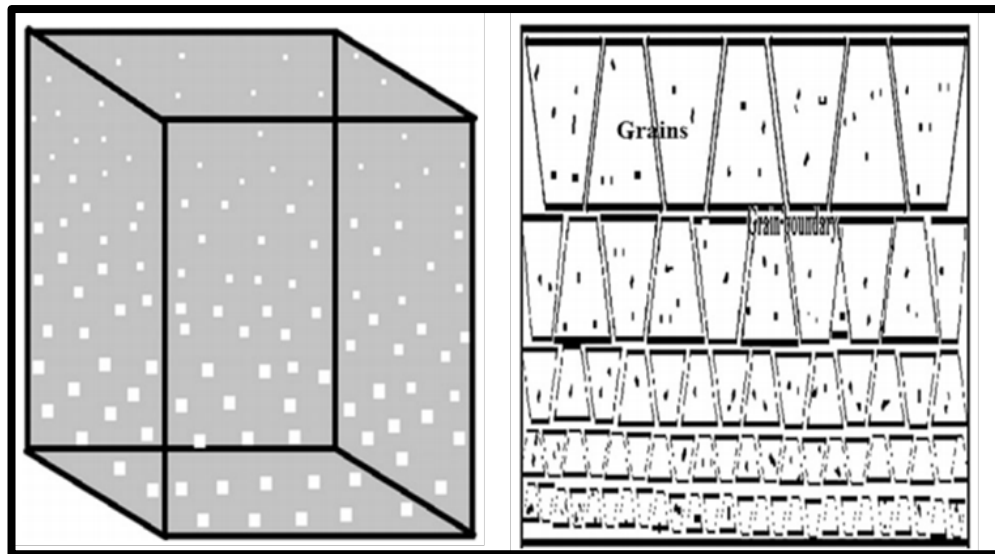
Graded bulk structures or functionally graded materials (FGM) have come to existence due to the conventional composite materials' threshold to ascertain spatial property gradation that fulfills the designated performance requirements [209, 210]. Figure 35 depicts the possible property variations achievable via FGMs when compared to conventional composites [211].



**Figure 35. Possible property variations achievable in conventional vs. FGMs [211].**

The current pools of alloys are constrained in cost, stringent processing, and unfavorable phases [212]. To overcome this barrier, an idea of FGMs was presented in 1972 for polymers and composites based on mimicking nature (teeth, bones, woods, fish scales, bamboo trees, etc.) [211]. Macro- and microstructure (for instance, density, grain size, texture), phases, and composition gradations are typically chosen as altering it could yield a significant change in material properties and, in turn, an efficient structural component [4, 5, 213].

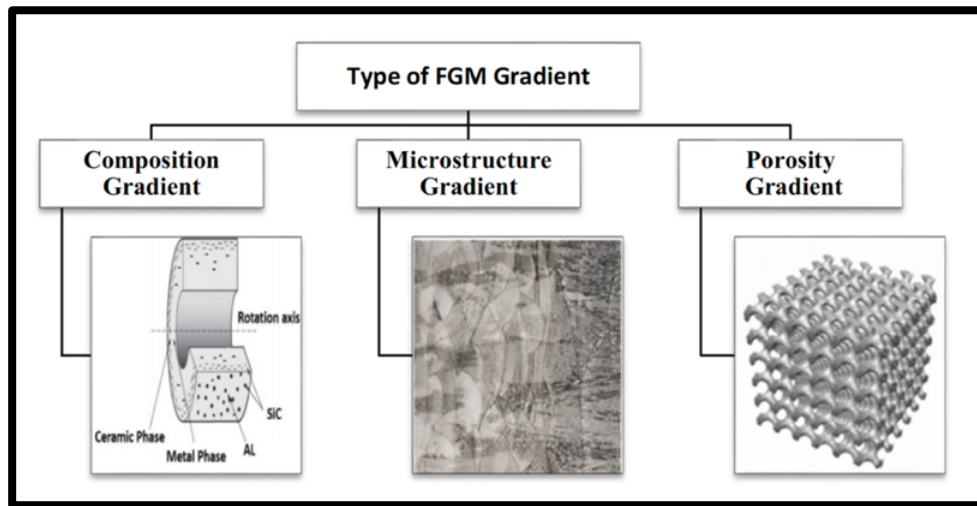
Figure 36 shows one such bulk FGM structure wherein the intended property variations have been achieved due to variations in the grain size and altering the mechanical properties.



**Figure 36. Schematic of property variations due to grain size in bulk FGM [214].**



Moreover, as illustrated in Figure 37 different types of FGM gradient can be achievable based on composition, microstructure, porosity [211].

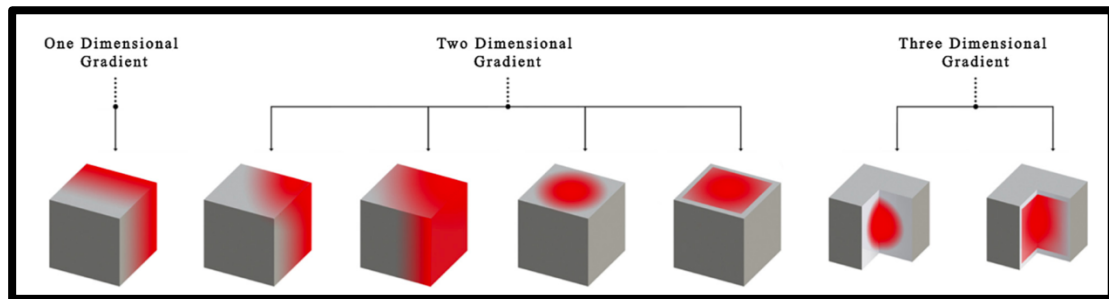


**Figure 37. Schematic of three types of FGM Gradient [211].**

### *2.6.1 Classifications of FGMs*

FGMs are a special class of advanced material that can be individually tailored to local mechanical, thermal, or electrical applications [2]. While fabricating FGMs, it is vital to control composition, structure, and texture distributions, and any other necessary elements [212]. They are characterized by their spatial variations in composition across the volume, thereby changing the corresponding material properties according to the functional requirements [4]. Graded materials can also achieve an amalgamation of usually irreconcilable properties of homogeneous materials.

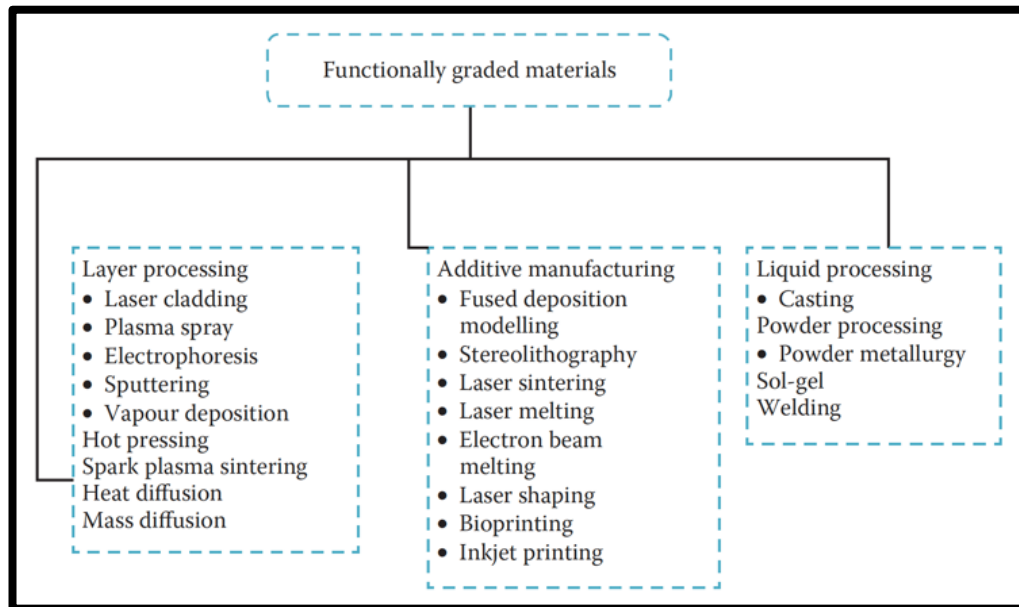
As seen in Figure 38, FGMs are categorized based on their ability to attain spatial variations in their compositions in one, two, or three-dimensions [215].



**Figure 38. Classification of types of gradient [216].**

### *2.6.2 Manufacturing Techniques for FGMs*

FGMs have been conventionally processed using techniques ranging from deposition methods (chemical vapor deposition/infiltration), castings (centrifugal/slip), powder metallurgy, surface chemical reaction methods, sol-gel method, plasma spraying methods, spark plasma sintering (SPS), and diffusion and reaction techniques as shown in Figure 39 [217].



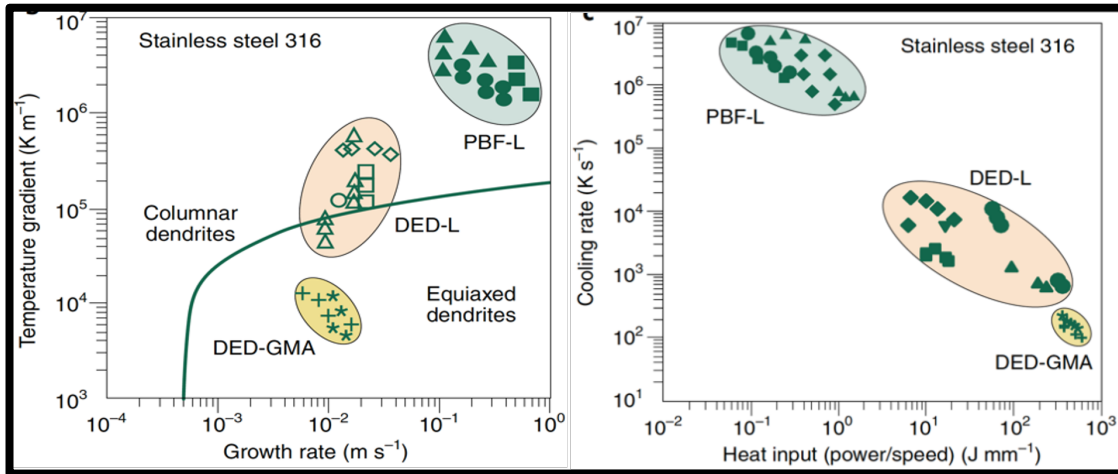
**Figure 39. Types of FGM fabrication methods [218].**

However, these methods are limited in their capability and often require specialized tooling, and involve significant post-processing [218]. Especially the multi-material compositional grading has several limitations such as weaker interfaces and chemical instabilities (e.g., brittle intermetallics), microstructure non-homogeneities leading to unpredictable properties, non-uniform post-processing needs, intricate mold design needs, varied working temperatures, stress concentration, and cracking, amongst others; hence, property/performance tuning is difficult. Yang et al. [219] have highlighted such mismatch issues in thermal properties for ceramic materials resulting in improper layer bonding. It remains crucial to justify the dependency on current FGM processing techniques amidst growing structures that showcase a certain mechanical response under various loading conditions [209].

### *2.6.3 Functionally Graded Additively Manufactured (FGAM) Materials*

Layer-wise tailoring is inherent to AM processing, and as such, various AM techniques have yielded promising results for fabricating spatially graded parts that artificially alter physical/mechanical properties within the parts [220-224]. Dehoff et al. [225] have exhibited a site-specific control of properties using electron beam melting (EBM) by switching the heat source from a line to a point, which resulted in the different crystallographic orientation of grains within the part. Tammis-Williams and Todd [226] have provided an in-depth review about how AM components can be optimized to reduce the financial burden of otherwise using all expensive materials throughout the component to fulfill the condition requirement of one location. Ilie et al. [227] fabricated SS 316L parts via SLM for a predictable mechanical failure by incorporating variation in density at strategic locations within the samples. However, they kept the VED of  $62 \text{ J/mm}^3$  constant with varying laser power (150-200 W) and exposure time (70-93  $\mu\text{s}$ ). For metals, directed energy deposition (DED) and gas metal arc (GMA) AM have been explored to create or repair 3D structures with compositional control [228-232].

Moreover, these techniques have limitations, including low resolution and precision, material wastage, and comparatively poor process control due to the powder-fed nature of the process. Moreover, the complex thermal histories, adjoining deposition tracks, interfaces, as well as frequent and intermittent deposition stoppages have resulted in uncontrolled distributions of the intended properties and have led to premature failure of graded components due to distortion, warpage, and cracking [233].



**Figure 40. Temperature gradients and cooling observed during solidification for SS316 parts using different AM methods. Oval shapes represent the ranges of various studies included [234].**

On the other hand, SLM has much higher heating-cooling rates ( $10^4$  to  $10^6$  K/s) than GMA and DED ( $10^3$  to  $10^5$  K/s), as shown in Figure 40. This magnitude difference in cooling rates of the DED process results in structures with predominantly columnar grains. Moreover, the slower scan speed impedes achieving equiaxed microstructure. However, Parimi et al. [235] have achieved equiaxed grains in a DEDed structure from Inconel by adjusting the heat flux. On the other hand, Spatially varying temperature gradients lead to diverse grain structures in the SLM, as shown in Figure 30. As has been understood in the literature, the SLM solidification microstructure within a single melt pool exhibits a mix of columnar grain (at the bottom) and equiaxed grains (on top). By varying the energy input within the melt pool, different grains can be achieved. When imparting higher laser power, re-melting the previously solidified layer, thereby re-melting the equiaxed grains again. This forms columnar grains that grow across the

melt pool boundary. However, when the laser power is kept low, the grain morphology remains within one-layer thickness. This feature of exhibiting multiple grain morphologies (microstructures) can be leveraged to fabricate FGAM parts exhibiting different physical/mechanical behaviors.

However, only a handful of studies have looked at SLM capabilities to assimilate different materials [204]. The early work of Mumtaz and Hopkinson [205] used SLM to fabricate bi-material specimens with Zirconia and Waspaloy using a high-power Nd:YAG laser. The experimental work by Niendorf [206] demonstrated the use of SLM to produce a step-change SS 316L structure by using two different laser powers (400 and 1000 W) along with powder layer thickness (50 and 150  $\mu\text{m}$ ) while keeping the VED constant. They found columnar coarse-grains for regions processed with 1000 W and fine-grains for 400 W and showcased a local difference in mechanical properties by employing hardness and tensile tests. Holzweissig et al. [20] fabricated a material transition between tool steel H13 and SS 316L by utilizing a reconfigured recoater design for SLM to accommodate two different materials. More recently, Attard et al. [207] have exhibited microstructural control for SLMed IN718 via altering the thermal history by tweaking process parameters (scan strategies, hatch spacing, laser power). They obtained two different types of microstructures (highly columnar and quasi-equiaxed) and concluded the level of preheating from the previous layer to be the key factor in the formation of the ultimate microstructure.

Based on the above discussion, it is clear that the SLM can be used for microstructural grading by artificial alteration of grain morphology, size, and texture by

imparting various process-specific means. However, limited literature is available for obtaining a single material gradation via SLM. Single material gradation is essentially vital for applications where it would be a catastrophe to have a mismatch between different materials by means of thermal expansions or under non-homogeneous loading conditions. Moreover, a single material grading can limit extraneous welds and joint's restrictions and vulnerabilities and minimize performance-related uncertainties of multi-material FGMs.

## 2.7 Knowledge Gaps

Based on the literature review, there has been significant effort in understanding the AM processing of SS 316L. However, a lack of clarity exists in how VED-related SLM process parameters could be used to control and tune the physical/mechanical property *distributions* that can realize FGAM structures. Furthermore, the existing PSPP framework is inadequate in correlating the feedstock pedigree, SLM machine specifications, build thermal histories, correlation in build-orientation-mechanical testing, and defect statistics, amongst others [236].

In the context of this research study, the following knowledge gaps were identified:

- A lack of knowledge of the functionally-usable property ranges achievable in a repeatable and reproducible (R&R) manner in SS 316L via pulsed SLM, and the multivariate process parameter ranges that can reliably impart them

- Although important contributions have been made in the processing- and structure-based causes of mechanical property variations and the data spread in SS 316L, there is a lack in the understanding of leveraging the significant variations that are achievable in the mechanical/physical properties
- Spatial property resolutions achievable via SLM are not known
- A lack of understanding of the local and global mechanical performance of single-alloy FGAM structures under various loading modes
- The role of FGAM interfaces (*i.e.*, locations of property change) in property resolution and performance
- Stress-strain evolution and failure of FGAM structures

In this context, SLM is a promising solution for fabricating application-specific FGAM structures that can be tuned for thermo-mechanical performance. Nonetheless, R&R, resolutions, and transferability are significant challenges to be addressed before end-use. To this end, our work systematically investigates the processing-structure-property-performance relationship of property-graded bulk structures made from a single metallic alloy via pulsed SLM. Analyses are presented to elucidate the underlying causes of the macro- and microstructures' variations in relation to process conditions, the resulting physical and mechanical property distributions, and its local/global mechanical performance evolution until failure. Altogether, this work strives to lay the groundwork for designing FGAM structures optimized for the application.



The novelty of this research work has been the achievements in property variations by altering only two process parameters, the effects of laser power and laser scan speed. Essentially, the work investigates how with the supplied heat energy (changing estimated cooling rates), the solidification microstructures (within local melt pool) are evolving and what causes changes in their physical/mechanical responses. The work also serves as a proof-of-concept for designing and fabricating single alloy FGAM parts for various loading conditions.

### 3. RESEARCH METHODOLOGY

This research's overarching goal was to systematically investigate the causalities within the processing-structure-properties-performance framework for the selective laser melting (SLM) of FGAM bulk structures. Specifically, this study aims to elucidate the relationships between AM process conditions and variations in macro- and microstructures and how such physicochemical traits affect the resulting property distributions.

The core premise of this work lies in the fact that understanding/tracking the thermal influences during processing allows for repeatable and reproducible macro/microstructures and properties, and hence systematically leveraging these is the key to FGAM structures. Several scientific inquiries are made and hypotheses tested in the process – from situating microstructure traits and property variations within the process parameter design space to correlating thermal-driven microstructure morphology to local/global performance and beyond. To elucidate the relationships within, a number of research questions (RQ) are formulated and corresponding tasks are laid out to answer them.

**RQ-1: What are the processing bounds of VED-related process parameters that will yield functionally-acceptable SS 316L bulk structures via a pulsed SLM process?**

Task 1A: Conduct a systematic mapping of the SLM process-parameter design space, formulate a design of experiments of dominant parameters, and manufacture SS 316L samples

Task 1B: Characterize the samples' resulting macro- and micro-structures (optical/electron microscopy, spectroscopy), physical properties (Archimedes density test, ImageJ porosity), and mechanical properties (Vickers microhardness, nanoindentation hardness, and modulus) to identify acceptable VED-related process parameter ranges for each property type

Outputs: Process parameters that will yield functionally-acceptable SS 316L samples, and a mapping of the subset design space detailing the property trends in relation to process conditions, which will enable one to select a process parameter combination that intentionally yields a different (but repeatable) property value for SS 316L

**RQ-2: What are the underlying processing-structure causes of physical and mechanical property variations?**

Task 2A: Quantify/correlate directional-porosity/defects vs. mechanical properties (microscopy)

Task 2B: Map the grain size/morphology variations and phase fractions (across longitudinal and transverse planes) vs. resulting mechanical properties (SEM, XRD, EBSD)

Task 2C: Quantify the spatial property resolutions achievable in SS 316L via SLM by fabricating continually smaller zones with intended property variations (in both XY/XZ planes), and investigate the causes

Outputs: Linking of the processing-based root causes with the variations in macro- and microstructures, and hence the resulting (intended) spatial mechanical property variations in longitudinal and transverse directions – the focus will be on elucidating the underlying principles behind each cause-effect pair and their implications

**RQ-3: How do FGAM bulk structures evolve under stress/strain-based control till failure?**

Task 3A: Fabricate stiffness-graded FGAM structures and map deformation behavior (DIC)

Task 3B: Map the spatial and temporal strain behavior (via DIC) in property-graded multi-zone FGAM bulk structures under stress states, and evaluate the behavior/influence of zonal interfaces as well as fracture surface

Outputs: Local and global strain evolution (spatial/temporal) and failure in bulk FGAM structures under different loading/stress states, a quantification of the spatial property resolutions that are repeatably achievable, and the role of zonal interfaces on strain evolution

Altogether, this effort will help lay the foundation for tailoring the structure, properties, and performance of single alloy FGAM bulk parts made using the SLM. This work contributes

to a greater understanding of the single alloy gradation with the obtainable mechanical/physical data spread in SS 316L. Furthermore, this work provides an opportunity to leverage the significant variations achievable in the property domains for SS 316L, which may potentially be used for mission-critical parts manufacturing.

## 4. MATERIALS & METHODS

In this chapter, a general description of the instrumentation and the material utilized for this study is presented. It is done to offer better insights into the SLM system's operation and raw materials used in the process. Figure 41 provides procedural steps that were followed in this study.

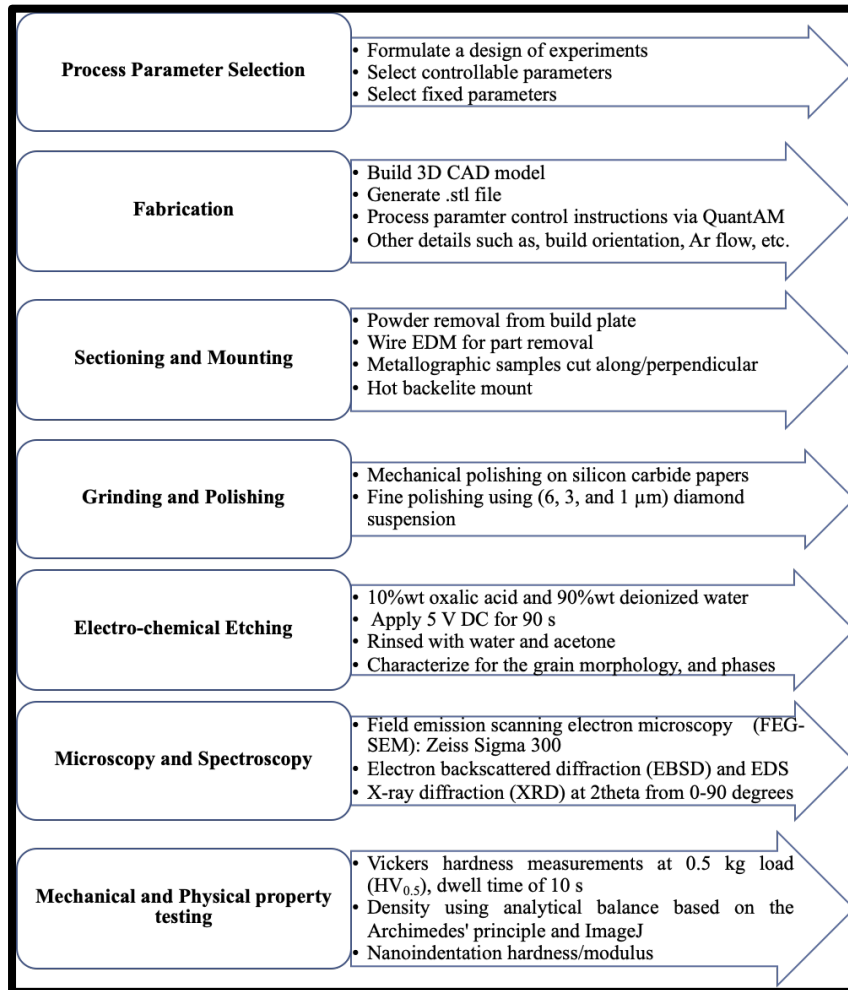


Figure 41. Procedural steps for manufacture and characterization of samples.

#### 4.1 SLM Machine Specifications

Renishaw AM 400 (Renishaw, Gloucestershire, England) platform, as shown in Figure 42, was employed to fabricate all the samples used in the present study.



**Figure 42. The Renishaw AM 400 SLM platform [237].**

The device is equipped with a Ytterbium fiber laser (YFL) (SPI Lasers, Southampton, UK) in Q-switched (pulsed wave) mode with a maximum power of 400 W. The maximum build size for this machine is 250 (L) mm x 250 (W) mm x 300 (H)

mm, and the maximum build rate of 20 cm<sup>3</sup>/h. No preheating of the build platform was considered during the build. To spread the powder dosage evenly across the build platform, a silicon wiper was used. Based on the manufacturer profile recommendations, a powder layer thickness of 50 μm and a hatch spacing of 110 μm were set along with other optimal parameters, as shown in Table 1.

**Table 1. Recommended process parameters by the manufacturer.**

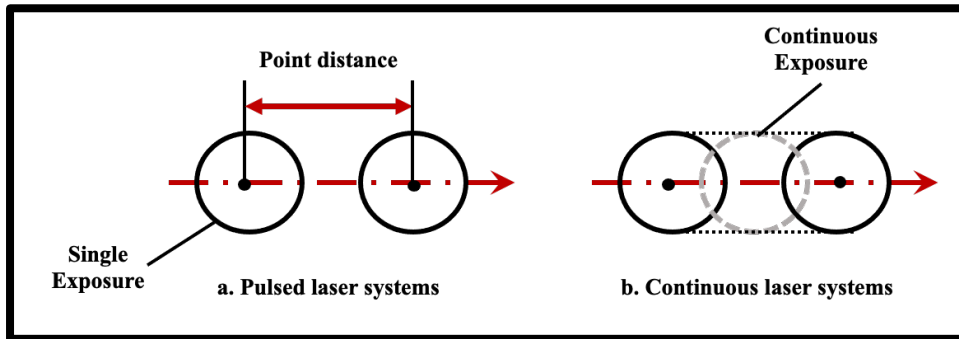
<b>System Parameters</b>	<b>Value</b>
Layer thickness, $L_T$ – (μm)	50
Hatch distance, $h$ – (μm)	110
Laser power, $P$ – (W)	150 to 250
Exposure time, $t$ – (μs)	60 to 100
Point distance, PD – (μm)	50
Scan speed, $V$ – (mm/s)	500 to 800

#### *4.1.1 Relevant Details of the Laser*

As illustrated in Figure 43, unlike continuous wave (CW) laser system, which is described by the velocity, the pseudo-modulated (“move-fire”) system provide discrete pulses for a fixed exposure time at a spot and moves to the next point by a set distance, called, point distance (PD). Jump speed (JS) is the speed with which the galvanometer-

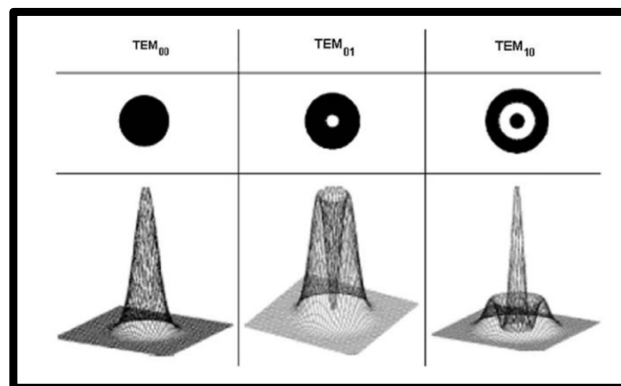


driven mirrors move per the raster motion of lasers from point to point. JS was kept constant at 5000 mm/s during the builds.



**Figure 43. Illustration of the types of laser exposure mechanisms for a) pulsed wave (Q-switched) laser systems and b) continuous wave (CW) laser systems.**

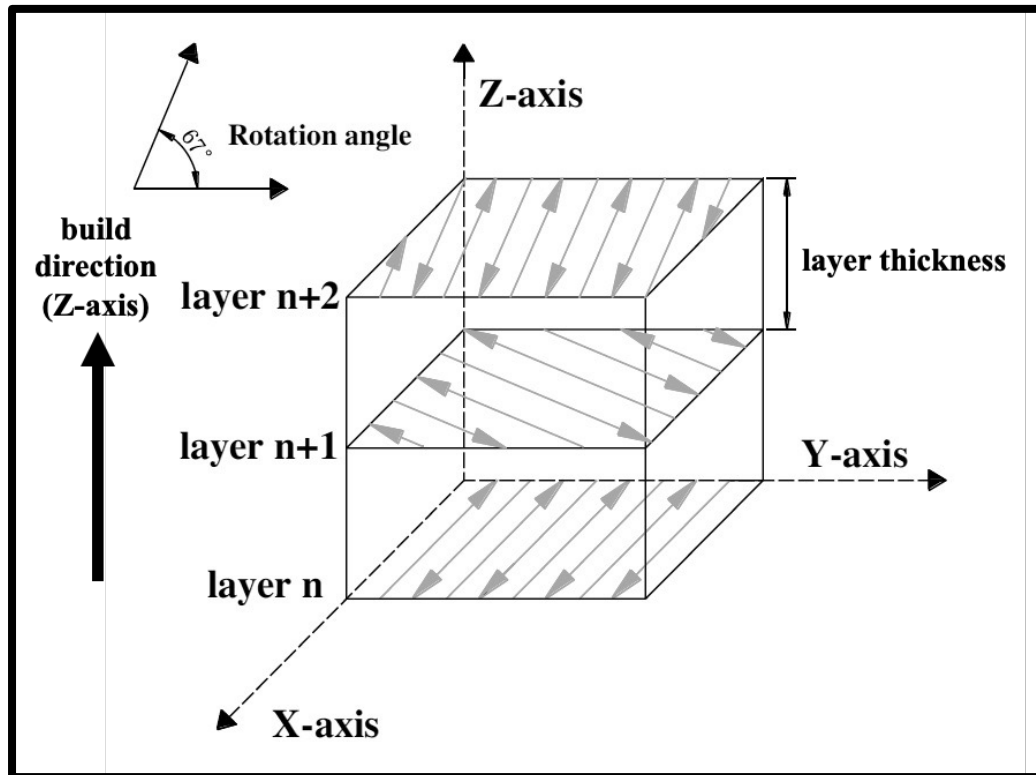
The laser beam has a wavelength of 1070 nm in the near-infrared and (spot) diameter based on  $D4\sigma$  was approximately 70  $\mu\text{m}$  with a  $\text{TEM}_{00}$  Gaussian beam profile, as shown in Figure 44.



**Figure 44. Illustration of various Gaussian beam profile modes [238].**

#### 4.1.2 Laser Scan Strategy

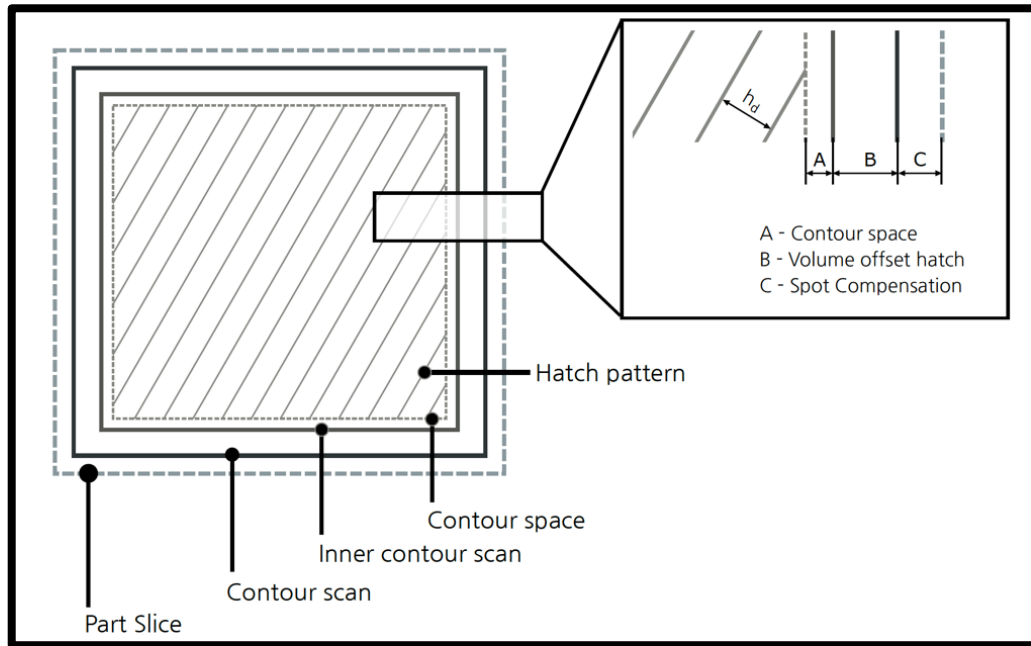
Laser beam scanning in the XY plane was done with a meander scan pattern for all the builds, as illustrated in Figure 45.



**Figure 45. Meander scanning strategy utilized for irradiation in SLM for the fabrication of SS 316L samples.**

Meander scan strategy was preferred for the parts having a small and homogeneous cross-section. The scanning was implemented in a clockwise direction with a scanning angle of  $67^\circ$  between adjacent layers ( $N^{\text{th}}$  and  $N + 1^{\text{st}}$ ) to reduce the anisotropy in the build direction (XY plane).

Quant AM software was used to specify build orientations and support structures with no border scans, down-skin, or up-skin strategies, as shown in Figure 46.



**Figure 46. Meander scanning strategy within a single slice of a part geometry [239].**

During the SLM, a laser beam scans multiple laser paths to build the required part geometries accurately. These include the hatch pattern, contour space, and point exposures. Most of the material is consolidated by a hatch pattern. The contour scan is typically at half of the beam diameter offset from the part boundary. It improves part accuracy, surface finish and eliminates regions not covered during the hatching. The laser point exposures will influence the defect formation during the process. With longer

point exposures, parts have shown a lower lack of fusion (LOF) defects but at the expense of higher build time [240].

#### 4.1.3 Build Chamber Conditions

Figure 47 illustrates the key elements inside the build chamber of RENISHAW AM 400 platform.

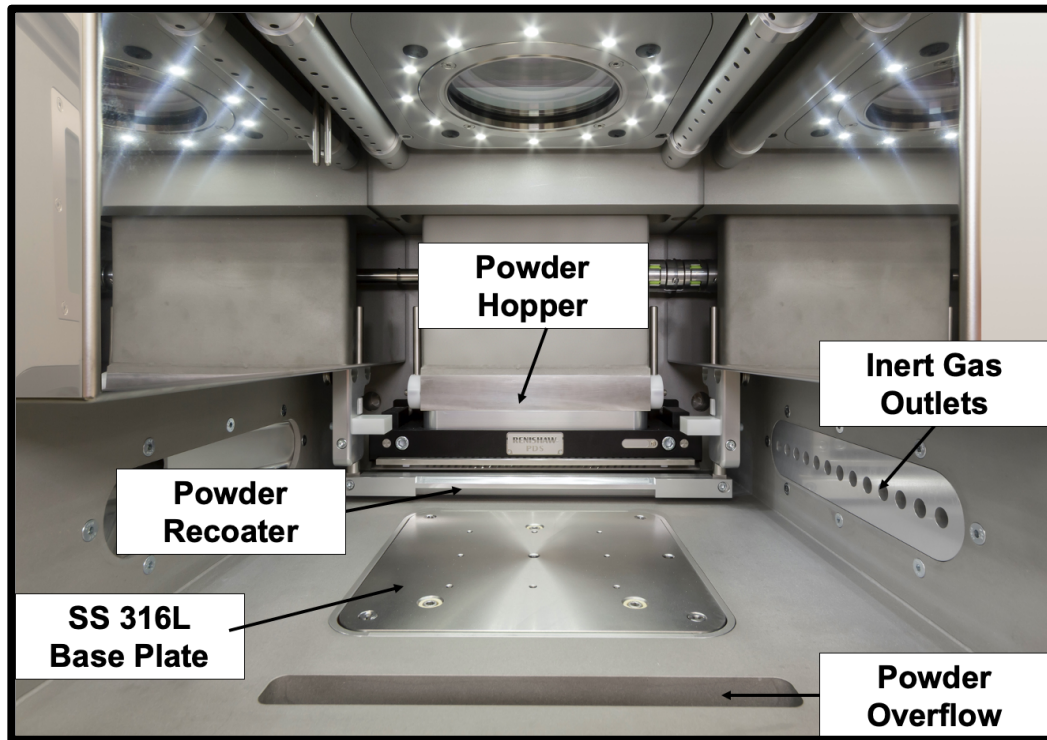


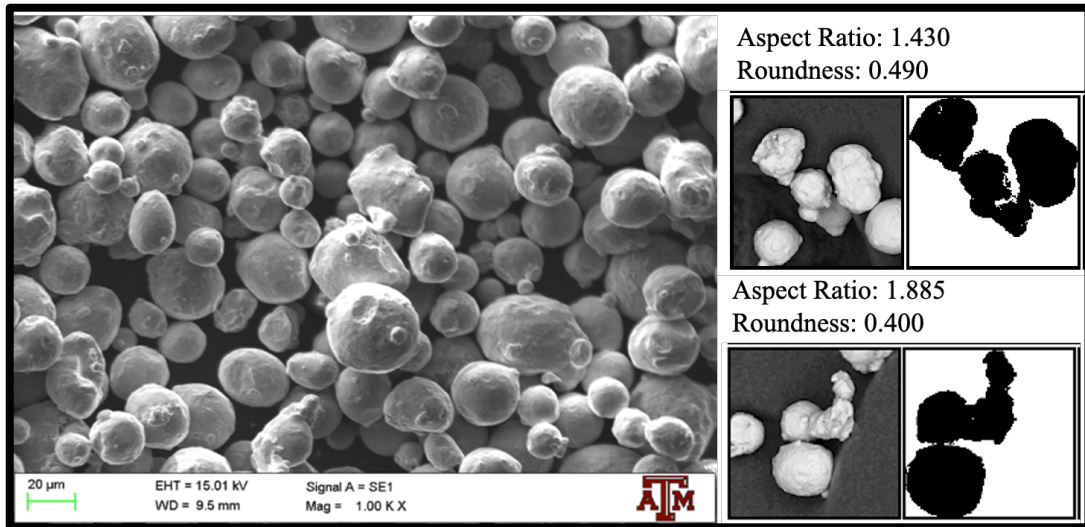
Figure 47. Key elements inside build chamber of RENISHAW AM 400.

This included the substrate material or base plate made of SS 316L and was commercially produced (cold-rolling and annealed). Before the process begins, the build

chamber is first vacuumed to a pressure of ~950 mbar. Next, argon is pumped from the outlets at constant pressure until the build chamber reaches 15 mbar and the oxygen level below 500 ppm. This helps minimize combustion alongside removing secondary byproducts such as weld spatter and fumes from the work area [100]. During the build, any extra powders are collected in the powder overflow containers and then can be sieved and reused in the next build. Post-build completion, air blasting is used to remove the loose powder particles, and samples were carefully hand-plucked with the help of pliers from the base plate. No post-processing was performed on the printed samples.

#### **4.2 Feedstock Material**

A commercially available N<sub>2</sub> gas-atomized AISI 316L stainless steel powder, sourced from Renishaw plc., was used as raw material for manufacturing of the samples, as seen in Figure 48. The virgin powder particles had a high volume of nearly spherical shape.

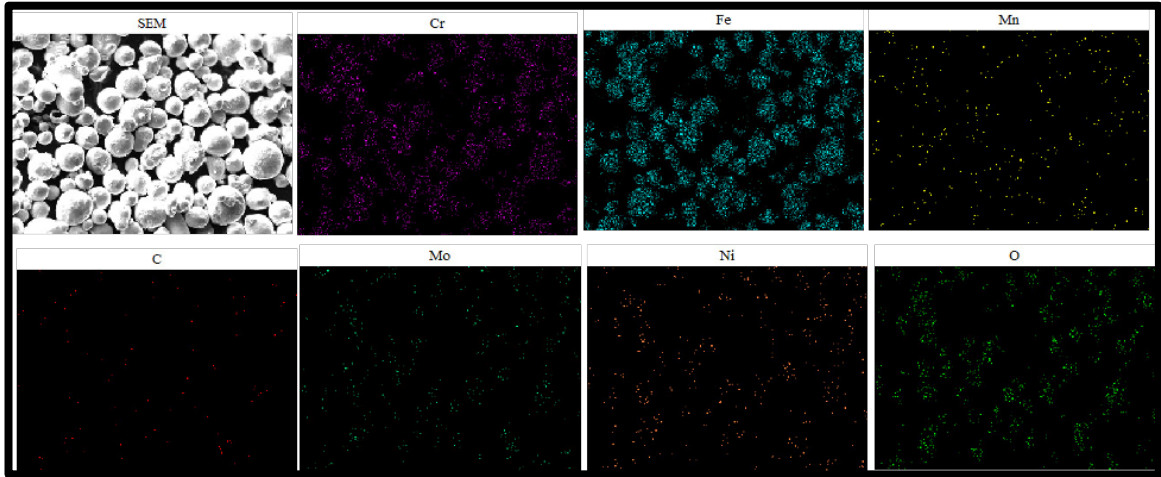


**Figure 48. Morphology of virgin SS 316L powder particles employed in the experiments, and aspect ratio as well as roundness for the powder particles.**

**Table 2. Nominal chemical composition (in wt %) of SS 316L powder (as supplied) [241] and the ASTM A240 [242] specified composition range of SS 316L.**

Element (wt.%)	Cr	Ni	Mo	Mn	Si	C	N	Fe
SS 316L powder	17.1	12.4	2.9	1.09	0.7	0.01	0.1	65.7
ASTM A240 - 20	16-18	10-14	2-3	< 2	< 1	< 0.03	< 0.1	bal.

Table 2 lists the powder’s chemical composition, as received from the Renishaw Inc. Figure 49 provides EDS analysis of virgin SS 316L powder. As seen, the low C contents in 316L SS reduce this material’s susceptibility to sensitization which could reduce the mechanical properties of the manufactured parts.



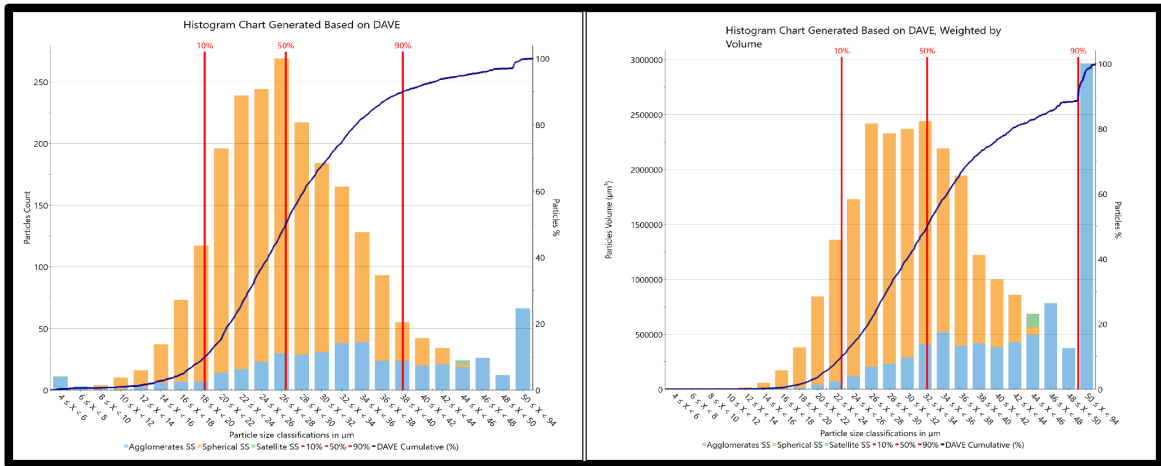
**Figure 49. EDS maps for virgin SS 316L powder showing high concentration of Cr, Ni, and Fe.**

**Table 3. Results from SS 316L PSD analysis.**

**Stainless Steel Particle Size Distribution Analysis**

DAvg Distribution			
Based on Davg	10%	50%	90%
Agglomerates SS	21.49 $\mu\text{m}$	34.75 $\mu\text{m}$	51.93 $\mu\text{m}$
Spherical SS	19.17 $\mu\text{m}$	26.35 $\mu\text{m}$	34.96 $\mu\text{m}$
Satellite SS	5.08 $\mu\text{m}$	45.40 $\mu\text{m}$	45.68 $\mu\text{m}$

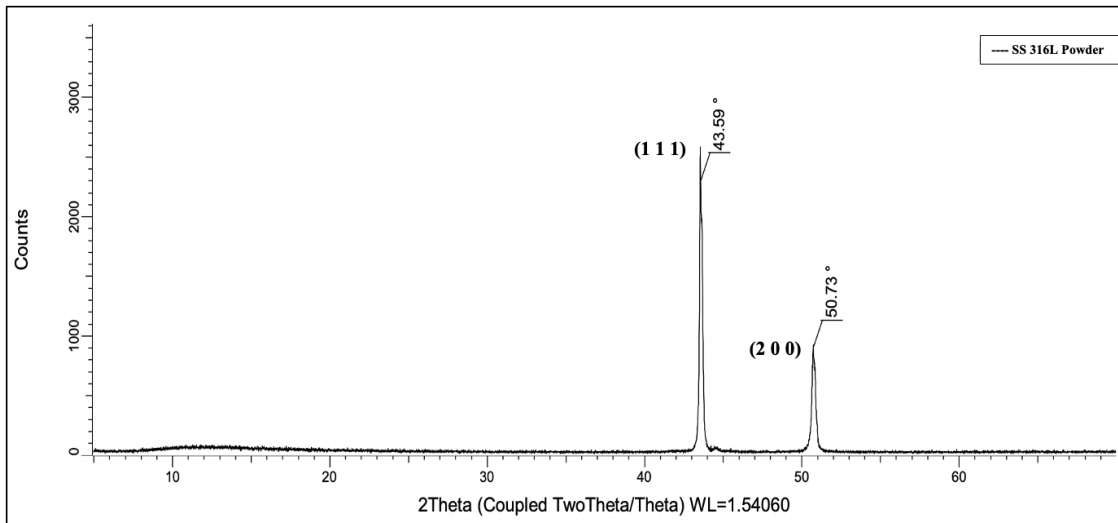
Table 3 provides the SS 316L virgin powder particle size distribution (PSD) analysis (courtesy: Nanoscience Instruments). A total of 2200 powder particles were analyzed for the D10, D50, and D90 distributions. More details about the powder particle analysis are found in Appendix A.



**Figure 50. Particle Size Distribution (PSD) of as received SS 316L powder based on (a) average particle count and (b) particle volume in  $\mu\text{m}^3$ .**

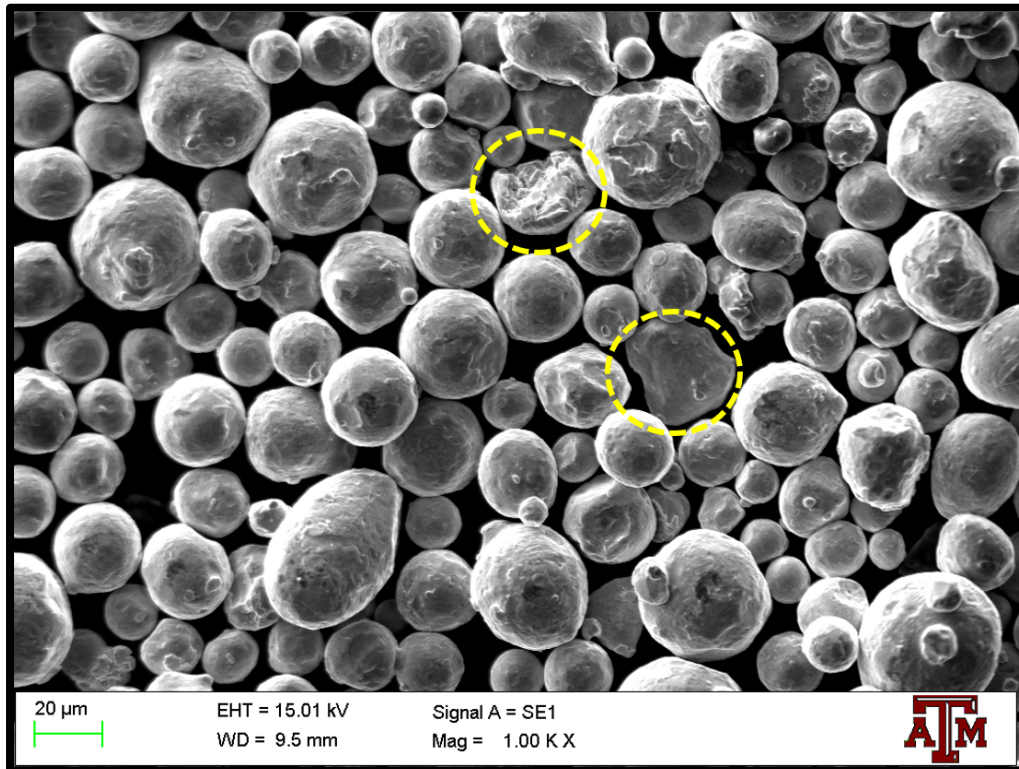
Figure 50 illustrates the powder size distributions (PSD) of  $D(10) = 19.17 \mu\text{m}$ ,  $D(50) = 26.25 \mu\text{m}$ , and  $D(90) = 37.96 \mu\text{m}$ . Previous studies showed similar powder characteristics have been reported in the literature for a successful build and investigating the microstructure and mechanical properties of SLM-fabricated 316L [145, 243].





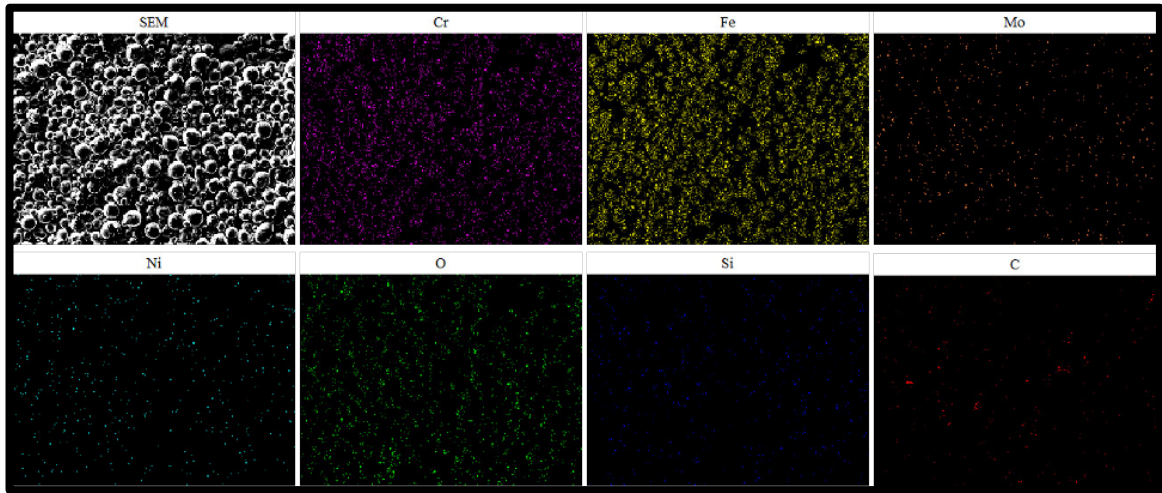
**Figure 51. Diffractograph for SS 316L precursor powder showing FCC austenitic diffraction peaks.**

Figure 51 illustrates representative X-ray diffraction (XRD) measurements performed on the virgin SS 316L powder. Miller indices were identified based on the diffracted angle (2Theta). Initial inquiry shows that the powder has a predominant face-centered cubic (FCC) austenite phase. However, small traces of ferrite/martensite may also exist in the austenite matrix. Figure 52 shows an SEM image of impure or recycled powder particles of SS 316L.



**Figure 52. SEM micrograph of loose impure SS 316L powder particles. Highlighted with yellow circles are non-spherical, partially sintered powder particles.**

Figure 53 illustrates concentrations of Cr, Fe, Mo, Ni, O, Si, and C, identified by EDS analysis. As highlighted, the particles showed irregularity in shape with an increase in powder particle agglomerations. Also, partially melted and sintered particles were also observed.



**Figure 53. EDS maps for impure SS 316L powder showing high concentration of Cr, Ni, and Fe.**

### **4.3 Testing and Measurement**

The following sub-sections provide brief descriptions of various physical and mechanical testing procedures.

#### *4.3.1 Bulk Density and Porosity Measurements*

The density of all samples was measured individually using the Archimedes method described by Spierings et al. [244]. A sample density was calculated by measuring the weight of samples measured in air and distilled water, as illustrated in Figure 54.



**Figure 54. Density test setup based on Archimedes method.**

The distilled water is held at a constant temperature of 23.1°C, with the density is 0.9975 g/cm<sup>3</sup> by considering the temperature and fluid-density dependencies [245]. Two repetitions were taken for each sample, and the density of which was then calculated by dividing the mass of the specimen in water by the volume of water displaced. The apparatus has a measuring accuracy of  $\pm 0.1$  mg. The relative density is expressed as the percentage of the nominal density of SS 316L powder (7.99 g/cm<sup>3</sup>).

#### *4.3.2 Hardness Measurements*

Vickers microhardness (HV) profile measurements were taken on the polished surfaces using the Beuhler Wilson VH1102 Microhardness tester (Illinois Tool Works). Following ASTM E92, a square-based pyramidal diamond indenter was used to probe

sample surfaces polished as per HV testing requirements [246]. The distance between successive indents was  $\sim 1$  mm, and indents were kept at least 1.5 mm away from the sample edges. The applied load was 0.5 kgf (denoted as HV<sub>0.5</sub>) with a dwell time of 10 s. The setup is shown in Figure 55.



**Figure 55. Beuhler Wilson VH1102 microhardness tester.**

#### *4.3.3 Nanoindentation Measurements*

Nanoindentation tests were carried out at the ambient temperature in the air chamber using the Hysitron TI 950 Triboindenter nanomechanical testing instrument as illustrated in Figure 56.



**Figure 56. Hysitron TI 950 Triboindenter nanomechanical test setup.**

It is equipped with a depth-sensing resolution of 0.04 nm and a load sensing resolution of 1 nN. To carry out the indentations, a Berkovich type of diamond indenter was used that has a tip radius of 150 nm. Fused silica was used for calibration of the frame and contact area. The collected data was then adjusted for elastic recovery, considering the unloading residual depth with less than 10% of the maximum load applied.

Room temperature nanoindentation testing were carried out on all samples based on the ASTM E-2546 standards and following the procedure as outlined by Oliver and Pharr [247].

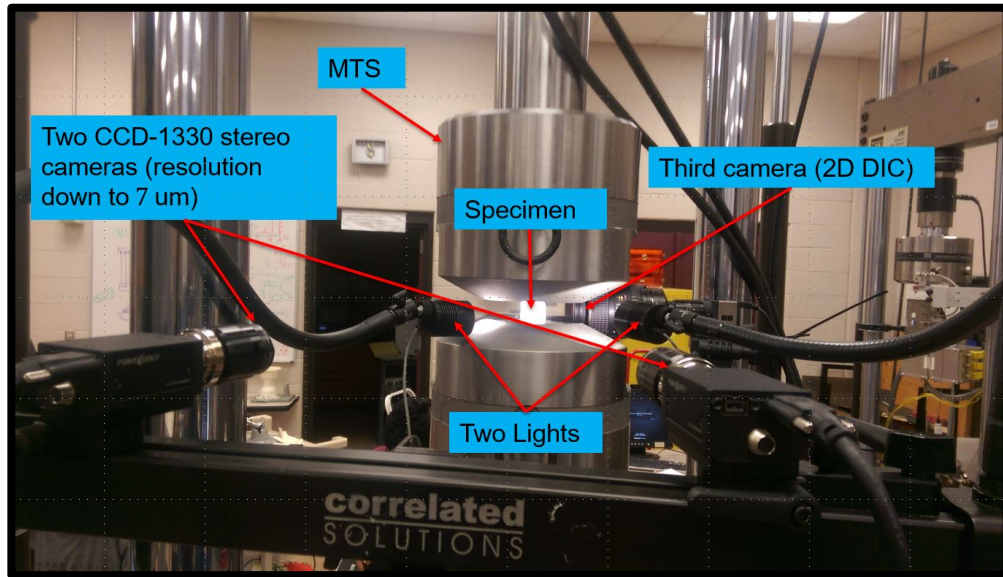


#### 4.3.4 Tensile Testing with Digital Image Correlation

Dog-bone-shaped rectangular cross-section tensile specimens of various sizes were designed based on the ASTM E8 specifications and tested at room temperature for all the samples used during this study [248]. The tests were performed on the MTS Insight system with a 30 kN load cell at an applied cross-head displacement rate of 0.05 mm/s along the building direction (BD). There was no grinding or post-processing performed on the built-surface of the samples. The average surface and area roughness of the surface was measured and found to be in the range of 6  $\mu\text{m}$ . Figure 57 shows the tensile test setup.



**Figure 57. MTS Insight tensile testing setup.**



**Figure 58. Overview of the 2D DIC experimental setup.**

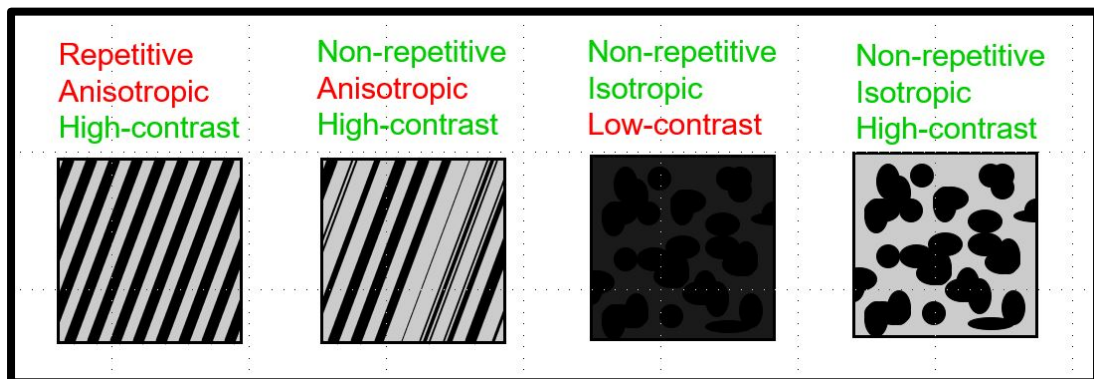
**Table 4. Summary of selected 2D DIC parameters.**  
**2D DIC system parameters**

<b>Camera</b>	CCD-130 stereo
<b>Lense</b>	35 mm compact
<b>Exposure</b>	1 ms
<b>Aperture</b>	f/8
<b>Resolution</b>	7 $\mu\text{m}$
<b>Software parameters</b>	
<b>Software</b>	Vic-2D
<b>Subset size</b>	17 pixels
<b>Step size</b>	3 pixels



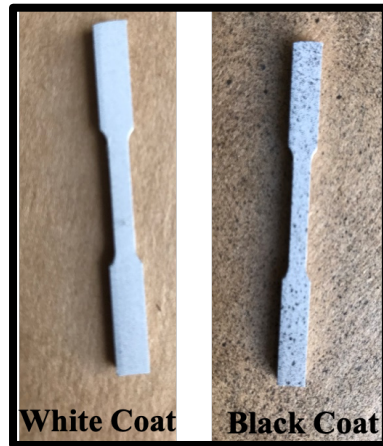
Two-dimensional digital image correlation (2D-DIC) technique was used to calculate the strain evolution in the sample's gauge section. The 2D-DIC system setup and relevant parameters are shown in Figure 58 and Table 4 respectively.

DIC is a technique which is based on the comparison of sequential images taken during the deformation of a test specimen [249]. DIC calculates the displacement based on a correlation algorithm by matching the grey scale values between two deformation states. To facilitate this, a speckle pattern is applied on the specimen surface. Moreover, in order to create the speckles on the surface of the samples, spray-painting was used. As previously reported by the Haddadi et al. [250] finer speckle patterns assist in obtaining more 'randomness' as against larger 'dotted' patterns. Figure 59 illustrates various types of speckle patterns that can be implemented during the DIC.



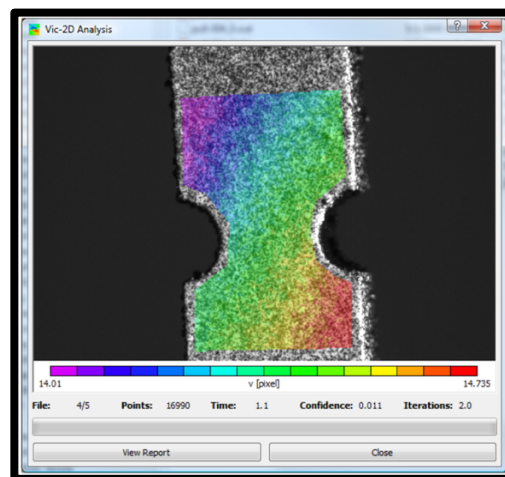
**Figure 59. Various types of speckle patterns used in DIC analysis.**

In order to prepare samples for DIC, first, a coat of white paint was sprayed and later the contrast was developed with the black paint as illustrated in Figure 60.



**Figure 60. Speckle pattern generation with white and black spray paint.**

The local and global performance during the tensile test were obtained by mapping the spatial and temporal strain behavior in property-graded multi-zones via commercial 2D Digital Image Correlation (DIC) software, VIC-2D, by Correlated Solutions Inc as shown in Figure 61.



**Figure 61. Vic-2D window showing overview of correlation in progress and results.**

#### 4.3.5 Four Point Bending Test with Digital Image Correlation

In order to investigate the material's bend or flexural strength, a four-point bending test set-up was used in accordance with the ASTM C1161-18 standard test procedure [251]. The bending tests were performed on the MTS Exceed system (Model E44) with a 30 kN load cell at an applied cross-head displacement rate of 0.5 mm/min perpendicular to the building direction (BD). Strain rate was kept at  $10^{-4} \text{ s}^{-1}$  displacement cutoff was 2.5 mm at the loading points. Furthermore, there were no grinding or post-processing performed on the built-surface of the samples. Similar to tensile samples, the average surface and area roughness of the surface was found to be in the range of  $6 \mu\text{m}$ . Figure 62 and Figure 63 shows the four-point bending fixture and DIC test setup, respectively.



**Figure 62. Four-point bending test setup on MTS Exceed test frame.**



**Figure 63. Four-point bending test setup with DIC.**

#### **4.4 Microstructural Characterization**

As-printed samples were sectioned for metallography on both the longitudinal (XY plane) and transverse (XZ plane) cross-sections using an alumina blade on an Allied TechCut 5 precision high speed saw as illustrated in Figure 64.



**Figure 64. Allied TechCut 5 precision saw to section specimens.**

The samples were then hot mounted in bakelite using Buehler SimpliMet 4000 mounting press as seen in Figure 65 and samples in Figure 66.



**Figure 65. Buehler SimpliMet 4000 mounting press.**



**Figure 66. Sectioned and mounted samples in bakelite.**

Samples were then grounded with silicon carbide (SiC) paper ranging grit #320-1200 and followed by MD-Largo (DiaPro Largo 9  $\mu\text{m}$  suspension). The samples were then polished with MD-Dac (DiaPro Largo 3  $\mu\text{m}$  suspension) [252]. Microstructural characterization was carried out using a LEICA DM 2500 M (Wetzlar, Germany) light optical microscope (LOM).



**Figure 67. ZEISS EVO LS 15 SEM platform.**



Figure 67 shows Zeiss EVO LS 15 field emission gun scanning electron microscopy (FEG-SEM) platform was used for capturing higher magnification imaging for this study. Also, energy dispersive spectroscope (SEM-EDS), and electron backscattered diffraction (EBSD) were also analyzed using it.

Moreover, the samples were electrochemically etched using 10%wt oxalic acid and 90%wt deionized water under 7 V DC for 20 s as illustrated in Figure 68. Post etching, the samples were rinsed with water and acetone and dried using compressed air.



**Figure 68. Electrochemical etching setup.**

X-ray diffraction (XRD) was done in a PSD (Lynx-Eye, Bruker-AXS) with a 1kW Cu X-ray tube, maintained at 40 kV and 25 mA. The  $2\theta$  range was from 0 - 60° with a step size of 0.015°.

## 5. MAPPING PROCESS PARAMETER BOUNDS AGAINST STRUCTURE & PROPERTY TRENDS (RQ-1)

This chapter is aimed at investigating the reliable fabrication of SS 316L samples that exhibit repeatable variation in mechanical properties, with a view to eventually design and manufacture functionally-graded bulk structures by SLM. In order to achieve it first the process parameter mapping was carried out for SS 316L alloy on a pulsed laser system. Overall, this part of the study aims to answer research question 1 (RQ-1), *i.e.*, “What are the ranges of VED-related process parameters that will yield functionally-acceptable SS 316L bulk structures via a pulsed SLM process?” This is the first step towards exploring the usable range of mechanical properties (such as hardness, density, and modulus) achievable for SS 316L by varying energy density-based process parameters.

### 5.1 Mapping SLM Process Parameters Design Space

A systematic design of experiments (DOE) that spanned the volumetric energy density (VED)-based process parameter design space was utilized to investigate the range of functionally-acceptable physical/mechanical properties achievable in SS 316L. For this, selection of process parameters were chosen after careful literature review within a range of usable relative densities between 90–100% [253]. Specifically, the laser power was varied in the step of 25 W between 150 to 250 W. The scan speed was



varied from 500-800 mm/s during the build by changing the exposure time from 60 to 100  $\mu$ s. PD of 50  $\mu$ m was kept constant. This was done to reliably and repeatedly obtain variations in mechanical properties (specifically hardness and density). Table 5 shows the VED-related process parameters used for the experiment.

**Table 5. VED-based process parameters used for experiments.**

<b>Sample #</b>	<b><math>P</math> (W)</b>	<b><math>t</math> (<math>\mu</math>s)</b>	<b><math>V</math> (mm/s)</b>	<b><math>P/V</math> (J/mm)</b>	<b><math>E_V</math> (J/mm<sup>3</sup>)</b>
1	150	63	800	0.19	34.09
2	150	71	723	0.21	37.72
3	150	80	652	0.23	41.83
4	150	92	577	0.26	47.27
5	150	108	500	0.30	54.55
6	175	63	800	0.22	39.77
7	175	71	723	0.24	44.01
8	175	80	652	0.27	48.80
9	175	92	577	0.30	55.14
10	175	108	500	0.35	63.64
11	200	65	779	0.26	46.68
12	200	68	750	0.27	48.48
13	200	71	723	0.28	50.30
14	200	74	698	0.29	52.10
15	200	77	674	0.30	53.95
16	200	80	652	0.31	55.77
17	200	84	625	0.32	58.18
18	200	88	600	0.33	60.61
19	200	92	577	0.35	63.02
20	200	97	550	0.36	66.12
21	200	108	500	0.40	72.73
22	225	71	723	0.31	56.58
23	225	80	652	0.35	62.74
24	225	92	577	0.39	70.90
25	225	108	500	0.45	81.82
26	250	80	652	0.38	69.72
27	250	92	577	0.43	78.78
28	250	108	500	0.50	90.91

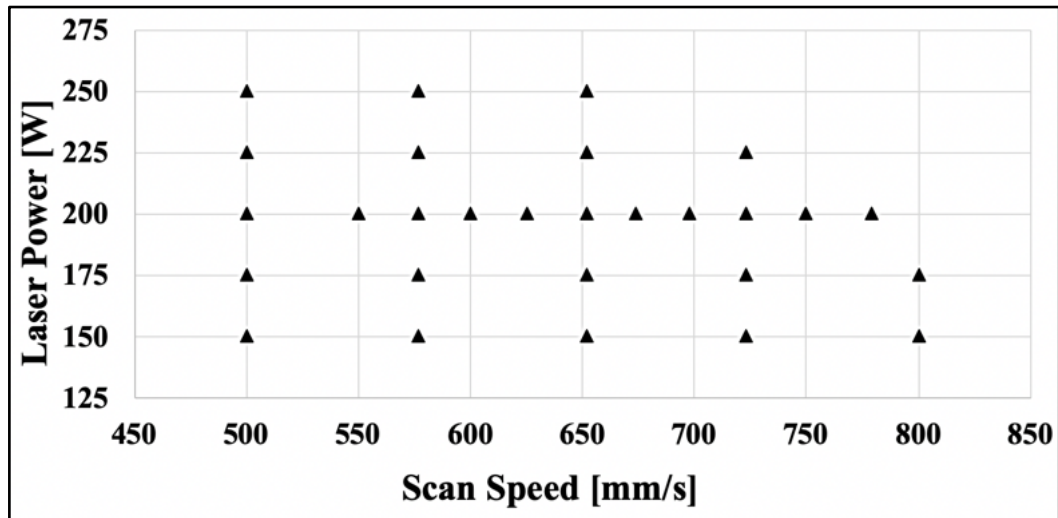


Figure 69. PV map implemented for processing 28 SS 316L samples.

Figure 69 shows the  $P$  and  $V$  design space utilized for fabricating 28 samples, each with unique processing conditions. This was done with a view on demonstrating the fabrication of single-alloy bulk structures with spatially-tailored properties by selectively varying the process parameters chosen from the pool of choices.

Renishaw QuantAM software was used to specify the build orientations and other arrangement of all 28 samples which were appended onto 4 standard dog bones (ASTM E8), as circled in Figure 70 and processed as shown in Figure 71.

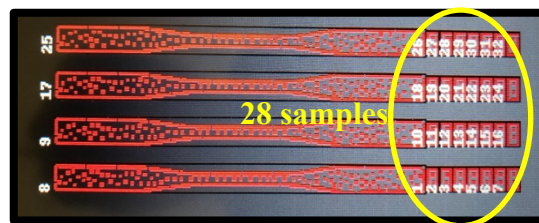
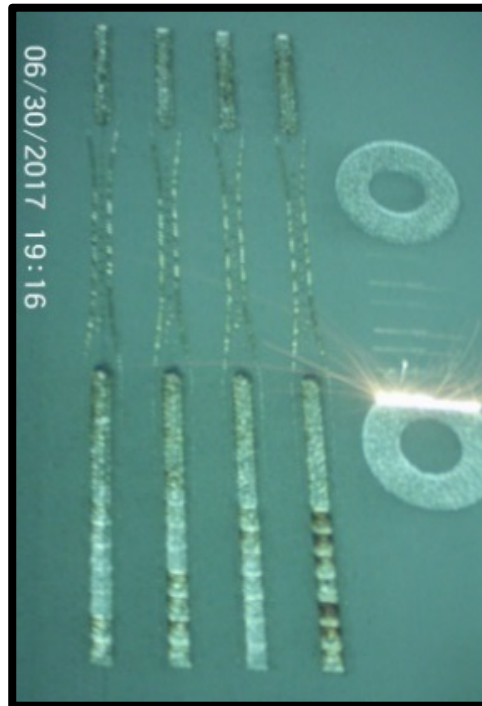


Figure 70. Layout of 28 samples (as circled) arranged using QuantAM software.

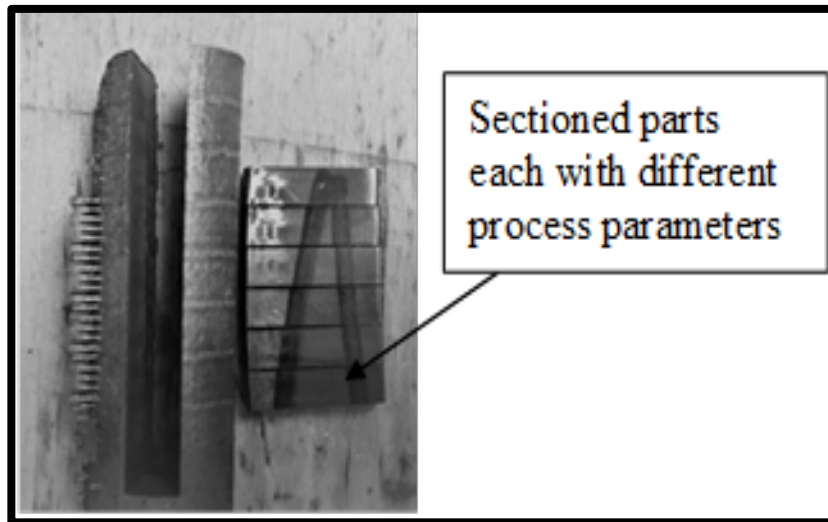


**Figure 71. Samples being processed inside the SLM build chamber.**



**Figure 72. As-built samples on the build plate with the support structures. Sample numbers are also indicated. Observe that sample #28 exhibited curling due to higher energy input.**

As-built samples are shown in Figure 72. Wire electrical discharge machining (EDM) was used to cut out the samples as shown in Figure 73. All the samples were cut from the middle region of the built sample.



**Figure 73. Samples were cut using wire-EDM from the middle region. Each sample is 7 mm long, 5 mm thick, and 5 mm wide.**

To characterize mechanical/physical properties, all the samples were carefully sectioned, hot mounted, and polished, following standard procedures as shown via the flowchart in Figure 41.

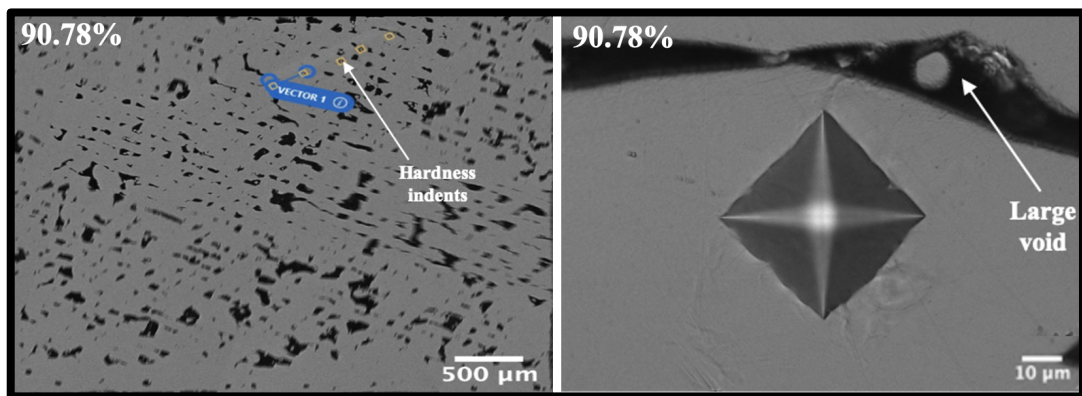
## **5.2 Properties and Characterization**

This section presents the findings of the experimental characterization of as-built SS 316L samples made via SLM. There were no post-processing steps performed

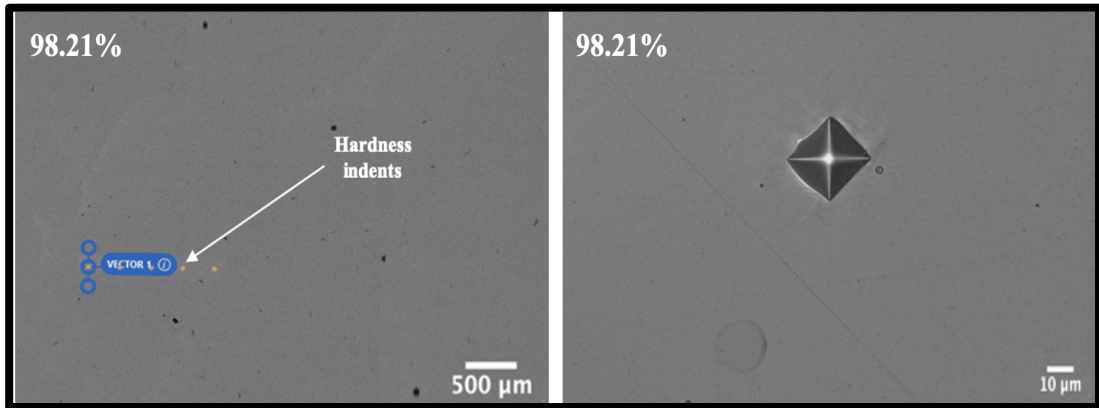
(thermal or surface finishing) on any of the samples. The microhardness results are reported first. The porosity results are discussed using both optical and bulk density techniques. Low-magnification optical images of polished specimens have also been presented.

### 5.2.1 Results of Physical and Mechanical Properties

Typically, hardness does get affected by the amount of porosity and the microstructure present in the material. Hardness measurements on all twenty-eight samples were performed. Figure 74 illustrates the Vickers hardness test surfaces and indent locations for sample #1, which had the lowest relative density value of 90.78%.



**Figure 74. Vickers hardness indents on the lowest density sample #1 (90.78%). Visible are hatch patterns and pores (pores were due to incomplete melting of the powder).**



**Figure 75. Vickers hardness indents on a higher density sample #12 (98.21%). Note the significantly less pores in comparison to Figure 74.**

Figure 75 on the other hand show the hardness test surfaces and indent locations for sample #12, which had one of the higher relative densities measured at 98.21%. The observed significant differences in porosities are directly responsible for the corresponding densities of the samples and is a significant contributor to the composite and nano-hardness measured on the samples.

**Table 6. Average hardness and density results.**

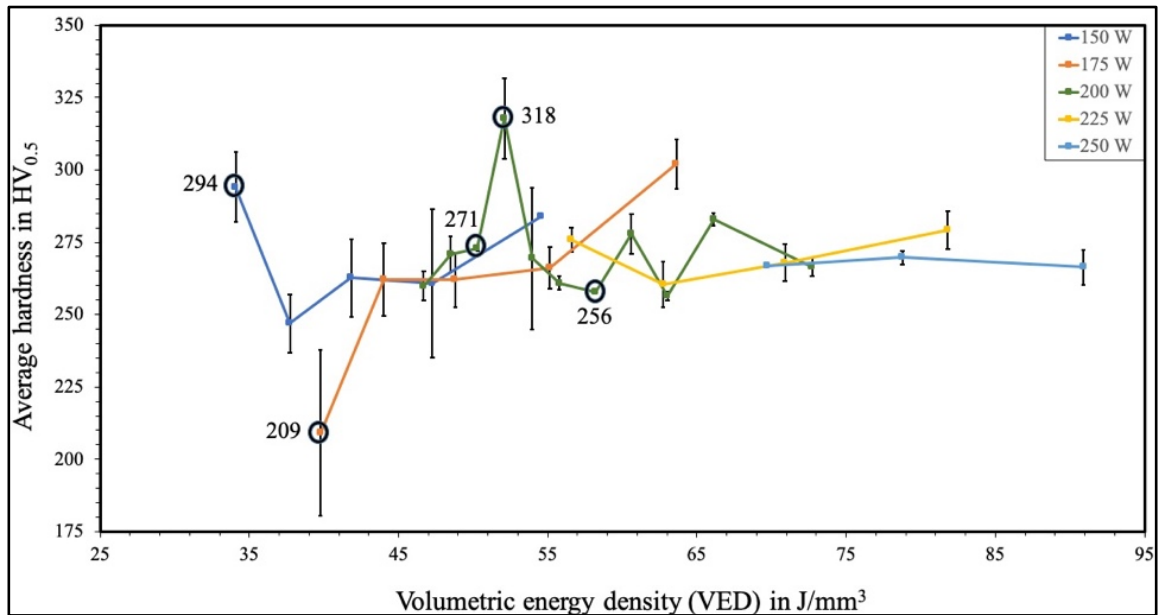
<b>Sample #</b>	<b>Avg. HV<sub>0.5</sub></b>	<b>Std. dev.</b>	<b>Avg. density (%)</b>
1	294.10	12.10	90.8
2	246.95	10.05	95.9
3	262.65	13.35	98.0
4	260.75	25.65	99.0
5	284.00	0.60	99.9
6	209.15	28.55	96.4
7	262.05	12.55	97.9
8	262.00	9.50	99.9
9	262.15	7.15	98.2
10	302.05	8.65	97.8
11	259.90	5.1	98.7
12	270.75	6.15	98.2
13	272.75	0.65	97.8
14	317.90	13.90	97.5
15	269.40	24.50	98.4
16	260.85	2.35	97.2
17	257.85	0.55	97.4
18	277.85	6.85	98.8
19	256.40	1.50	97.2
20	282.90	2.20	98.1
21	266.40	3.10	98.8
22	275.80	4.20	99.1
23	260.50	7.80	98.9
24	267.85	6.35	98.6
25	279.20	6.50	99.2
26	266.80	0.30	98.4
27	269.70	2.30	99.9
28	266.45	6.05	99.4

As shown in Table 6, results show a broad range of microhardness values varying with VED.

Significant hardness variations were achieved by imparting different energy inputs. Samples processed with low powers (150-200 W) showed relatively higher hardness variations than the remaining samples. The highest microhardness measured across the samples was 318 HV<sub>0.5</sub> ( $P = 200$  W;  $V = 698$  mm/s;  $E_v = 52.10$  J/mm<sup>3</sup>), which was closest to the one reported by Saeidi et al. [174] of 320 HV. They reasoned such exceptional hardness on two main factors, the first being the existence of cellular subgrain microstructure (with dimension ranging between 0.5 – 1  $\mu$ m) that believed to accumulate more considerable stresses and provide extra strength—the second being oxide inclusions that blocking the dislocation movement and results in higher strength.

On the other hand, the lowest microhardness measured was 209 HV<sub>0.5</sub> ( $P = 175$  W;  $V = 800$  mm/s;  $E_v = 39.77$  J/mm<sup>3</sup>), which also was in line with the values reported by Tucho et al. [254] and Sun et al. [199]. Figure 76 summarizes the hardness variations of measured across 28 samples, each with a varying VED values.

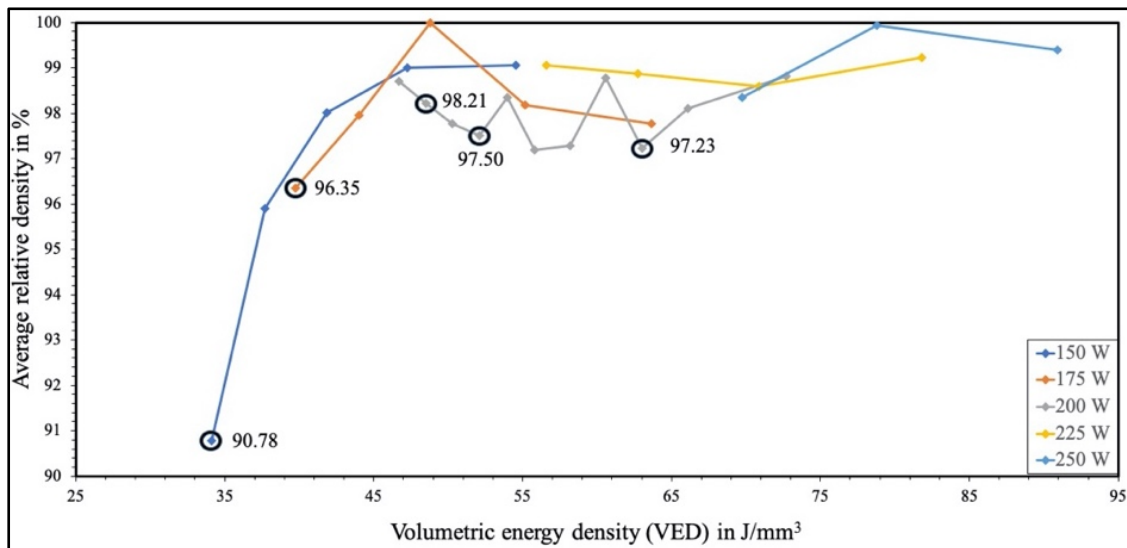




**Figure 76. Vickers hardness of 28 samples showing the effects of VED. Highlighted circles show five selections of hardness values incorporate for fabricating gradient samples.**

In general, the obtained hardness range for samples (209-318 HV<sub>0.5</sub>) was significantly higher when compared to conventionally casted SS 316L (150-160 HV). The reason being, SLMed components tend to exhibit much more refined (smaller) grains due to higher thermal gradient (higher cooling rates) [255]. Generally, higher VED results in the re-melting of the already solidified layer and promotes grain refinements. Finer (smaller) grains enhance hardness, whereas the coarser (larger) grains yield lower strength to withstand deformation due to indentation (Hall-Petch relationship) [256]. The existence of phases (other than austenite) can also impact the observed hardness differences.

Relative density (via Archimedes method) [257] and porosity measurements were obtained for all twenty-eight samples. As reported earlier in Table 6, results with a range of 90-99% and minimal spread across the samples due to their unique processing combinations. Figure 77 illustrates density measurements across all 28 samples.



**Figure 77. Relative density graph for the SLM-built SS316L samples with varying process parameters. The average density data represented was measured by the Archimedes method. Notice the five circled values chosen for the gradient sample fabrication.**

As frequently reported in the literature and discussed earlier, the input energy imparted on the powder bed, amongst other processing conditions, plays an important role in the final part microstructure. Having low energy input results in unmolten material and thereby increased porosity by forming lack-of-fusion (LOF) defects. It was evident in the case of sample 4 with the lowest density ( $\rho$ ) of 90.78% ( $P = 150$  W;  $V =$

800 mm/s;  $E_v = 34.09 \text{ J/mm}^3$ ). However, a similar trend for higher energy input was not observed. Typically, too high energy input results in eliminating pores and defects (such as voids, balling, LOF) but at the same time can cause serious evaporation of material as well as re-melting of the already solidified layer below, resulting in keyhole defects. Moreover, as-built samples surface roughness may also influence the bulk density outcomes. However, it was noticeable that near-theoretical densities of 99.9+% could be repeatedly achievable with certain process parameter combinations.

### 5.3 Down-selection of Five Process Parameter Combinations

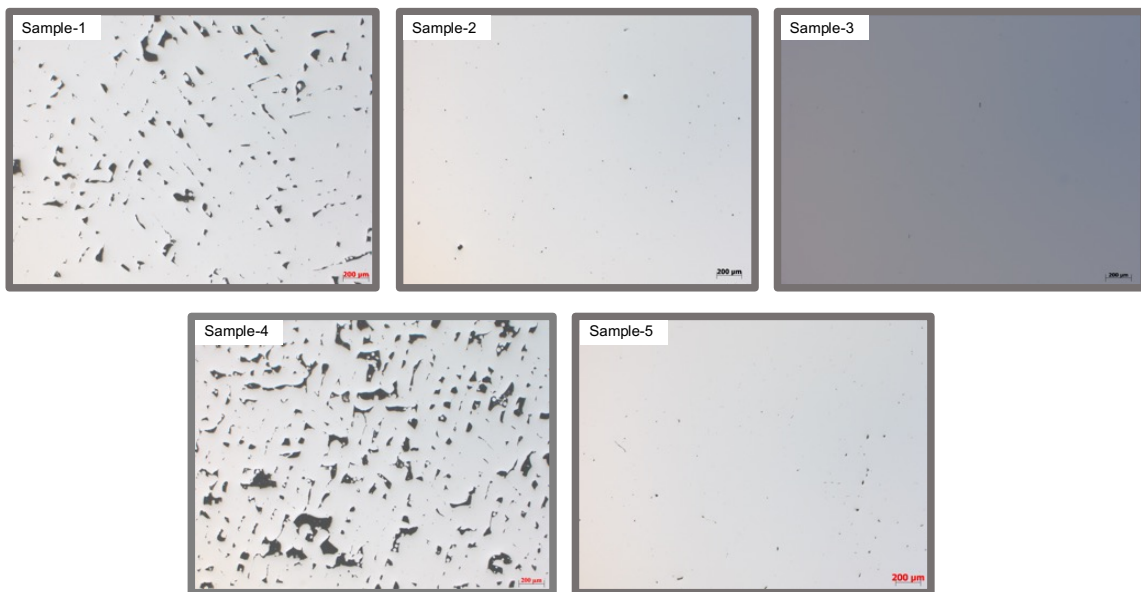
Five process parameter sets with different VED-based process parameter sets were down-selected from 28 samples as summarized in Table 7.

**Table 7. Selected five process parameter configurations.**

<b>Sample #</b>	<b>Laser Power (P) [W]</b>	<b>Scan Speed (V) [mm/s]</b>	<b>Energy Density (<math>E_v</math>) [J/mm<sup>3</sup>]</b>	<b>P/V [J/mm]</b>
1	175	800	39.77	0.22
2	200	577	63.02	0.35
3	200	750	48.48	0.27
4	150	800	34.09	0.19
5	200	698	52.10	0.29

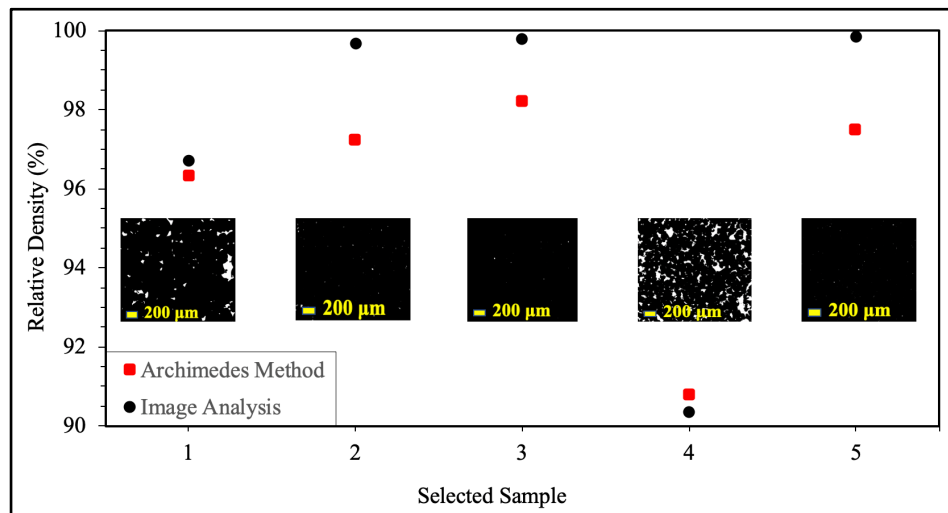
These process combinations were chosen to yield a repeatable and monotonic change in specific mechanical properties, which will be employed to design and additively manufacture functionally-graded structures for performance tailoring along with an in-depth analysis of microstructure and mechanical and physical properties (hardness, density/porosity, Young's modulus).

Furthermore, optical images were used to measure the defect free region of the sample surface in transverse (XY) plane, each captured at equal magnification having the same size as shown in Figure 78.



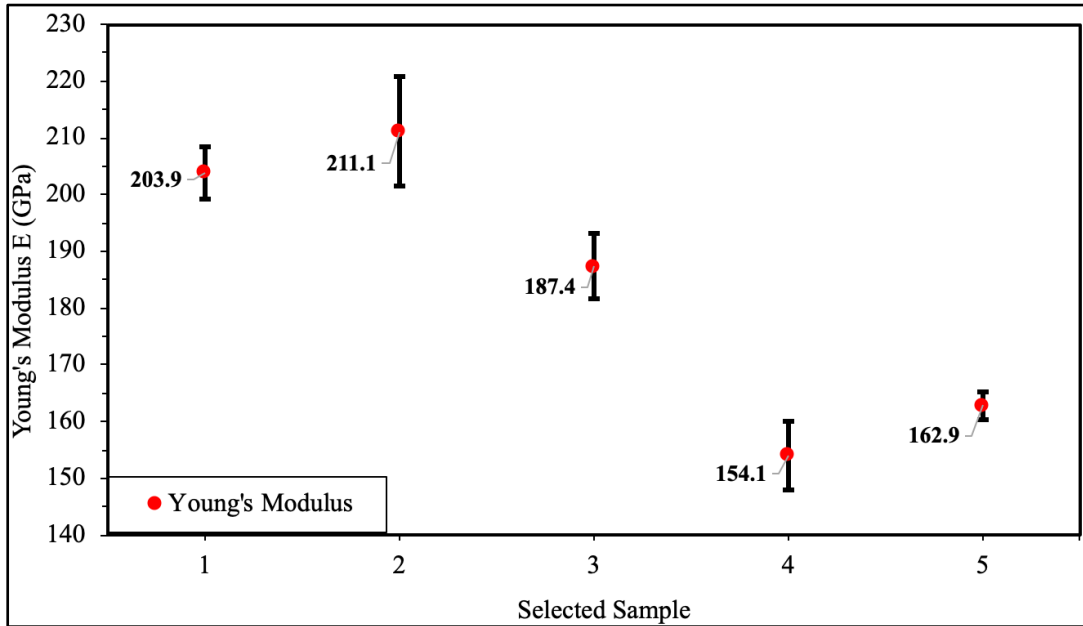
**Figure 78. Light optical images of five-selected samples which will be used for fabricating graded bulk structures.**

Density comparisons were made for the selected five samples using the Archimedes method (bulk sample) as well as with the Image J (2D plane), as seen in Figure 79.



**Figure 79. Comparison of densities: the red square markers are data points from the Archimedes method, whereas the black circle markers represent data points of the optical method (Image J).**

The density values based on the optical images seems to be in-line with the Archimedes method for sample #1 and #4. On the other hand, for higher density samples the images at the given magnification did not exhibit defects. It is important to note that this difference is largely due to the relatively smaller area of measurement in case of Image J when compared to the bulk volume in case of the Archimedes method.



**Figure 80. Nanoindentation measurements of Modulus of Elasticity (GPa) for selected five SLM-built SS316L samples.**

Figure 80 summarized the results of the nanoindentation tests, Young's modulus. Like density and hardness, a similar trend of variations can be seen across selected five samples in the modulus of elasticity. A total of eight (4 x 2) indents performed on the five selected samples at a span of 20  $\mu\text{m}$  (over 10 times the depth of penetration) with a loading/unloading rates of 0.05 mm/s and dwell time of 12 s. The maximum depth of penetration was approximately 1.5  $\mu\text{m}$ , and the applied load was around 250 mN.

Specifically, the modulus values for sample 1, and sample 2 were  $203.9 \pm 4.66$  GPa and  $211.1 \pm 9.62$  GPa, respectively. Simultaneously, the lowest and the highest hardness values were found to be  $3.83 \pm 0.17$  GPa and  $4.81 \pm 0.52$  GPa for sample 1 and sample 2, respectively. According to Hitzler et al. [258], the mismatch between the modulus and the hardness results could be due to individual grain having different

crystallographic orientations. Moreover, the location-dependent anisotropy, inhomogeneous melting of powder particles, and indentation near defects such as lack-of-fusion defects or voids might have caused variations in the obtained results. In the present study, samples 1 and 2 were processed with the VED of  $39.77 \text{ J/mm}^3$  and  $63.02 \text{ J/mm}^3$ , respectively. Additionally, these variations in the VED could have likely caused the accumulation of higher residual stresses in sample 2, also exhibiting the highest average modulus of elasticity across all the samples. Typically for SLM processing, it was recommended to keep low power and increased exposure levels to better nanoindentation response [259].

Table 8 gives an overview of the physical and mechanical properties observed across five selected samples. The observed difference between the Vickers and nano hardness results could be due to possibilities in the latter case of indenting over one grain, grain boundary, or intersection of two grains since the material is polycrystalline.

**Table 8. Summary of physical and mechanical properties of selected five samples.**

#	<i>P</i> [W]	<i>V</i> [mm/s]	<i>E<sub>v</sub></i> [J/mm <sup>3</sup> ]	<i>ρ</i> [%]	HV <sub>0.5</sub> (Std. Dev.)	Nano Hardness [GPa] (Std. Dev.)	<i>E</i> [GPa] (Std. Dev.)
1	175	800	39.77	96.35	209 (28.5)	3.83 (0.17)	203.9 (4.66)
2	200	577	63.02	97.23	256 (1.5)	4.81 (0.52)	211.1 (9.62)
3	200	750	48.48	98.21	271 (6.2)	4.01 (0.11)	187.4 (5.79)
4	150	800	34.09	90.78	294 (12.1)	3.98 (0.30)	154.1 (6.1)
5	200	698	52.10	97.5	318 (13.9)	4.62 (0.23)	162.9 (2.43)



## 5.4 Observations and Deductions

In this part of the study, several SS 316L samples were additively fabricated using the Renishaw AM400, a pulsed selective laser melting (SLM) system, to systematically investigate the range of mechanical properties (such as hardness, density, Modulus, and stress-strain behavior) achievable for selected alloy system. The design of experiments (DOE) revolved around varying volumetric energy density (VED)-related process parameters such as laser power and scanning speed, which in combination signifies the amount of energy imparted into the melt pool.

Moreover, VED-based factors that may affect the correlations between different samples due to their processing bounds. Processing within these bounds provides useful information about the types of processing defects the sample would exhibit, as illustrated in Figure 81.

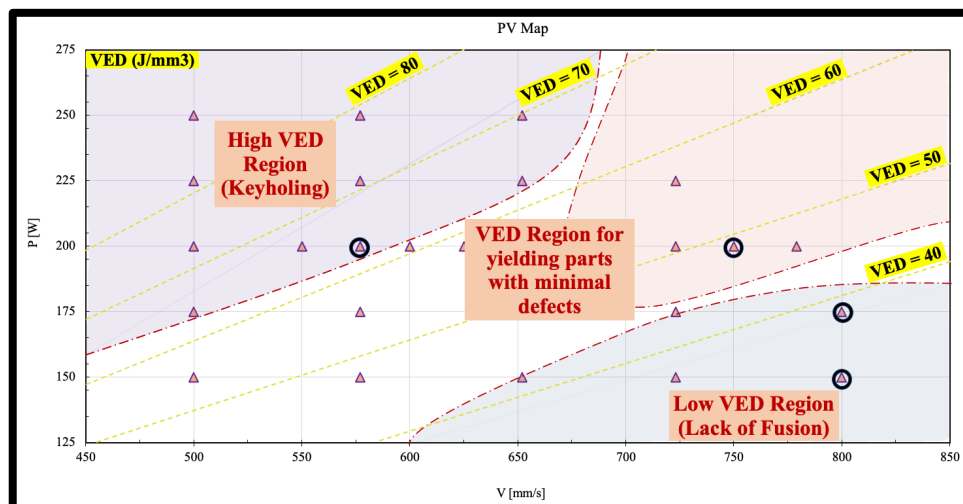


Figure 81. VED-based bounds indicating different regions of defects.

Throughout the experiments, the samples' macro- and microstructural investigations as well as physical (hardness, moduli, etc.) and mechanical properties (Vickers microhardness, nanoindentation hardness, and modulus) were measured. Several significant variations across the hardness (209-318 HV<sub>0.5</sub>), Archimedes density (90-99%), nano hardness (3.83-4.81 GPa), and modulus of elasticity (154.1-211.1 GPa) were measured and recorded.

Archimedes density measurements of all 28 samples on a PV map is shown in Figure 82. As noticed, at a very high scan speed, samples seemed to exhibit low densities (high porosities), indicating the presence of lack-of-fusion (LOF) type defects due to insufficient VED due to low laser power and high scan speed values. Figure 83 highlights trends observed for the Archimedes densities across all 28 samples.

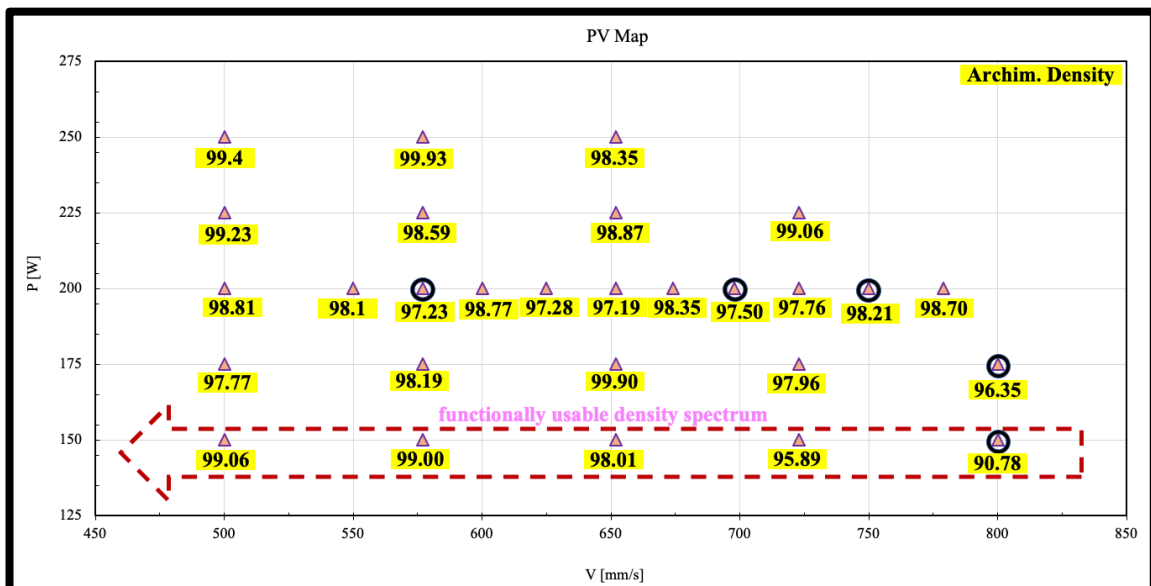
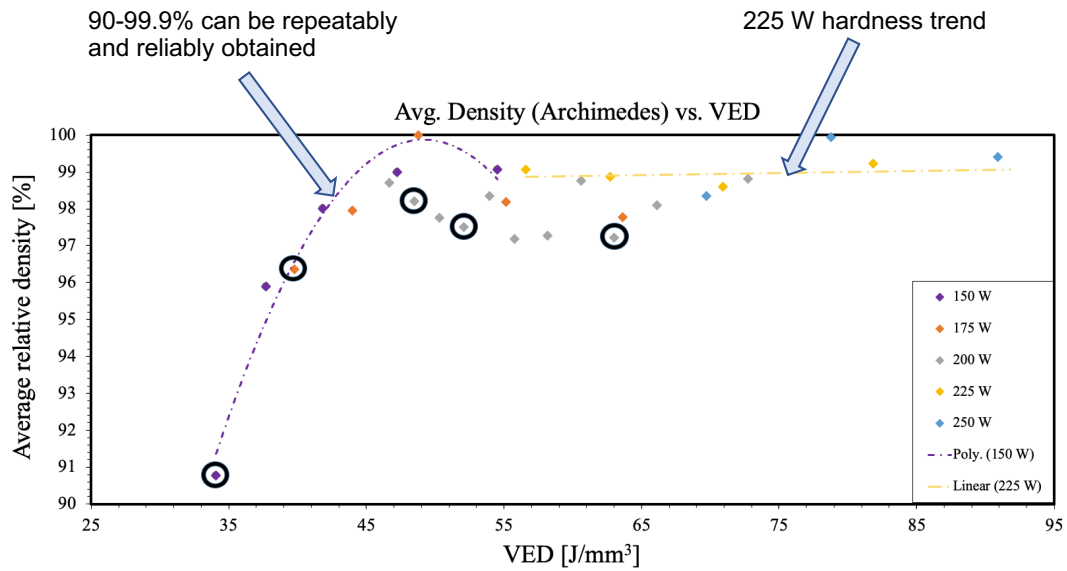
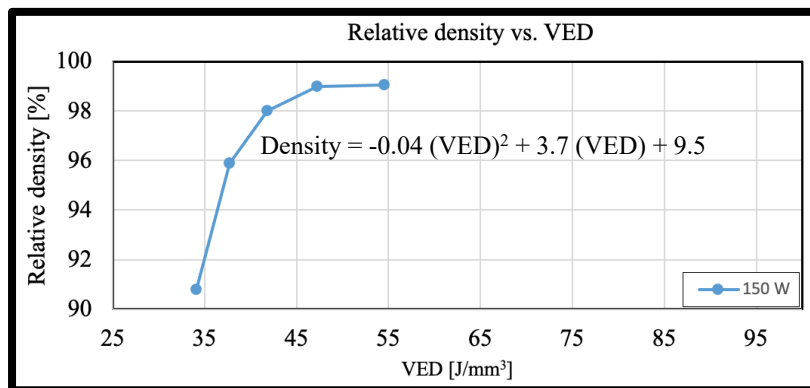


Figure 82. Archimedes density for all 28 samples. Highlighted is monotonic change in density with a single power.



**Figure 83. Archimedes density for all 28 samples. Highlighted in black circles are the five selected samples for graded bulk structure fabrication.**

For example, at a constant power of 150 W, a monotonic decrease in density (99.9 to 90%) was achievable, whereas, at a higher power of 225 W, density ranges were mostly 99%+.

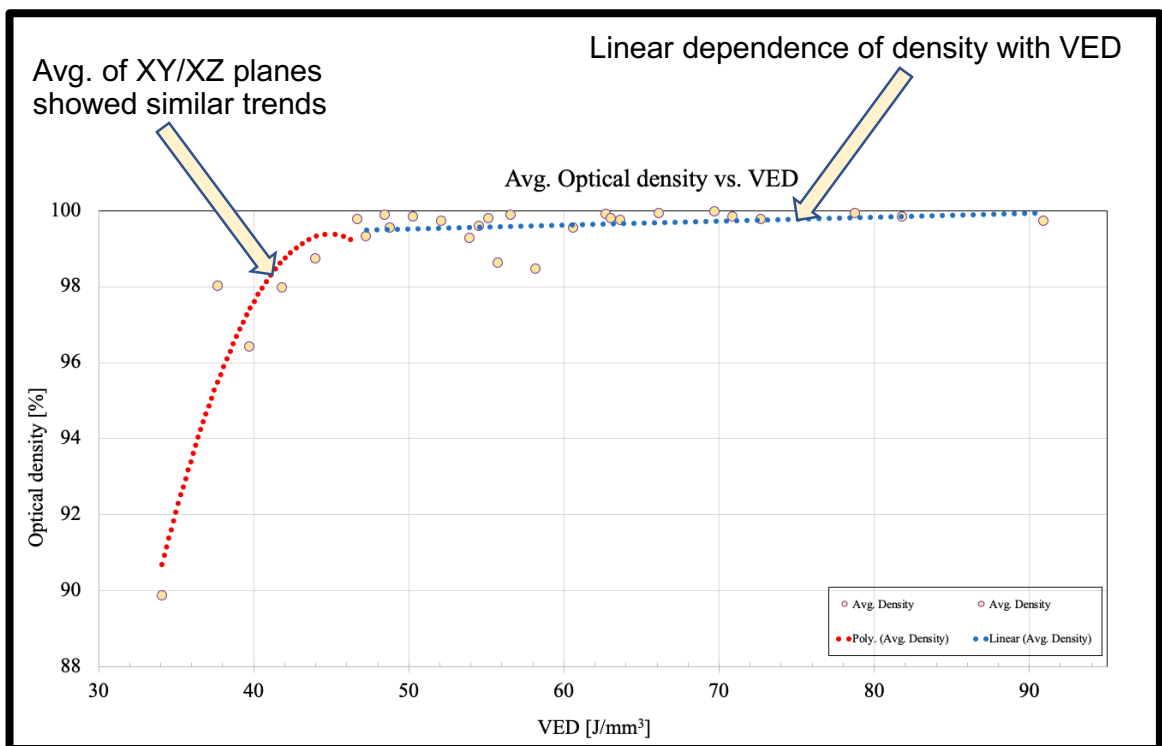


**Figure 84. Single parameter control of relative density is achievable at constant laser power of 150 W.**

Figure 84 highlights a second order equation for lower densities (~90-99 %) by single parameter control, which in this case, is keeping the laser power constant at 150 W and varying V from 500-800 mm/s. Density can be expressed within the selected processing bounds with the equation,

$$Density = -0.04 (VED)^2 + 3.7 (VED) + 9.5 \quad (3)$$

Similar trends have been observed for the optical density measured across both XY/XZ planes for all 28 samples as highlighted in Figure 85.



**Figure 85. Optical density for all 28 samples across both XY/XZ planes. A second order equation for lower densities (~90-99%) and a linear fit for higher densities (~99%+).**

Overall, decreasing the laser exposure time, thereby increasing VED, leads to better melting of powder particles and thereby obtaining near full density samples. Saturation point for VED was found to be 44 J/mm<sup>3</sup>, below which there was significant drop in density, below ~97%.

In case of average microhardness, similar to density, a PV map was constructed with measurements done across all 28 samples, as illustrated in Figure 86. As highlighted, hardness could be monotonically controlled from 302-209 HV<sub>0.5</sub> by increasing the scan speed at a constant laser power of 175 W.

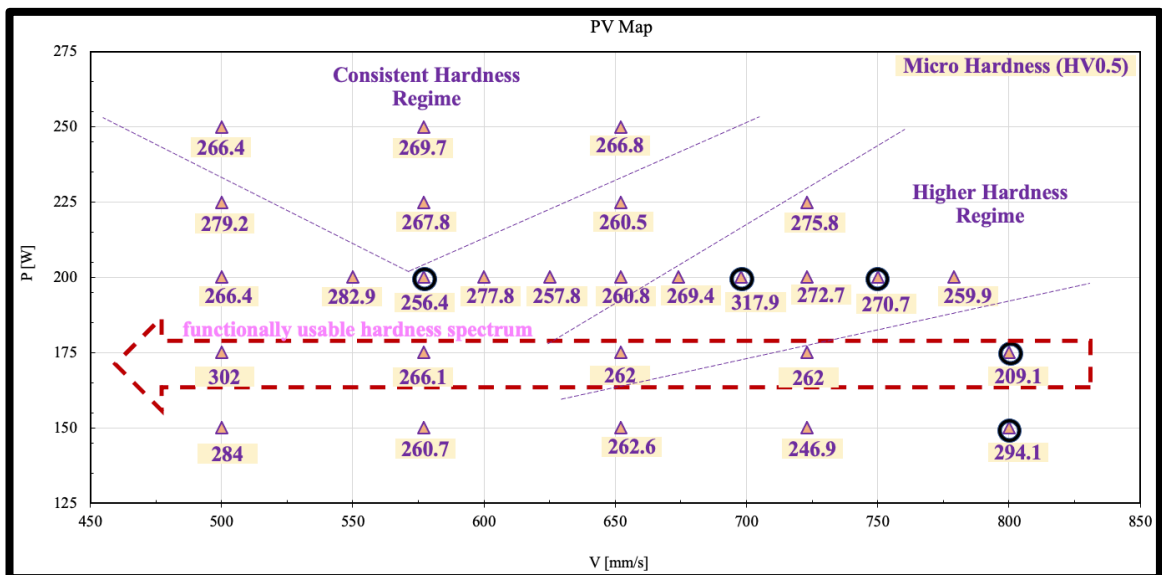
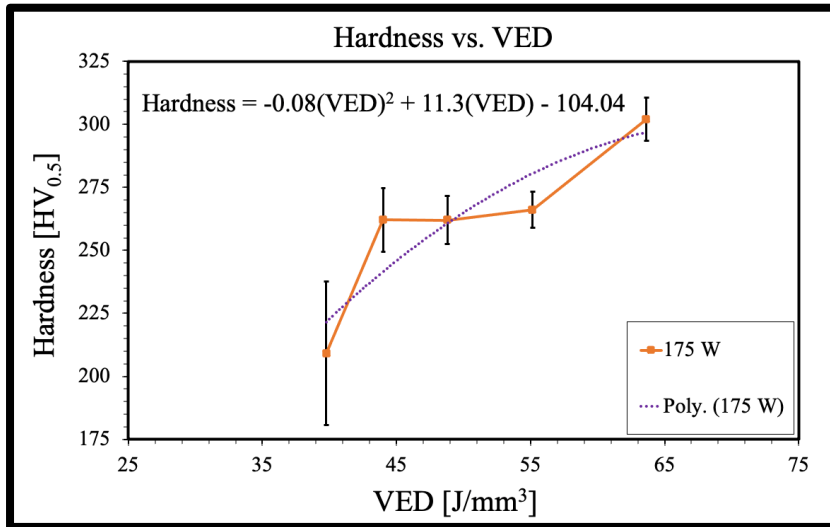


Figure 86. Hardness for all 28 samples. Highlighted is monotonic change in hardness with a single power.



**Figure 87. Monotonic change in hardness is achievable at constant laser power of 175 W.**

Figure 87 depicts a second order equation for hardness which can be expressed as,

$$\text{Hardness} = -0.08 (\text{VED})^2 + 11.3 (\text{VED}) - 104.04 \quad (4)$$

However, hardness it is important to note that hardness is dependent on a combination of factors such as pore fractions, phase fractions, grain sizes, etc. Within the processing bounds, these equations and findings will form a valuable catalogue of data for optimal selection of processing parameters to yield repeatable and reproducible SS 316L samples within a functionally-acceptable range.

In summary, this part of the experiments yielded a catalogue of process parameters that can yield repeatable and reproducible SS 316L samples. This could also enable one to select a process parameter combination that intentionally yields a different (but repeatable) property value within a functionally acceptable range.

## 6. INFLUENCE OF PROCESSING AND MICROSTRUCTURE ON PROPERTIES

### (RQ-2)

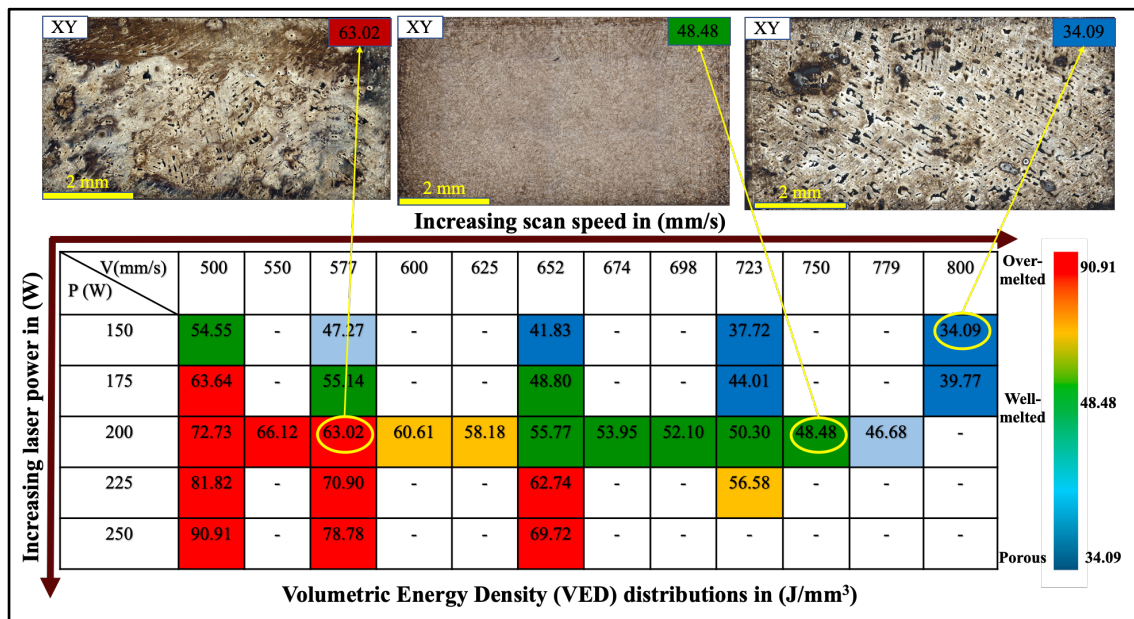
In this chapter, set of studies were carried out to investigate the causes of mechanical property variations. In order to achieve the objectives, firstly, the in-depth microscopy and spectroscopy were performed to study the variations in macro- and microstructures with reference to VED-related process parameters of all 28 samples. Next, phase identifications were carried out to better understand how different physicochemical traits affect the resulting property distributions across both longitudinal and transverse planes for all 28 samples. Furthermore, five samples were down-selected with a view to create FGAM bulk structures and were further analyzed. In depth, defect characterizations were carried out which shows defect population varying within the selected processing window. This investigation helped in linking of the processing-based root causes with resulting property variations and showed that how property variations resulted from combinations of porosity types/amounts, martensitic phase fractions, and grain sizes.

Overall, this part of the study aims to answer research question 2 (RQ-2), *i.e.*, “What are the underlying causes of mechanical property variations?” The outcome of this chapter will provide catalogue of process parameters to yield repeatable and reproducible SS 316L samples. Moreover, it provided mapping of the subset design space detailing property trends, defects, etc. in relation to process conditions.

## 6.1 Macro-scale Observations

Microstructure investigation not only helps study the melting process but also the defects formation in relation to process parameters. To reveal microstructure on a small scale, representative images of the transverse (XY) and longitudinal (XZ) sectioned polished surfaces of as printed SS 316L are obtained.

Figure 88 shows low-magnification optical images of polished surfaces of select samples in the transverse (XY) plane.



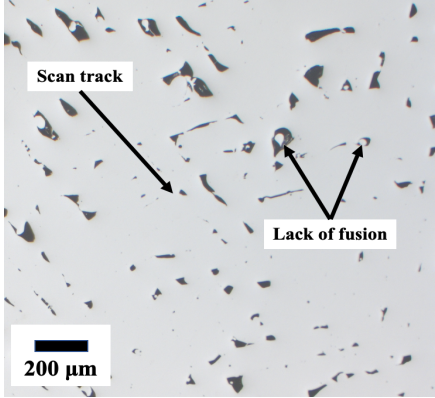
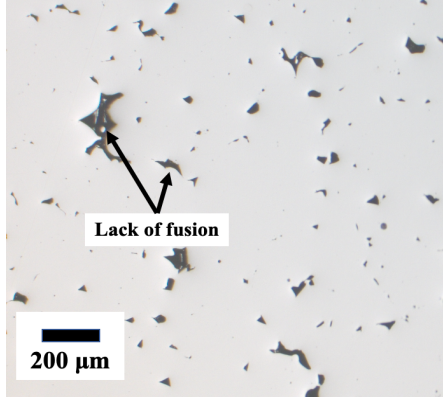
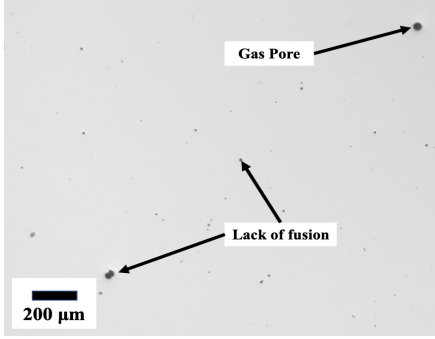
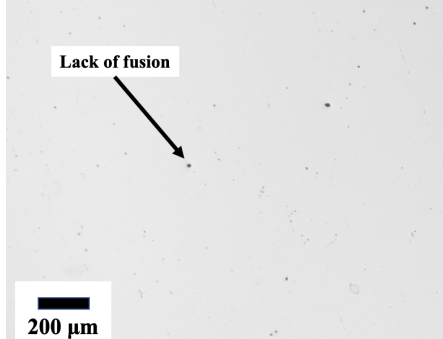
**Figure 88. DoE of the process parameters design space for SLM of SS 316L samples. Representative optical micrographs of the etched top build surfaces show over-melted, well-melted, and porous regions highlighted with different colors as per the color bar on the right.**



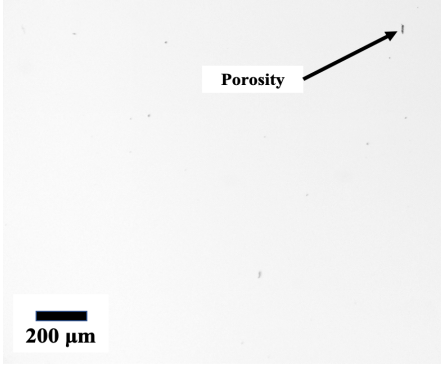
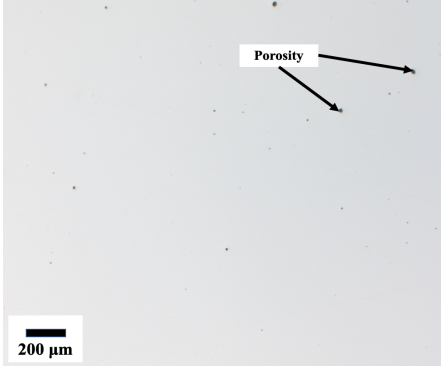
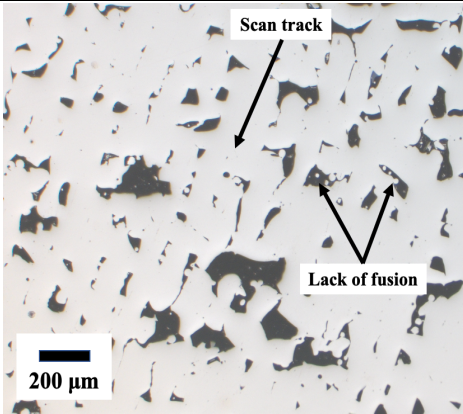
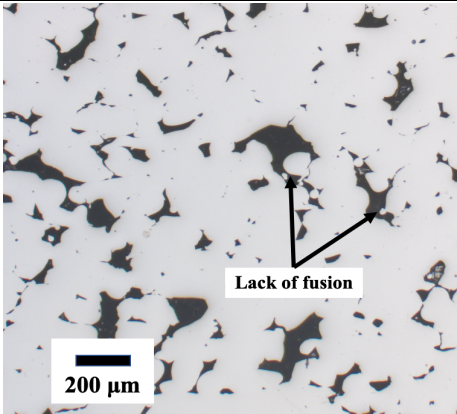
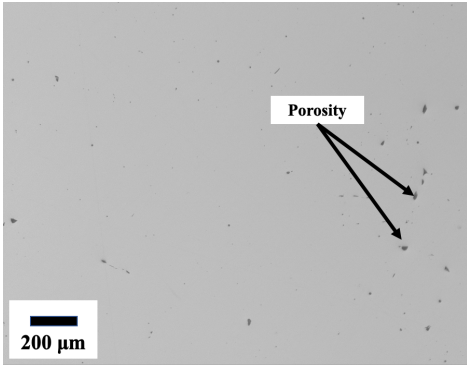
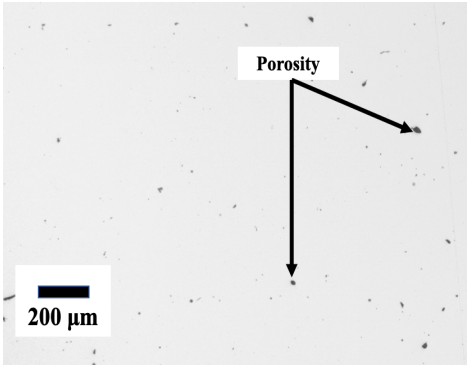
Highlighted VEDs were calculated from equation (1) and depicted by a color-coded scale bar. The experimental design centered on the recommendations from OEM supplier (Renishaw, Gloucestershire, England) which suggested  $Ev = 48.48 \text{ J/mm}^3$  ( $P = 200 \text{ W}$ ,  $V = 750 \text{ mm/s}$ ) for near-full density parts. At a lower  $Ev = 34.09 \text{ J/mm}^3$  ( $P = 150 \text{ W}$ ,  $V = 800 \text{ mm/s}$ ) for instance, there was insufficient melting of powder particles as well as inadequate melt pool overlaps, leading to significant lack-of-fusion (LOF) defects. In contrast, at higher  $Ev = 63.02 \text{ J/mm}^3$  ( $P = 200 \text{ W}$ ,  $V = 577 \text{ mm/s}$ ) for instance, porosities decreased due to adequate melting and fusion, as corroborated by the work of Choo et al. [198] and others [145, 165, 171].

Light optical images of mirror-polished surfaces of select five samples were obtained in both XY-plane (transverse) and XZ-plane (longitudinal) directions. Each captured at equal magnification has the same size to reveal microstructure on a small scale. Representative optical micrographs of the transverse (XY) and longitudinal (XZ) sectioned polished surfaces of as printed SS 316L are highlighted in Table 9.

**Table 9. Summary of optical micrographs in both XY and XZ plane of five samples.**

Details	XY-Plane	XZ-Plane
<p>Sample -1                      P=175W,                      E=39.77                      J/mm<sup>3</sup>,                      ρ= 96.35%</p>		
<p>Sample -2                      P=200W,                      E=63.02                      J/mm<sup>3</sup>,                      ρ= 97.23%</p>		

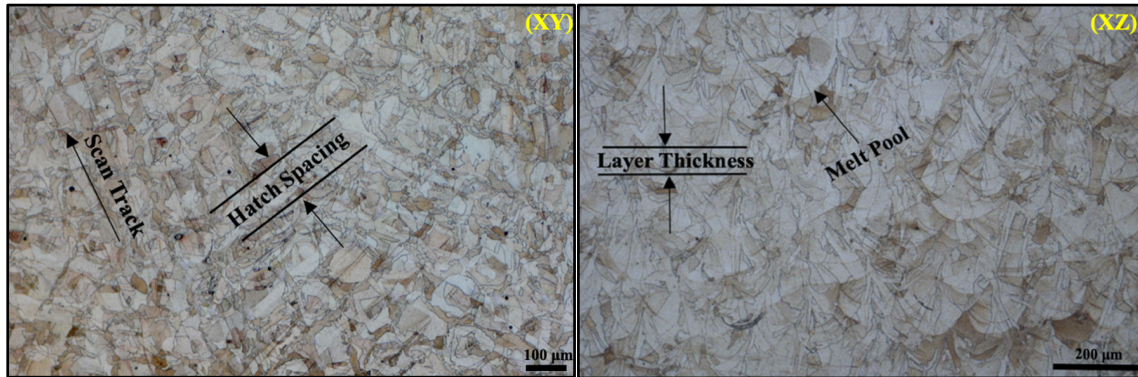
**Table 9. Continued.**

Details	XY-Plane	XZ-Plane
<p>Sample -3  P=200W,  E=48.48  J/mm<sup>3</sup>,  <math>\rho</math>= 98.21%</p>		
<p>Sample -4  P=150W,  E=34.09  J/mm<sup>3</sup>,  <math>\rho</math>= 90.78%</p>		
<p>Sample -5  P=200W,  E=52.10  J/mm<sup>3</sup>,  <math>\rho</math>= 97.50%</p>		

The comparisons were carried out for investigating the optical porosities and correlating it to the observed property changes. Some of the pores and lack of fusion

defects were seen on the sample surfaces, even with naked eyes. Amongst the selected five processing parameter combinations, there were two processing windows in particular, for sample 4 and sample 2, which had the lowest and the highest energy densities, respectively. At a lower energy input sample 4 ( $E_v = 34.09 \text{ J/mm}^3$ ,  $P = 150 \text{ W}$ ,  $V = 800 \text{ mm/s}$ ), for instance, there was insufficient melting of powder particles as well as inadequate melt pool overlaps, leading to significant visible holes, voids, and lack-of-fusion (LOF) defects. This sample showed the highest porosity of 9.22% amongst the five samples. This was most likely due to a low power value and high scan speed that may have produce discontinuities in the melt pool tracks and hence generated poor weldability, resulting in low density and high porosity. In contrast, at higher energy input processed sample 2 ( $E_v = 63.02 \text{ J/mm}^3$ ,  $P = 200 \text{ W}$ ,  $V = 577 \text{ mm/s}$ ) for instance, porosities decreased to 2.77 %. It could be due to sufficient melting and fusion, leading to also change in melt pool shape, grain size/texture, and residual thermal stresses, as corroborated by the work of Choo et al. [198] and others [145, 165, 171]. However, the lowest porosity was about 1.79% for Sample 3, which also had the optimum energy density input.

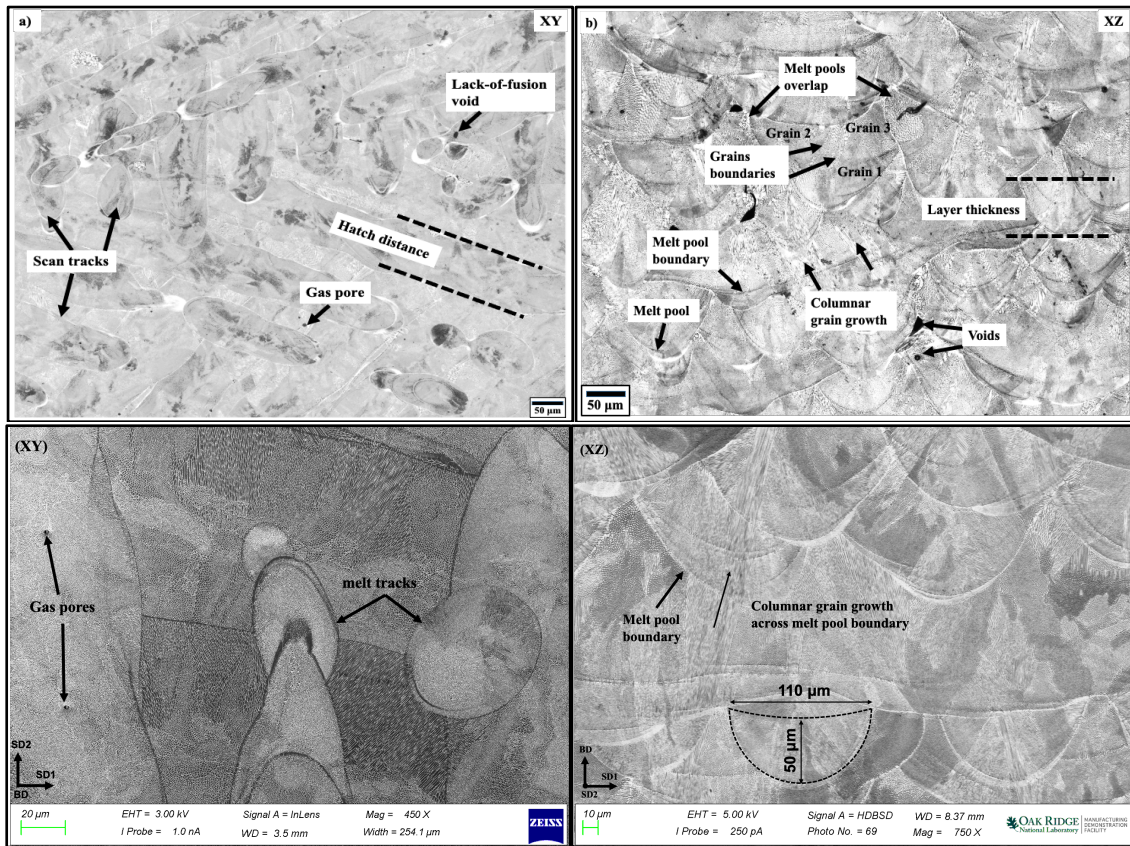
Figure 89 shows the light optical micrographs of sample 3 ( $E_v = 48.48 \text{ J/mm}^3$ ,  $\rho = 98.21\%$ ) in both transverse and longitudinal planes to represent SLM processing characteristics. Notice the hatch lines/distance in relation to the scan direction, well overlapped melt pools, layer thickness, and strong bonding across the layers, all indicating a successful and complete fusion of powder particles.



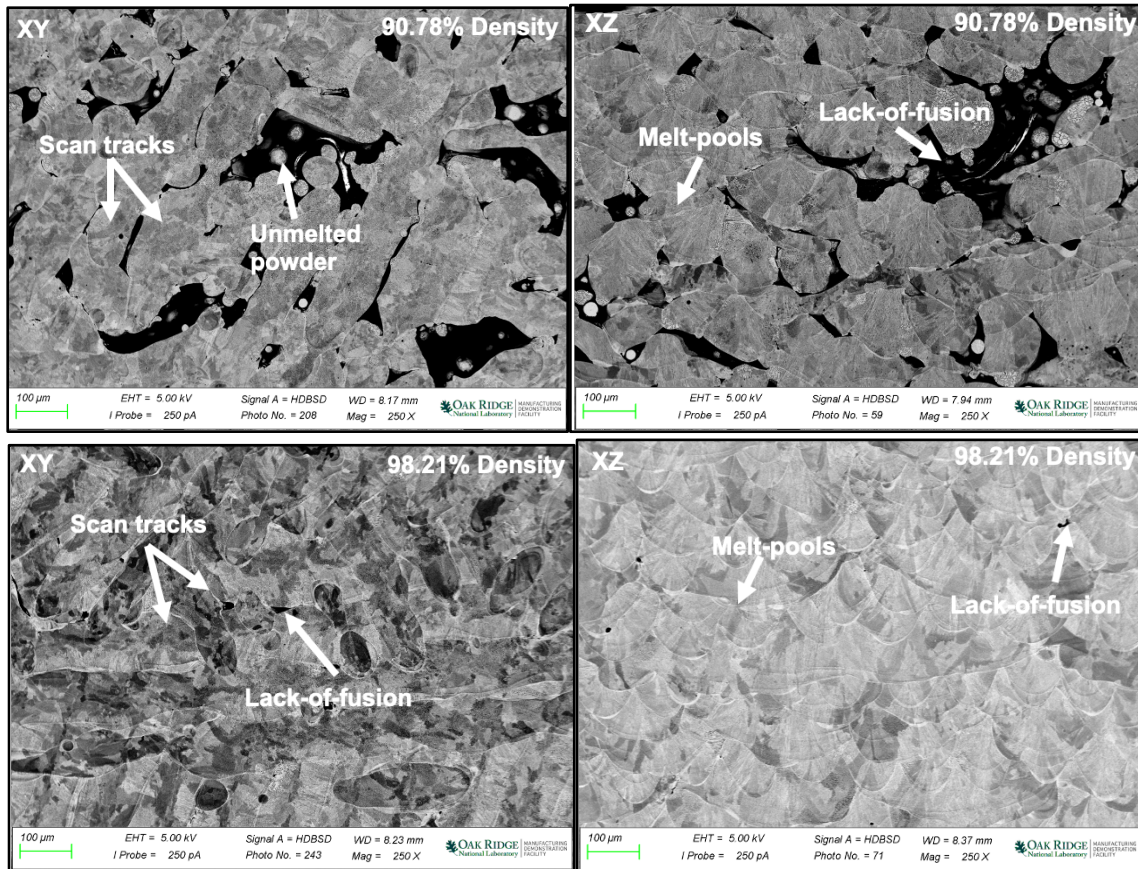
**Figure 89. Optical images showing hatch overlapped regions and laser scan tracks and half-cylindrical contours of melting pools and layer thickness in transverse (XY) and longitudinal (XZ) sections, respectively.**

Figure 90 illustrates the scanning electron microscopy (SEM) images with more detailed microstructural characteristics. Notice SLM process specific features visible at higher magnifications, including size and shape of melt pools. These images reveal how the grain morphologies and orientations along with distributions would look like along different planes. For clarity, the following direction nomenclatures were used: building direction (BD) along Z-axis, scanning direction 1 (SD1) along X-axis, and scanning direction 2 (SD2) along Y-axis of build chamber.





**Figure 90. SEM images of SLM processed SS 316L sample 2 in (a) XY plane showing the laser scan tracks and hatch overlapped regions, and (b) XZ plane showing the half-cylindrical melt pools and layer thickness.**



**Figure 91. SEM images showing the laser scan tracks, melting pools morphology, and defects (for instance, un-melted powder particles, voids, Lack-of-fusion voids) in transverse (XY) and longitudinal (XZ) sections for sample 4 ( $\rho = 90.78\%$ ) and sample 3 ( $\rho = 98.21\%$ ).**

An interlayer adhesion or bonding becomes a critical factor in fabricating fully dense parts. If the energy density imparted would be insufficient to melt the powder particles and part of the underneath material, there will be a lack of adhesion between the layers and can induce lack-of-fusion (LOF) porosity in the final parts, as illustrated in Figure 91.

The defects size found to be between 30 μm to 1 mm. Also, small spherical gas pores (~10-20 μm in size) are noticeable. They formed due to entrapped gas pockets

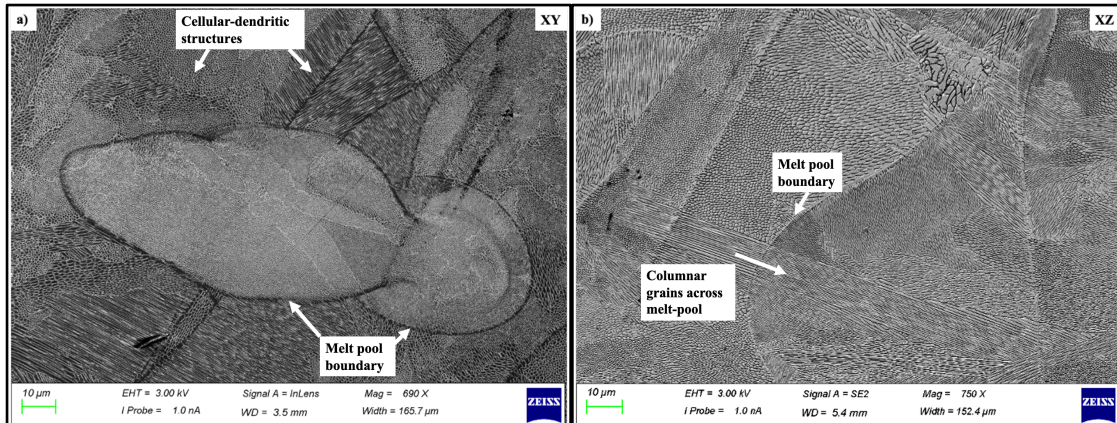
during the powder production process or between the powder particles that did not escape the melt pool before solidification. [198, 199, 260].

## **6.2 Micro-scale Observations**

To reveal microstructural characteristics on an even smaller scale, several high-magnification scanning electron microscopy (SEM) images of both transverse (XY) and longitudinal (XZ) sectioned etched surfaces of as printed SS 316L were studied as highlighted in Figure 92.

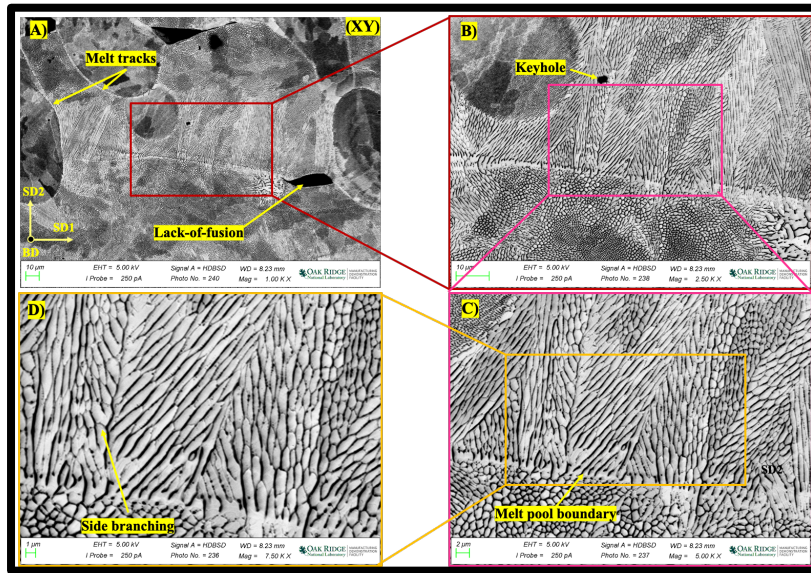
Microstructures exhibited long elongated grains parallel to BD and consistent with earlier studies on SLM fabrication of 316L [29, 161, 171, 173, 199]. It is interesting to note that more defects (pore-type) were observed for sample 1 and sample 4, processed with low energy inputs, including lack-of-fusion (LOF) defects and keyhole porosity. The keyhole pores are relatively large and are predominantly observed in samples processed at higher energy inputs, such as sample 2 and sample 5 [122].



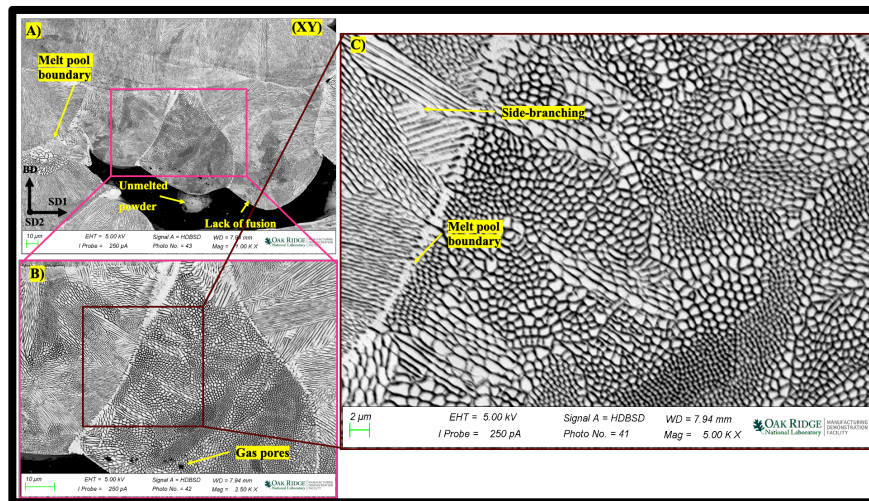


**Figure 92. SEM micrographs of sample 3; (a) the transverse (XY) plane illustrated with the white arrows, and (b) the longitudinal (XZ) plane fusion line between the two melt pools is seen with grain refinements of cell structure illustrated with the white arrows.**

A complex cell growth mechanism, known as side-branching, was seen inside the melting pool [197]. This phenomenon occurs especially at melting pool boundaries due to a change in local thermal gradient and is responsible for an alteration in the direction of growth for coarse elongated grains, which typically favors growing perpendicular to the half-cylindrical contours of the melt pool boundaries (fusion lines). Equiaxed grains are visible at the center of the melt pool and are believed to have been formed at the end of the solidification. Moreover, the epitaxial grain growth was also seen across the melt pool boundaries.



**Figure 93. SEM images showing the defects in XY plane of the sample. A) Melt tracks with lack-of-fusion defect, B) Solidification defect due to incomplete binding is visible, C) and D) Cellular cells inside a melt pool.**



**Figure 94. SEM micrographs showing the defects in (XZ plane of the sample. A) Lack-of-fusion pore and unmelted powder particle, B) Zoom-in region of fusion line between the two melt pools along with spherical gas pores, C) Higher magnification of fusion line region depicting side-branching of cell structure.**

Figure 93 and Figure 94 reveal how the grain morphologies and orientations, and distributions would seem to form along different planes to the build directions. Within the melt pool, cells initially grow in preferential directions parallel to the direction of local thermal gradients. Further, as they continue to grow, a changing thermal gradient affects the cell growth, promoting side-branching of cells. Such side instabilities promote dendritic growth from cellular and can cause significant detrimental effects on the overall mechanical properties of the sample. The presence of the side branching was visible on both the transverse/longitudinal planes.

Overall grain structures observed here have been equiaxed, columnar, and mixed. The average planar grain sizes (diameter) were measured following the intercept method per ASTM standards [261]. Typically, equiaxed grains have grain size (diameter) in the range of 2-10  $\mu\text{m}$ , whereas columnar grain size (diameter) can be greater than 10  $\mu\text{m}$  [262]. Moreover, we also noticed grains smaller than 1  $\mu\text{m}$  in size. In the case of grain shape and size measurements, in general, it is both ambiguous and challenging to come up with accurate measurements. The values of the grain size presented should be taken into account with caution.

### 6.3 Defects Characterizations

The solidification defects can be catastrophic to printed parts intended functionality and service life. Defects are the aspects that limits the SLM processed SS 316L structures for applications that calls for strict part quality. Therefore, it becomes vital to understand the evolution of porosity, voids, various other defects and their distinctive morphologies (shape, size, and orientation) [263]. It is widely reported that the process-induced pores and defects are primarily governed due to alteration in processing conditions. Figure 95 highlights the different defect regions found to be prevalent during SLM fabrication.

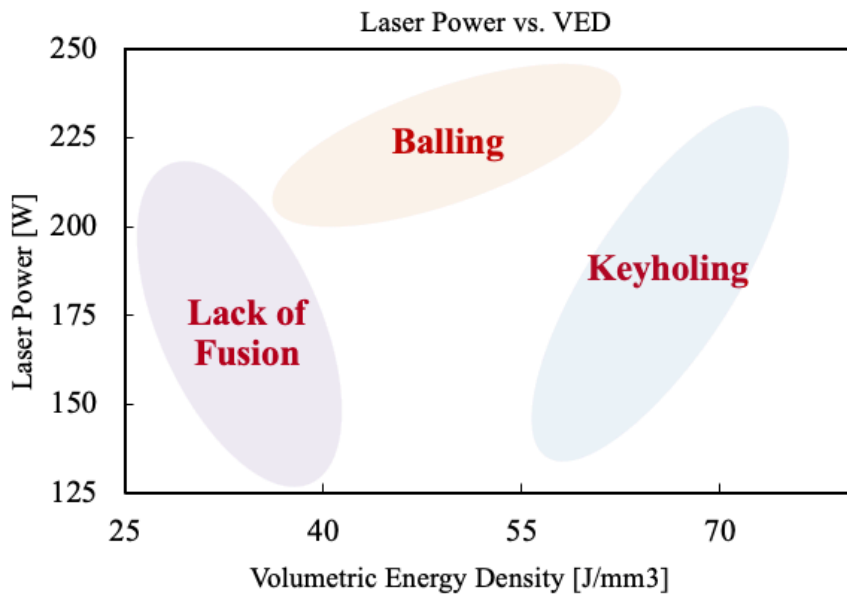


Figure 95. SLM processing regimes showing different defect regions.



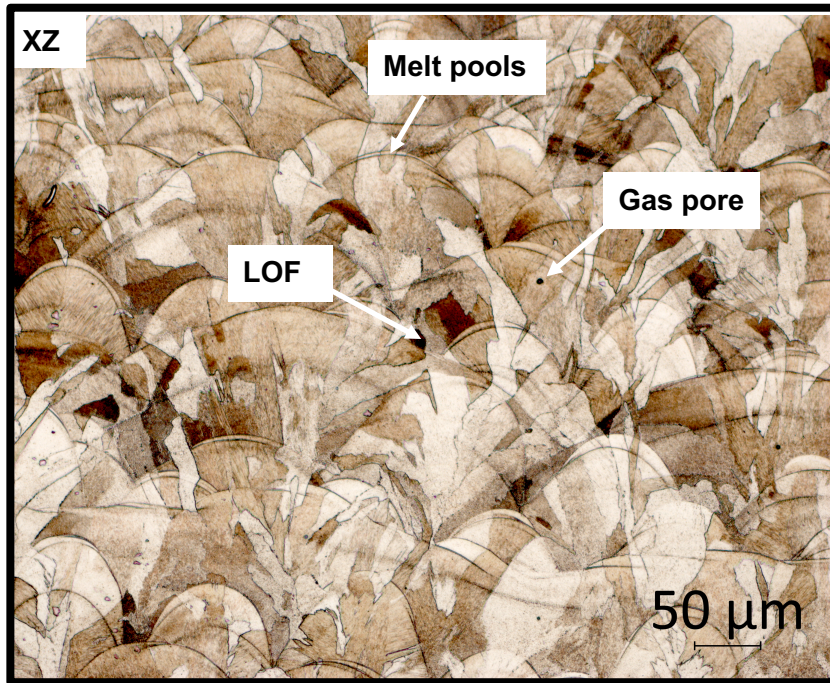


Figure 96. Optical image of etched surface showing the LOF and gas pore.

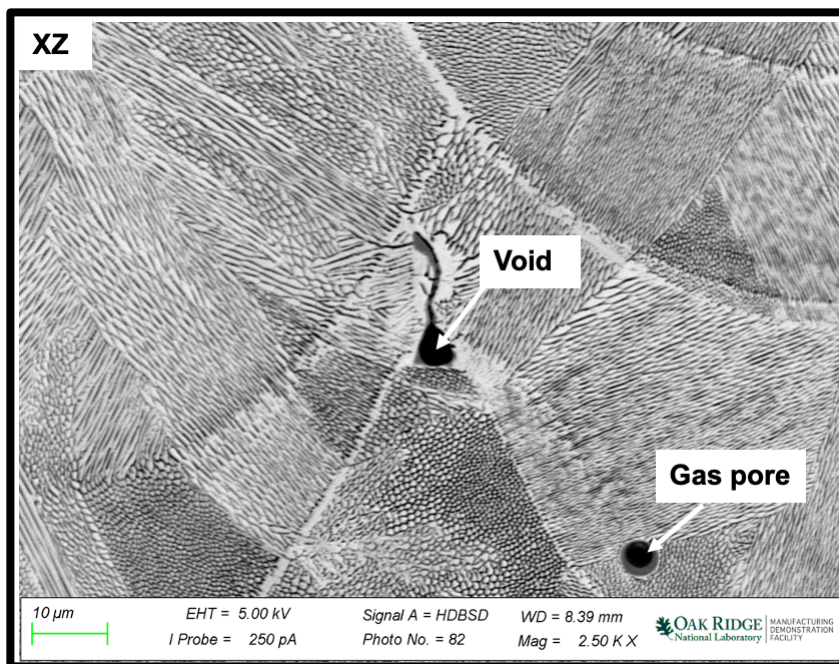
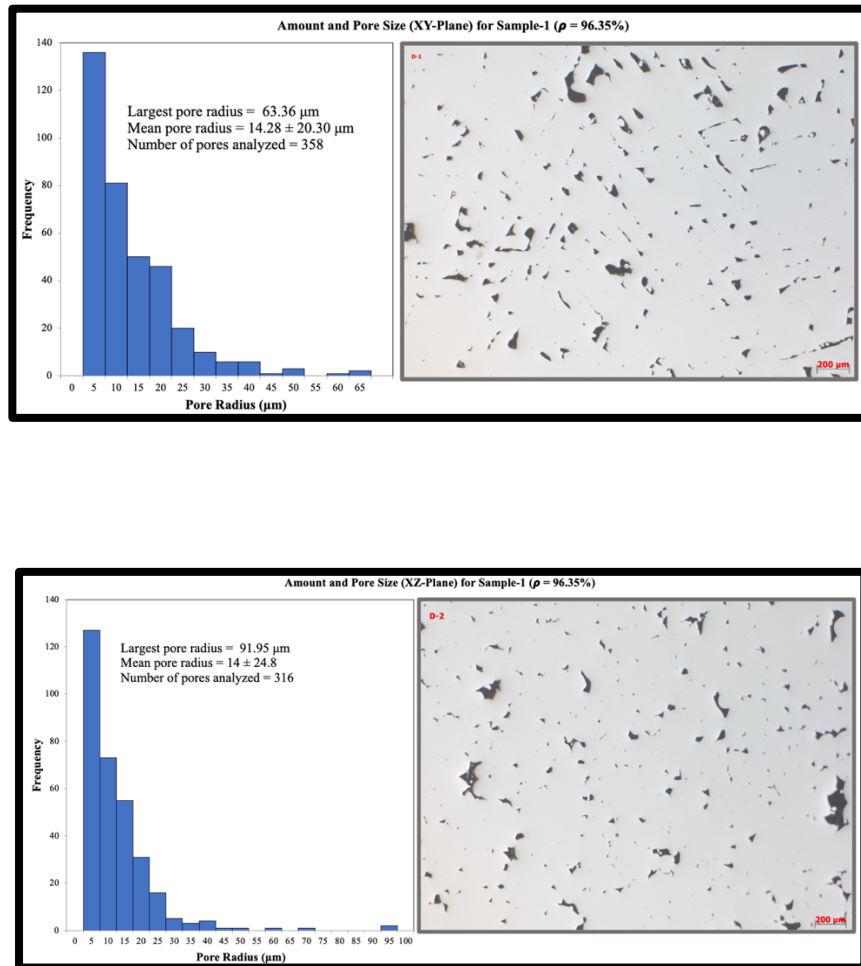


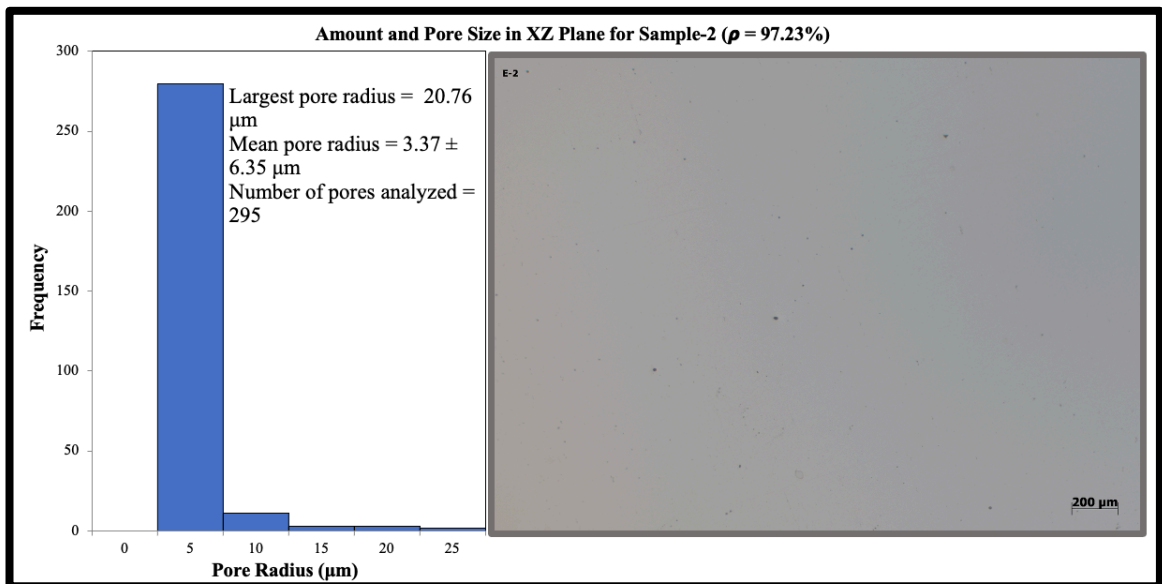
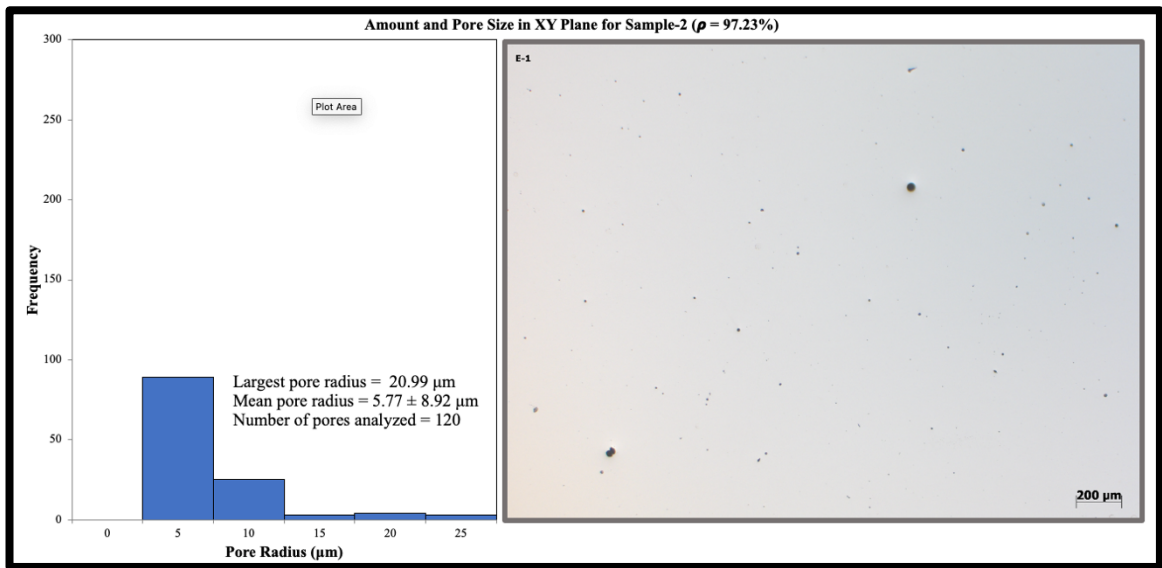
Figure 97. SEM image showing the void and spherical gas pore.

Figure 96 and Figure 97 shows OM and SEM micrographs of sample in XZ plane showing melt pools, LOF voids, pores, and spherical gas pore. To understand the defect morphologies (circularity, pore radius, aspect ratios), both XY and XZ planes for all 28 samples have been analyzed. Figure 98 represents the defect analysis of both planes for sample 1. Largest pore radius was 91.95  $\mu\text{m}$  for XZ plane whereas highest mean pore radius was  $14 \pm 24.8 \mu\text{m}$  and highest aspect ratio  $2.12 \pm 1.4 \mu\text{m}$ .

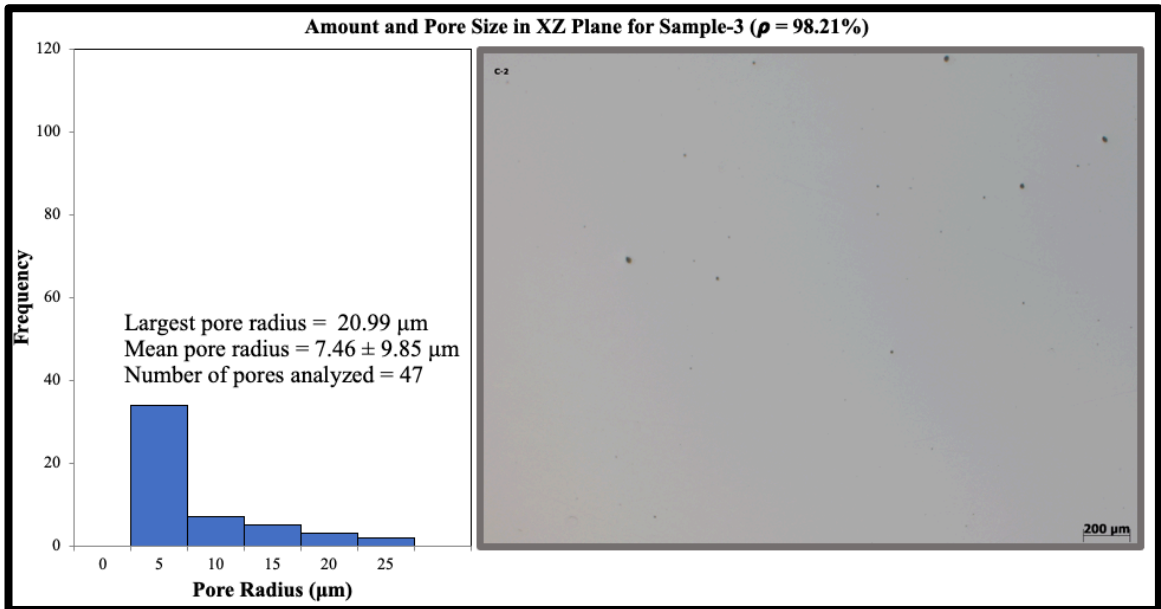
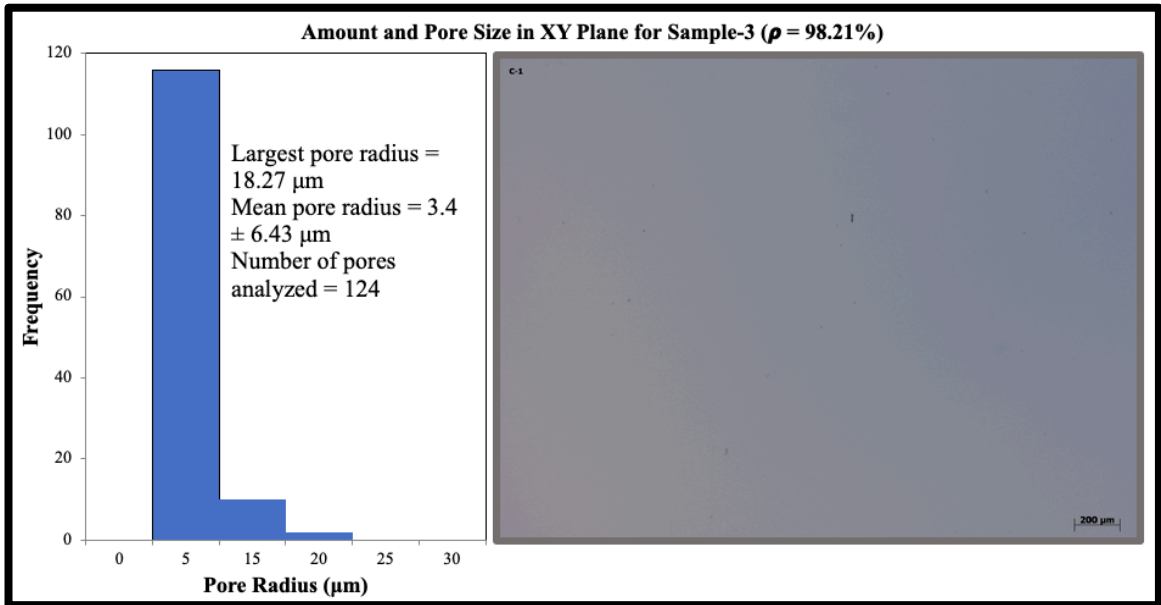


**Figure 98. Defect analysis of (Top) XY plane and (Bottom) XZ plane for sample 1.**

Similarly, Figure 99, Figure 100, Figure 101, and Figure 102 shows the defect analysis of both planes for sample 2, 3, 4, and 5, respectively.

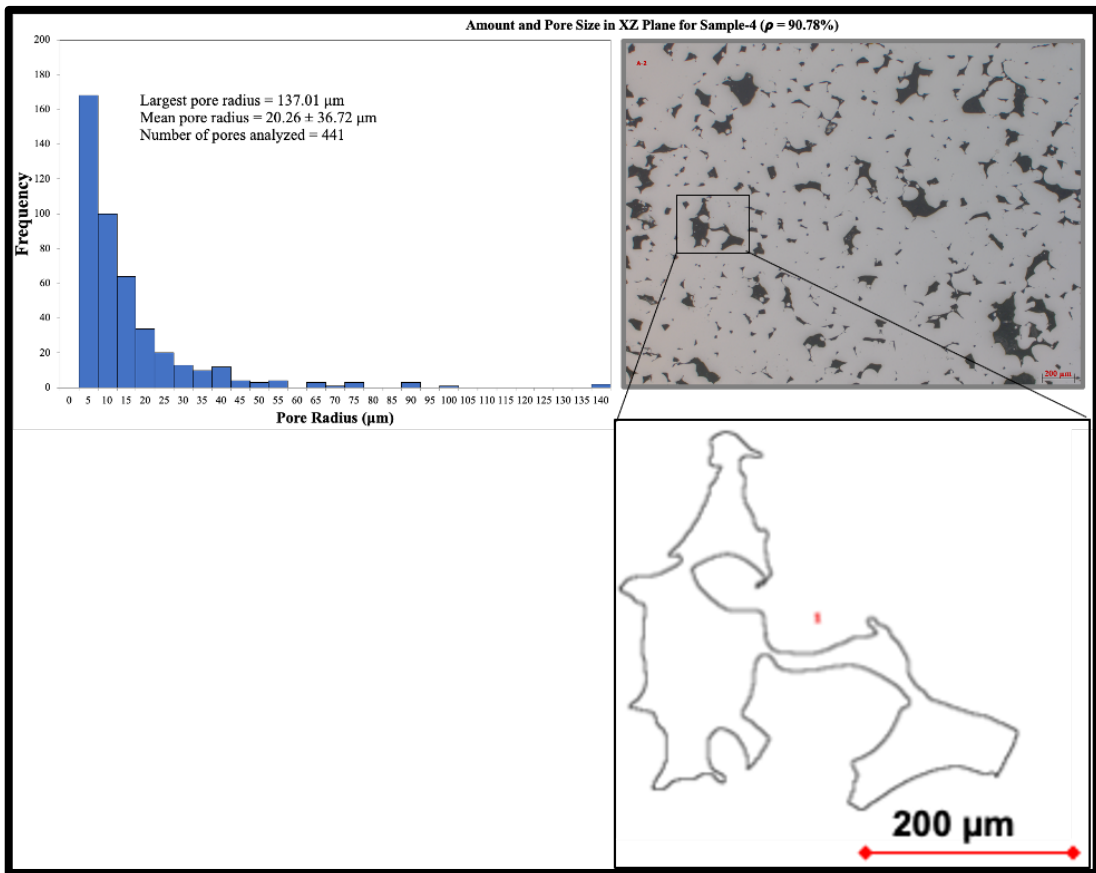
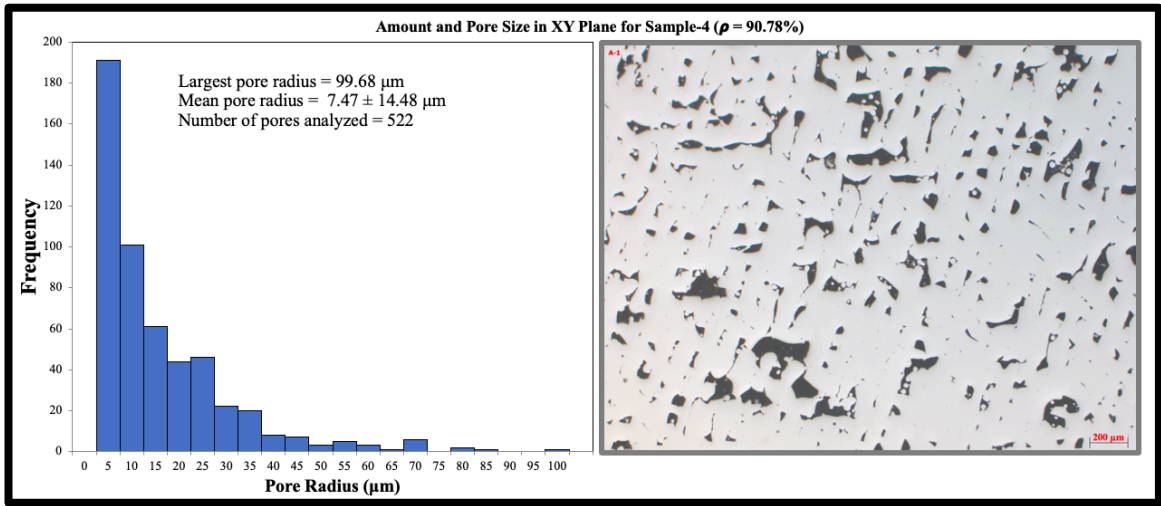


**Figure 99. Defect analysis of (Top) XY plane and (Bottom) XZ plane for sample 2.**

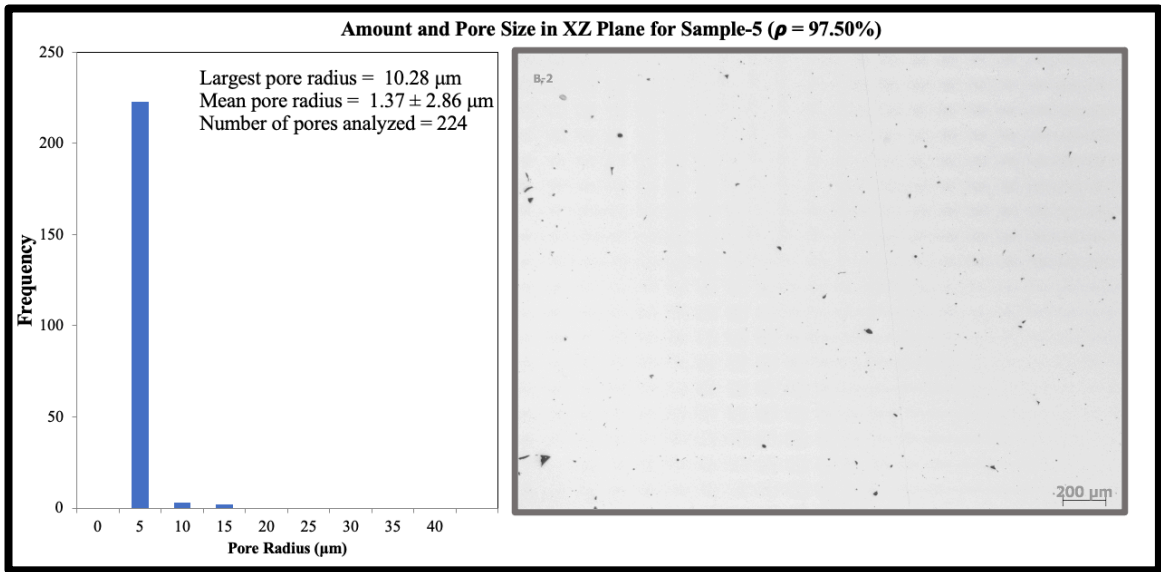
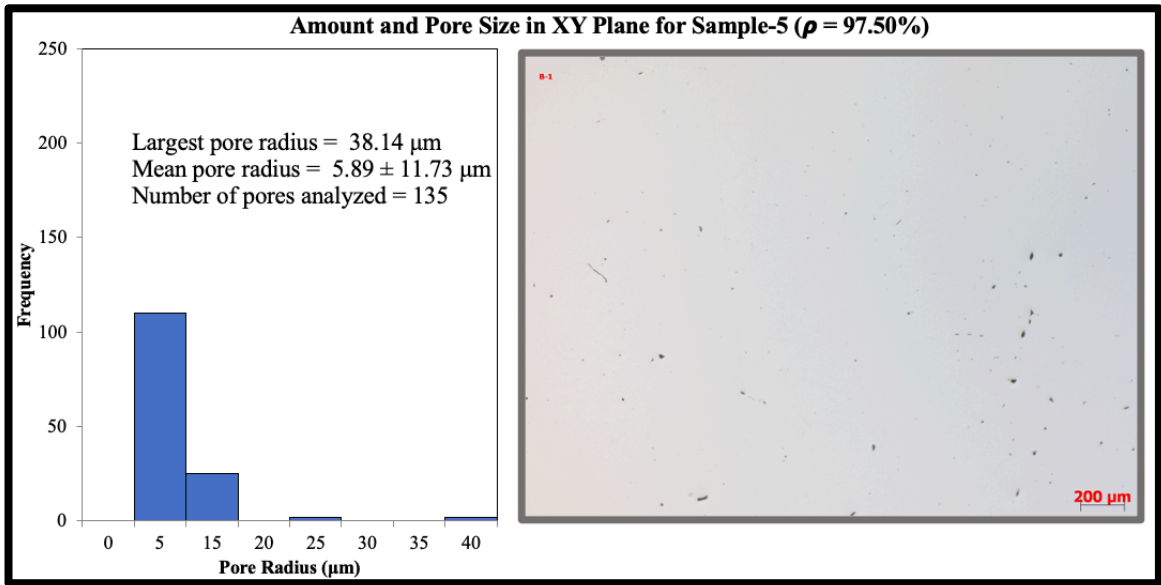


**Figure 100. Defect analysis of (Top) XY plane and (Bottom) XZ plane for sample 3.**





**Figure 101. Defect analysis of (Top) XY plane and (Bottom) XZ plane for sample 4.**

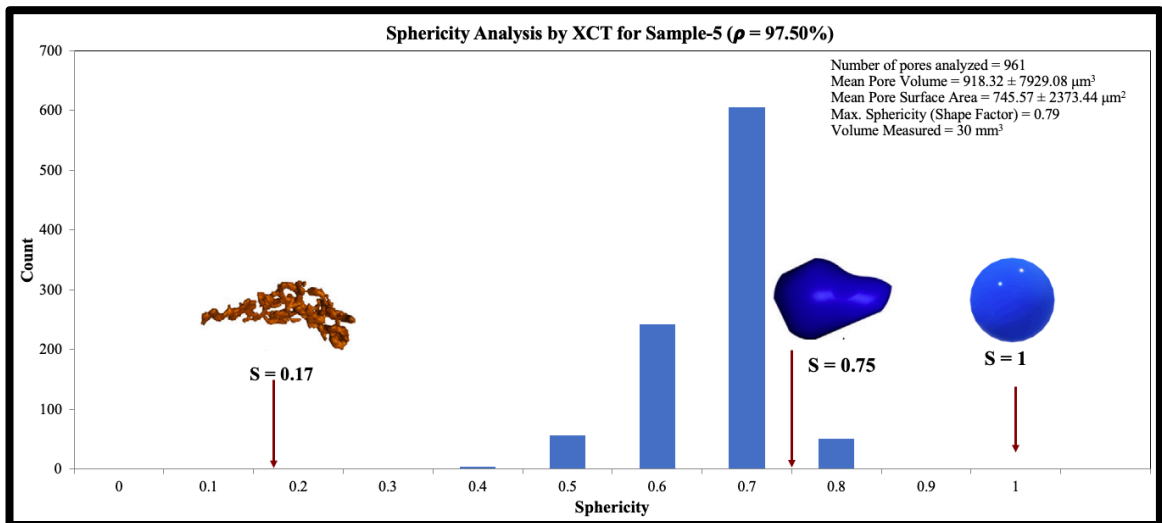


**Figure 102. Defect analysis of (Top) XY plane and (Bottom) XZ plane for sample 5.**

Furthermore, XCT analysis was conducted to study the sphericity for sample 5 as shown in Figure 103. Table 10 shows the system parameters used for capturing the images in both planes.

**Table 10. Summary of XCT parameters used in analysis of 3D defects for sample 5.**

Sample:	B1	B1	B2	B2
Scan Type:	Scout	Zoom	Scout	Zoom
Source Voltage (kV):	160	160	160	160
Source Power (W):	25	25	25	25
Source Current ( $\mu\text{A}$ ):	156	156	156	156
Exposure time (s):	0.7	12	0.8	12.5
Optical magnification:	0.4x	4x	0.4x	4x
Voxel size ( $\mu\text{m}$ ):	15.0444	2.0074	15.01	2.0295
Number of projections:	801	801	801	801
Frames per projection:	1	1	1	1
Detector binning:	2	2	2	2
Versa Filter:	HE6	HE6	HE6	HE6
Individual Scan Time: [HH:MM:SS]	0:51:06	4:49:43	0:53:54	4:37:55

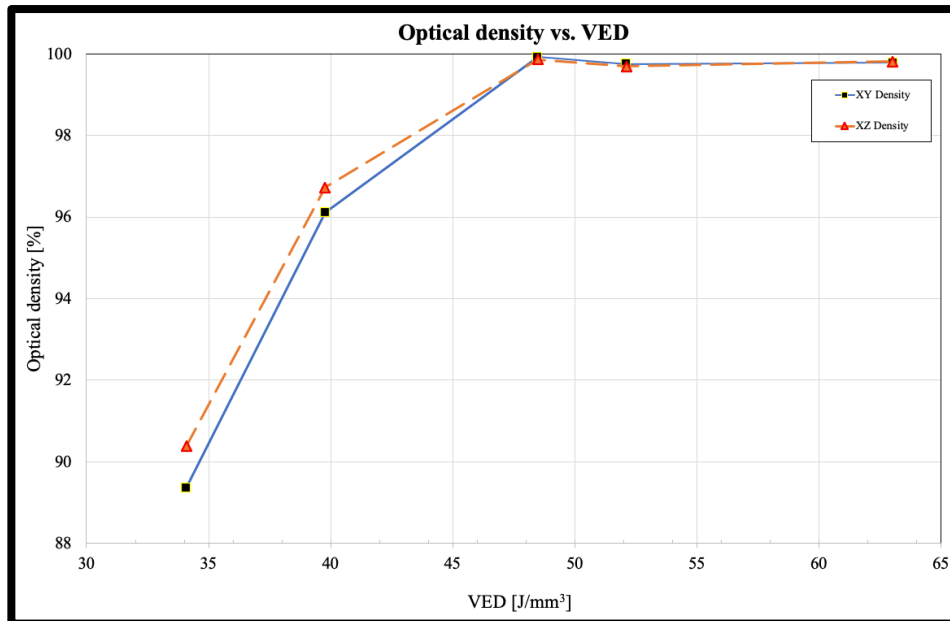


**Figure 103. Sphericity analysis by XCT for sample 5.**

**Table 11. Summary of defects in both XY and XZ plane of select five samples.**

Sample Details	1		2		3		4		5	
	XY	XZ	XY	XZ	XY	XZ	XY	XZ	XY	XZ
Density (Archimedes) (%)	96.35		97.23		98.21		90.78		97.5	
Density (Image J) (%)	96.12	96.73	99.78	99.81	99.92	99.86	89.35	90.38	99.75	99.69
Largest Pore Radius (µm)	63.36	91.95	20.99	20.76	18.27	20.99	99.68	137.01	38.14	10.28
Mean Pore Radius (µm)	14.28 ± 20.30	14 ± 24.8	5.77 ± 8.92	3.37 ± 6.35	3.4 ± 6.43	7.46 ± 9.85	7.47 ± 14.48	20.26 ± 36.72	5.89 ± 11.73	1.37 ± 2.86
Mean Circularity	0.58 ± 0.20	0.63 ± 0.18	0.89 ± 0.11	0.85 ± 0.14	0.48 ± 0.24	0.86 ± 0.17	0.52 ± 0.22	0.53 ± 0.22	0.77 ± 0.20	0.56 ± 0.19
Mean Aspect Ratio	2.12 ± 1.40	1.96 ± 0.95	1.26 ± 0.45	1.68 ± 0.67	1.76 ± 0.83	1.27 ± 0.48	2.21 ± 1.71	2.12 ± 1.19	1.82 ± 1.86	1.65 ± 0.9
Mean Roundness	0.47 ± 0.20	0.51 ± 0.19	0.79 ± 0.16	0.59 ± 0.18	0.56 ± 0.20	0.78 ± 0.17	0.45 ± 0.20	0.47 ± 0.20	0.55 ± 0.24	0.6 ± 0.21

Table 11 summarizes the results of select five samples in both planes. As the VED increases from 34.09 to 63.02 J/mm<sup>3</sup>, an increase in average circularity, decrease in pore radius, decrease in aspect ratio and increase in roundness was observed. Figure 104 shows the XY and XZ plane density (optical) against VED.



**Figure 104. Optical density in both planes for select five samples against VED.**

Figure 105 and Figure 106 shows the mean circularity and mean pore radius for select five samples against VED.

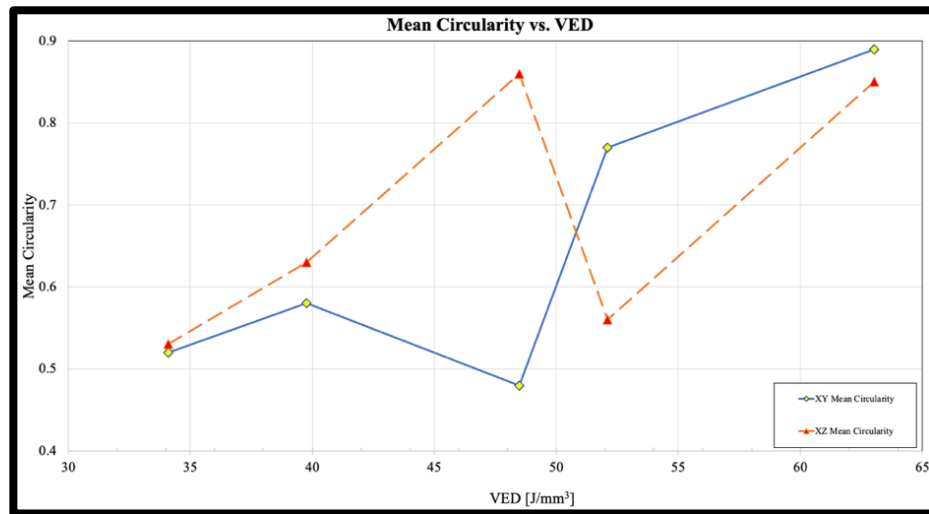


Figure 105. Mean circularity in both planes for select five samples against VED.

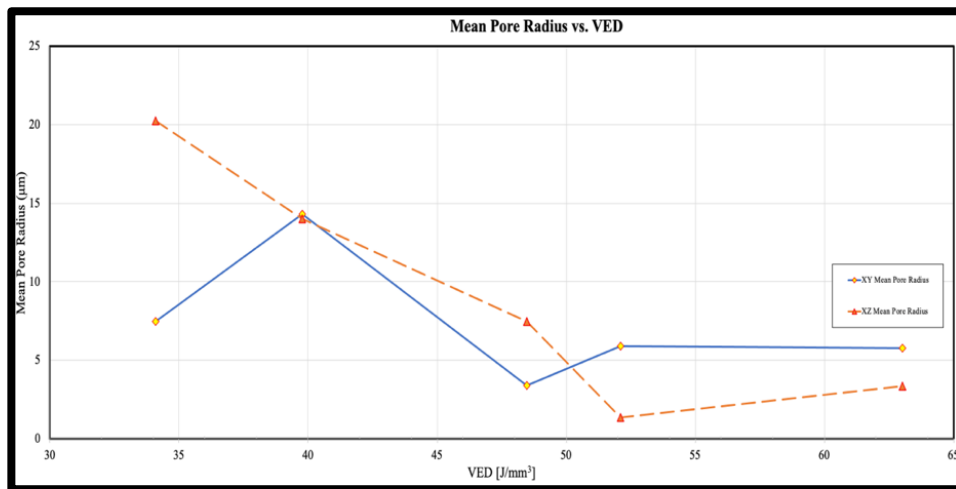


Figure 106. Mean pore radius in both planes for select five samples against VED.

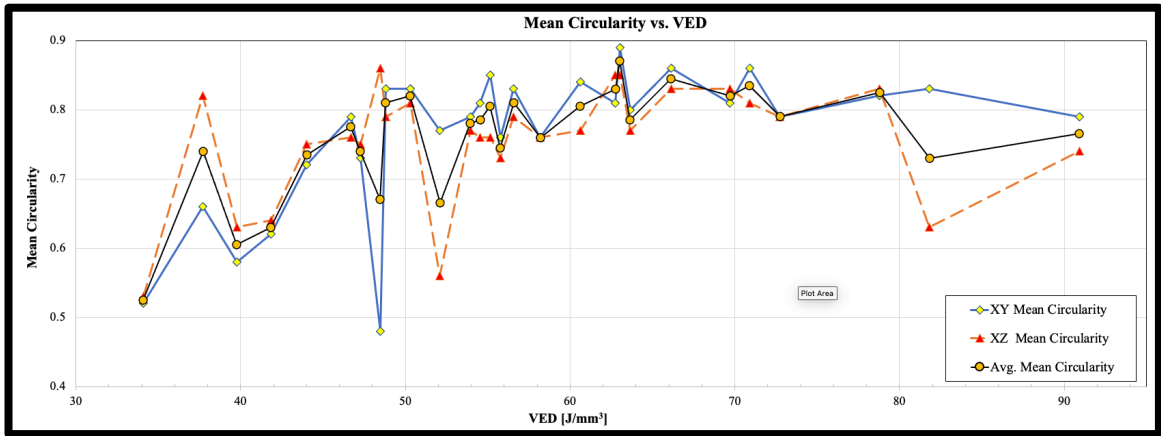


Figure 107. Mean circularity in both planes for all samples against VED.

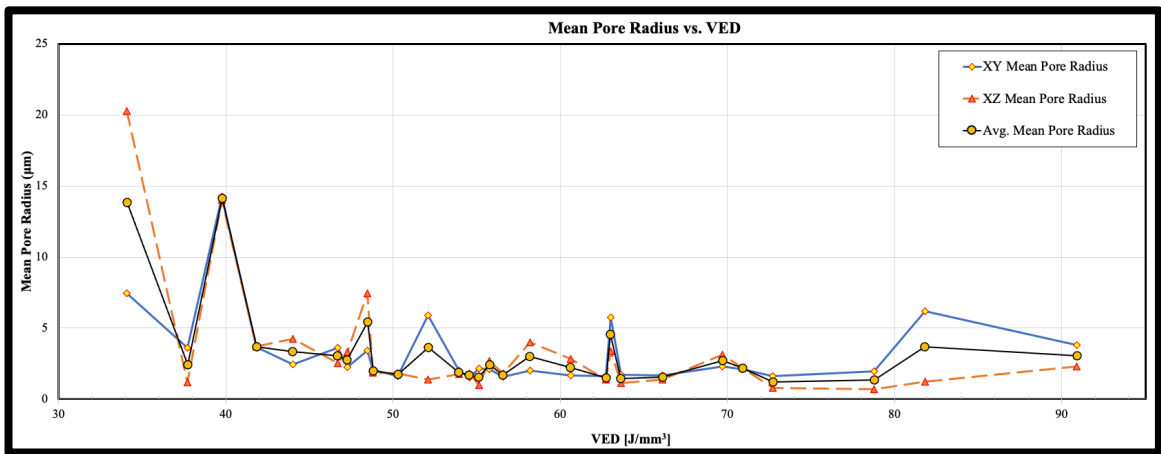


Figure 108. Mean pore radius in both planes for all samples against VED.

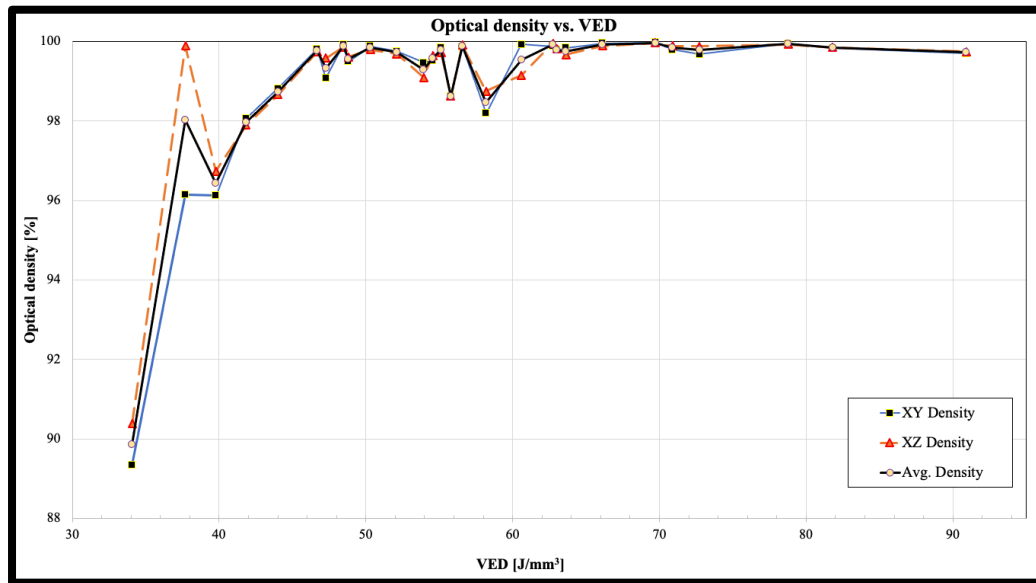


Figure 109. Optical density in both planes for all samples against VED.

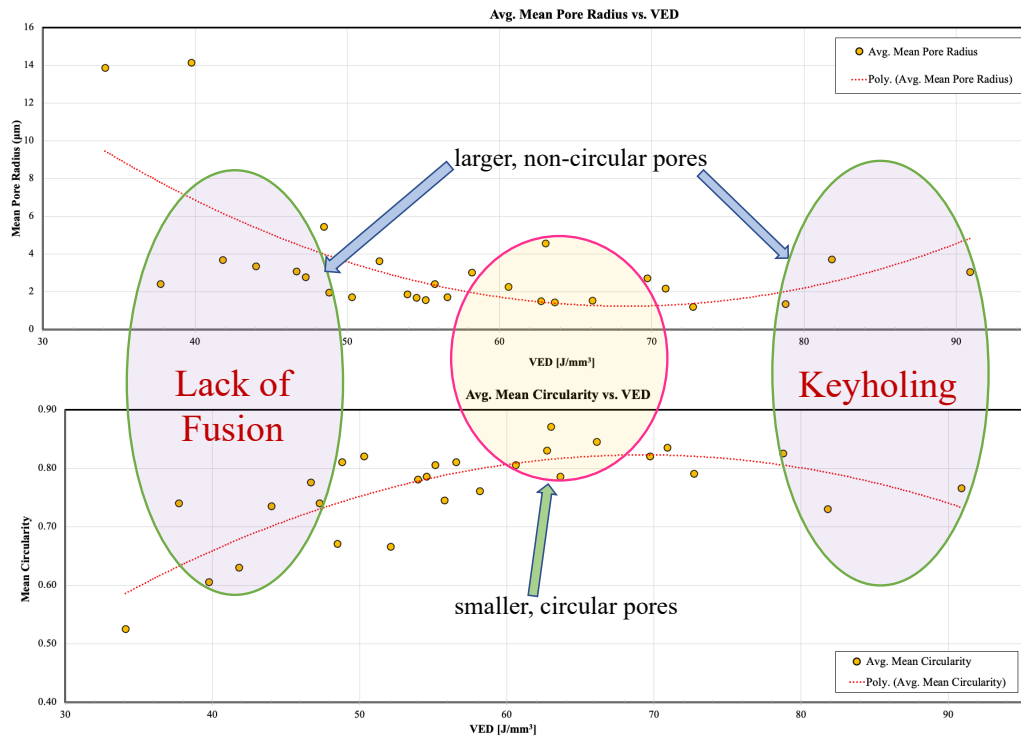


Figure 110. Optical defects in both planes for all samples against VED.

**Table 12. Summary of directional defects for all samples. Highlighted in grey color are select five samples.**

Sample #	VED	XY Density	XZ Density	Avg. Density	XY Mean Pore Radius	XY Mean Pore SD	XZ Mean Pore Radius	XZ Mean Pore SD	Avg. Mean Pore Radius	XY Mean Circularity	XY Mean Circularity SD	XZ Mean Circularity	XZ Mean Circularity SD	Avg. Mean Circularity
1 4 (1_3)	34.09	89.35	90.38	89.87	7.47	14.48	20.26	36.72	13.87	0.52	0.22	0.53	0.22	0.53
2 (1_4)	37.72	96.15	99.89	98.02	3.62	7.81	1.19	2.6	2.41	0.66	0.21	0.82	0.14	0.74
6 1 (2_5)	39.77	96.12	96.73	96.43	14.28	20.3	14	24.8	14.14	0.58	0.2	0.63	0.18	0.61
3 (1_5)	41.83	98.06	97.89	97.98	3.64	7.22	3.71	7.09	3.68	0.62	0.22	0.64	0.21	0.63
7 (2_6)	44.01	98.81	98.66	98.74	2.43	4.46	4.25	6.27	3.34	0.72	0.18	0.75	0.16	0.74
11 (3_1)	46.68	99.81	99.73	99.77	3.61	3.3	2.52	4.31	3.07	0.79	0.16	0.76	0.18	0.78
4 (1_6)	47.27	99.07	99.58	99.33	2.24	5.01	3.3	3.73	2.77	0.73	0.17	0.75	0.17	0.74
12 3 (3_2)	48.48	99.92	99.86	99.89	3.4	6.43	7.46	9.85	5.43	0.48	0.24	0.86	0.17	0.67
8 (2_7)	48.8	99.49	99.61	99.55	2.06	1.77	1.87	1.99	1.97	0.83	0.14	0.79	0.14	0.81
13 (3_3)	50.3	99.88	99.79	99.84	1.62	1.67	1.82	4.41	1.72	0.83	0.13	0.81	0.13	0.82
14 5 (3_4)	52.1	99.75	99.69	99.72	5.89	11.73	1.37	2.86	3.63	0.77	0.2	0.56	0.19	0.67
15 (3_5)	53.95	99.47	99.09	99.28	1.99	3.29	1.76	1.86	1.88	0.79	0.15	0.77	0.16	0.78
5 (1_7)	54.55	99.52	99.65	99.59	1.52	2.01	1.83	2.8	1.68	0.81	0.14	0.76	0.16	0.79
9 (1_1)	55.14	99.85	99.72	99.79	2.16	1.61	0.98	0.83	1.57	0.85	0.11	0.76	0.18	0.81
16 (3_6)	55.77	98.61	98.62	98.62	2.13	3.81	2.69	4.83	2.41	0.76	0.16	0.73	0.18	0.75
22 (4_4)	56.58	99.86	99.91	99.89	1.58	1.64	1.82	3.28	1.70	0.83	0.13	0.79	0.15	0.81
17 (3_7)	58.18	98.19	98.75	98.47	2.03	3.98	4.01	5.85	3.02	0.76	0.16	0.76	0.17	0.76
18 (2_1)	60.61	99.93	99.15	99.54	1.65	2.58	2.83	2.75	2.24	0.84	0.12	0.77	0.17	0.81
23 (4_5)	62.74	99.88	99.95	99.92	1.62	1.6	1.36	1.03	1.49	0.81	0.13	0.85	0.1	0.83
19 2 (2_2)	63.02	99.78	99.81	99.80	5.77	8.92	3.37	6.35	4.57	0.89	0.11	0.85	0.14	0.87
10 (1_2)	63.64	99.84	99.67	99.76	1.74	3.01	1.13	4.75	1.44	0.8	0.14	0.77	0.17	0.79
20 (2_3)	66.12	99.95	99.89	99.92	1.69	2.05	1.38	3.18	1.54	0.86	0.09	0.83	0.11	0.85
26 (4_1)	69.72	99.97	99.96	99.97	2.31	2.1	3.13	3.63	2.72	0.81	0.15	0.83	0.13	0.82
24 (4_6)	70.9	99.79	99.89	99.84	2.13	8.72	2.21	5.13	2.17	0.86	0.08	0.81	0.12	0.84
21 (2_4)	72.73	99.68	99.88	99.78	1.64	5.15	0.77	1.01	1.21	0.79	0.14	0.79	0.14	0.79
27 (4_2)	78.78	99.94	99.93	99.94	1.95	2.15	0.72	0.53	1.34	0.82	0.12	0.83	0.12	0.83
25 (4_7)	81.82	99.83	99.85	99.84	6.19	7.83	1.22	3.02	3.71	0.83	0.15	0.63	0.26	0.73
28 (4_3)	90.91	99.7	99.74	99.72	3.81	12.72	2.28	3.59	3.05	0.79	0.16	0.74	0.18	0.77



## 6.4 Phase Identification Analysis

SLM-processed SS 316L has been shown to form different phases, including face-centered cubic (fcc) austenite, body-centered cubic (bcc) ferrite, and body-centered tetragonal (bct) martensite [264]. In order to correlate the mechanical property differences across samples, grain size calculations and phase fraction identification were performed.

### 6.4.1 Major Phases & Grain Size

We have observed and identified three distinct phases in selected five samples and grouped them based on the samples having the martensite phase fraction and others without it, as shown in Figure 111.

Ferrite phase formation in austenitic stainless steel is typically due to diffusion or segregation [265]. However, the volume fraction of ferrite depends on the cooling rate, and a higher cooling rate can obstruct diffusion. Also, both Austenite and ferrite phase fractions are critical in controlling the ductility and hardness of steel. Martensite (with a needle-like (acicular) structure), on the other hand, is formed due to diffusion-less transformation. As the formation of the martensitic phase from austenite involves interatomic movements, three possible martensite crystal structures could include bct alpha prime, bcc alpha prime, or hexagonal close-packed epsilon (hcp) martensite [266].

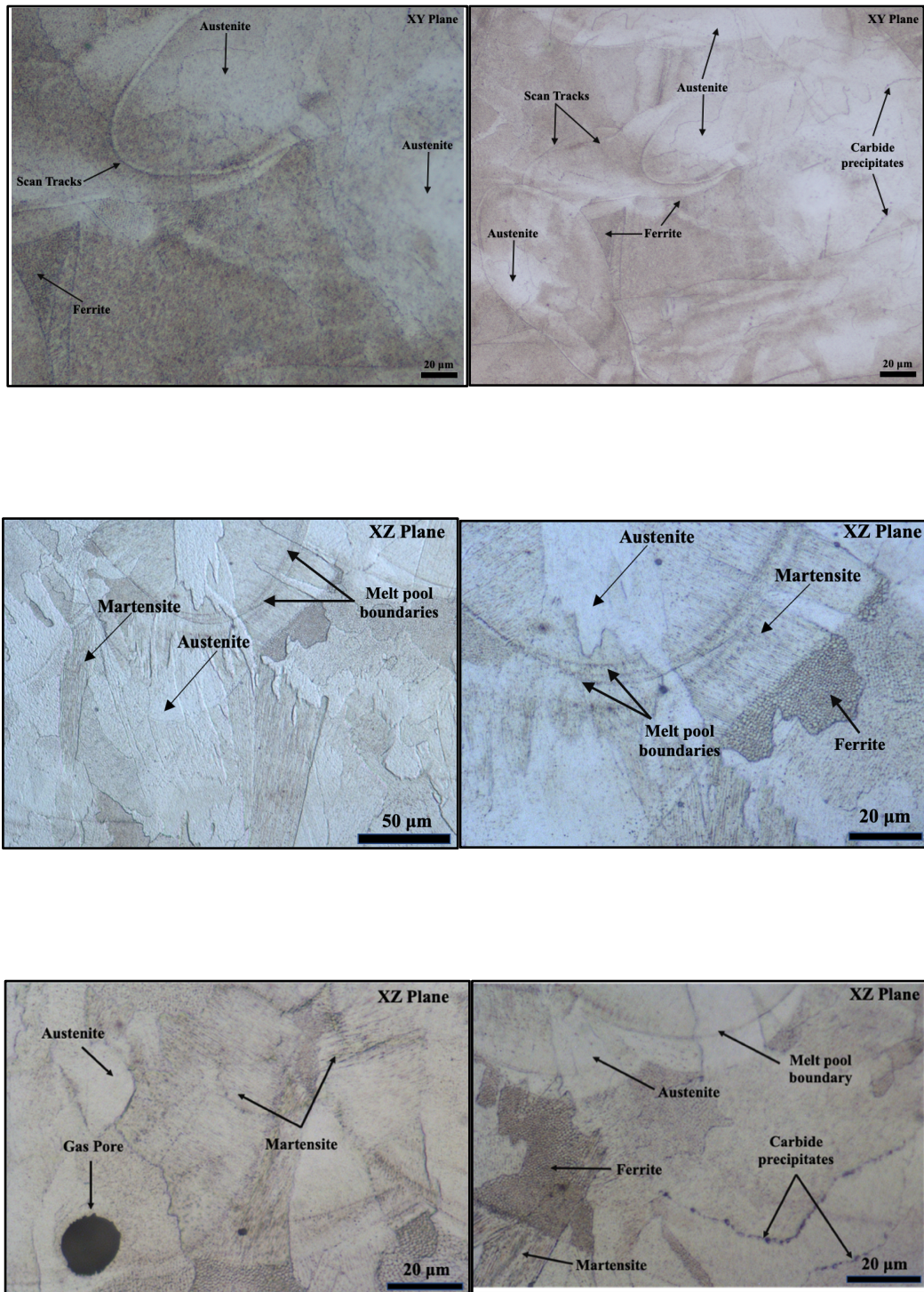


Figure 111. Representative optical images of sample #2 ( $E_v = 39.77 \text{ J/mm}^3$ ;  $\rho = 96.35\%$ ), #3 ( $E_v = 48.48 \text{ J/mm}^3$ ;  $\rho = 98.21\%$ ), and #5 ( $E_v = 52.10 \text{ J/mm}^3$ ;  $\rho = 97.50\%$ ) showing phases of ferrite, austenite, and martensite [264].

Additionally, martensite has two types of morphology – laths and plate, the formation of which depends on the carbon content. Lath martensite is typically seen in low C (<0.6 wt%) stainless steel, such as 316L, whereas plate martensite is seen in high carbon steels [267]. Small traces of the martensite phase were identified alongside the significant presence of austenite and ferrite phases across all the samples, which is summarized in Table 13.

**Table 13. Summary of identified phases for all samples. Highlighted in grey color are select five samples.**

Sample #	XY Opt. Den (%)	XZ Opt. Den (%)	Phases in XY Plane	Phases in XZ Plane
1 4 (1 3)	89.35	90.38	ferrite and austenite	ferrite dominates with some austenite
2 (1 4)	96.15	99.89	ferrite and austenite	ferrite dominates with some austenite
6 1 (2 5)	96.12	96.73	ferrite and austenite	ferrite dominates with some austenite
3 (1 5)	98.06	97.89	ferrite and austenite	austenite dominates with some ferrite
7 (2 6)	98.81	98.66	ferrite and austenite	austenite dominates with some ferrite
11 (3 1)	99.81	99.73	ferrite, austenite, some martensite	austenite dominates with some ferrite and martensite
4 (1 6)	99.07	99.58	ferrite and austenite	austenite dominates with some ferrite
12 3 (3 2)	99.92	99.86	ferrite, austenite, some martensite	austenite dominates with some martensite
8 (2 7)	99.49	99.61	ferrite, austenite, some martensite	austenite dominates with some ferrite and some martensite
13 (3 3)	99.88	99.79	ferrite, austenite, some martensite	austenite dominates with some ferrite and martensite
14 5 (3 4)	99.75	99.69	ferrite, austenite, some martensite	austenite dominates with some martensite
15 (3 5)	99.47	99.09	ferrite, austenite, some martensite	austenite dominates with some ferrite and martensite
5 (1 7)	99.52	99.65	ferrite, austenite, some martensite	ferrite, austenite with some martensite
9 (1 1)	99.85	99.72	ferrite, austenite, some martensite	ferrite, austenite with some martensite
16 (3 6)	98.61	98.62	ferrite, austenite, some martensite	austenite dominates with some ferrite and martensite
22 (4 4)	99.86	99.91	ferrite, austenite, some martensite	austenite dominates with some ferrite and martensite
17 (3 7)	98.19	98.75	ferrite, austenite, some martensite	austenite dominates with some ferrite and martensite
18 (2 1)	99.93	99.15	ferrite, austenite, some martensite	ferrite, austenite, and martensite
23 (4 5)	99.88	99.95	ferrite, austenite, some martensite	austenite dominates with some ferrite and martensite
19 2 (2 2)	99.78	99.81	ferrite and austenite	austenite dominates with some ferrite
10 (1 2)	99.84	99.67	ferrite and austenite	ferrite dominates with some austenite
20 (2 3)	99.95	99.89	ferrite, austenite, some martensite	austenite dominates with some ferrite
26 (4 1)	99.97	99.96	ferrite, austenite, some martensite	austenite dominates with some ferrite and martensite
24 (4 6)	99.79	99.89	ferrite, austenite, some martensite	austenite dominates with some ferrite and martensite
21 (2 4)	99.68	99.88	ferrite, austenite, some martensite	ferrite, austenite with some martensite
27 (4 2)	99.94	99.93	ferrite, austenite, some martensite	austenite dominates with some ferrite and martensite
25 (4 7)	99.83	99.85	ferrite, austenite, some martensite	ferrite dominates with some austenite and martensite
28 (4 3)	99.7	99.74	ferrite, austenite, some martensite	austenite dominates with some ferrite and martensite

**Table 14. Summary of five samples with processing conditions, and test results.**

#	$E_v$ [J/m <sup>3</sup> ]	HV <sub>0.5</sub> (Std. Dev.)	Nano Hardness [GPa] (Std.Dev.)	E [GPa] (Std. Dev.)	$\rho$ [%]	Major Phases Identified	Grain Size [ $\mu$ m] (Std. Dev.)
1*	39.77	209 (28.5)	3.83 (0.17)	203.9 (4.66)	96.35	Ferrite, Austenite	~ 3-5 ( $\pm$ 0.5)
2*	63.02	256 (1.5)	4.81 (0.52)	211.1 (9.62)	97.23	Ferrite, Austenite	~ 3-5 ( $\pm$ 0.5)
3†	48.48	271 (6.2)	4.01 (0.11)	187.4 (5.79)	98.21	Ferrite, Austenite, Martensite	~ 2-4 ( $\pm$ 0.5)
4*	34.09	294 (12.1)	3.98 (0.30)	154.1 (6.1)	90.78	Ferrite, Austenite	~ 2-4 ( $\pm$ 0.5)
5†	52.10	318 (13.9)	4.62 (0.23)	162.9 (2.43)	97.5	Ferrite, Austenite, Martensite	~ 1-2 ( $\pm$ 0.5)

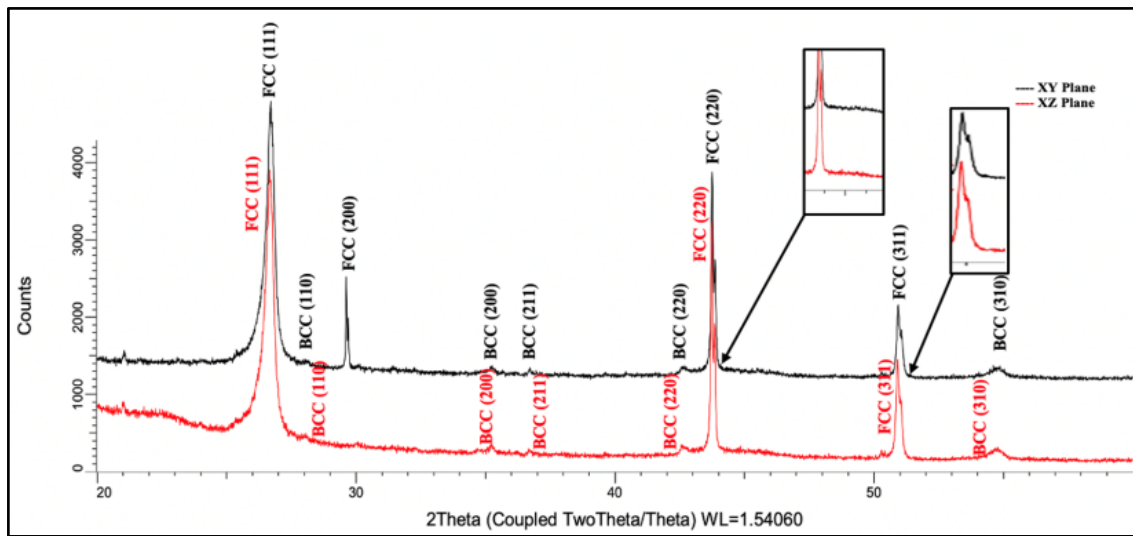
\* samples with mostly ferrite and austenite phases in the microstructure

† samples with martensite, ferrite and austenite phases in the microstructure

Table 14 shows the five-selected samples have been grouped on the basis of major constituent phases identified along with their physical/mechanical properties that were later used in fabricating FGAMs. The observed difference between the Vickers and nano hardness results could be due to possibilities in latter case of indenting over one grain, grain boundary, or intersection of two grains since the material is polycrystalline.

### 6.4.2 XRD Analysis

The diffraction patterns were measured using X-ray diffraction (XRD) analysis, and diffractograms are generated for the specimens on both side surfaces (longitudinal/XZ plane) and the top surface (transverse/XY plane). For the sake of brevity, diffractograms for sample 3 are presented in Figure 112.



**Figure 112. XRD diffractogram of SLM-fabricated SS 316L on two different surface planes for sample 3 showing the prominent diffraction peaks of phases. Black color represents the transverse (XY) plane or top surface, whereas the red color represents the longitudinal (XZ) plane or side surface pattern.**

The data collected considers both the depth and surface of sample 3 that exhibited the predominant presence of face-centered cubic (fcc) austenite phase, typical for austenitic steel having a single austenite phase, based on the literature [198, 199]. For top surface austenite, peaks were found at  $2\theta$  of approximately 26.71°, 29.63°, 43.76°,

43.87°, and 50.94°. For the side surface,  $2\theta$  was 26.67°, 43.74°, 43.85°, and 50.92°. We also observed a small amount of a body-centered cubic (bcc) ferrite phase for both top and side surfaces at  $2\theta$  of 28.37°, 35.34°, 36.86°, 42.71°, and 54.85°. Similar peak position observations were also made previously in a relevant study [268]. XRD analysis of top and side surfaces also suggests the presence of small (relatively weak) peaks of the body-centered tetragonal (bct) martensite phase along with other significant phases (austenite/ferrite). However, due to subtle changes between ferrite and martensite peaks, care is needed when identifying them.

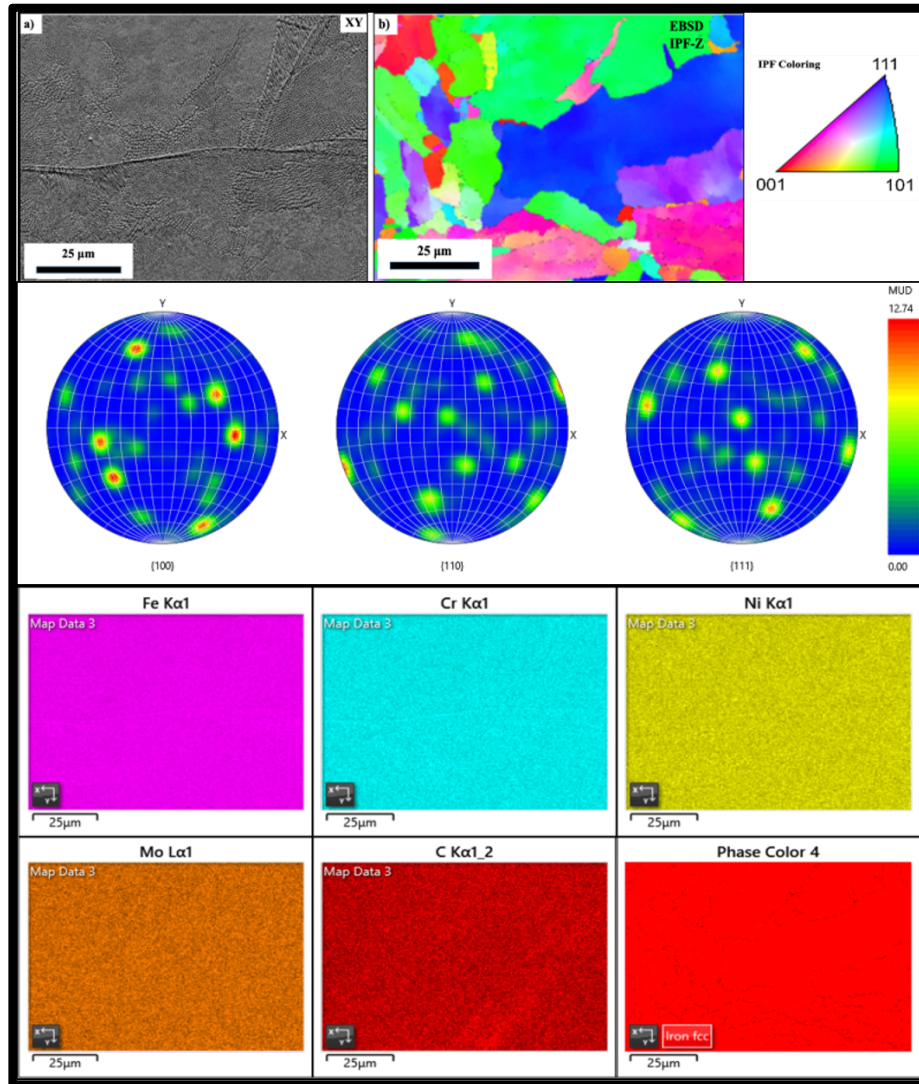
Our observations indicate that rapid solidification and high thermal stresses due to repeated heating-cooling cycles lead to non-equilibrium microstructures leading to the formation of different phase fractions [161, 254]. Moreover, the XRD findings are in agreement with the optical observations that were conducted for sample 3. The peak widths at full-width at half maximum (FWHM) near the asymptotic part of the tails of XRD peaks were estimated at  $2\theta$  of approximately 26.71° and 28.37° for top and side surface, respectively. The top surface has shown more peak broadening, with FWHM is equal to 0.5034, and that of the side surface is equal to 0.4198. Such peak broadening indicates higher residual thermal stresses induced due to higher laser irradiation on the top surface than the side surface. Such accumulated residual stresses have altered the mechanical properties such as hardness as per Murr et al. [269].

### *6.4.3 EBSD/EDS Analysis*

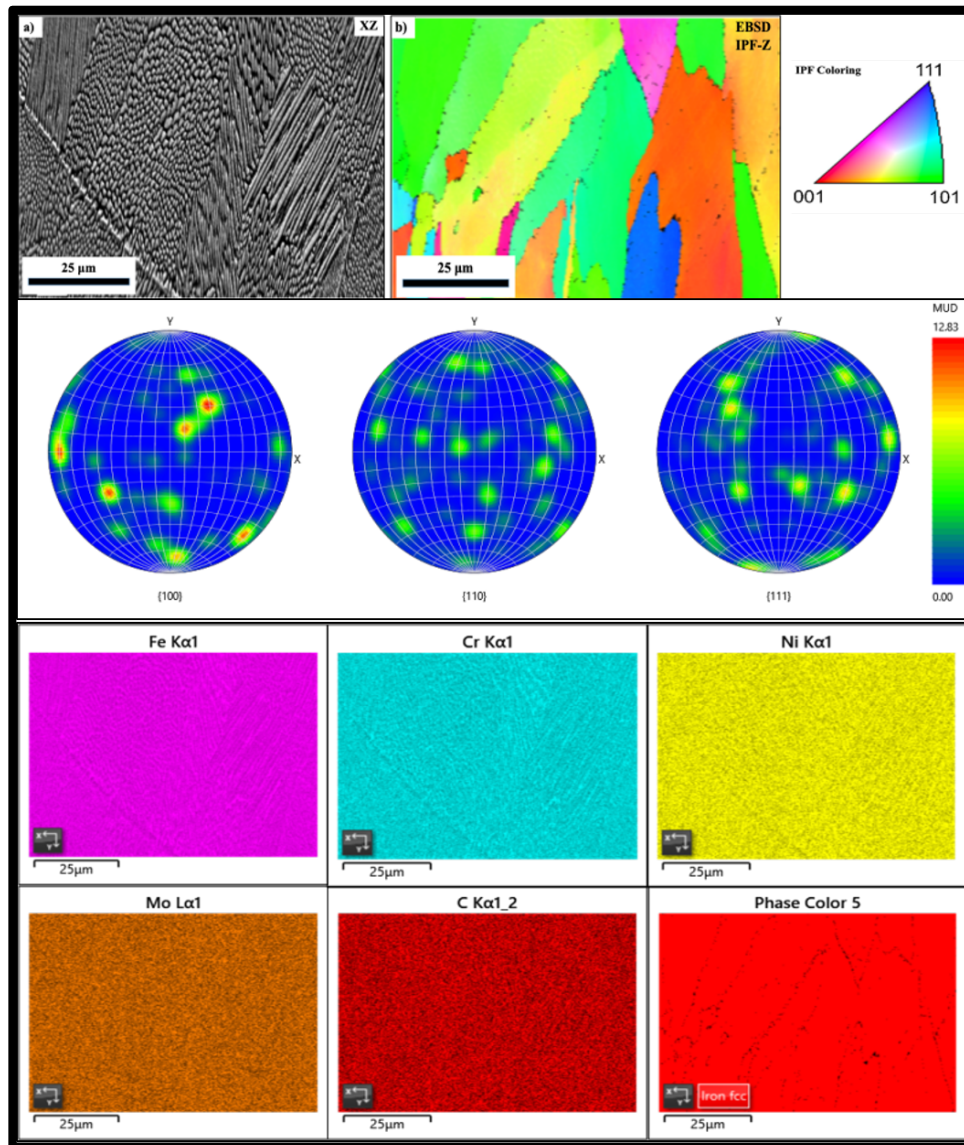
Electron backscatter diffraction (EBSD) analyses were used for mapping the crystallographic orientation and localized crystal structures of sample 5 in different cross-sections of the as-built samples as shown in Figure 113 and Figure 114.

The present analyses were done over polished sample surfaces with an approximately scan area of  $100 \mu\text{m}^2$  at higher magnifications, which would usually detect very localized information about the sample surfaces. Comparing information qualitatively can help understand the change in grain size and morphology. Nonetheless, both samples have shown mostly cellular (equiaxed) and columnar sub-grain microstructures and differences in grain orientations, textures, and grain sizes were also noticeable, as reported [163, 270, 271]. These are typically present when a Gaussian beam profile is used for SLM of SS 316L.





**Figure 113. (A) EBSD (2D) maps of the as-built SS 316L sample in a transverse (XY) plane. Pole figures and inverse pole figures are also shown. (B) EDS mapping of the sub-structure with selected region's elemental distributions with corresponding Fe, Cr, Ni, Mo, C elemental maps.**



**Figure 114. (A) EBSD (2D) maps of the as-built SS 316L sample in a longitudinal (XZ) plane. Pole figures and inverse pole figures are also shown. (B) EDS mapping of the sub-structure with selected region's elemental distributions with corresponding Fe, Cr, Ni, Mo, C elemental maps.**

The inverse pole figure (IPF) maps shown have been calculated from the EBSD data of sample 5 in the transverse (XY) plane and longitudinal (XZ) plane. The IPF orientation maps indicate the preferred grain orientations in the given surfaces and

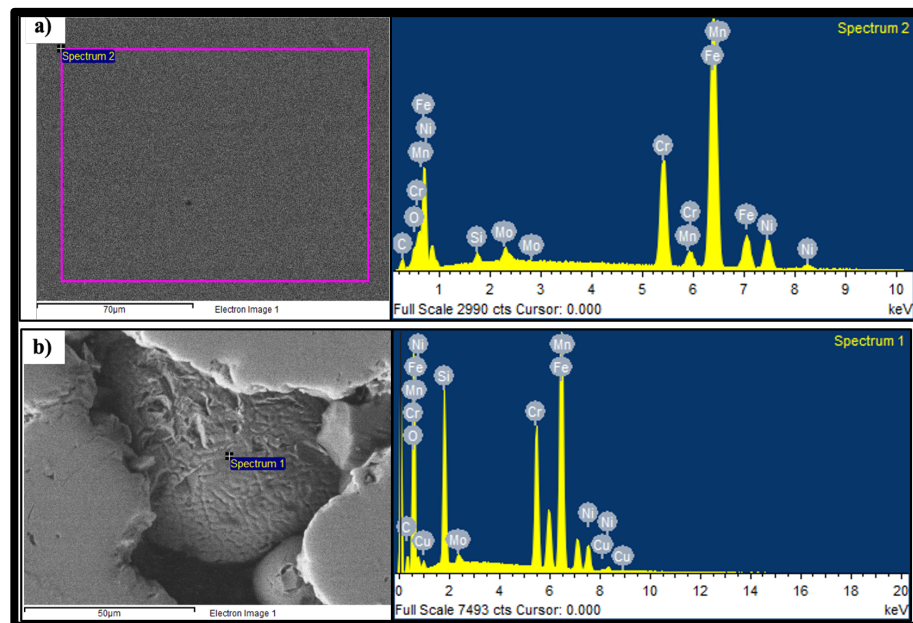
confirm this behavior with the three-color (red, green, and blue) value corresponding to the crystal direction. We noticed multicomponent cubic textures in XY and XZ planes for sample 5, as reported in another similar study for SLM-fabricated SS 316L [166]. As can be seen in XY plane sample that it shows partial bands with no crystallographic orientation affinity for the [100], [110], and [111] poles for the XY plane. This phenomenon could be explained by the change in solidification mode and structure from columnar to equiaxed grain transitions [207, 272].

The EBSD map of the sample's side surface in XZ plane shows a lack of apparent domination of one of the orientation maps' colors. This suggests the absence of a preferred alignment of the  $\langle 100 \rangle$ ,  $\langle 110 \rangle$ , and  $\langle 111 \rangle$  axes with the build directions. Also, noticed the clusters of highest pole densities in the [100] pole figure at  $\langle 001 \rangle$  positions of the standard stereographic projection. The sample exhibits no clear indication of melting pools. Also, the columnar grains can be seen growing near perpendicular to the building direction (across melt pool boundaries), as reported by other literature [273]. This phenomenon suggests that most grain growth took place across the melt pool boundaries and that new grains are formed by epitaxial columnar grain growth due to rapid solidification rates of the SLM process [254, 274].

However, other literature on SLM of SS 316L reported  $\langle 001 \rangle$  orientation (in build direction) as preferred because of the high thermal gradient [263, 275, 276]. There were no preferred crystallographic orientations for the XY plane samples, which could be due to the scan pattern and scan orientations, which will significantly influence SLM parts' final texture. We employed a meander scan strategy that rotates  $67^\circ$  between the

consecutive layers. This phenomenon causes a mismatch on the melt tracks and alters the thermal profile in both transverse and build directions, ending in highly randomized crystal orientations. In addition, cells grow in preferential directions also tend to get influenced by the local thermal gradient inside the melt pool formed due to scan pattern, promoting cell side-branching. Such side instabilities promote dendritic growth from cellular and can cause significant detrimental effects on the sample's overall mechanical properties.

Energy dispersive spectroscopy (EDS) analysis of the as-printed SLM SS 316 L reveals low variation, randomly distributed compositions maps for Fe, Cr, Ni, MO, and C for sample 5 in both transverse (XY) and longitudinal (XZ) planes are seen in Figure 115.



**Figure 115. EDS spectrum of SLM fabricated SS 316L for, a) selected top surface area for sample 5, b) point analysis chosen over an unmelted powder particle.**

This non-quantitative analysis provides a spatial contrast of the presence of different elements and inclusions seen at the SS 316L samples' cellular sub-grains. Table 15 provide relative comparison with virgin SS 316L powder, area EDS, and point EDS.

**Table 15. Composition (wt %) distributions of before and after SLM processing.**

<b>Element (wt.%)</b>	<b>Cr</b>	<b>Ni</b>	<b>Mo</b>	<b>Mn</b>	<b>Si</b>	<b>C</b>	<b>N</b>	<b>Fe</b>
SS 316L powder	17.1	12.4	2.9	1.09	0.7	0.01	0.1	65.7
Area EDS	16.15	11.05	2.57	0.58	0.71	6.93	-	60.60
Point EDS	13.58	5.99	1.11	5.69	8.31	6.86	-	35.05

At the onset, the element distributions seemed inhomogeneous. SS 316L powder has a very high nominal composition (wt %) for both Cr and Ni. Typically, Mo and Cr tend to increase surface tension and can assist with promoting ferritic growth. During the melt pool solidification, Cr may react with residual oxygen inside the SLM processing chamber to form oxide inclusions, which later could precipitate with Mo at the sub-grain boundaries due to Marangoni convections [174]. For wrought SS 316L, Mn-S inclusions can be formed near the austenite grain boundaries, which with the Cr-depletion, may promote local pitting corrosion [163]. However, we couldn't locate any Mn-S clusters or Cr depleted regions on both sample surfaces. This could be due to the rapid cooling rates of SLM processing that reject Mn-S inclusions and promotes Cr-depletion. However, few sites show some presence of carbide precipitates. Furthermore, Cr and Ni have

dissimilar diffusion coefficients; however, relatively even distributions can be observed on element maps for both elements [277].

We also observed a large presence of oxygen and carbon elements. We believe that most oxygen contents were detected due to the remaining oxygen inside the build chamber or left in between the powder particles due to the atomization process or due to the oxide formations. On the other hand, a large presence of carbon could be due to the steps involved in sample preparations or the formation of soot or carbide precipitants. Similar observations have been reported in previous studies for higher oxygen and carbon presence [234, 278, 279]. Superior corrosion resistance provided by SS 316L mostly comes from the addition of Cr, Ni, and Mo, which seems to be maintained across most of the sample except when encountered by any unmelted powder particles.

## **6.5 Resolution Study**

This part of the study aims to quantify spatial property resolutions by fabricating continually smaller zones with intended property variations and to investigate causes. In short, it examines resolution of pulsed SLM platform to fabricate SS 316L structures by varying process parameters up to 1-layer thickness. In this case, four configurations following the DOE, as shown in Figure 116, were designed. The configurations were named as 1-layer, 2-layers, 4-layers, and 8-layers and arranged on build plate with support structures as illustrated in Figure 117.



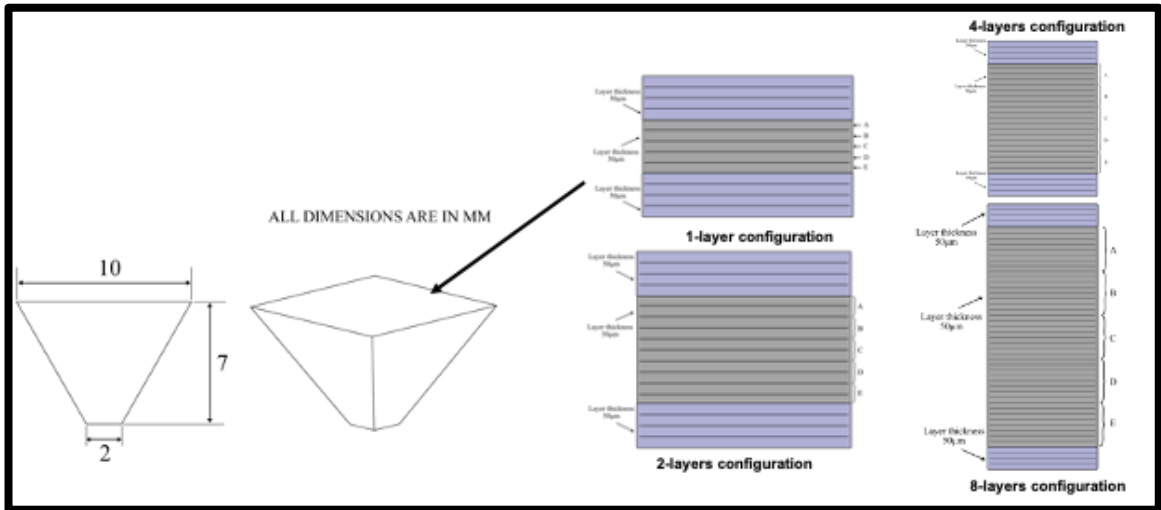


Figure 116. Resolution study DOE with 1-layer, 2-layers, 4-layers and 8-layers configurations. Each layer is 50  $\mu\text{m}$  in thickness. Layers shown in purple color are processed using standard process parameters.

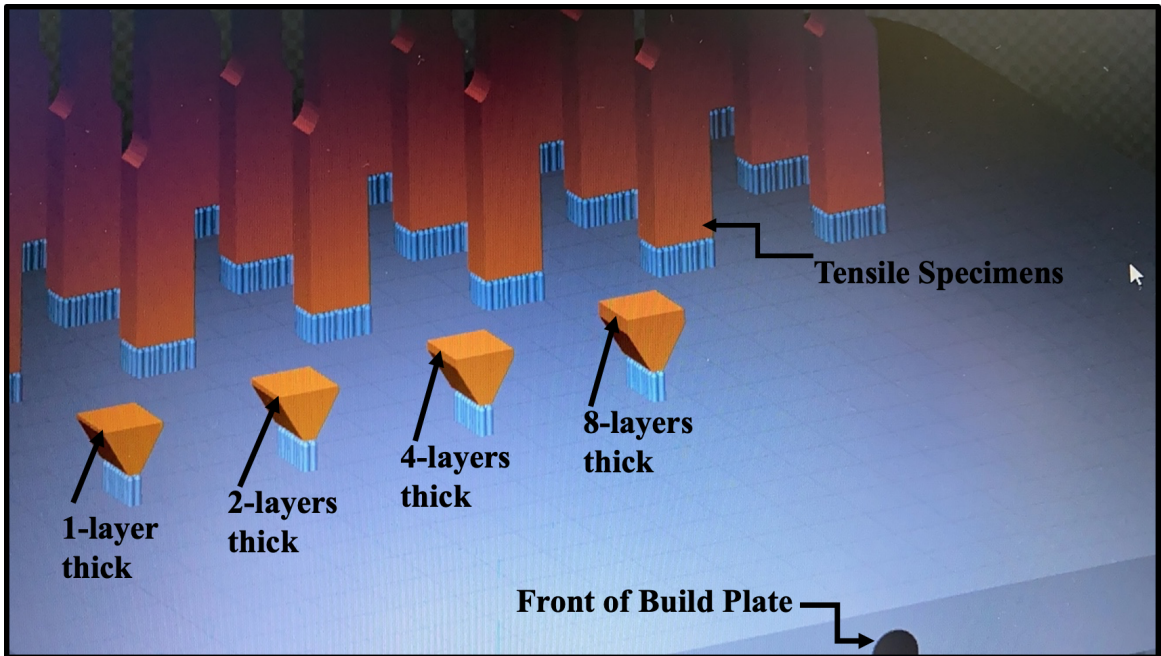
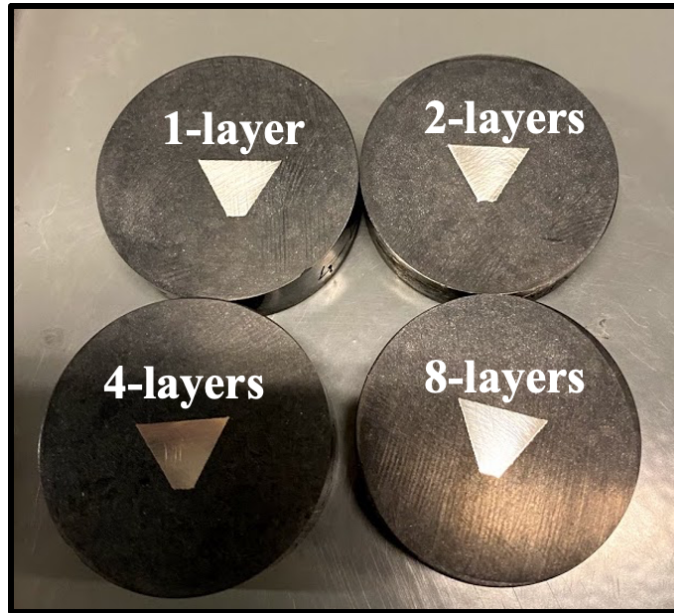


Figure 117. Resolution study (pyramids) samples arranged on the build plate.

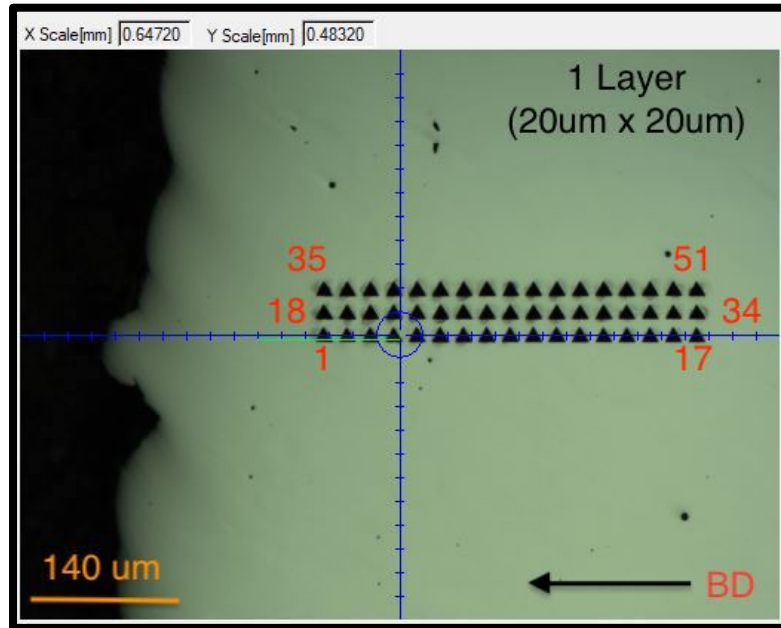


**Figure 118. Mounted and polished resolution study samples.**

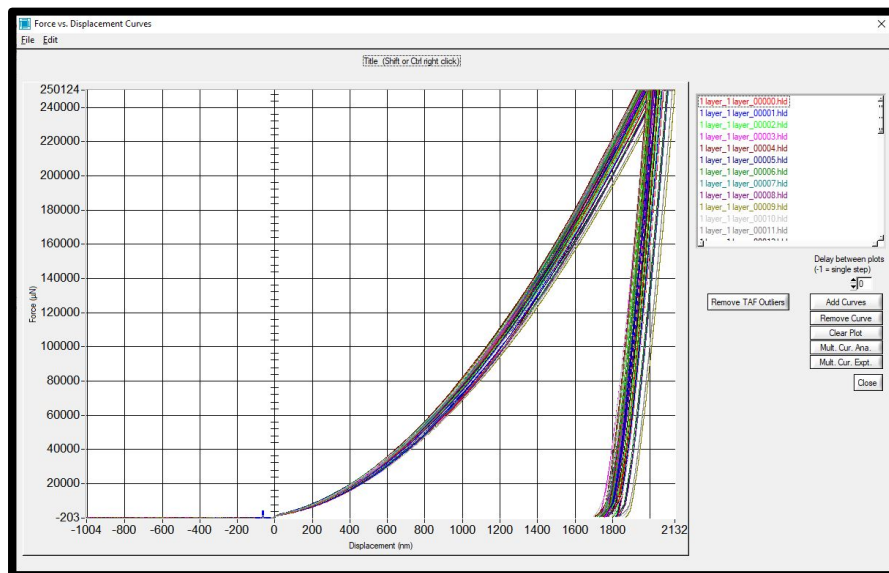
Figure 118 illustrates all four configurations of the samples sectioned and mounted for subsequent grinding and fine polishing. This was done to prepare samples for the nanoindentation test.

Total of 51 (17 rows, 3 columns) indents were carried out on each of the four sample configurations. Between adjacent rows of indents, span of 20  $\mu\text{m}$ , 40  $\mu\text{m}$ , 80  $\mu\text{m}$  and 160  $\mu\text{m}$  were kept for sample with 1-layer, 2-layers, 4-layers, and 8-layers configurations. Figure 119 illustrates the numbering of all 51 indents and spacing of 20  $\mu\text{m}$  between adjacent rows and columns for 1-layer configuration sample. Furthermore, there was 140  $\mu\text{m}$  distance kept from the top surface before starting the indentations to ensure valid conditions for the test.





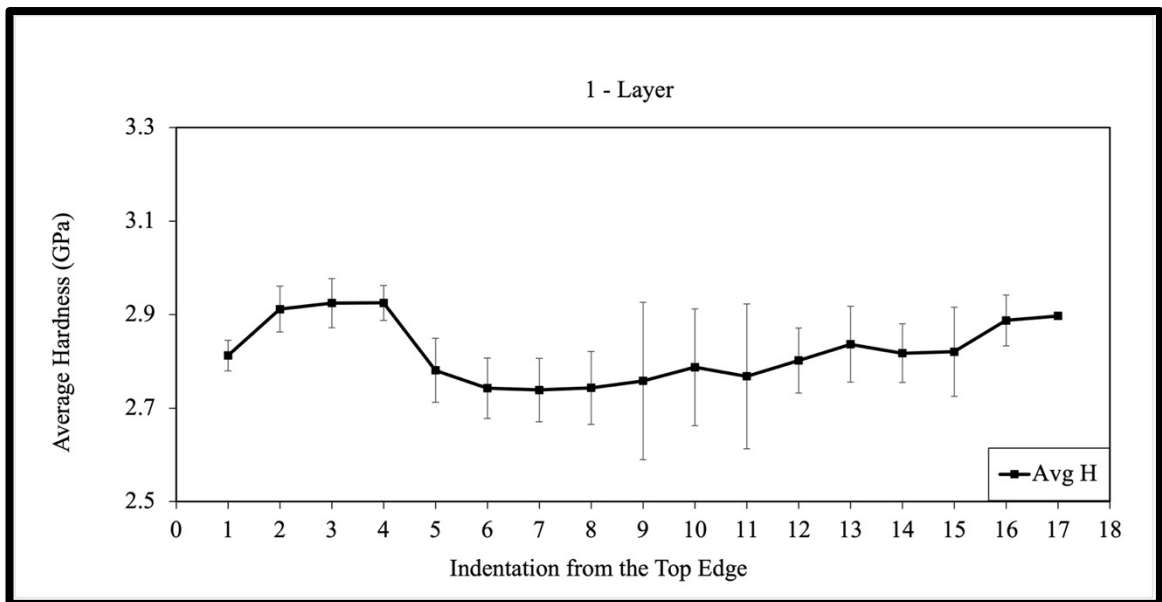
**Figure 119. 1-layer grid arrangements for nanoindentations. Each layer has three indents at 20  $\mu\text{m}$  x 20  $\mu\text{m}$  grid with indents starting from lower left (1) to top-right corner (51).**



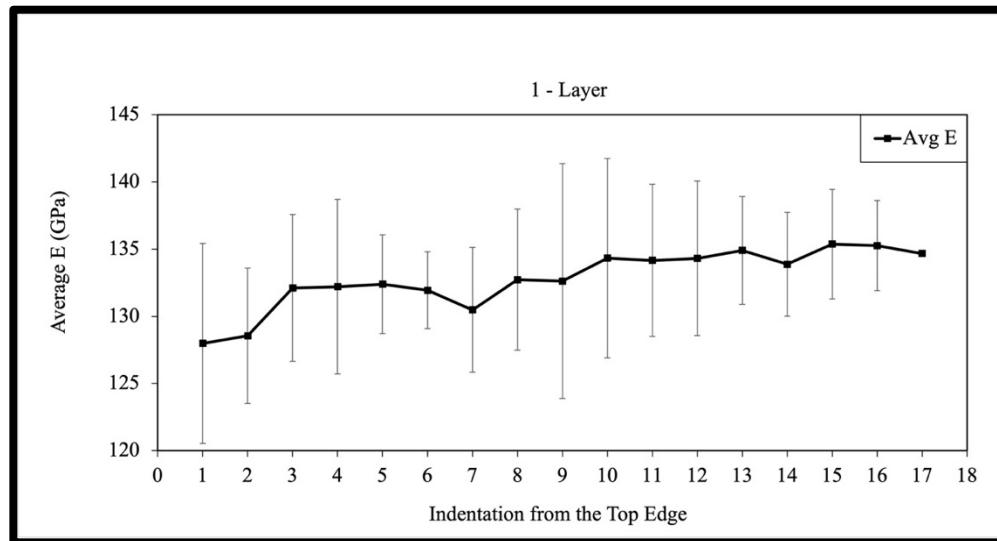
**Figure 120. Force-Displacement plots for 51 indents for 1-layer sample.**

Figure 120 shows the force-displacement curves for all 51 indents of 1-layer configuration sample. As seen, there were no anomalies detected in the curves that resembled tight grouping and repetition.

Figure 121 and Figure 122 shows the result of average hardness and average nano modulus for 1-layer configuration sample. The results showed average hardness variations between  $\sim 2.6 - 2.9$  GPa and average modulus  $\sim 121 - 141$  GPa for 1-layer configuration sample. The results show relatively lower values when compared to the reference hardness values of  $\sim 3.8 - 4.81$  GPa and modulus values of  $154.1 - 211.1$  GPa. This could be due to resulting melt pool overlaps and remelting as well as defects and pores which might alter the properties in adjacent layers.



**Figure 121. Average hardness for 1-layer sample.**



**Figure 122. Average modulus for 1-layer configuration sample.**

Figure 123 and Figure 124 shows the overview of polished sample surfaces for 1-layer, 2-layers, 4-layers, and 8-layers configurations. All samples have been mounted in XZ plane and have shown presence of process-induced defects such as, LOF, gas pores, keyhole across different layers. Furthermore, comparisons have been made across all four types of samples for hardness and modulus and illustrated in Figure 125 and Figure 126, respectively. Overall, the hardness tends to be lower across all sample configurations, however, 8-layers configuration (yellow color) showed sharp variations. In terms of modulus, 4-layer configuration (grey color) showed higher average modulus whereas 1-layer configuration (blue color) showed lower average modulus. These results indicate that in order to achieve sufficient variations there should be minimum number (at least 4-layers) of layers needed.

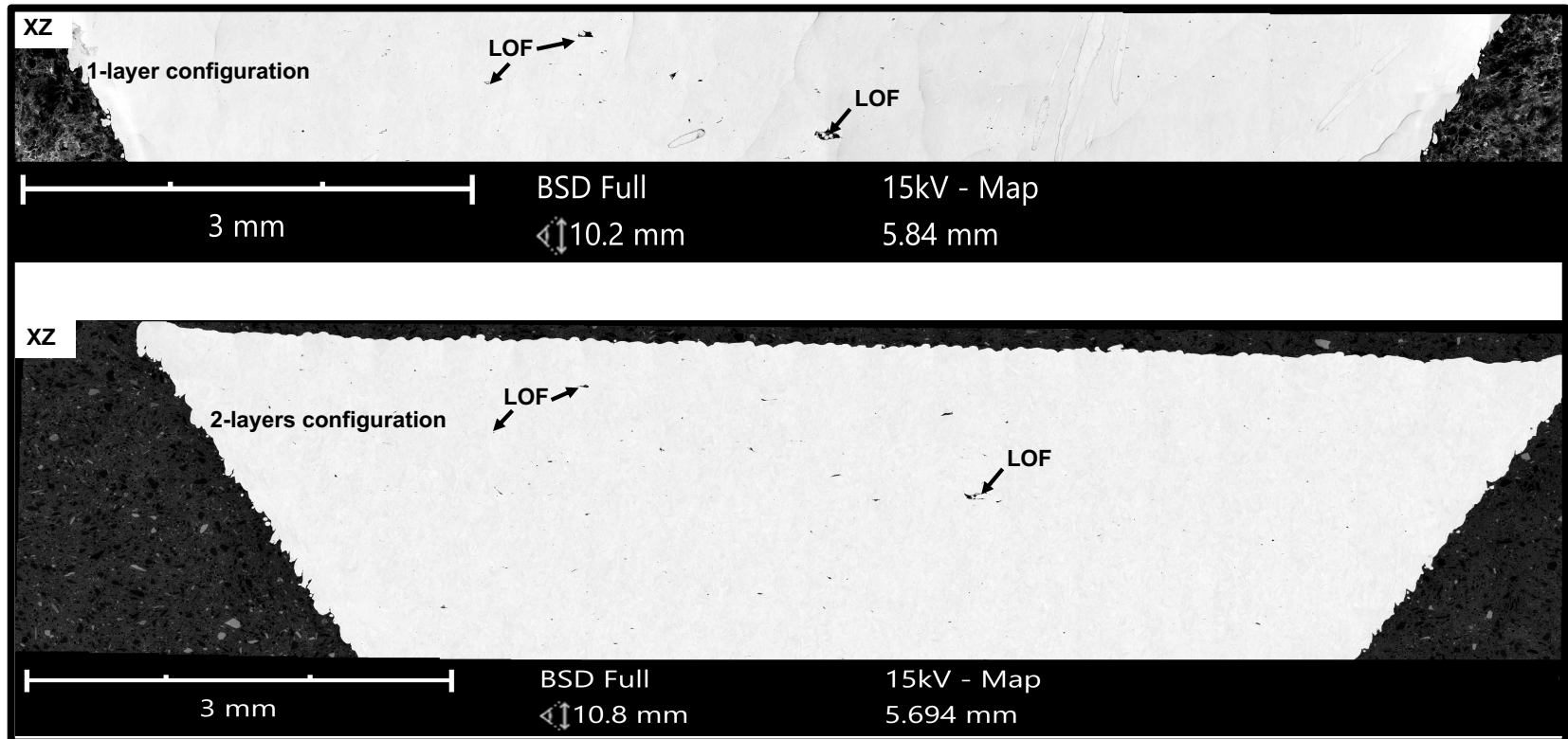


Figure 123. Light optical overview of polished surfaces of 1-layer and 2-layer samples.

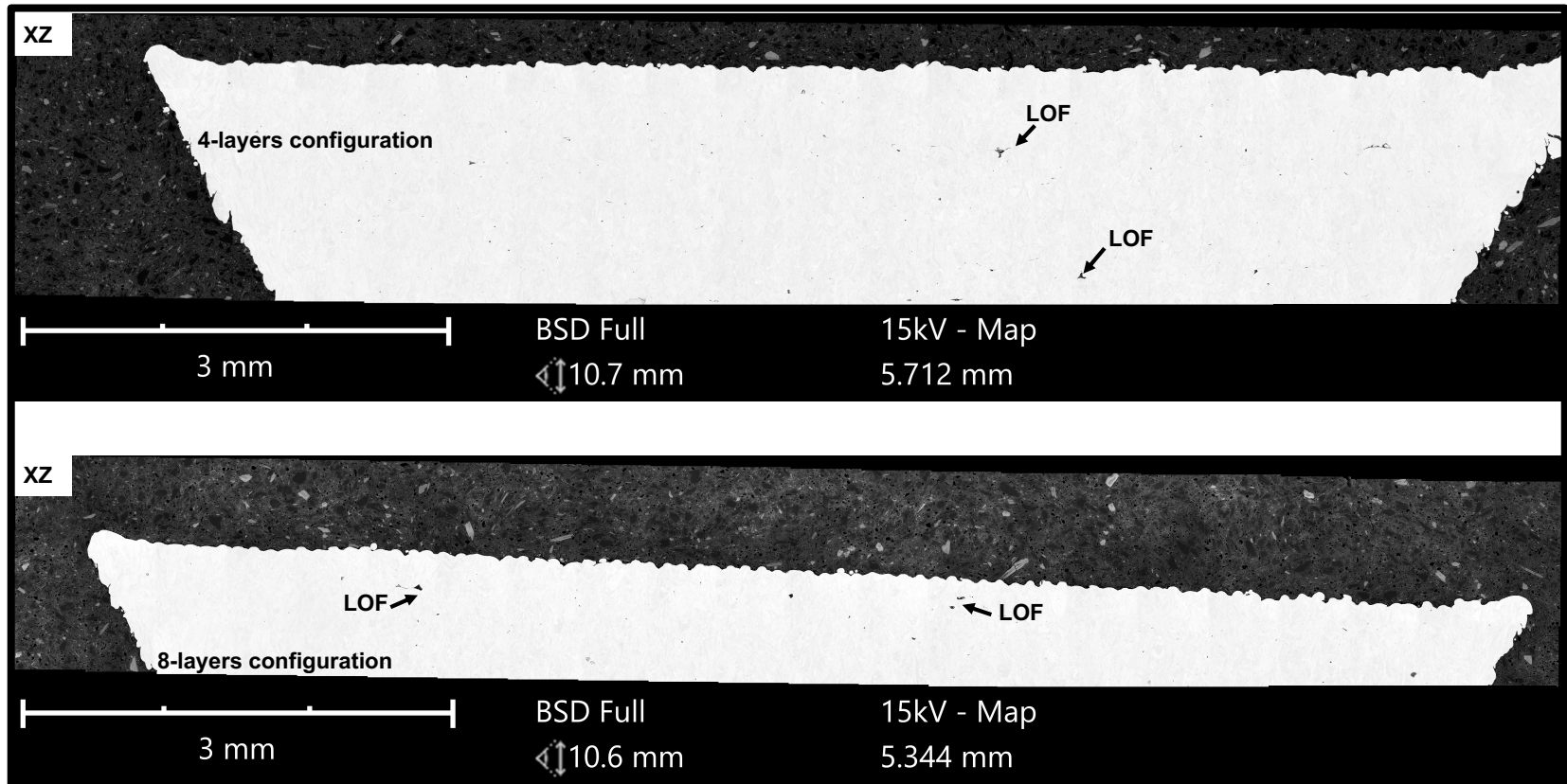


Figure 124. Light optical overview of polished surfaces of 4-layers and 8-layers samples.

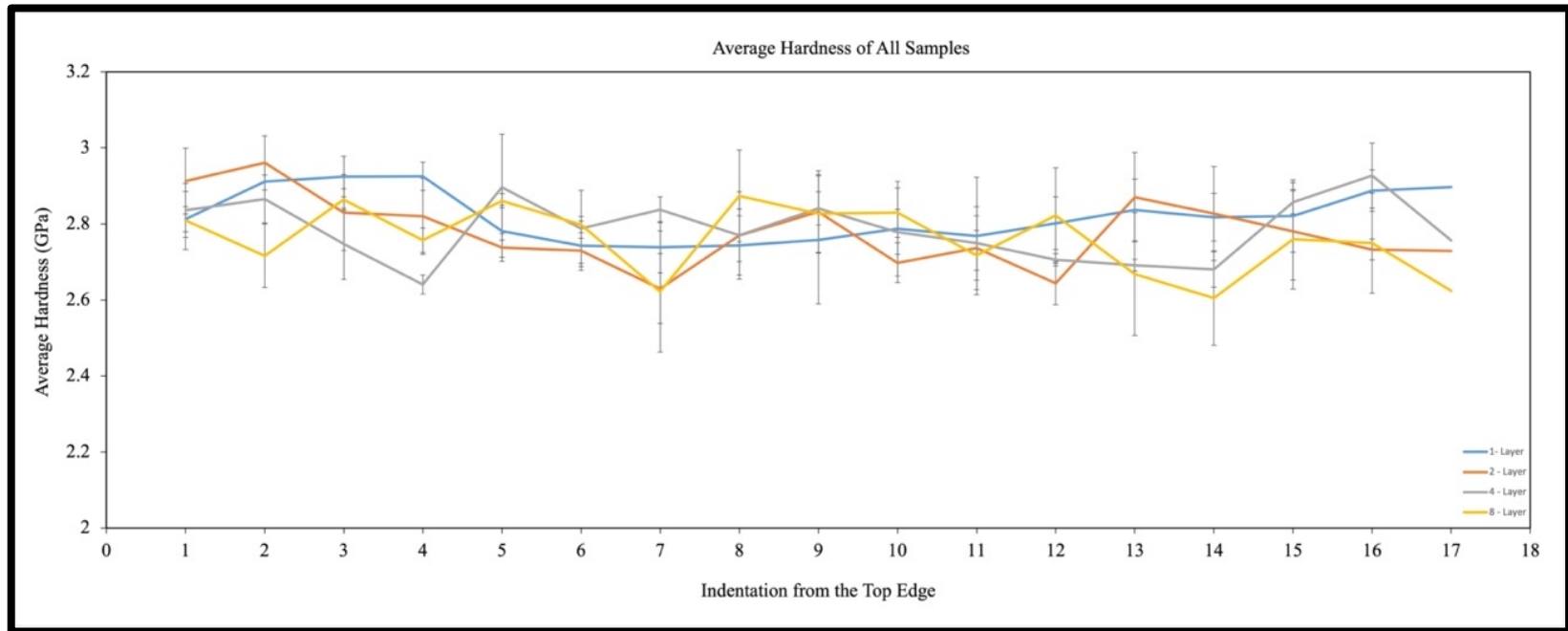


Figure 125. Comparisons of average hardness of all four sample configurations.

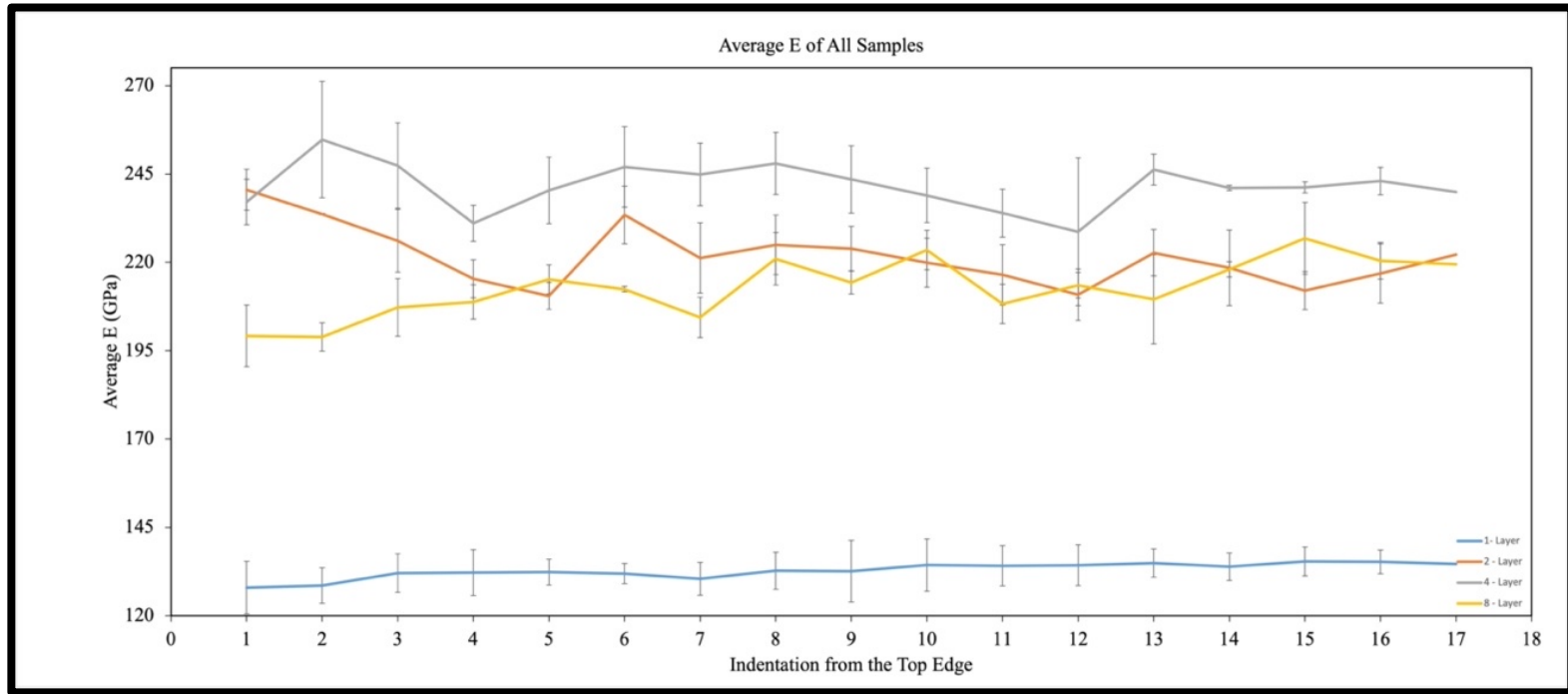


Figure 126. Comparisons of average modulus of all four sample configurations.



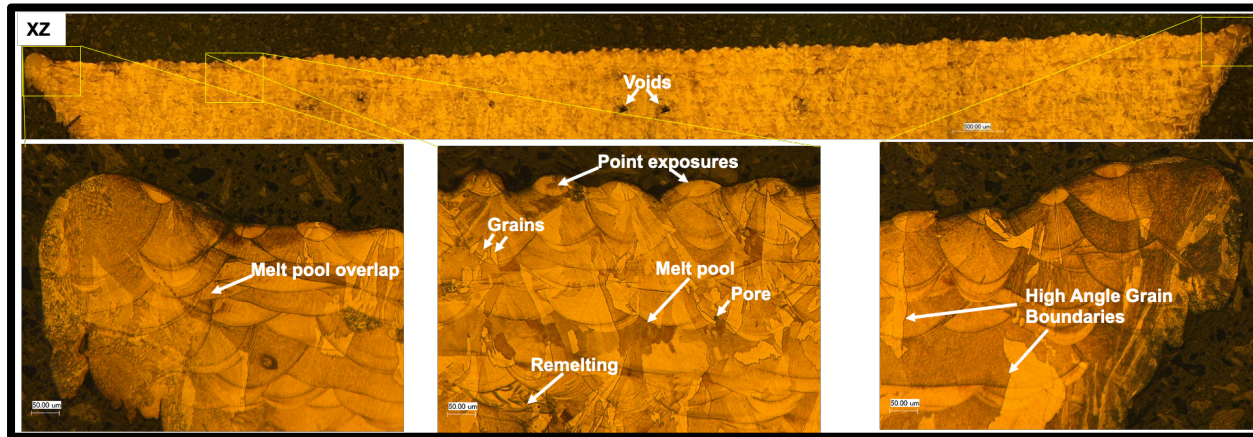


Figure 127. Light optical images of etched 2-layers sample configuration.

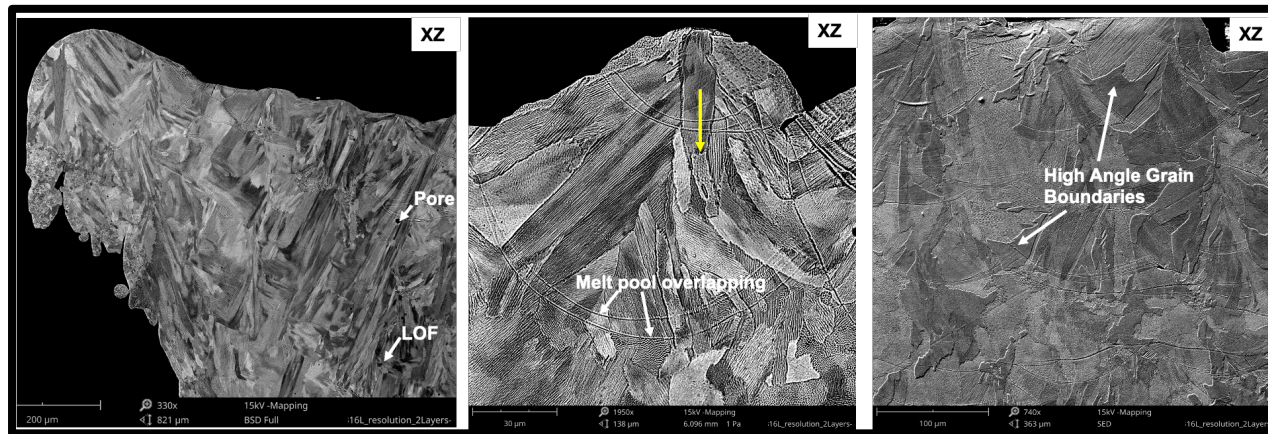
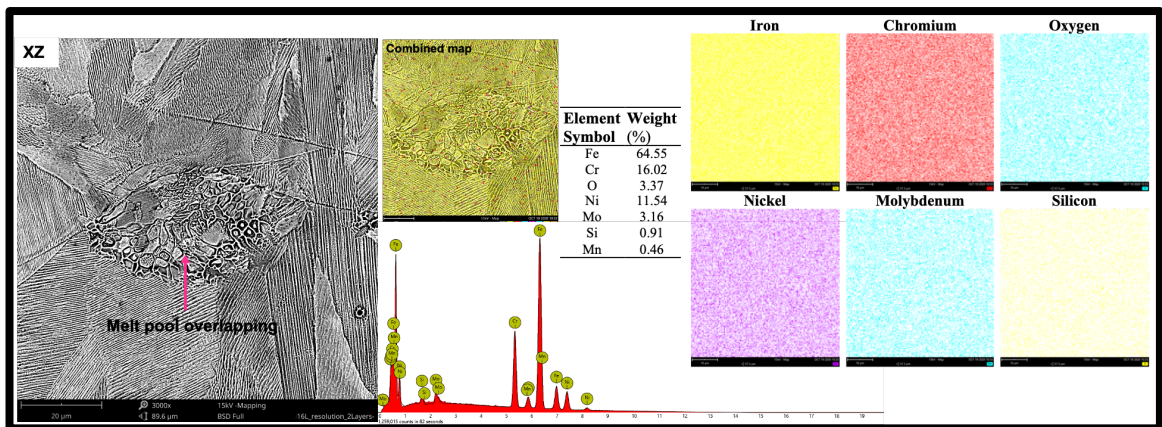


Figure 128. SEM images of etched 2-layers sample configuration.



Figure 127 and Figure 128 shows light optical and SEM images of the etched sample surface for 2-layers configuration in XZ plane. As marked, the sample exhibits number of curved melt pools, remelting of already solidified layers, melt pool overlaps, pores, voids, and presence of high angle grain boundaries (HAGB), which could potentially have influenced the hardness and modulus values. Moreover, to capture the elemental distributions at the overlapped regions, EDS analysis was conducted as showed in Figure 129.



**Figure 129. EDS analysis of on melt-pool overlap region for 2-layers sample.**

Presence of Cr, Ni, and Fe within the acceptable levels, however, the substantial presence of O<sub>2</sub> levels were also noticed. This could be due to formations of oxides in the overlap regions. The remaining elements distributions seemed to be in line with that of the virgin SS 316L powder.

## 6.6 Observations and Deductions

The overall theme of this investigation was focused on elucidating the underlying causes of property variations through material characterization in order to provide insights into grain size/morphology variations and phase fractions (across longitudinal and transverse planes) for SLM-fabricated samples. The processing- and microstructure-based dependencies of property variations were mapped across all 28 samples in order to identify cause-effect pair for property changes and their implications. As illustrated in Figure 130, process parameter bounds for achieving dominance of specific microstructures were defined.

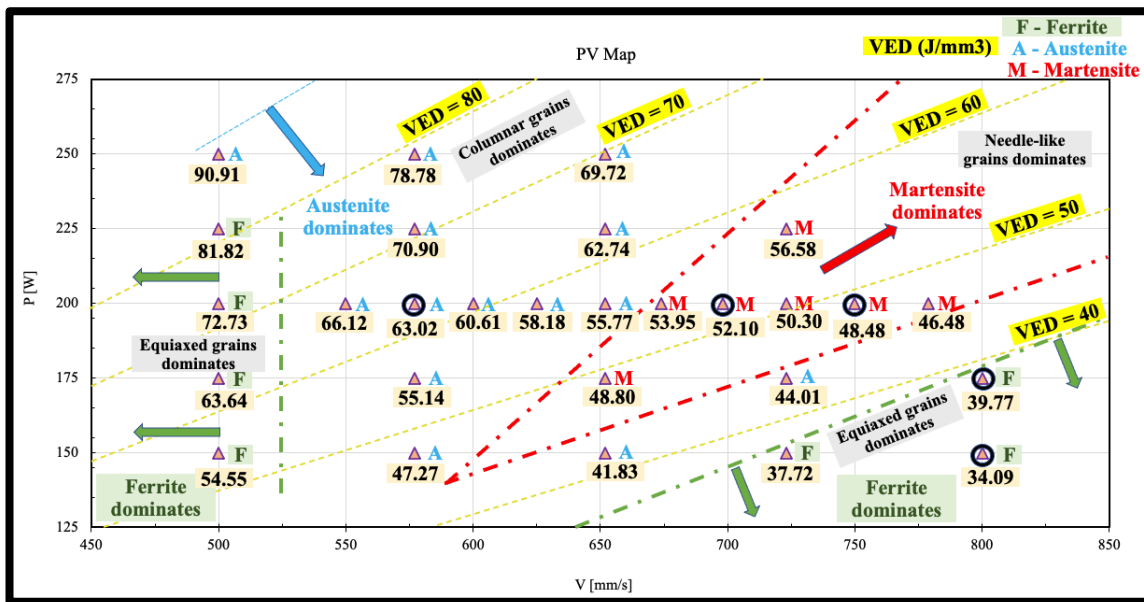


Figure 130. Summary of phases in both planes for all 28 samples.

For instance, scan speed bounds of  $\sim 550$  mm/s or less yields ferrite dominance, whereas VED between  $\sim 44-64$  J/mm<sup>3</sup> leads to formation of highly martensitic grains. The underlying reasoning for differences observed in phase dominance can be explained in terms of cooling rates. Lower VED results in shallower melt pools, yielding more randomly oriented, equiaxed/fine ferrite grains. This lower VED bounds can be achieved at higher scan speeds by keeping low laser power or vice versa. Similarly, at a higher VED, melt pools are relatively deep and forms coarser/elongated austenitic grains. Dominance of martensite within VED bounds have resulted in higher hardness zone within the processing bounds.

Ferrite (equiaxed grains) seemed to be dominating when the scan speed bounds are too low ( $\sim 500$  mm/s) or too high ( $\sim 700$  mm/s). It could be due to more spherical grains formed due to shallower melt pool features. In case of austenite (angular grains), the presence was found to be outside the VED threshold of  $44-64$  J/mm<sup>3</sup>; correlating well with relatively coarser grains which were observed across the multiple sample optical images. They could be formed due to the lower cooling rates, allowing grains to grow. Finally, martensite (needle-like structure) was observed within the VED window  $\sim 40-60$  J/mm<sup>3</sup>. The formation of martensite most likely affected by cooling rates (rapid cooling rates). The martensite was found to increase the hardness across these samples.

Additionally, the boundaries of defect regions based on observations and supported by VED-based logic are presented in Figure 131.

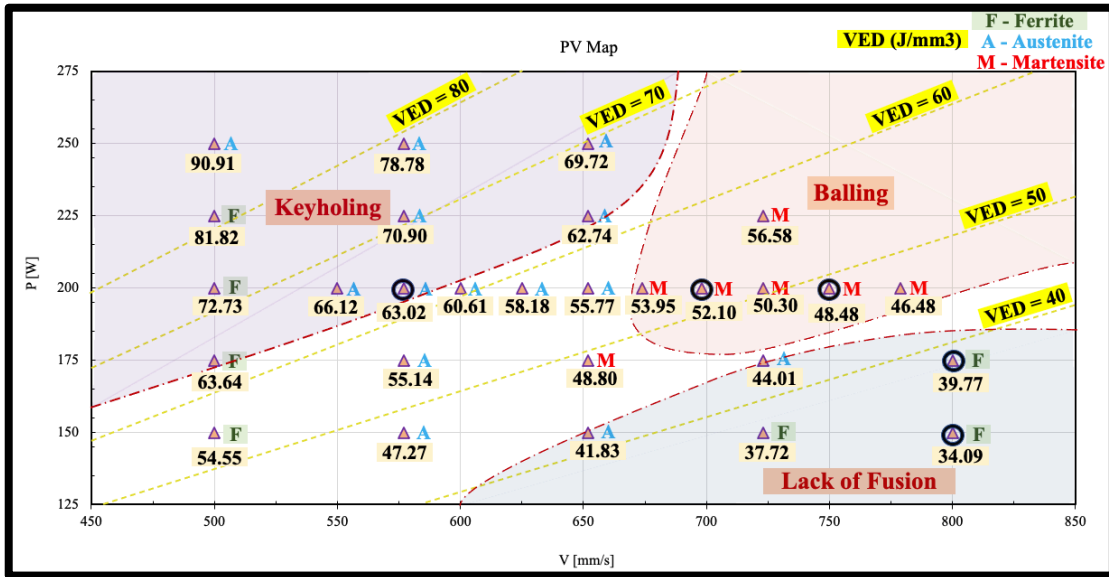


Figure 131. PV map for defects across all samples.

As highlighted, in a lower VED regime, because of the insufficient input energy imparted which resulted in insufficient melting, lot of LOF defects were observed. These defects were significant over scan speed value of ~600 mm/s at a laser power of 125 W. Within higher VED regime, due to mostly sufficient energy to melt and fuse the powder, overall resulted in lower porosity. Above threshold value of VED ~60 J/mm<sup>3</sup>, increase in keyhole/gas pores (entrapped gases) were predominant.

Overall, these results can be implemented to perform microstructural engineering with precise and repeatable control at localized level (for instance, melt pool shape, grain size) and global level (for instance, phases, texture). Altogether, potentially, this work lays the foundation for understanding and tuning the global mechanical performance of FGAM bulk structures as well as the role of interfacial zones.

## 7. STRAIN BEHAVIOR OF GRADED FGAM BULK STRUCTURES (RQ-3)

In this chapter, a set of studies are performed to investigate property-graded multi-zone bulk structures with pre-defined parameters. First part of the study looks at fabricating the stiffness-graded FGAM structures and map their deformation behavior (DIC) under stress/strain-based control till failure. Fractography was conducted on the samples to ascertain and correlate fracture mechanisms. Next, the role of interfaces between graded zones were examined to understand how they affect local/global (stress-strain) performance of FGAM structures. Finally, resolution study is undertaken to observe and quantify the R&R of mechanical property variations. Overall, this chapter answers research questions 3 (RQ-3), *i.e.*, “What are the spatial property resolutions achievable in SS 316L via a pulsed SLM?”, research question 4 (RQ-4), *i.e.*, “How do zonal interfaces affect local and global (stress-strain) performance of FGAM structures under various loading modes?”, and research question 5 (RQ-5), *i.e.*, “How do FGAM bulk structures evolve under stress/strain-based control till failure?”

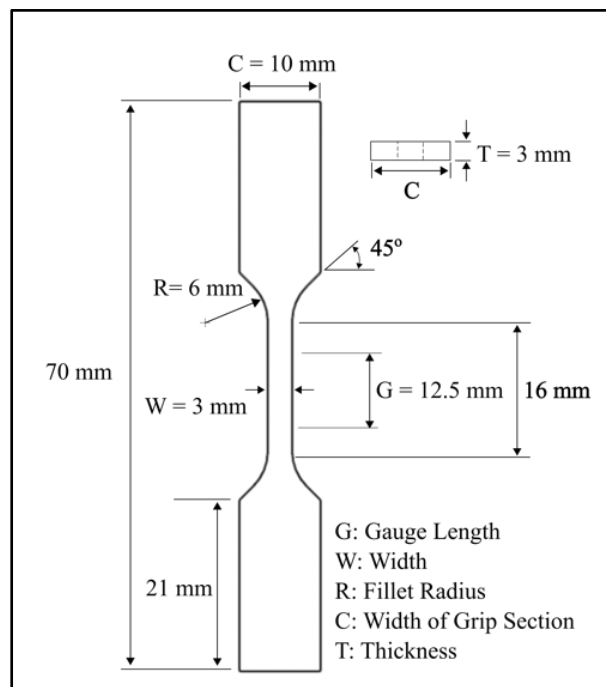
### 7.1 Sample Fabrication and Performance Tests

This part of the study investigates the tensile and fatigue behavior, spatial/temporal strain evolution, and fractography of samples comprised of different-property zones both individually and composites. 2D digital image correlation (DIC) technique has been implemented for FGAM to correlate strain patterns observed in test

samples' graded gauge length. Furthermore, additional mechanical and fracture behavior have been evaluated by designing specific FGAM specimens subjected to four-point bending (FPB) tests. All sample preparations have been based on following the respective ASTM guidelines, maintaining the dimension ratios to yield accurate test results.

### 7.1.1 Tensile Tests

Tensile tests were performed at room temperature following the ASTM E8 guidelines and methodology described in chapter 4 [280]. A representative tensile specimen geometry is shown in Figure 132.



**Figure 132. Dimensions of tensile specimen based on ASTM E8 [248].**

**Table 16. Tensile specimen nomenclatures with hardness and density values.**

<b>Group</b>	<b>Sample</b>	<b>HV<sub>0.5</sub></b>	<b>Density (%)</b>
	209_F		
1	209_M	209	96.35
	209_B		
	256_F		
2	256_M	256	97.23
	256_B		
	271_F		
3	271_M	271	98.21
	271_B		
	294_F		
4	294_M	294	90.78
	294_B		
	318_F		
5	318_M	318	97.5
	318_B		
	260_F		
6	260_M	260	97.2
	260_B		

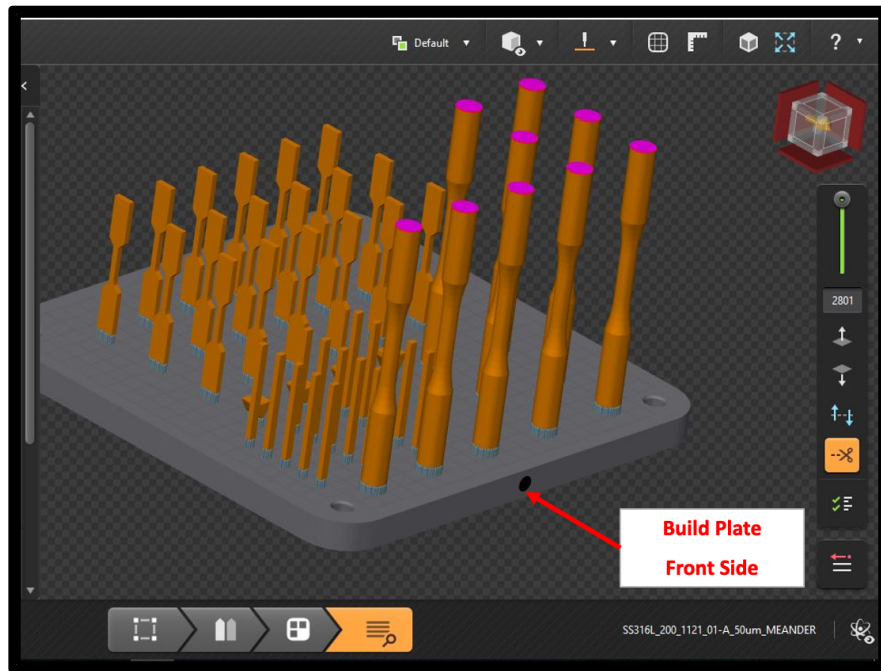


Figure 133. Build plate layout showing sample arrangements.

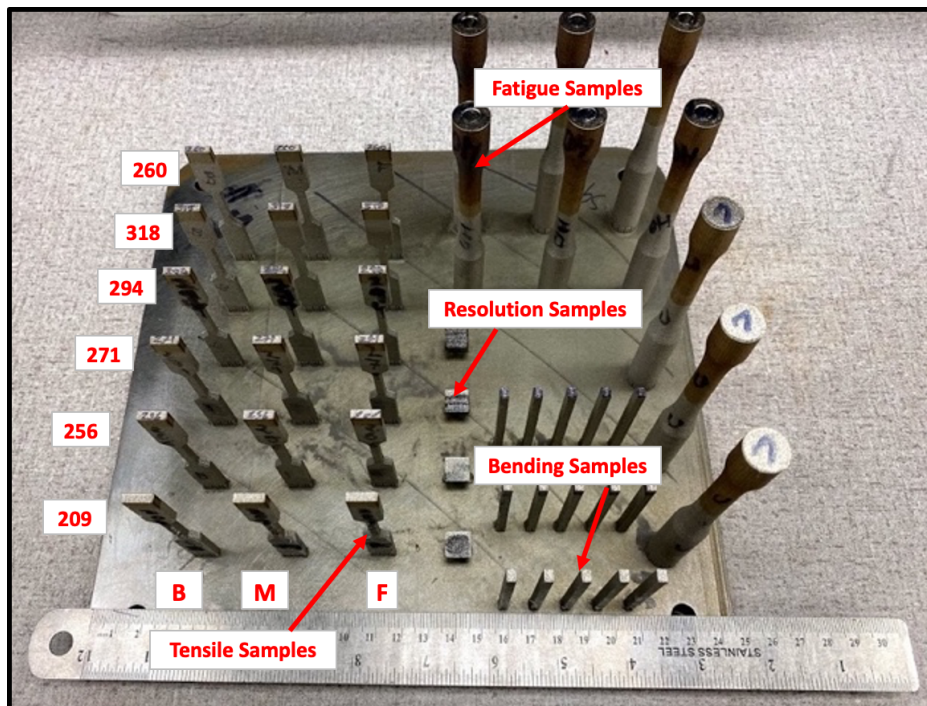
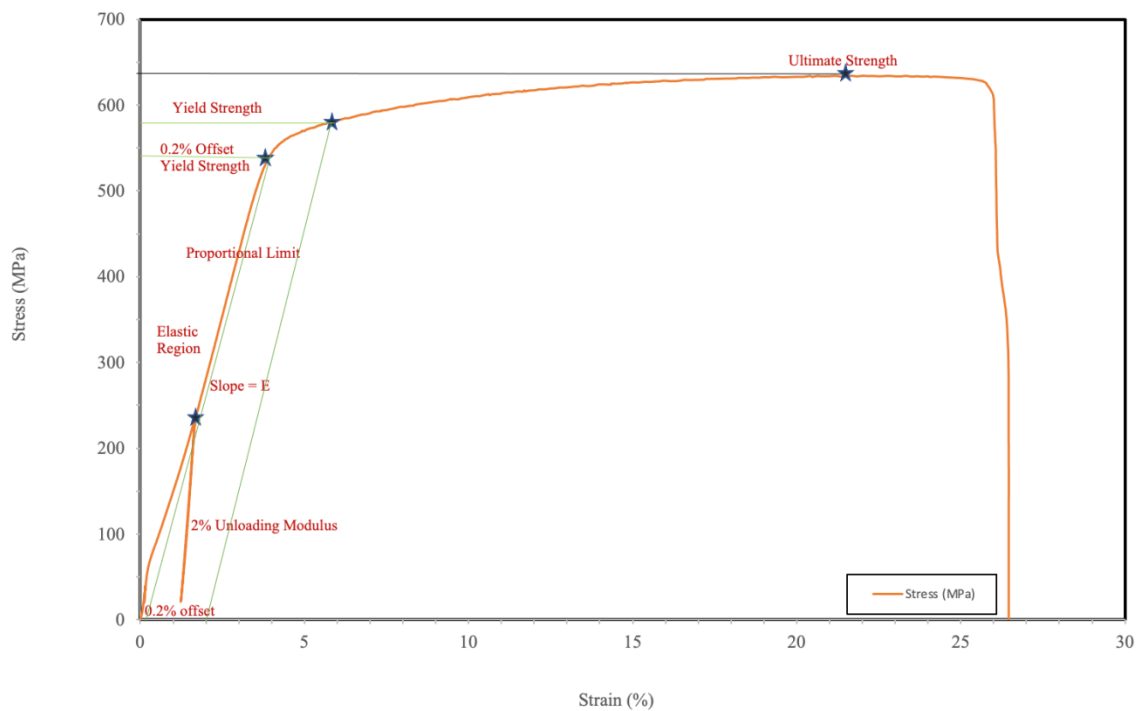


Figure 134. SLM printed SS 316L tensile, bending, fatigue, and resolution samples.



Table 16 provides a summary of six group of samples that were selected for tensile test behavior. Figure 133 illustrates the build plate with sample arrangement. Notice the build plate front side marked with the red color arrow to locate the Front (F), Middle (M), and Back (B) tensile samples. Figure 134 shows as-built SS 316L samples with support structures.

Tensile tests for all 18 samples at room temperature were performed and tensile properties have been obtained. For sake of brevity a detailed tensile property analysis for group 1 sample (209\_F) is presented in Figure 135 and results are tabulated in Table 17.



**Figure 135. Stress-strain plot for 209\_F sample.**

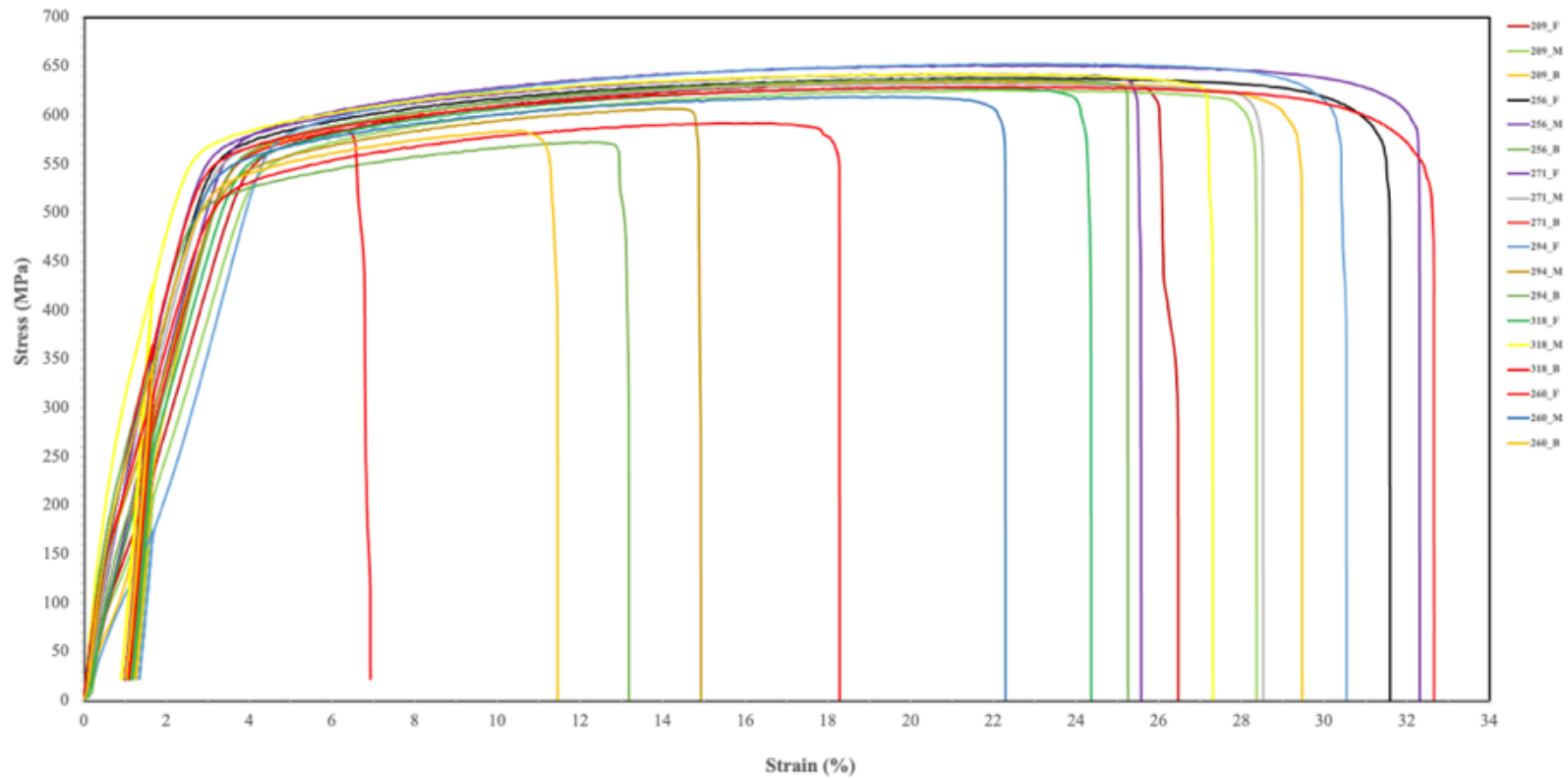


Figure 136. Stress-strain plot for all 18 samples.

**Table 17. Tensile properties for 209 F sample.**

<b>Property</b>	<b>Value</b>
0.2% Yield Strength (MPa)	542.33
2% Yield Strength (MPa)	576.77
Ultimate Tensile Strength (MPa)	634.22
Elongation (%)	26.47
Youngs Modulus (GPa)	34.28
0.2% Unloading Modulus (MPa)	500
2% Unloading Modulus (MPa)	494.83

To ascertain individual bulk mechanical performance, along with determining their spatial property resolutions achievable, all test samples were tested in single run of experiments. Figure 136 illustrates how all 18 samples showed significant variations in UTS, modulus and elongation. Table 18 further summarizes tensile properties.

**Table 18. Tensile performance for six variants across three sample positions.**

<b>Sample</b>	<b>Place</b>	<b>Grp.1 (209)</b>	<b>Grp.2 (256)</b>	<b>Grp.3 (271)</b>	<b>Grp.4 (294)</b>	<b>Grp.5 (318)</b>	<b>Grp.6 (260)</b>
	Front	634.22	638	642.11	652.78	628.44	628.89
UTS (MPa)	Middle	626.11	651.55	632.89	606.78	642.78	619.11
	Back	634.89	572.44	584.78	636.78	591.78	584.11
	Front	34.28	35.45	25.5	15.81	14.14	32.7
Modulus (GPa)	Middle	24.29	24.24	26.67	33.9	53.70	53.70
	Back	16.96	43.24	24.13	40.28	32.22	40.28
	Front	26.47	31.60	25.58	30.55	24.37	32.66
Elongation (%)	Middle	28.37	32.32	28.53	14.93	27.32	22.30
	Back	29.47	13.19	6.93	25.26	18.29	11.46

Table 19 shows the tensile performance comparison for SLM and traditionally processed tensile specimens.

**Table 19. SLM tensile performance when compared to traditionally made samples.**

<b>Parameter</b>	<b>As-cast</b>	<b>Annealed</b>	<b>SLMed 316L (99.9% density) (as-built)</b>	<b>SLMed 316L (99.9% density) (post- processed)</b>
0.2% YS (MPa)	365 ± 22	241	444 ± 27	375 ± 11
UTS (MPa)	596 ± 16	586	567 ± 19	635 ± 17
Modulus (GPa)	200	-	150-200	-
Elongation (%)	69 ± 9	50	44 ± 7	51 ± 3

There are several possible explanations for observing such differences. The first and the foremost is that the vertically build sample typically exhibits a reduction in strength due to boundary layers being perpendicular to the loading direction as opposed to horizontally build samples [274]. This orthogonal alignment between the layers and principal loading direction causes sample to yield prematurely with low elongation and UTS. Next, and the most important reason is the presence of intentionally large porosity

levels due to tailored processing conditions. The wide spreads of elongations were also reported in other similar studies on SLMed 316L samples [281, 282].

There were significant differences across UTS, modulus and elongation across front sample-to-sample. Traditionally as-cast SS 316L has ~200 GPa modulus, 590 MPa of UTS, and elongation of around 70%. The reasoning could be ductility-limiting flaws generated when fabricating these samples and calls for further investigation.

### *7.1.2 Fractography*

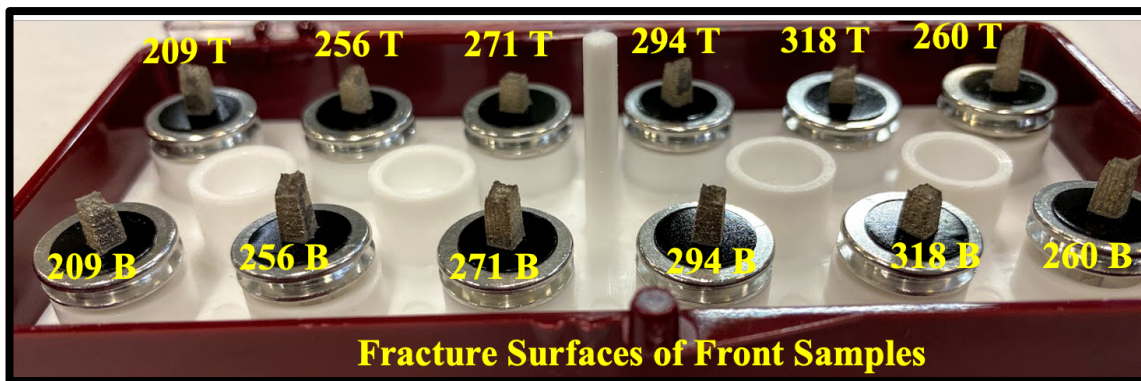
Generally, SS 316L is a low stacking fault energy material with dominant deformation mechanism of dislocation slip [283]. SLM processed SS 316L has shown to produce unique nonequilibrium microstructural features including but not limited to semi-spherical fusion boundaries, large fractions of LAGBs (as high as ~ 57% of total boundaries), local lattice misorientations, elemental segregations (along the HAGBs and cellular walls), precipitates, and impurities [284].

To understand the reduced mechanical performance and characterizing the material performance across the samples, fracture surface examinations were carried out. Figure 137 shows side by side comparisons of front tensile specimens for locating failure regions.



**Figure 137. Side by side comparison of fracture location in the gauge section of front tensile samples.**

All samples showed that fracture was initiated in the gauge length, aligning with ASTM test guidelines. Samples were prepared for fractography as shown in Figure 138.

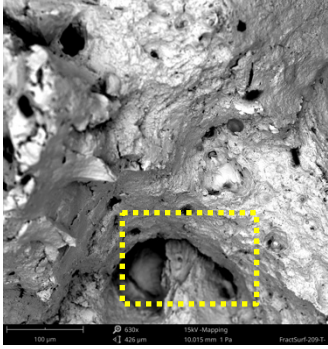
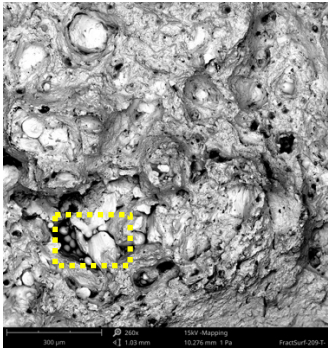

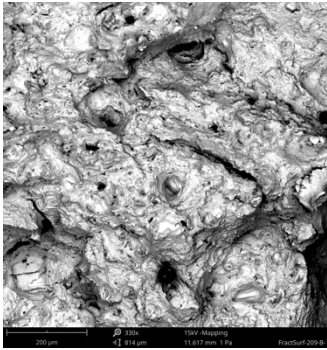


**Figure 138. Fracture surfaces (top & bottom) mounted for six front tensile samples.**

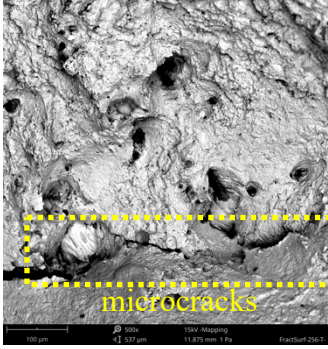
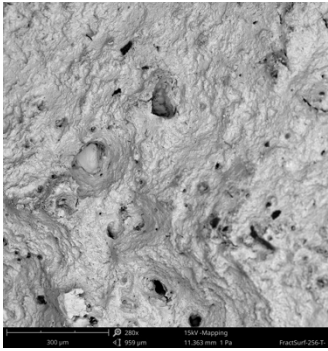
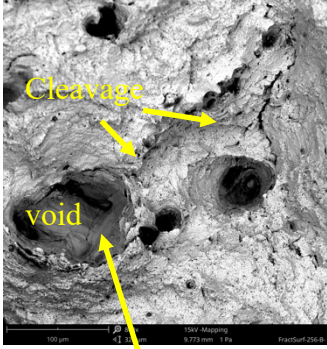
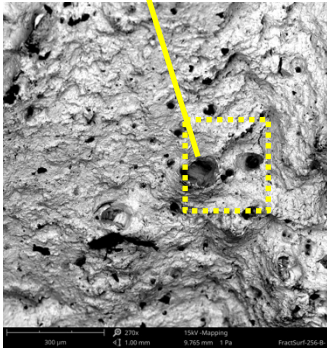
Furthermore, Table 20 illustrates the top and bottom fracture surfaces for each of the six front tensile samples. Several features and defects have been highlighted (with yellow color dotted lines) that were observed across the samples. Table 21 shows the reference wrought SS 316L sample for the comparison.




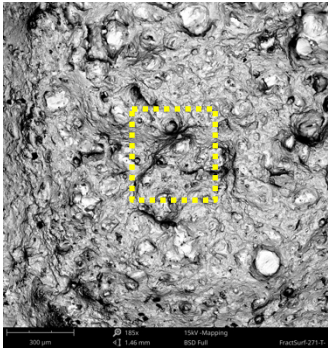
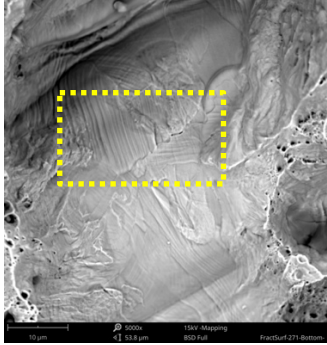
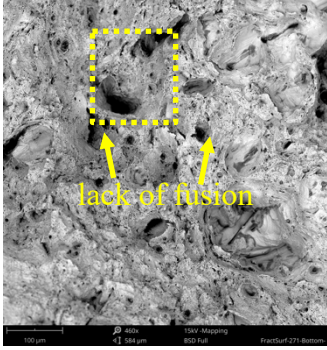
**Table 20. Fractography observations for front 6 samples.**

Sample details	Top surface	Bottom surface
<p>Sample # 1</p> <p>HV = 209</p> <p>Power = 175 W</p> <p>VED = 39.77</p> <p>J/mm<sup>3</sup></p> <p>Density = 96.35 %</p>	 	 
<p>Key observations (meso and macro-level)</p>	<ul style="list-style-type: none"> <li>- Defects at different length scales (tens of microns to a fraction of a millimeter)</li> <li>- Clusters of several unmelted powder particles visible, may be due to insufficient melt pool overlaps</li> <li>- Macro-level pores (~0.1 mm) and large voids, due to process-induced defects, may be important factor in sample failure</li> <li>- Micro-level unmelted powder particles (~20 microns)</li> <li>- Dark color patches of pores in SEM images may suggest presence of non-metallic inclusions, e.g. SiO<sub>2</sub></li> </ul>	

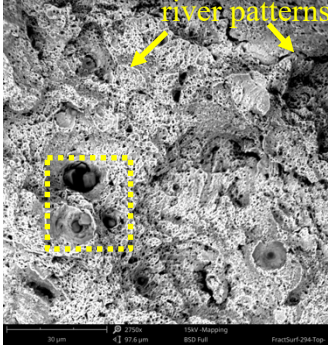
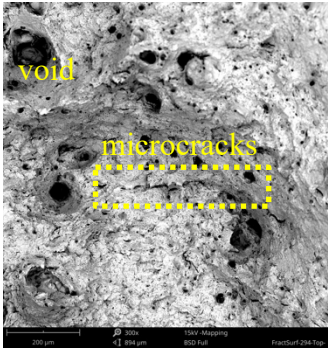
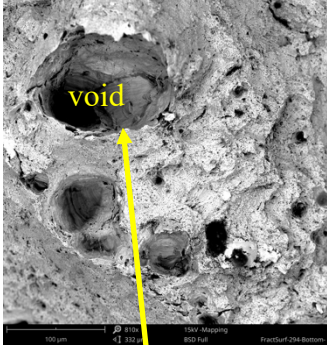
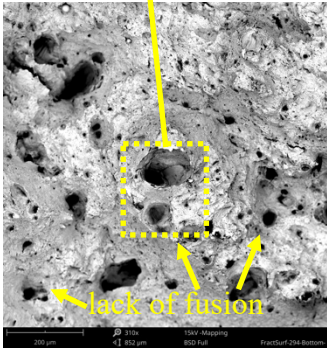
**Table 20. Continued.**

Sample details	Top surface	Bottom surface
<p>Sample #2</p> <p>HV = 256</p> <p>Power = 200 W</p> <p>VED = 63.02</p> <p>J/mm<sup>3</sup></p> <p>Density = 97.23 %</p>	 	 
<p>Key observations (meso and macro-level)</p>	<ul style="list-style-type: none"> <li>- Macro-level pores and large voids (~0.1 mm)</li> <li>- No visible unmelted powder particles</li> <li>- Cracks noticeable around pores/voids</li> <li>- Evidence of secondary cracking, fracture noticeable at different height</li> <li>- Microvoid coalescence mechanism of separation was evident indicating ductile failure mode</li> <li>- Narrow, knife-like fracture line</li> </ul>	

**Table 20. Continued.**

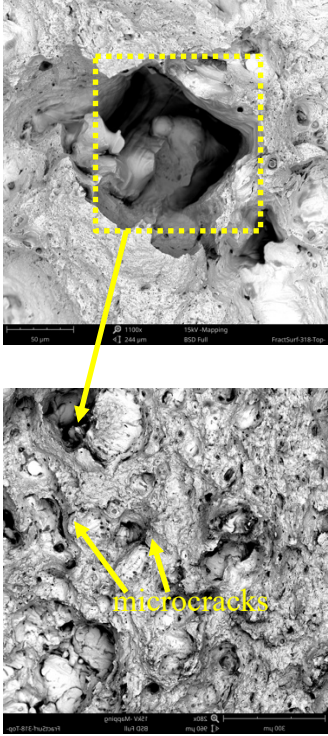
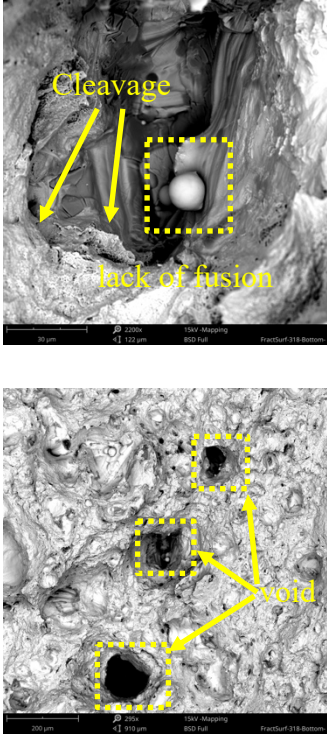
Sample details	Top surface	Bottom surface
<p>Sample #3</p> <p>HV = 271</p> <p>Power = 200 W</p> <p>VED = 48.48</p> <p>J/mm<sup>3</sup></p> <p>Density = 98.21 %</p>	 	 
<p>Key observations (meso and macro-level)</p>	<ul style="list-style-type: none"> <li>- Partially unmelted powder particles (~ 20 microns) present</li> <li>- Micro-pores (~ 10 - 60 microns) present,</li> <li>- Few regions show microvoid coalescence as well as plastic flow</li> <li>- Multiple cracks visible with multiple origins</li> </ul>	

**Table 20. Continued.**

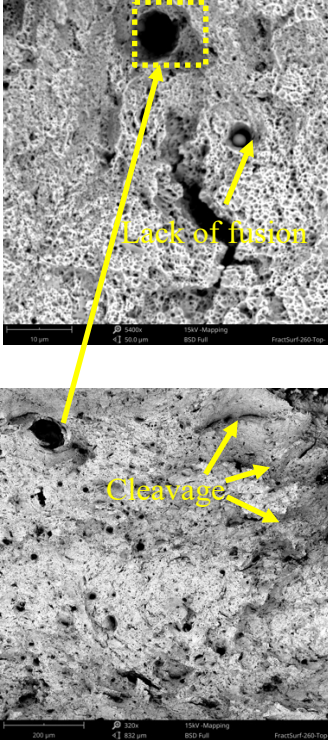
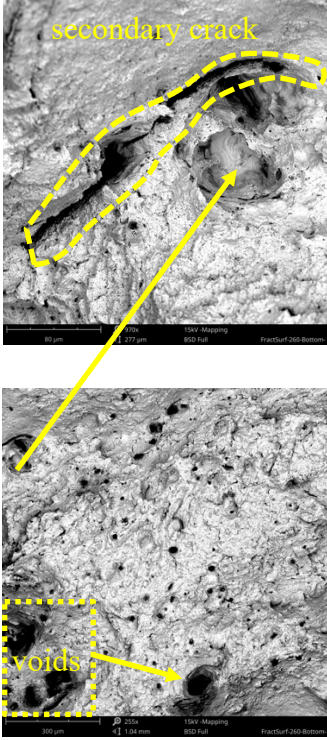
Sample details	Top surface	Bottom surface
<p>Sample #4</p> <p>HV = 294</p> <p>Power = 150 W</p> <p>VED = 34.09</p> <p>J/mm<sup>3</sup></p> <p>Density = 90.78 %</p>	 	 
<p>Key observations (meso and macro-level)</p>	<ul style="list-style-type: none"> <li>- Microvoid coalescence mechanism of separation was evident, indicating ductile failure mode</li> <li>- Defects significant, river patterns indicating multiple crack initiations</li> <li>- Macro-level pores and large voids noticeable (~0.1 mm)</li> <li>- Few unmelted powder particles</li> </ul>	



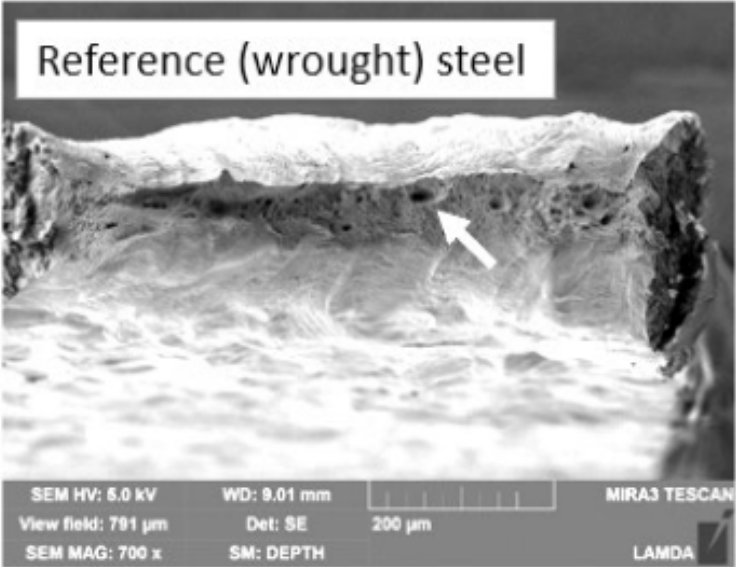
**Table 20. Continued.**

Sample details	Top surface	Bottom surface
<p>Sample #5</p> <p>HV = 318</p> <p>Power = 200 W</p> <p>VED = 52.10</p> <p>J/mm<sup>3</sup></p> <p>Density = 97.50 %</p>		
<p>Key observations (meso and macro-level)</p>	<ul style="list-style-type: none"> <li>- Occasional presence of unmelted powder particles</li> <li>- Large voids of unmelted powder particles, with average size (~ 50 microns) visible</li> <li>- Inclusions may be invisible/hidden under the surface</li> <li>- Pore-nucleated microcracks are visibly present</li> </ul>	

**Table 20. Continued.**

Sample details	Top surface	Bottom surface
<p>Sample #6</p> <p>HV = 260</p> <p>Power = 200 W</p> <p>VED = 55.77</p> <p>J/mm<sup>3</sup></p> <p>Density = 97.19 %</p>		
<p>Key observations (meso and macro- level)</p>	<ul style="list-style-type: none"> <li>- Typical ductile dimple fracture, microvoid coalescence</li> <li>- Evidence of secondary cracking (~ 0.1 mm)</li> <li>- Few unmelted powder particles</li> </ul>	

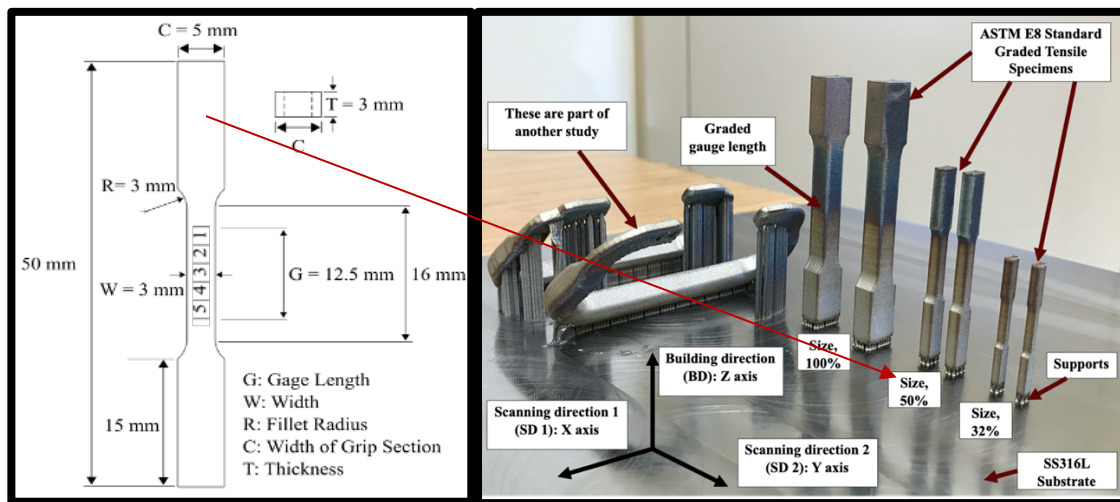
**Table 21. Fractography observations for reference wrought SS 316 L.**

Sample	Top surface
<b>details</b>	
Wrought SS 316L  Study by Byun et al. 2021 [284]	
Key observations (macro- level)	<ul style="list-style-type: none"> <li>- Typical narrow, knife-edge shaped fracture surface</li> <li>- Ductile failure mode, due to large number of dimples/ductile ridges</li> <li>- Less number of pores visible</li> </ul>

## 7.2 Graded Structures Fabrication and Performance

### 7.2.1 Tensile Samples (Normal Stresses)

A selected subset of process parameter combinations was utilized for fabricating ASTM E8 standard tensile specimens with monotonic changes in hardness along its gauge length. Three pairs of standard tensile specimens with different gauge volumes were fabricated: (25 mm x 10 mm x 6 mm) marked as size 100%, (12.5 mm x 5 mm x 3 mm) marked as a size 50%, and (8 mm x 3.2 mm x 1.92 mm) marked as a size 32%, as depicted in Figure 139.



**Figure 139. Dimensions of medium size (50%) tensile specimen in mm based on ASTM E8 [285]. Notice the five different zones having monotonic changes in hardness along its gauge length. Also shown is the picture of the post-build base plate and other relevant details.**



### 7.2.1.1 Comparison of Hardness Measurements

Vickers hardness tests were conducted for each zone as well as at the transitional regions within the graded (tensile) samples, and results were compared with the HV from the original DOE, as illustrated in Figure 140.

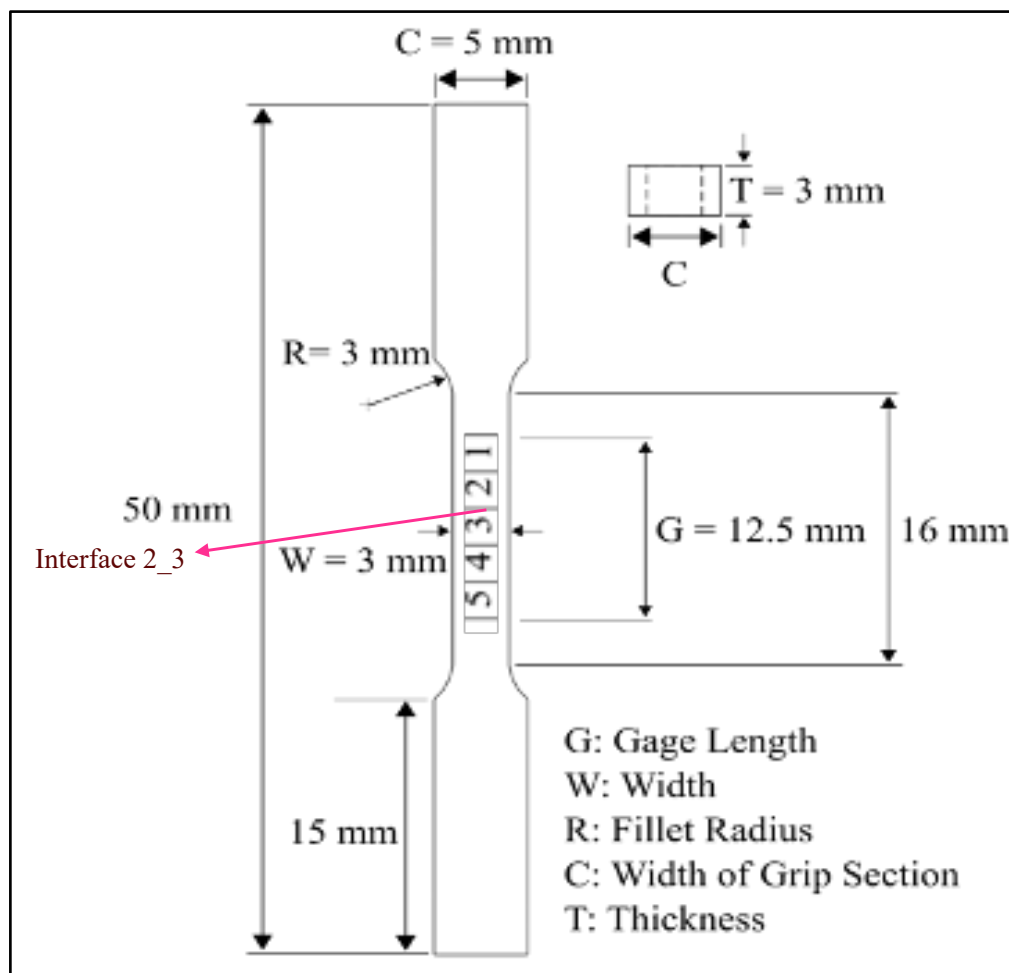
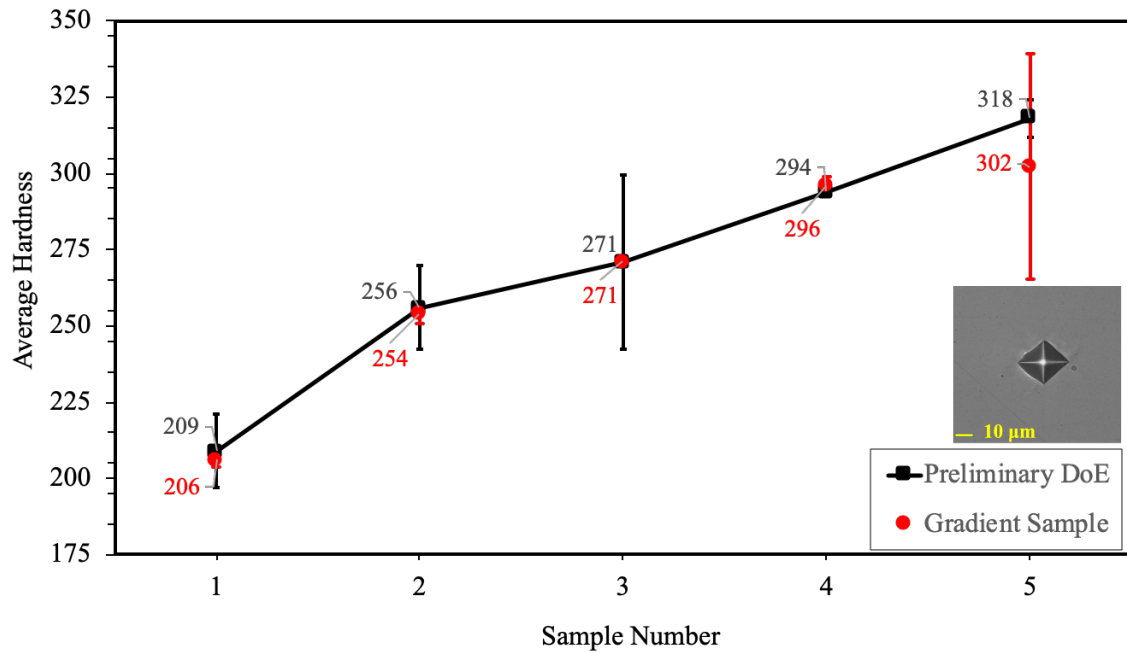


Figure 140. Pre-and post-tensile hardness measurements were taken at the transitional regions (common boundaries between two zones) as highlighted with arrowhead.

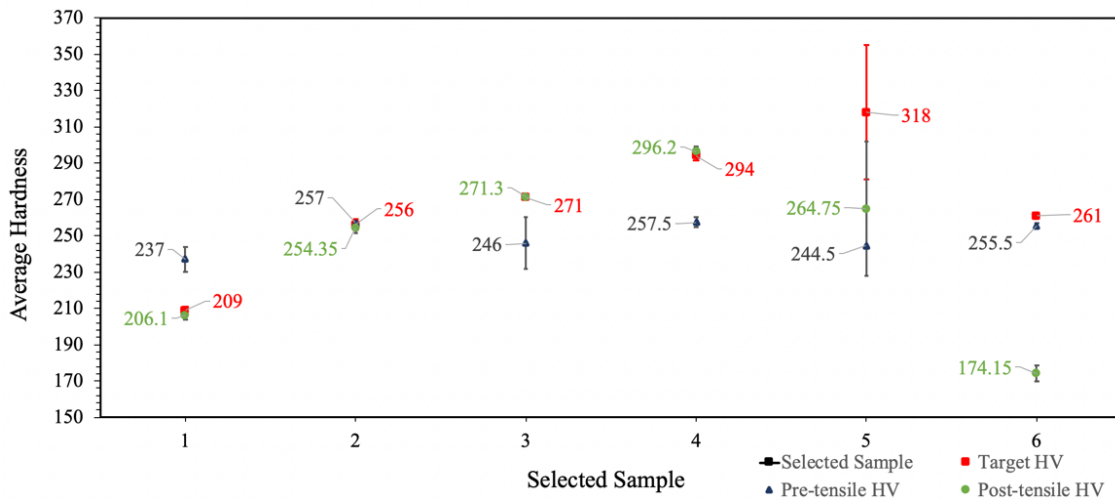


**Figure 141. Comparison of microhardness: the square markers show target, whereas the red circle markers represent data points of the gradient sample for medium size graded sample.**

From Figure 141, it is clear that most hardnesses matched that of the preliminary results (except for sample 5). As noted earlier, SLM part hardness is affected by amalgamation of several phenomena affecting at multiple scales. At macro-scale (porosity), micro-scale (grain morphology including sizes/distributions, dislocation networks, triple junctions, etc.), and nano-scale (atomic crystal defects) [286]. Figure 142 provides comparison amongst hardness of pre and post tensile for medium FGAM sample.

**Table 22. Post-tensile hardness for each zone and interfaces for medium sample.**

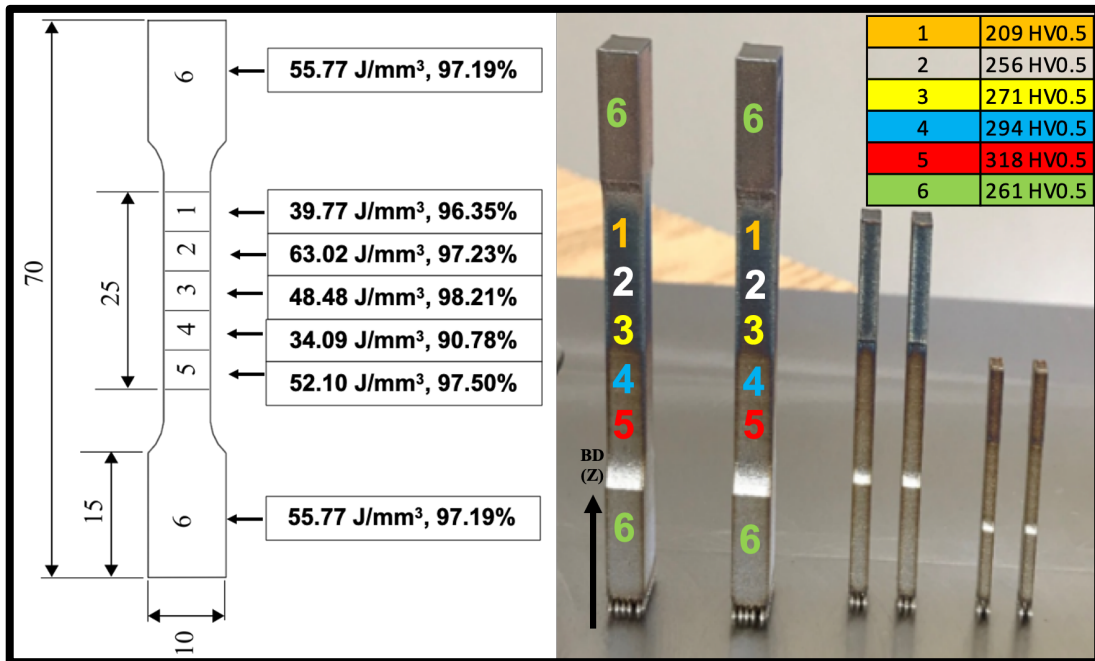
<b>Zone</b>	<b>Avg. HV<sub>0.5</sub></b>	<b>Target HV<sub>0.5</sub></b>
1	237 ± 7	209
1_2	249 ± 13	N/A
2	257 ± 1	256
2_3	228.5 ± 3.5	N/A
3	246 ± 14	271
3_4	240 ± 4	N/A
4	257.5 ± 2.5	294
4_5	214.5 ± 1.5	N/A
5	244.5 ± 0.5	318
5_6	241 ± 8	N/A
6	255.5 ± 1.5	261



**Figure 142. Comparison of microhardness: the red square markers show target, whereas the green circle markers represent data points from post-tensile measurements for medium size graded sample.**

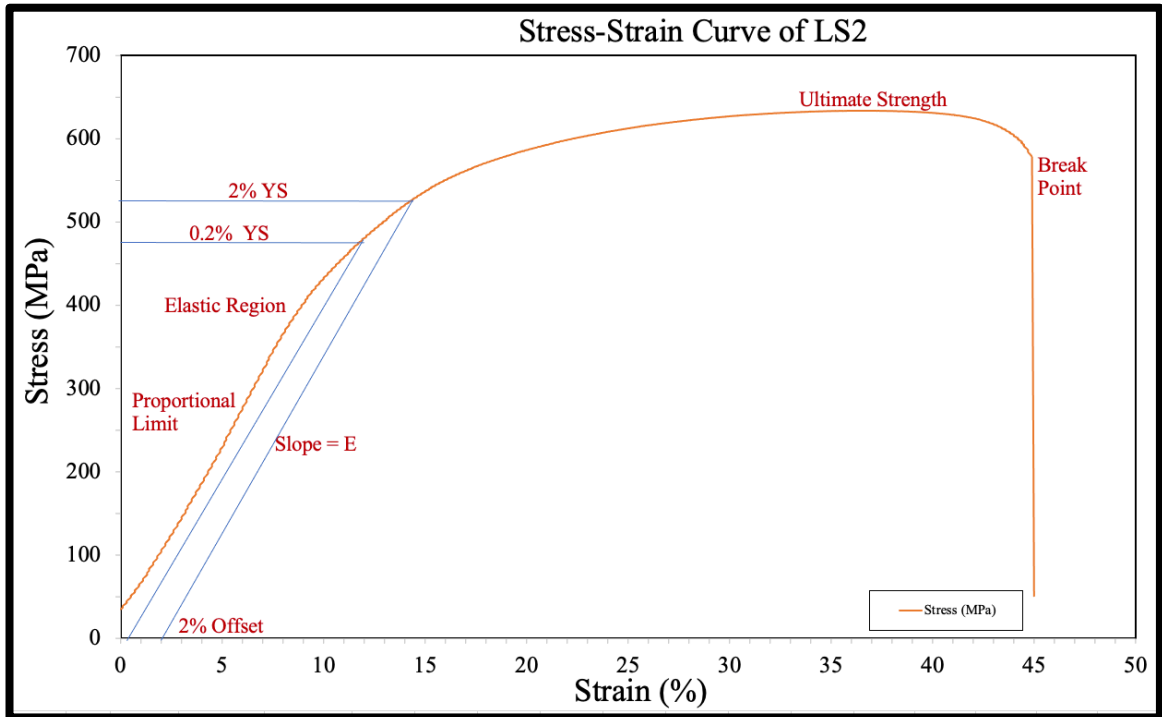
### 7.2.1.2 Tensile Testing & Digital Image Correlation (DIC)

Tensile testing was carried out on the large, medium, and small size samples as illustrated in Figure 143.



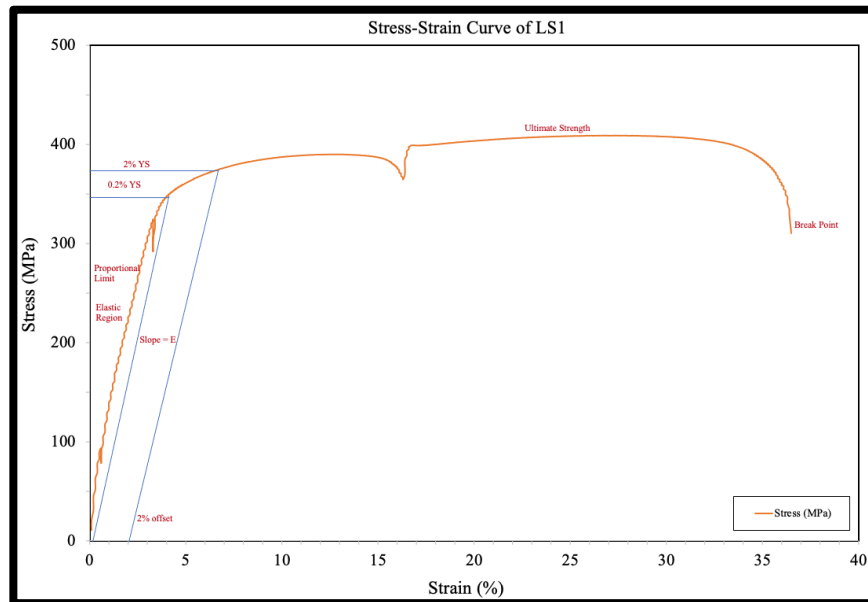
**Figure 143. Location and properties (HV,  $E_v$ ,  $\rho$ ) of different zones highlighted on large samples.**

Figure 144 illustrates the stress-strain curve for the large FGAM sample, showing relatively low UTS, yield strength and elongation when compared to the other SLM 316L samples.



**Figure 144. Stress-strain curve of graded large sample #2.**

From the stress-strain curve of the large composite sample 2, as seen from Figure 144, a linear elastic behavior is observable till a YS of ~535 MPa, with E found to be about 42 MPa. The UTS was ~634 MPa and an elongation at break of 45%. This is expected since graded sample has a gauge volume with composite properties causing it to perform differently. These findings, when compared with homogeneous SLMed SS 316L, in terms of UTS (382-492 MPa) is higher, YS (~442-582 MPa) is closely relatable, whereas the elongation is high (about 12% higher than previous results) but very similar to HIP processed samples (~49 %). Tensile performance for the remaining large composite sample is depicted in Figure 145.



**Figure 145. Stress-strain curve of graded large sample #1.**

**Table 23. Graded sample tensile performance.**

Parameter	MS-1	MS-2	LS-1	LS-2
0.2% YS (MPa)	560.78	572.55	344.39	477.97
2% YS (MPa)	587.13	594.14	372.78	535.25
UTS (MPa)	641.69	650.07	409.09	633.82
Modulus (GPa)	36.57	117.75	78.86	42.97
Elongation (%)	56.60	52.31	36.50	45

Table 23 summarizes the tensile property parameters of the medium sample (MS) and large sample (LS) determined from the stress-strain data obtained during the uniaxial tensile testing. The strength (YS, UTS) and ductility (Elongation) parameters for the two tests for each MS and LS variants demonstrates a variability in terms of mechanical behaviors due to differences in gauge length processing conditions. As reported by Byun et al. [284] YS signifies the strength of the material in early plastic deformation region and should be carefully considered as it is typically sensitive to the defect density as well as its distributions, and that microstructure-dependence of UTS is smaller than that of YS. One of the regions (zone-4) in the gauge length has processing parameters that showed significant porosity and LOF defects (confirmed in the tensile postmortem analysis).

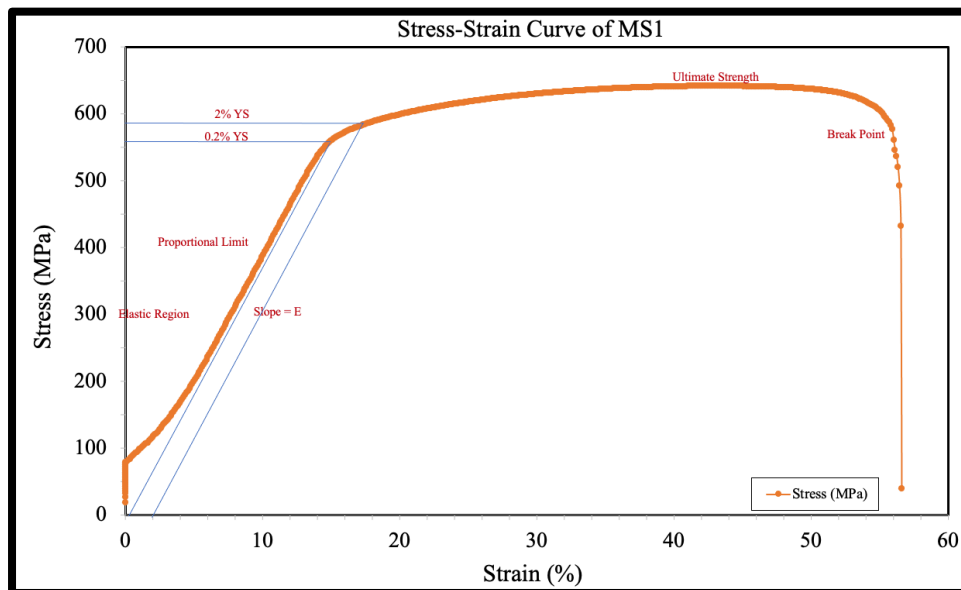
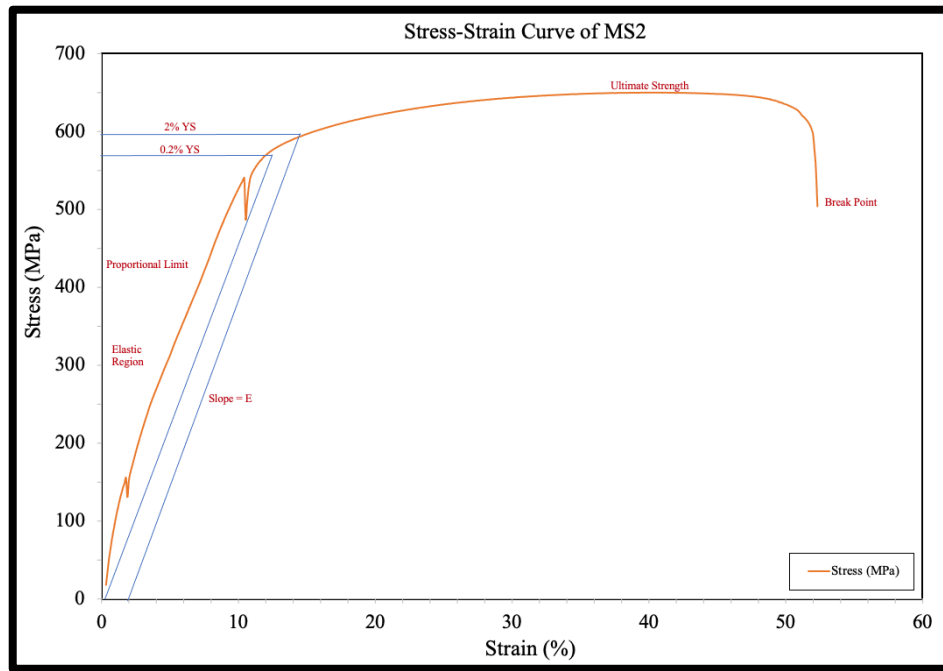


Figure 146. Stress-strain curve of graded medium sample #1.



**Figure 147. Stress-strain curve of graded medium sample #2.**

Figure 146 and Figure 147 shows tensile performance of both medium graded samples. The UTS, elongation and 2% yield strength matched between them, however, the modulus were inferior for sample 1. It could be due to the initial slippage experienced by the sample within the jaws. Generally, the observed values across samples were higher for UTS and YS, with about 10% decrease in average elongation at break, when compared to traditionally-made samples.

Moreover, both large samples revealed the evolution of the similar strain patterns as shown in Figure 148. Successive strain build up is depicted at different time intervals within the stress-strain curve for a large sample 2 is shown in Figure 149 and depicted via successive DIC images in Figure 150.



A region of interest (ROI) was selected enclosing the entire gauge length (fillet to fillet) to evaluate the strain induced in the longitudinal direction.

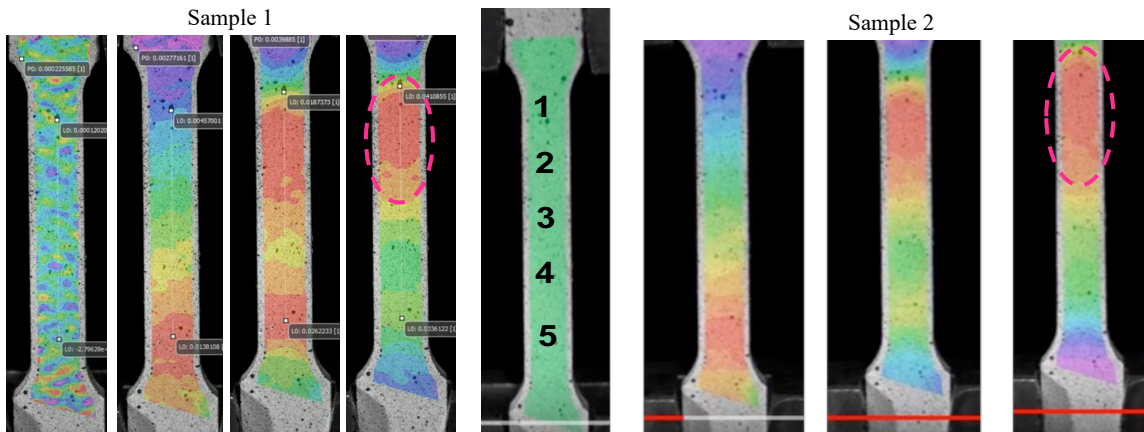


Figure 148. DIC images of longitudinal strains across the graded gauge length of sample1 and sample 2 are shown. Highlighted marks showed the similar behavior of maximum strain regions.

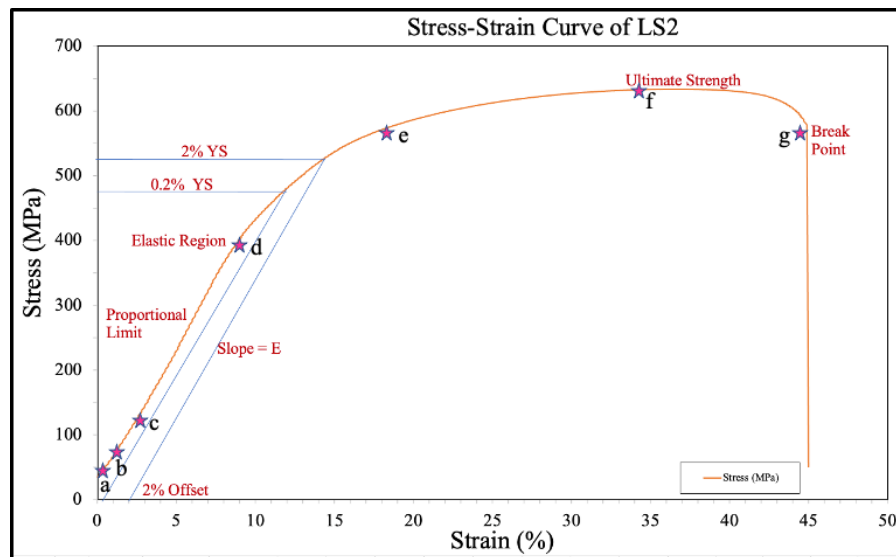


Figure 149. Stress strain curve for graded large sample 2 with highlighted points indicating maximum localized strains captured via DIC during the test.

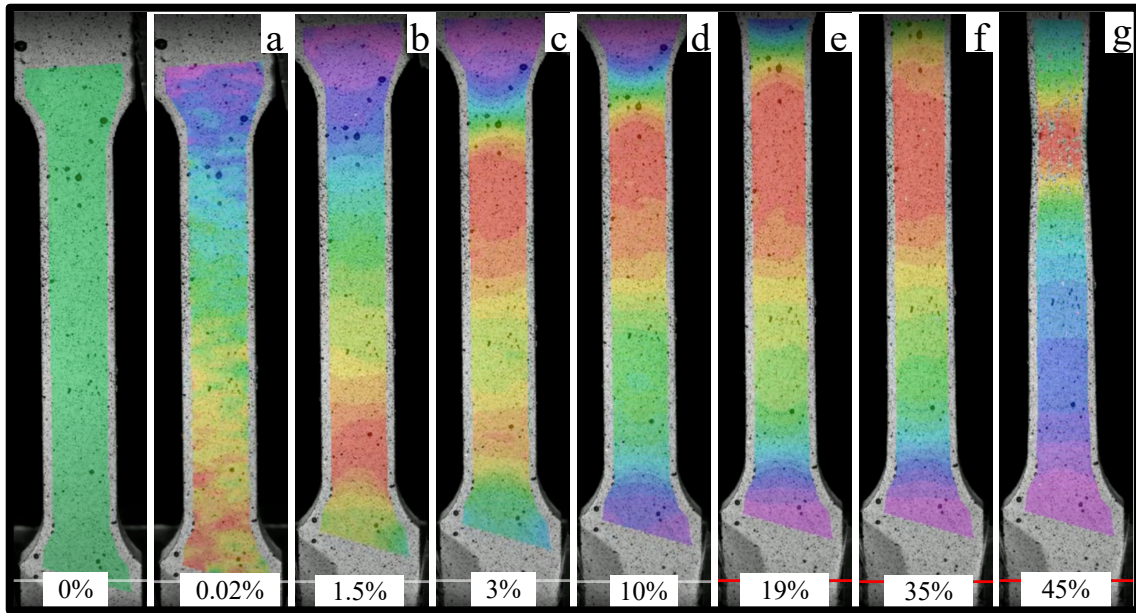


Figure 150. Successive DIC images of longitudinal strains in % of the large sample of highlighted points on the stress-strain curve.

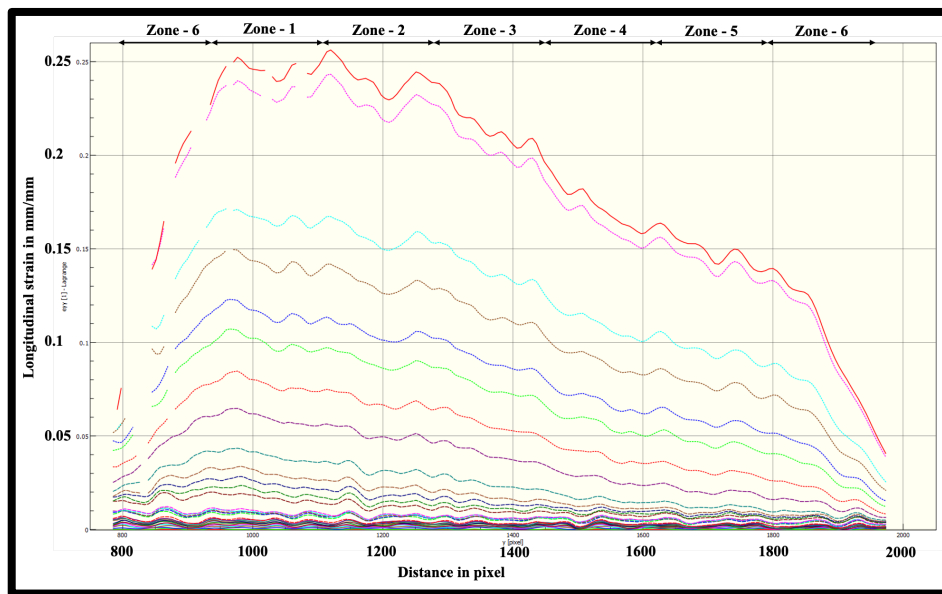
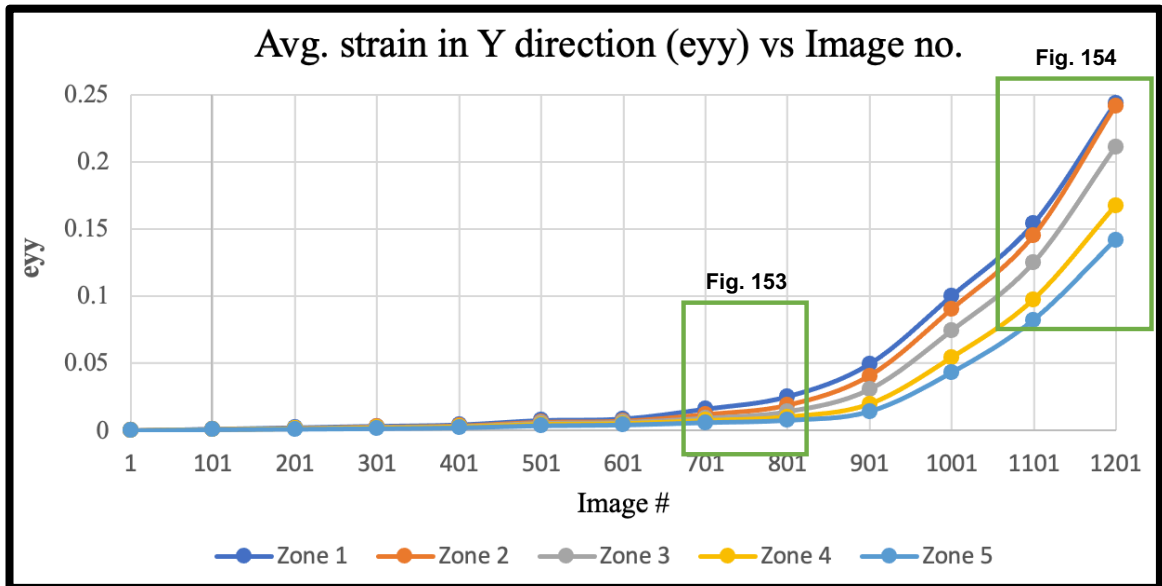


Figure 151. Temporal strain evolution induced in each zone (shown as pixels) during the tensile test until 26% global strain.

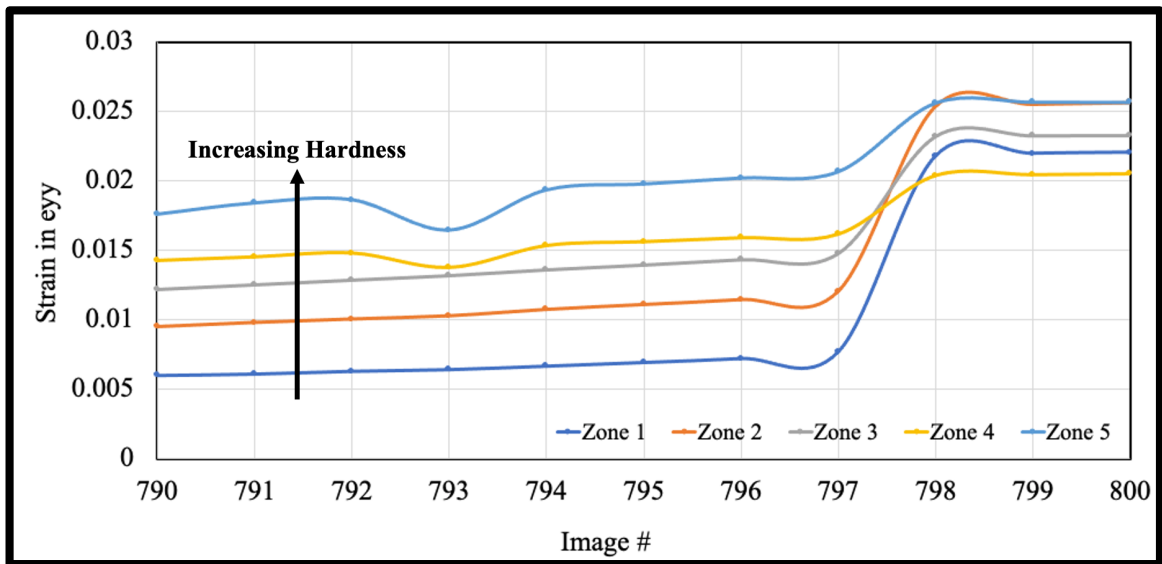
As seen from Figure 151 different line colors indicate different strains during different test instances. As the test progressed, the maximum-strained regions shifted across the zones. Up until ~1-2% strains all zones showed direct correlation to their individual hardness. After that, the strain in zones shifted due to combination of factors such as density, modulus, phase fractions, as well as microstructures. These trends have been captured and represented in Figure 152.



**Figure 152. Zone-wise temporal strain evolution induced in each of the five zones. Highlighted regions in green color showed shifts in strains during the test.**

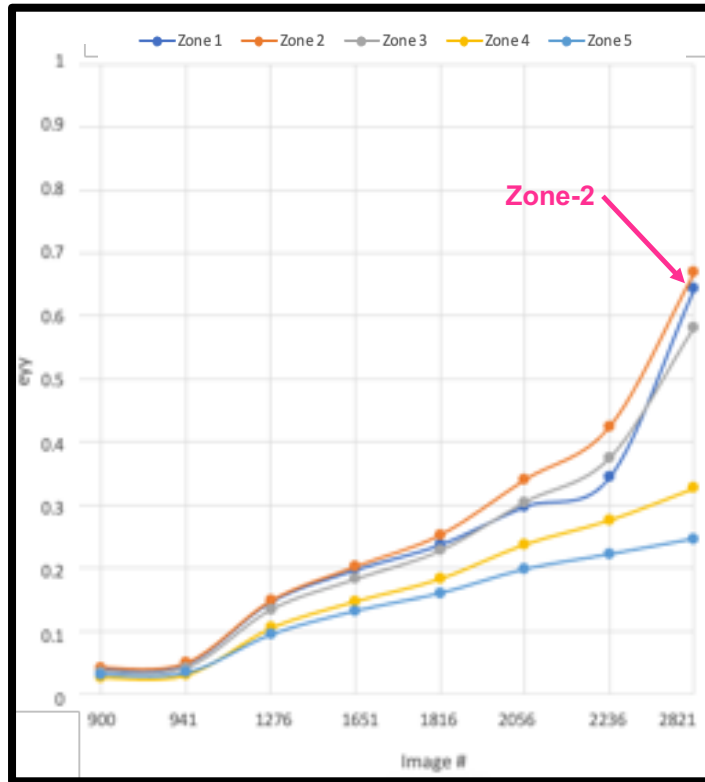
Figure 153 and Figure 154 represents the highlighted trends wherein zones of highest strain shifted from 5 (maximum HV) to 2 (maximum nano E) as the test progressed, eventually failing within zone 2. As noted earlier, the observed response could be due to the influence of several different property characteristics (density,

hardness, thermal histories, microstructures, phase fractions etc.) attributed to each zone and their unique processing conditions.



**Figure 153. Temporal strain evolution (jumping around) across the five zones during the elastic regime of tensile testing.**

Moreover, as seen earlier that imparting different VED, significant variations in microstructure have been obtained. These processing variabilities have, for example, altered the cooling rates within each zone. With decreased cooling rates, grains have more time to grow in a preferred crystallographic orientation [198]. Conversely, finer (smaller) grains form due to higher cooling rates. This suggests potential differences in strain hardening responses across zones with different original properties (among other phenomena). Similar indicators were also observed in the subsequent fractography analysis.



**Figure 154. Zone-2 induced the maximum strain at the end of tensile test.**

It is common to observe high levels of scatter amongst mechanical properties measured for SLMed parts. Such variations are inherent to both controllable and difficult to control parameters, such as, scan strategies, build directions, SLM machine platforms, etc. For tensile testing, the build orientation plays a key role in the obtained desired properties. Vertically built samples are found to have a lower tensile strength during vertical loading than that of horizontally built samples [156]. In addition, the performance comparison across the samples fabricated on the continuous laser to the modulated laser beam should be carefully considered. This is due to the underlying melt pool formation which is different in each case.

Moreover, to understand the interlinkage between tensile performance and feature sizes, Roach et al. [287], investigated 153 samples of different sizes and reported that yield strength (YS), ultimate tensile strength (UTS), and modulus (E) generally decreased with decreasing specimen size. They also found surface roughness (due to geometry) as a critical factor that increased stress concentrations and hence triggered fracture.

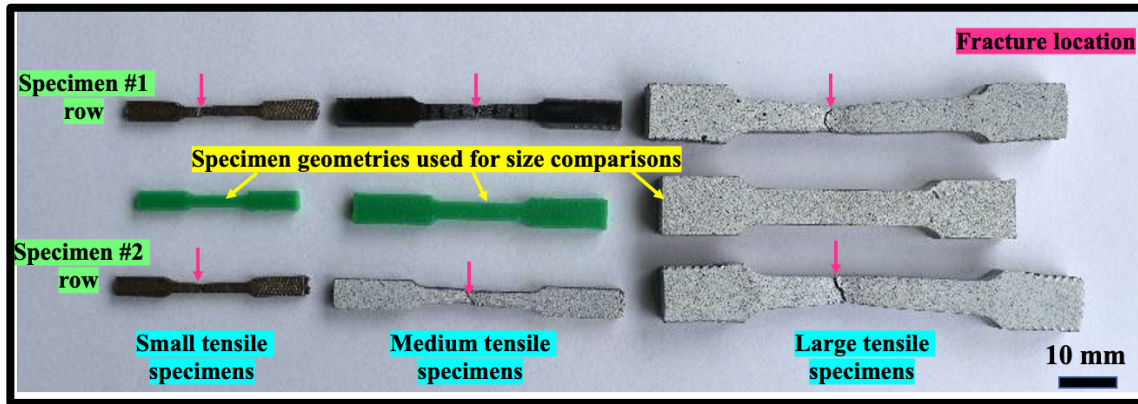
A brief comparison of different results from previous studies that reported the tensile performance of SLM processed homogeneous SS 316L are summarized. Donik et al. [116] used an AconityMINI SLM platform, and varied laser power (between 150 to 350 W) and scan speed (between 400 mm/s to 800 mm/s) to fabricate quad coupons in vertical direction (converted in Metric ISO thread M6 test probes). They reported results (average of three tests) and found YS (582-606 MPa), UTS (691-715 MPa), and elongations (26.4-33.4 %). Ilie et al. [227], used Renishaw SLM 125 to vertically build three sets of tensile samples (ASTM E8) with laser power (150, 175, 200 W) and corresponding exposure time (93, 80, and 70  $\mu$ s) while maintaining constant VED. With around 3% porosity variations across the samples, giving 0.2% yield point (442-582 MPa), UTS (382-492 MPa), and elongation (17-26 %). Lavery et al. [145], used Renishaw AM250 machine to fabricate 42 rectangular and 6 cylindrical tensile bars with scan speed of 590 mm/s and VED of 49.13 J/mm<sup>3</sup>, giving UTS as-built ( $469 \pm 72$  MPa), UTS post HIP ( $513 \pm 49$  MPa), and elongation for as-built ( $21.83 \pm 12.4$  %) whereas elongation for post HIP ( $40.89 \pm 9$  %) for vertically built samples. In other relevant study, Zhang and coworkers [288] used MCP Realizer SLM250 system with vertical and

horizontal samples, resulting in modulus (E) (150-200 GPa), UTS (500-600 MPa) and deformation exceeding 10%. Recently, Chadha et al. [289], reported 130% increase in ductility of as-built samples when post-processed with a combination of HIP and annealing heat treatment without scarifying UTS.

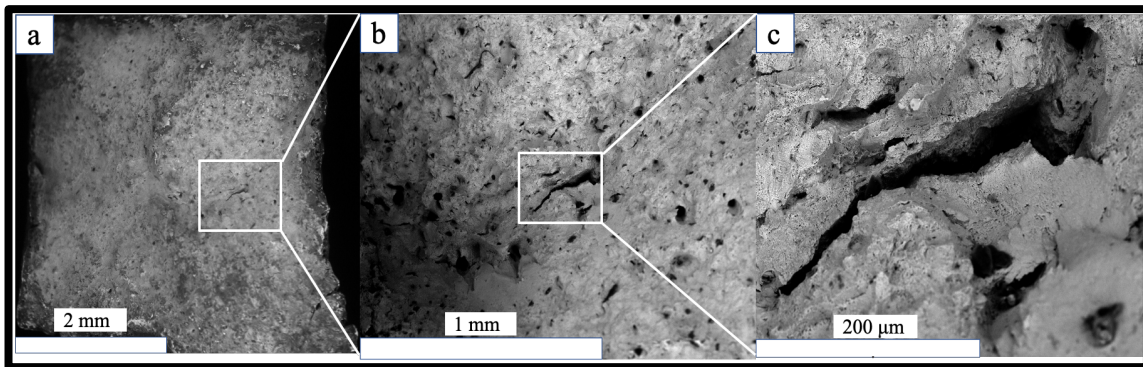
Conventionally processed (wrought, sheet or rolled) SS 316L (with relative density of 7.79-7.97 g/cm<sup>3</sup>) results in E (~193-196 GPa), UTS (~550-560 MPa), YS (~230-235 MPa), and elongation of (55 ± 2 %) [290-292]. However, Hutchinson [293] reported a drastic decrease in the value of E (~101 GPa) for SS 316L having [001] texture orientation. According to Li et al. [294], SLMed 316L tends to show anisotropy in the YS and UTS in comparison to wrought material, however, the elongation till break is about 45% lower than for the rolled material.

### **7.2.1.3 Fractography**

The size comparison between the pre- and post-tensile samples are presented in Figure 155. A representative specimen for each configuration is placed in the middle for size comparison. Across all samples, reasonable agreement is witnessed for the maximum-strained region and location of fracture.



**Figure 155.** Size comparison post-tensile test amongst different sample sizes. Notice the fracture location highlighted by the pink arrowheads.



**Figure 156.** Fracture morphologies of large tensile sample tested along build direction (a-b) low magnification and (c) high magnification views on the fracture surfaces. River marks are visible along with pores.

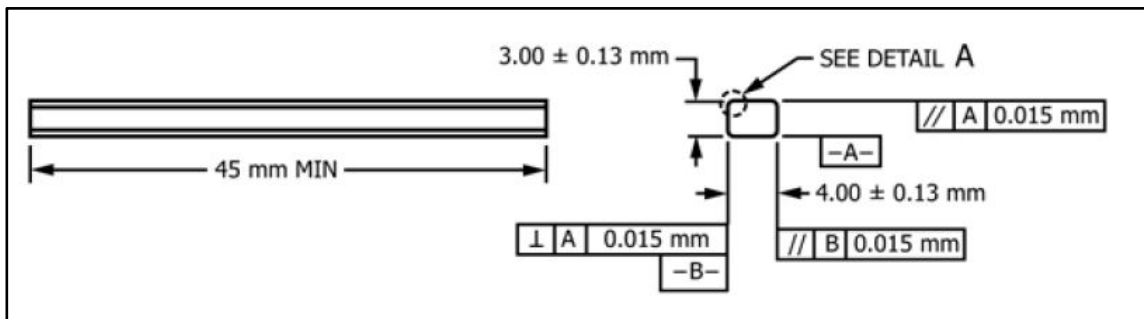
The fracture morphologies of large tensile sample are shown in Figure 156. The close-up view shows a typical ductile mode of failure. This kind of localized stress arises due to presence of pores and other unmelted regions that introduces a reduction in effective cross-sectional area and eventually increase the structural heterogeneity [262]. The magnified view shows a river marks indicating the direction of crack growth which



was along the build direction. The fracture surface also showed the process induced defects (LOF porosity, unmelted powder particles) indicative of high scanning speed used during the processing.

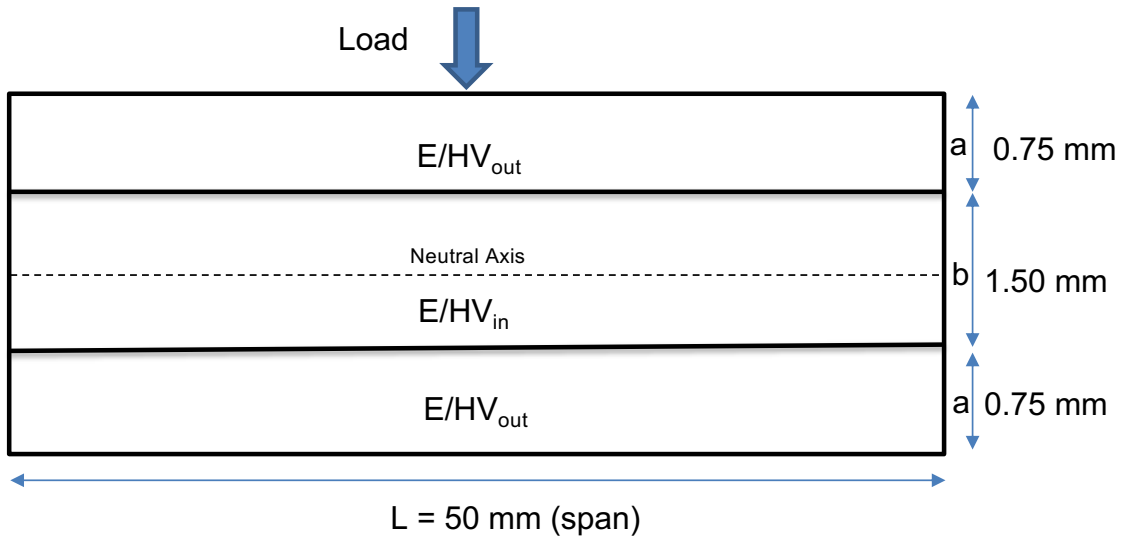
### 7.2.2 Bending Test with DIC

Four-point bending (FPB) tests performed on the homogeneous (with uniform property) and graded (with graded properties) specimen with the same dimensions of length×width×height (L×B×H) =50 mm×4mm×3mm. FPB test were conducted in accordance with the ASTM C1161-18 standards to investigate the behavior of as-printed SLM SS 316L FPB samples as illustrated in Figure 157.

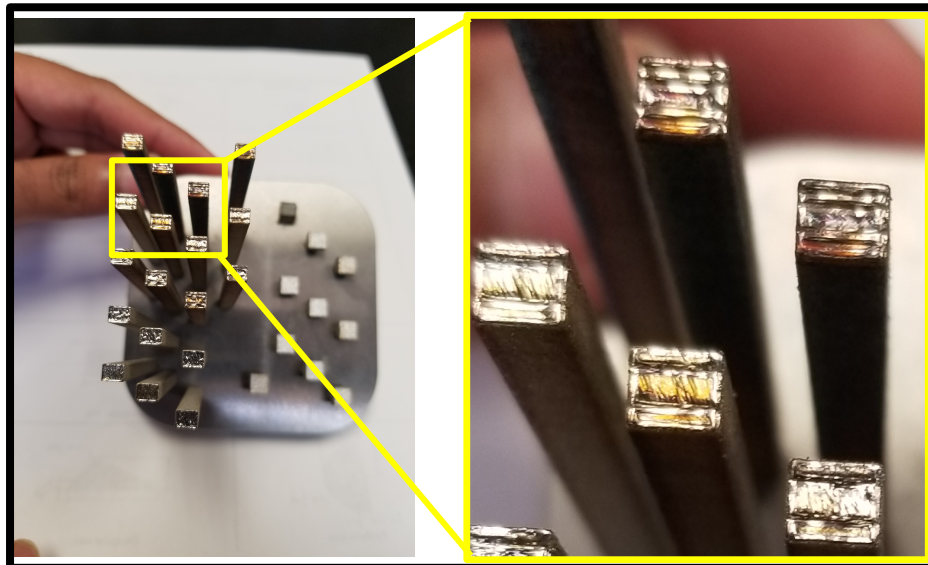


**Figure 157. Dimensions of FPB samples as per the ASTM C1161-18 [251].**

The homogeneous samples were designed to have the uniform properties in each of the outside and inside regions, whereas the graded samples had different hardness/modulus (HV/E) properties between the inside and outside regions of the samples as illustrated in Figure 159.

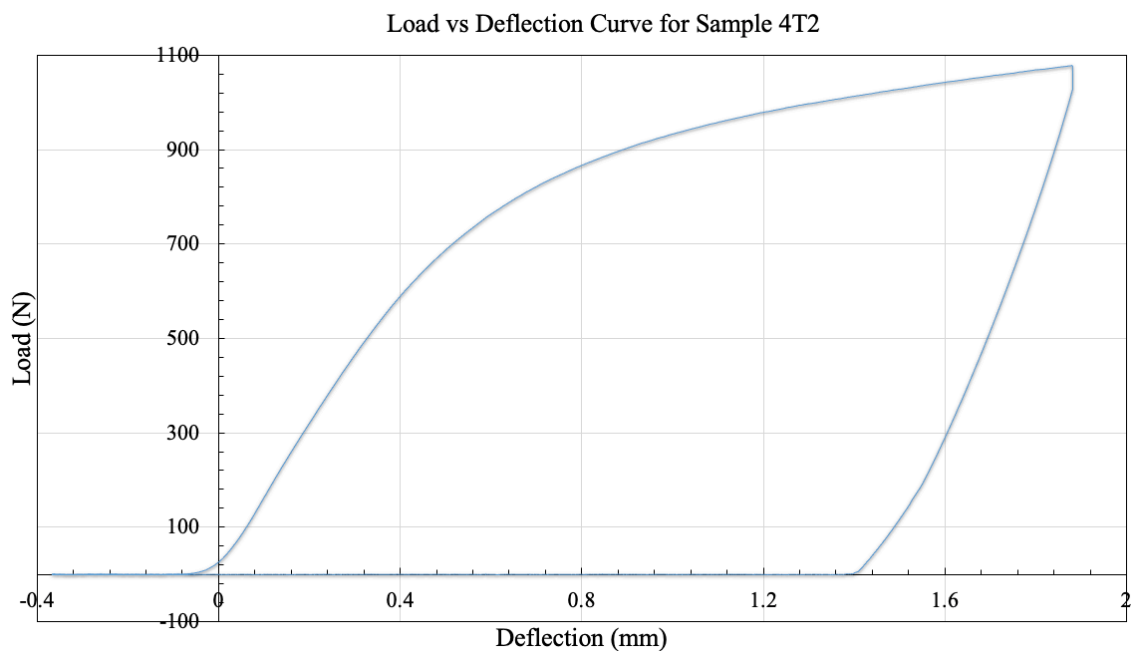


**Figure 158. Schematic representation of the FPB test. Regions denoted with a and b were graded with select process parameters.**



**Figure 159. As-printed homogeneous and graded FPB specimens. Notice the outer and inner regions with different properties.**

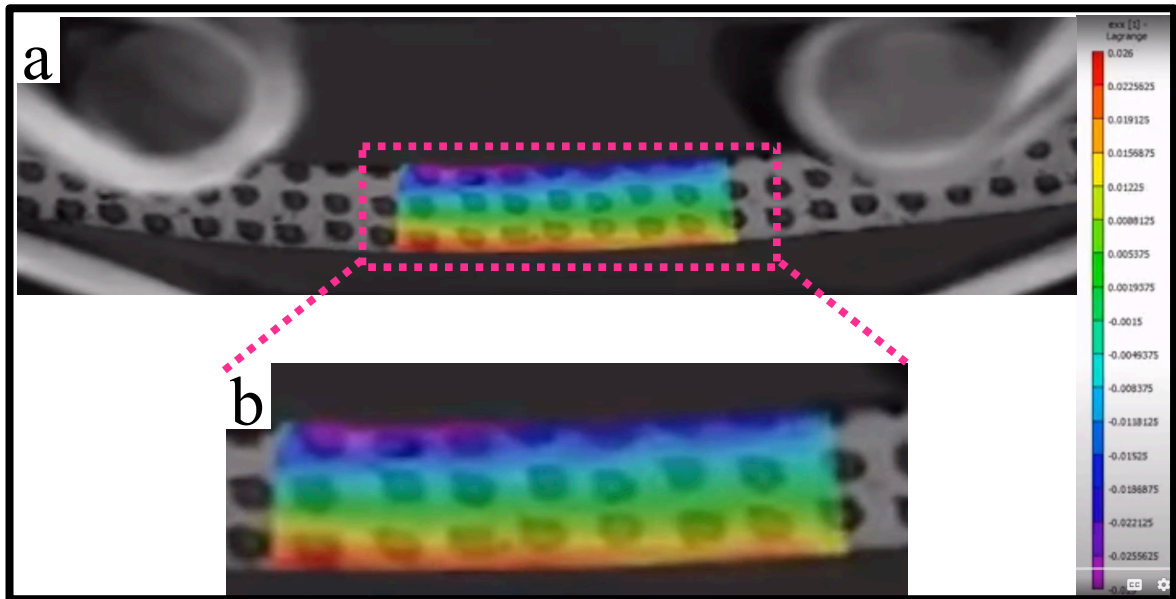
Figure 159 illustrates the vertically built as-printed FPB specimens with different property arrangements on build plate. There were total of 18 samples with different configurations were built for FPB test. As can be observed from Figure 160, load-deflection curve of sample 4T2 was loaded up to the peak load and subsequently unloaded. Throughout FPB test, sample showed little divergence thereby establishing good repeatability and bulk behavior. In general, results showed the consistency of FPB test procedure employed.



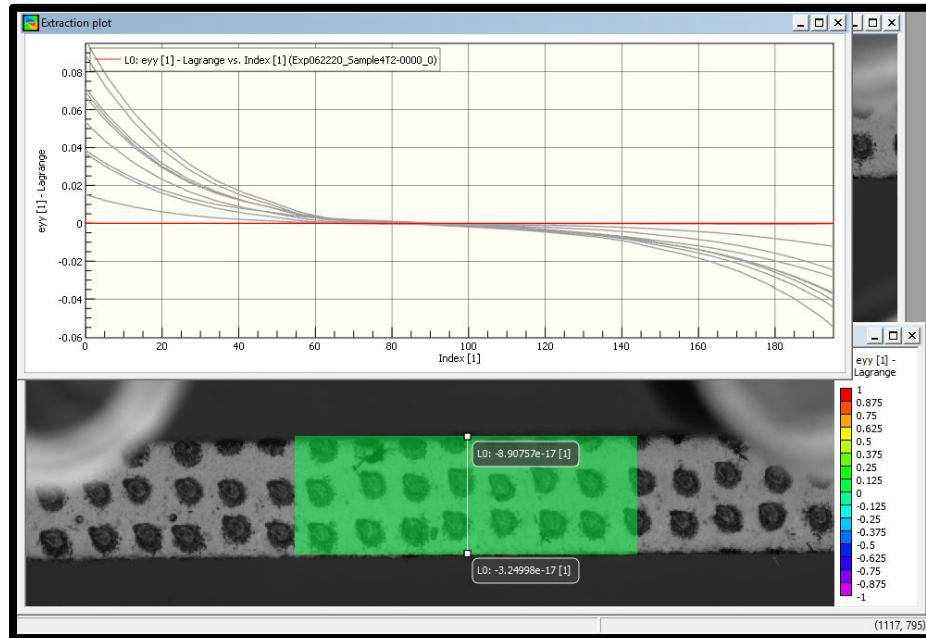
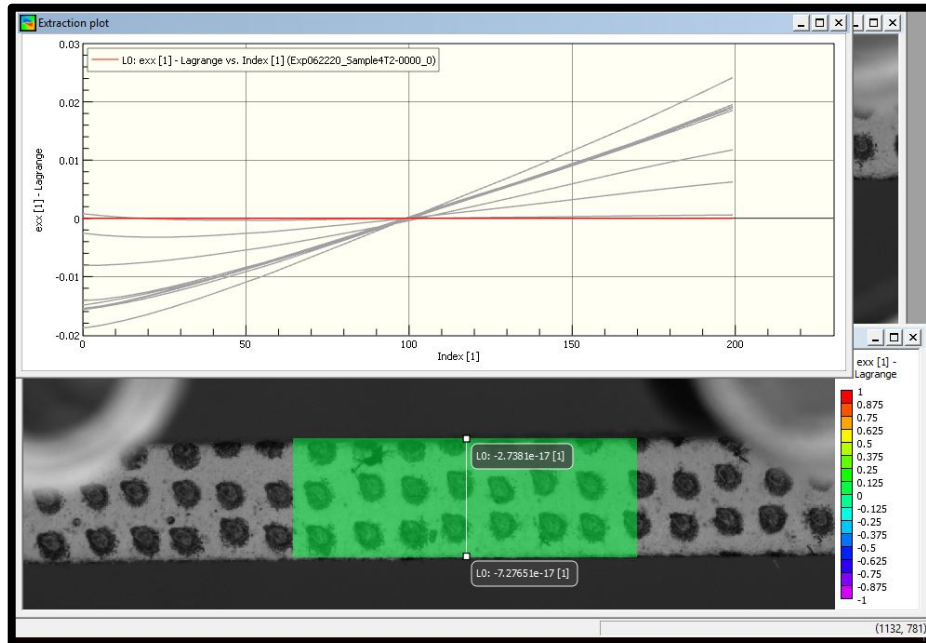
**Figure 160. Load-deflection curves for FPB sample 4T2.**

Furthermore, to showcase the feasibility of gradation, one composite sample 4T2 (combination of parameters used in processing sample 2 and sample 4) and its analysis in both Exx and Eyy directions have been provided. Figure 161 represents the selected

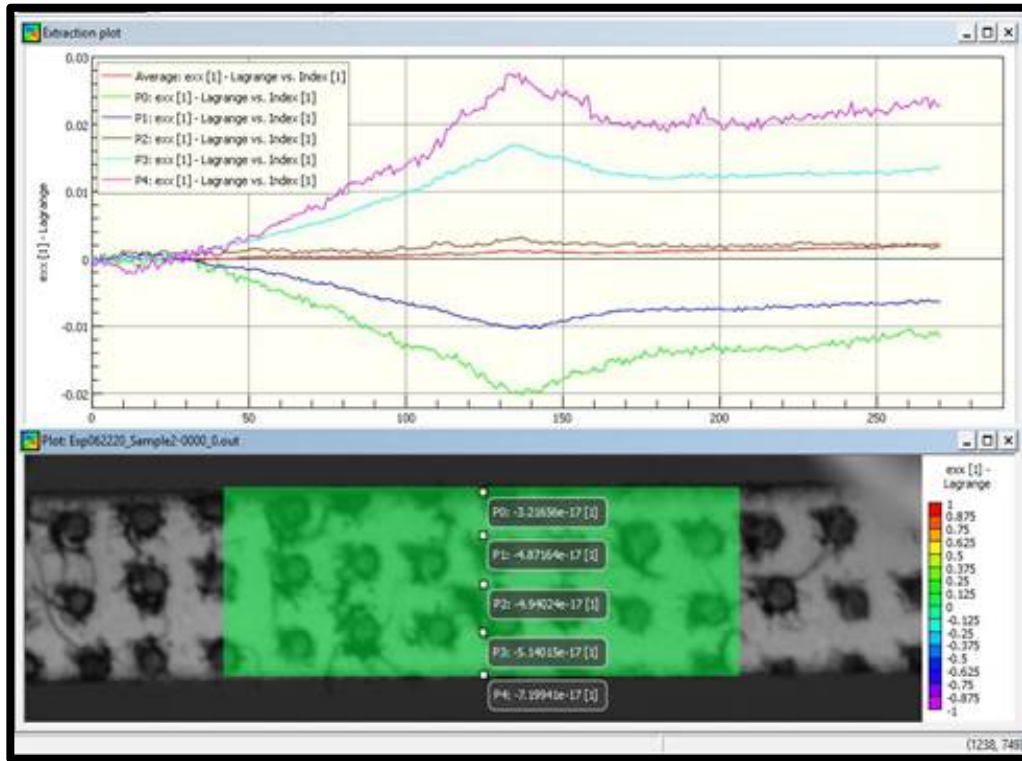
ROI in central area of the sample (to capture pure bending) for DIC analysis and progression from beginning till the end of test for sample 4T2.



**Figure 161. DIC image of sample 4T2 from (a) during the test (b) bands of different colors shows the strains in Exx direction during FPB test. Note the transition from tension (red color) to compression (blue color) at the bottom and top of the beam, respectively.**



**Figure 162. Line analysis and strain distributions of sample 4T2 in (Top) Exx direction and, (Bottom) Eyy direction during FPB test. Note the lines were symmetrical with respect to the neutral axis.**

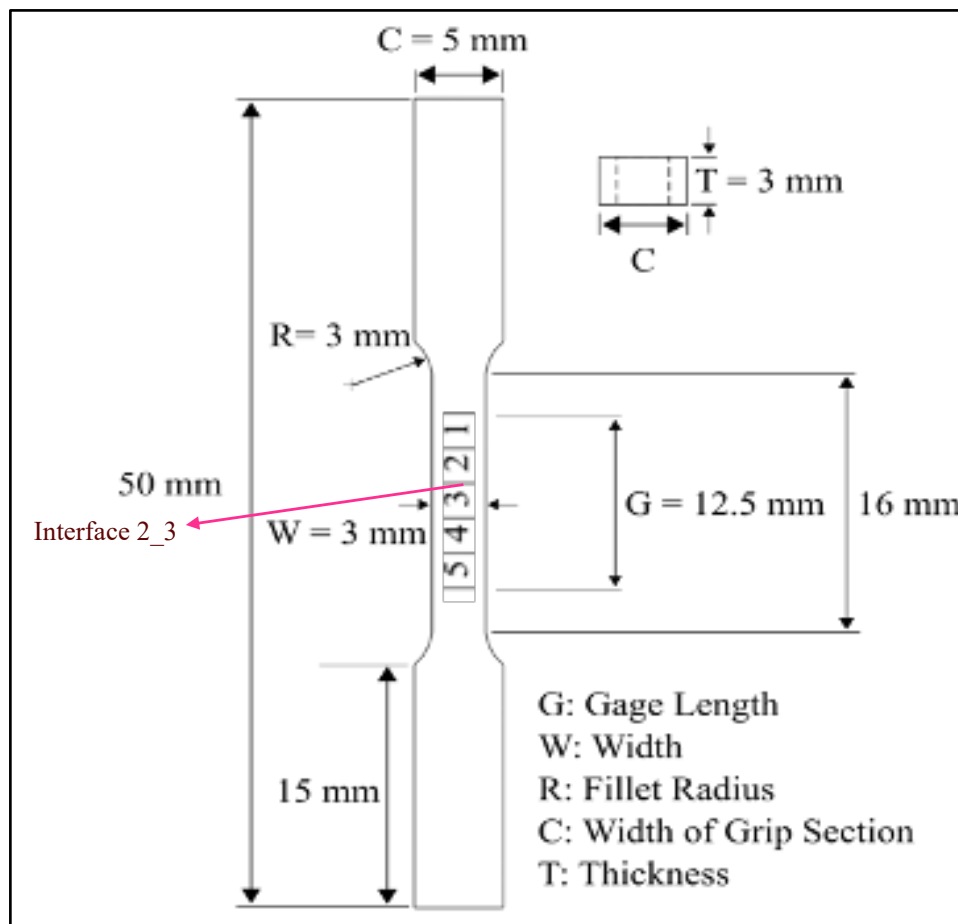


**Figure 163. Point analysis of sample 4T2 in Exx direction during FPB test. The curves represent strains at select points in Exx. Note the lines passing through the middle point showed very little deflection due to vicinity to the neutral axis.**

Figure 162 and Figure 163 shows the line and point DIC analysis of FPB test of sample 4T2, respectively. As the test progressed, the load experienced by the top surface was compressive whereas the tension at the bottom surface. Strain distributions (especially, Exx strain lines) at the center had very little deflections due to vicinity to the neutral axis. It was evident in both line and point analysis that compressive strains were observed in the inspected regions at the top of the sample (points P0 and P1), wherein almost similar pattern can be identified for regions at the bottom of the sample (points P3 and P4) at the opposite ends.

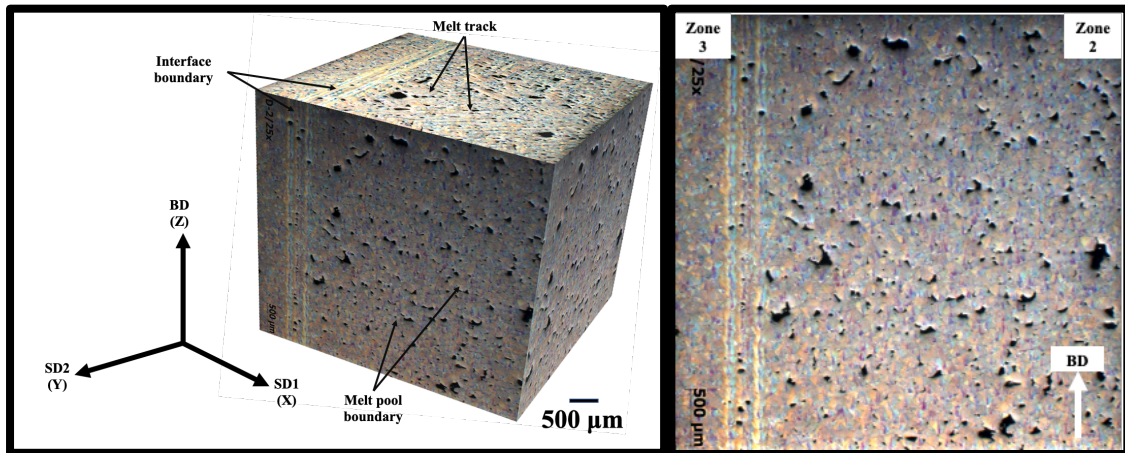
### 7.3 Interfaces

Interfaces were found to be present in the boundary between two distinct zones within the gauge length. Figure 164 illustrates interface region within the gauge length of medium tensile sample.



**Figure 164. Interface region within the gauge length of medium tensile sample. Note 2\_3 represents region between zone 2 ( $P = 200$  W;  $E_v = 39.77$  J/mm<sup>3</sup>;  $\rho = 96.35\%$ ) and zone 3 ( $P = 200$  W;  $E_v = 48.48$  J/mm<sup>3</sup>;  $\rho = 98.21\%$ ).**

The interfaces showed a clear transition in physical/mechanical properties as well as microstructures, thereby affecting the global behavior of the FGAMs. Interfaces could be thought of as buffer regions due to their dissimilar and discontinuous properties. However, understanding the role of the interface becomes rather critical to avoid compromising the structure integrity, and attaining the desired performance for graded parts.



**Figure 165. A portion of the interface reconstructed from a set of optical micrographs in different planes. The features are marked on two different planes along with the interface. Pore defects on the surface of zone 2 are visible, whereas relatively denser surface is seen for zone 3.**

Figure 165 illustrates a reconstructed image of transition or interface region (zone 2 into zone 3). Melt tracks are visible in XY plane due to laser scan pattern (meander with  $67^\circ$  rotation) whereas melt-pool morphologies are present in XZ plane (along BD). Comparing the two surfaces, larger pores are observable for zone 2 as



opposed to denser surface for zone 3. These surface pores in zone 2 are identified as LOF pores and typically present due to insufficient VED, higher scan speed, or larger hatch spacing than optimum [295]. As noted in the previous section, the hardness measurements were carried out on the interfaces and reported in Figure 142.

Carefully observing the interface region reveals presence of pores, however, these pores have a smaller size. These could be ascribed to combination of different phenomenon, such as, melt pool overlap in the vicinity of interface region, a laser scan rotations, a mismatch of the melt pool position, as well as size effects [296]. This could be leveraged to design structures having predictable properties and control, as well as to transition between zones based on the application requirements.

#### **7.4 Observations and Deductions**

This phase of the study looked at the fabrication and performance of homogeneous and graded bulk structures of SS 316L for mapping their deformation behaviors via tensile and bending tests. It turns out that during tensile test, non-uniform and localized strains were jumping around the gauge length throughout the test. As noted earlier, the underlying reason for such jumping of strains could be due to the combination of porosity, hardness, microstructures, phase fractions etc. attributed to each zone due to their unique processing conditions. Moreover, both large tensile samples showed similar trends of the spatial and temporal strain behavior in property-graded multi-zones, indicative repeatable behavior.

Analysis of fracture surfaces of each individual (homogeneous) and graded (composite) samples indicated a typical ductile failure mode. Across front, middle, and back tensile sample configurations, back samples showed the most variations in their tensile properties, indicating the placement of parts on the build plate with respect to the build chamber conditions (for instance, laser incident angle, direction of inert gas flow, etc.) could play a role in final part properties. Furthermore, during postmortem several unmelted powder particles and large voids were noticed at the fracture surfaces, indicating high stress concentration regions.

Additionally, FPB test with DIC captured both localized strains and global performance of homogeneous and graded specimens. As expected, the homogeneous sample showed consistent and repeatable bulk behavior. The analysis of graded sample provided the strains in both  $E_{xx}$  and  $E_{yy}$  directions under tension and compression. It would be interesting to consider fabricating the bending specimens in horizontal build direction to compare and contrast the performance.

Lastly, the interfaces between the graded regions were investigated to research their influence on the property gradations. This is especially important when designing components/structures with predictable properties and failure.

## 8. CONCLUSIONS AND FUTURE WORK

The present study was focused on understanding the causalities within the processing-structure-properties-performance (PSPP) framework for the SLM of SS 316L to realize functionally-graded additively manufactured (FGAM) bulk structures. The focus was to elucidate the relationships between AM process conditions and variations in macro- and microstructures, and how such physicochemical traits affect the resulting physical/mechanical property distributions. Specifically, this study involved investigating the role of VED-based process parameters and their processing bounds for SLM processed SS 316L in functionally-usable property bracket, and their influence on the resulting solidification macro/microstructures. Further, their impact on property distributions (and the resulting local/global strain performance under various loading modes), the spatial resolutions achievable, and the role of interfaces were investigated as well. The following conclusions are derived from this work:

- Density can be reliably controlled (within 90-99.9%, defined as the ‘functional’ range) by altering just one process variable, namely, laser exposure time (which directly affects laser scan speed). At a constant laser power of 150 W, by increasing the scan speed from 500-800 mm/s, the density can be monotonically decreased from 99.9% to 90%. This would be a preferred and more reliable approach rather than altering multiple parameters simultaneously.

- This is in alignment with the fact that as the exposure time (and scan speed) increases, it proportionally reduces the volumetric energy density (VED) imparted. This was confirmed by the evidence of a larger percent fraction of lack of fusion (LOF) pores that are primarily attributed to not having the needed energy to sufficiently melt the power.
- Across the (28) samples, it was possible to reliably obtain/impart a hardness variation spanning 209 - 318 HV<sub>0.5</sub>, with the lowest and highest hardness obtained at  $P = 175 \text{ W}$ ,  $V = 800 \text{ mm/s}$  and  $P = 200 \text{ W}$ ,  $V = 698 \text{ mm/s}$ , respectively. Unlike density, imparting intended hardness differences (209-318 HV<sub>0.5</sub>) needed more than just single parameter to be controlled. Nonetheless, a monotonic hardness decreases from 294 to 209 HV<sub>0.5</sub> can be reliably obtained at a laser power at 175 W, and increasing the scan speed from 500-800 mm/s.
  - Unlike relative density (primarily due to pore size/fraction) which can be monotonically controlled by a single process parameter (*viz.*, scan speed), harness is dependent on a combination of factors – pore fraction, phase fraction, grain size, etc., justifying the need to use multiple parameters.
  - This is also evidenced by the higher hardness observed in samples that contained a ‘detectable’ volume fraction of martensite, vs. those with just austenite and ferrite.

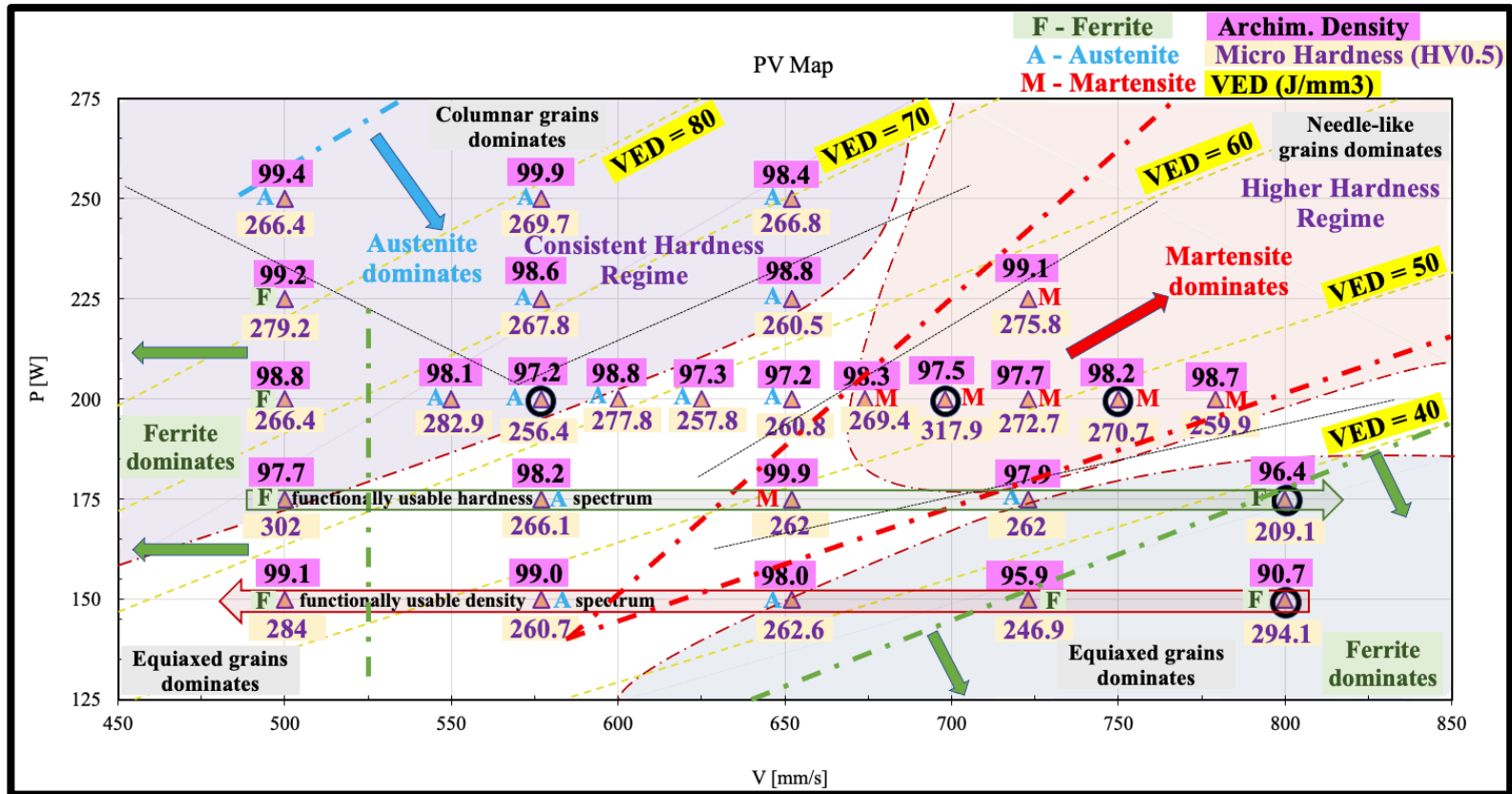


Figure 166. Summary of process parameter bounds on PV map highlighting processing-structure-property relationships for all samples.

- Altering VED ( $E_v$ ) enables intended variations in as-built part density/porosity. Higher porosities and defects were found in samples processed with  $E_v$  lower than  $\sim 44 \text{ J/mm}^3$ , which resulted in a significant drop in densities (below 97%). Solidification defects such as lack-of-fusion (LOF) was significant in these low-density samples. The higher density samples showed smaller micro-pores, suggesting that the variation in density is primarily rooted in pore morphologies.
  - This was evidenced by the LOF pores (non-spherical) observed at low VED vs. gas pores (spherical) observed at too high of a VED.
- Microscopy revealed differences in microstructural morphology with identification of varying fractions of austenite, ferrite, and martensite phases. The presence of martensite (with a needle-like (acicular) structure) was found to be affected by the VED magnitudes. Samples processed with  $E_v$  within 44-54  $\text{J/mm}^3$ , have shown martensite phase fractions. Nevertheless, at higher VED ( $E_v \sim 60 \text{ J/mm}^3$ ) there were gas pores (entrapped gases) observed due to either pre-existing gas inside the powder (gas atomization processing or chamber oxygen) and/or vaporized material during fusion which could lead to changes in the local thermal field (cooling times) and therefore, alter the formation of solidification microstructure. Similarly, the absence of martensitic phase fractions at lower VED ( $E_v \sim 40 \text{ J/mm}^3$ ) could be result of disruptions and thermal insulations due to the large lack of fusion (irregular pores) defects and voids.
- It is deduced that the overall property variations result from a combination of porosity types/amounts, martensitic phase fractions, and grain sizes.

- DIC analysis was performed to capture mapping of the spatial and temporal strain behavior in property-graded multi-zones of composite tensile samples. Results showed non-uniform and localized strains in different zones (within the gauge length) throughout the test with zones of maximum strain shifting between zone of different properties.
  - Up until  $\sim 1\text{-}2\%$  strains all zones showed direct correlation to their individual hardness. After  $\sim 2\%$ , the relative magnitudes of strains within individual zones shifted.
  - This could be due to combination of factors such as porosity, modulus, and phase fractions, among others affecting the plastic deformation.
  - It was observed that zone with the lowest (nano) modulus deformed first and then maximum strain region shifted to the zones with higher modulus. These modulus values were from nanoindentation measurements.
  - UTS values across five zones varied between  $\sim 607$  to  $653$  MPa whereas the strain at break ranged from  $\sim 20$  to  $28\%$ . Furthermore, the moduli obtained were not consistent with the previous test.
  
- Four-point bending tests on composite samples (hardness/modulus varying as a function of the distance from the neutral axis) showed expected trends in axial ( $E_{xx}$ ) and lateral ( $E_{yy}$ ) strain evolutions. By using different property combinations and configurations (*e.g.*, thickness ratio between zones), controllable lateral deflections and stress/strain distributions could be obtained.

- The ability to vary hardness (and other properties) as a function of the depth from the surface has significant applicability in tribological applications.
- Zone interfaces within the gauge length showed microstructure heterogeneities. Such difference can be attributed to the varying thermal history induced due to different processing conditions and effects (VED, porosity, melt pool morphologies, etc.). The interfaces could be leveraged to design structures with predictable properties and failure.
- Fracture surface analysis reveals typical ductile failure. It also shows the presence of unmelted regions and LOF defects which increase the local stress concentration thereby reducing real cross-sectional areas and serving as crack initiation sites.

Altogether, this research endeavor helped generate the knowledgebase of the processing-structure-property-performance (PSPP) chain for SLM of a single metallic alloy from the perspective of designing and fabricating FGAM parts.



## REFERENCES

1. Delfosse, D., *Fundamentals of Functionally Graded Materials*. Materials Today, 1998. **1**(4): p. 18.
2. Kawasaki, A. and R.J.C.i. Watanabe, *Concept and P/M fabrication of functionally gradient materials*. 1997. **23**(1): p. 73-83.
3. Kieback, B., A. Neubrand, and H. Riedel, *Processing techniques for functionally graded materials*. Materials Science and Engineering: A, 2003. **362**(1-2): p. 81-106.
4. Oxman, N., S. Keating, and E. Tsai. *Functionally graded rapid prototyping*. in *Fifth International Conference on Advanced Research in Virtual and Rapid Prototyping (VRAP), Leiria, Portugal, Sept. 2011*.
5. Hirai, T., *Functional Gradient Materials*. Materials Science and Technology, 2006.
6. Bohidar, S.K., R. Sharma, and P.R. Mishra, *Functionally graded materials: A critical review*. International Journal of Research, 2014. **1**(4): p. 289-301.
7. Naebe, M. and K. Shirvanimoghaddam, *Functionally graded materials: A review of fabrication and properties*. Applied Materials Today, 2016. **5**: p. 223-245.
8. Parikh, Y., J. Carter, &, and M.A. Kuttolamadom. *Investigation of Porosity & Microstructure-Induced Property Variations in Additive Manufactured Stainless Steel 316l* in *Manufacturing Science and Engineering Conference*. 2020. Cincinnati, Ohio, USA. : ASME.

9. Wang, Y.M., et al., *Additively manufactured hierarchical stainless steels with high strength and ductility*. Nature materials, 2018. **17**(1): p. 63-71.
10. Zhang, D., et al., *Additive manufacturing of ultrafine-grained high-strength titanium alloys*. Nature, 2019. **576**(7785): p. 91-95.
11. Debroy, T., et al., *Scientific, technological and economic issues in metal printing and their solutions*. Nature materials, 2019: p. 1.
12. Ngo, T.D., et al., *Additive manufacturing (3D printing): A review of materials, methods, applications and challenges*. Composites Part B: Engineering, 2018. **143**: p. 172-196.
13. Khorram Niaki, M. and F. Nonino, *Additive manufacturing management: a review and future research agenda*. International Journal of Production Research, 2016. **55**(5): p. 1419-1439.
14. Bikas, H., P. Stavropoulos, and G. Chryssolouris, *Additive manufacturing methods and modelling approaches: a critical review*. The International Journal of Advanced Manufacturing Technology, 2016. **83**(1-4): p. 389-405.
15. Bourell, D.L., *Perspectives on additive manufacturing*. Annual Review of Materials Research, 2016. **46**: p. 1-18.
16. Huang, S.H., et al., *Additive manufacturing and its societal impact: a literature review*. The International Journal of Advanced Manufacturing Technology, 2013. **67**(5-8): p. 1191-1203.
17. Frazier, W.E., *Metal additive manufacturing: a review*. Journal of Materials Engineering and Performance, 2014. **23**(6): p. 1917-1928.

18. T, W., *Wohlers report 2018: annual worldwide progress report. 3D Printing and Additive Manufacturing State of the Industry*. 2018.
19. Loh, G.H., et al., *An overview of functionally graded additive manufacturing*. Additive Manufacturing, 2018. **23**: p. 34-44.
20. Hengsbach, F., et al., *Inline additively manufactured functionally graded multi-materials: microstructural and mechanical characterization of 316L parts with H13 layers*. Progress in Additive Manufacturing, 2018: p. 1-11.
21. Bobbio, L.D., et al., *Additive manufacturing of a functionally graded material from Ti-6Al-4V to Invar: Experimental characterization and thermodynamic calculations*. Acta Materialia, 2017. **127**: p. 133-142.
22. Gu, D.D., et al., *Laser additive manufacturing of metallic components: materials, processes and mechanisms*. International Materials Reviews, 2012. **57**(3): p. 133-164.
23. Huang, Y., et al., *Additive Manufacturing: Current State, Future Potential, Gaps and Needs, and Recommendations*. Journal of Manufacturing Science and Engineering, 2014. **137**(1): p. 014001.
24. Gao, W., et al., *The status, challenges, and future of additive manufacturing in engineering*. Computer-Aided Design, 2015. **69**: p. 65-89.
25. Jared, B.H., et al., *Additive manufacturing: Toward holistic design*. Scripta Materialia, 2017. **135**: p. 141-147.
26. Ralph, B., *Method of making decorative articles*. 1925, Google Patents.
27. BLANTHER, J., *Manufacture of Contour Relief Maps*. 1892, US Patent 473,901.

28. ASTM, I., *ASTM F2792-10: standard terminology for additive manufacturing technologies*. ASTM International, 2010.
29. Liverani, E., et al., *Effect of selective laser melting (SLM) process parameters on microstructure and mechanical properties of 316L austenitic stainless steel*. *Journal of Materials Processing Technology*, 2017. **249**: p. 255-263.
30. Dutta, B. and F. Froes, *Additive manufacturing of Titanium alloys: state of the art, challenges and opportunities*. 2016: Butterworth-Heinemann.
31. Markillie, P., *A third industrial revolution*. *The economist*, 2012. **21**: p. 3-12.
32. Dietrich, D.M., M. Kenworthy, and E.A. Cudney, *Additive Manufacturing Change Management : Best Practices*. 2019, Milton, UNITED KINGDOM: Taylor & Francis Group.
33. <https://www.digitalalloys.com/>, D.A.
34. Singh, R., et al., *Powder bed fusion process in additive manufacturing: An overview*. *Materials Today: Proceedings*, 2020.
35. Thompson, M.K., et al., *Design for Additive Manufacturing: Trends, opportunities, considerations, and constraints*. *CIRP annals*, 2016. **65**(2): p. 737-760.
36. *Electro Optical Systems GmbH*. Available from: [www.eos.info](http://www.eos.info).
37. *SLM Solutions Group AG*. Available from: [www.slm-solutions.com](http://www.slm-solutions.com).
38. *GE Additive*. Available from: [www.ge.com](http://www.ge.com).
39. *Trumpf GmbH & Co. KG*. Available from: [www.trumpf.com](http://www.trumpf.com).

40. Parikh, Y., J. Carter, and M.A. Kuttolamadom. *Investigation of Porosity & Microstructure-Induced Property Variations in Additive Manufactured Stainless Steel 316L*. in *Manufacturing Science and Engineering Conference*. 2020. Cincinnati, Ohio, USA. : ASME.
41. Bandyopadhyay, A. and S. Bose, *Additive manufacturing*. 2019: CRC press.
42. Sun, S., M. Brandt, and M. Easton, *Powder bed fusion processes: An overview*, in *Laser Additive Manufacturing*. 2017, Elsevier. p. 55-77.
43. Ghose, S., et al., *The influence of laser parameters and scanning strategies on the mechanical properties of a stochastic porous material*. *Materials & Design*, 2017. **131**: p. 498-508.
44. DebRoy, T., et al., *Additive manufacturing of metallic components – Process, structure and properties*. *Progress in Materials Science*, 2018. **92**: p. 112-224.
45. Badiru, A.B., V.V. Valencia, and D. Liu, *Additive manufacturing handbook: product development for the defense industry*. 2017: CRC Press.
46. Bandyopadhyay, A. and B. Heer, *Additive manufacturing of multi-material structures*. *Materials Science and Engineering: R: Reports*, 2018. **129**: p. 1-16.
47. Sahasrabudhe, H., S. Bose, and A. Bandyopadhyay, *Chapter 17 - Laser-Based Additive Manufacturing Processes*, in *Advances in Laser Materials Processing (Second Edition)*, J. Lawrence, Editor. 2018, Woodhead Publishing. p. 507-539.
48. Schleifenbaum, H., et al., *Individualized production by means of high power Selective Laser Melting*. *CIRP Journal of Manufacturing Science and Technology*, 2010. **2**(3): p. 161-169.

49. Kruth, J.-P., et al., *Selective laser melting of iron-based powder*. Journal of materials processing technology, 2004. **149**(1-3): p. 616-622.
50. Kamath, C., et al., *Density of additively-manufactured, 316L SS parts using laser powder-bed fusion at powers up to 400 W*. The International Journal of Advanced Manufacturing Technology, 2014. **74**(1): p. 65-78.
51. Brandt, M., *Laser additive manufacturing: materials, design, technologies, and applications*. 2016: Woodhead Publishing.
52. Dutta, B., S. Babu, and B.H. Jared, *Science, technology and applications of metals in additive manufacturing*. 2019: Elsevier.
53. Killi, S.W., *Additive Manufacturing : Design, Methods, and Processes*. 2017, Milton, UNITED KINGDOM: Jenny Stanford Publishing.
54. Bahnini, I., et al., *Additive manufacturing technology: the status, applications, and prospects*. The International Journal of Advanced Manufacturing Technology, 2018. **97**(1-4): p. 147-161.
55. Sing, S.L., et al., *Laser and electron-beam powder-bed additive manufacturing of metallic implants: A review on processes, materials and designs*. Journal of Orthopaedic Research, 2016. **34**(3): p. 369-385.
56. Sing, S.L. and W.Y. Yeong, *Laser powder bed fusion for metal additive manufacturing: perspectives on recent developments*. Virtual and Physical Prototyping, 2020. **15**(3): p. 359-370.

57. Bikas, H., A. Lianos, and P. Stavropoulos, *A design framework for additive manufacturing*. The International Journal of Advanced Manufacturing Technology, 2019. **103**(9-12): p. 3769-3783.
58. Busachi, A., et al., *A review of additive manufacturing technology and cost estimation techniques for the defence sector*. CIRP Journal of Manufacturing Science and Technology, 2017. **19**: p. 117-128.
59. Conner, B.P., et al., *Making sense of 3-D printing: Creating a map of additive manufacturing products and services*. Additive Manufacturing, 2014. **1**: p. 64-76.
60. Culmone, C., G. Smit, and P. Breedveld, *Additive manufacturing of medical instruments: A state-of-the-art review*. Additive Manufacturing, 2019.
61. Eyers, D.R. and A.T. Potter, *Industrial Additive Manufacturing: A manufacturing systems perspective*. Computers in industry, 2017. **92**: p. 208-218.
62. Hu, Z. and S. Mahadevan, *Uncertainty quantification and management in additive manufacturing: current status, needs, and opportunities*. The International Journal of Advanced Manufacturing Technology, 2017. **93**(5-8): p. 2855-2874.
63. Konda Gokuldoss, P., *Design of next-generation alloys for additive manufacturing*. Material Design & Processing Communications, 2019. **1**(4): p. e50.
64. Fousová, M., et al., *Promising characteristics of gradient porosity Ti-6Al-4V alloy prepared by SLM process*. Journal of the Mechanical Behavior of Biomedical Materials, 2017. **69**: p. 368-376.

65. Rashid, R., et al., *Effect of scan strategy on density and metallurgical properties of 17-4PH parts printed by Selective Laser Melting (SLM)*. Journal of Materials Processing Technology, 2017. **249**: p. 502-511.
66. Sungail, C. and A. Abid, *Spherical tantalum feed powder for metal additive manufacturing*. Metal Powder Report, 2018.
67. Zhu, Y., J. Zou, and H.-y. Yang, *Wear performance of metal parts fabricated by selective laser melting: a literature review*. Journal of Zhejiang University-SCIENCE A, 2018. **19**(2): p. 95-110.
68. Wang, Z. and A.M. Beese, *Effect of chemistry on martensitic phase transformation kinetics and resulting properties of additively manufactured stainless steel*. Acta Materialia, 2017. **131**: p. 410-422.
69. Liu, S. and Y.C. Shin, *Additive manufacturing of Ti6Al4V alloy: A review*. Materials & Design, 2019. **164**: p. 107552.
70. Raabe, D., C.C. Tasan, and E.A. Olivetti, *Strategies for improving the sustainability of structural metals*. Nature, 2019. **575**(7781): p. 64-74.
71. Freeman, R., *Measuring the flow properties of consolidated, conditioned and aerated powders—a comparative study using a powder rheometer and a rotational shear cell*. Powder Technology, 2007. **174**(1-2): p. 25-33.
72. Li, R., et al., *Densification behavior of gas and water atomized 316L stainless steel powder during selective laser melting*. Applied surface science, 2010. **256**(13): p. 4350-4356.



73. Nemat-Alla, M.M., et al., *Powder metallurgical fabrication and microstructural investigations of aluminum/steel functionally graded material*. Materials Sciences and Applications, 2011. **2**(12): p. 1708.
74. Boisselier, D. and S. Sankaré, *Influence of Powder Characteristics in Laser Direct Metal Deposition of SS316L for Metallic Parts Manufacturing*. Physics Procedia, 2012. **39**: p. 455-463.
75. Alkahari, M.R., et al., *Consolidation characteristics of ferrous-based metal powder in additive manufacturing*. Journal of Advanced Mechanical Design, Systems, and Manufacturing, 2014. **8**(1): p. JAMDSM0009-JAMDSM0009.
76. Clayton, J., D. Millington-Smith, and B. Armstrong, *The application of powder rheology in additive manufacturing*. Jom, 2015. **67**(3): p. 544-548.
77. Mani, M., et al., *Measurement science needs for real-time control of additive manufacturing powder bed fusion processes*. 2015.
78. Strondl, A., et al., *Characterization and control of powder properties for additive manufacturing*. Jom, 2015. **67**(3): p. 549-554.
79. Samal, P. and J. Newkirk, *Powder metallurgy methods and applications*. ASM handbook of powder metallurgy, 2015. **7**.
80. Tan, J.H., W.L.E. Wong, and K.W. Dalgarno, *An overview of powder granulometry on feedstock and part performance in the selective laser melting process*. Additive Manufacturing, 2017. **18**: p. 228-255.

81. Chen, W., et al., *Effect of powder feedstock on microstructure and mechanical properties of the 316L stainless steel fabricated by selective laser melting*. Metals, 2018. **8**(9): p. 729.
82. Bertoli, U.S., et al., *In-situ characterization of laser-powder interaction and cooling rates through high-speed imaging of powder bed fusion additive manufacturing*. Materials & Design, 2017. **135**: p. 385-396.
83. Murphy, R.D. and E.C. Forrest, *A Review of In-situ Temperature Measurements for Additive Manufacturing Technologies*. 2016, Sandia National Lab.(SNL-NM), Albuquerque, NM (United States).
84. Melia, M.A., et al., *How build angle and post-processing impact roughness and corrosion of additively manufactured 316L stainless steel*. npj Materials Degradation, 2020. **4**(1): p. 21.
85. Laleh, M., et al., *A critical insight into lack-of-fusion pore structures in additively manufactured stainless steel*. Additive Manufacturing, 2021. **38**: p. 101762.
86. Ladewig, A., et al., *Influence of the shielding gas flow on the removal of process by-products in the selective laser melting process*. Additive Manufacturing, 2016. **10**: p. 1-9.
87. Kopf, R., et al., *Cost-oriented planning of equipment for selective laser melting (SLM) in production lines*. CIRP Annals, 2018. **67**(1): p. 471-474.
88. Malekipour, E. and H. El-Mounayri, *Common defects and contributing parameters in powder bed fusion AM process and their classification for online*

- monitoring and control: a review*. The International Journal of Advanced Manufacturing Technology, 2018. **95**(1): p. 527-550.
89. Lee, H., et al., *Lasers in additive manufacturing: A review*. International Journal of Precision Engineering and Manufacturing-Green Technology, 2017. **4**(3): p. 307-322.
90. Pinkerton, A.J., *[INVITED] Lasers in additive manufacturing*. Optics & Laser Technology, 2016. **78**: p. 25-32.
91. Dursun, G., et al., *Influence of laser processing parameters on the surface characteristics of 316L stainless steel manufactured by selective laser melting*. Materials Today: Proceedings, 2020.
92. Mertens, R., et al., *Application of base plate preheating during selective laser melting*. Procedia CIRP, 2018. **74**: p. 5-11.
93. Liu, J., et al., *Effect of scanning speed on the microstructure and mechanical behavior of 316L stainless steel fabricated by selective laser melting*. Materials & Design, 2020. **186**: p. 108355.
94. Liu, C., et al., *Effect of scanning strategy on microstructure and mechanical properties of selective laser melted reduced activation ferritic/martensitic steel*. Materials Science and Engineering: A, 2019. **766**: p. 138364.
95. Cao, L., *Mesosopic-scale simulation of pore evolution during laser powder bed fusion process*. Computational Materials Science, 2020. **179**: p. 109686.
96. Brenne, F. and T. Niendorf, *Damage tolerant design by microstructural gradation—Influence of processing parameters and build orientation on crack*

- growth within additively processed 316L*. Materials Science and Engineering: A, 2019. **764**: p. 138186.
97. Leicht, A., U. Klement, and E. Hryha, *Effect of build geometry on the microstructural development of 316L parts produced by additive manufacturing*. Materials Characterization, 2018. **143**: p. 137-143.
98. Matthews, M.J., et al., *Denudation of metal powder layers in laser powder bed fusion processes*. Acta Materialia, 2016. **114**: p. 33-42.
99. Anwar, A.B. and Q.-C. Pham, *Study of the spatter distribution on the powder bed during selective laser melting*. Additive Manufacturing, 2018. **22**: p. 86-97.
100. Ferrar, B., et al., *Gas flow effects on selective laser melting (SLM) manufacturing performance*. Journal of Materials Processing Technology, 2012. **212**(2): p. 355-364.
101. Ghayoor, M., et al., *Selective laser melting of 304L stainless steel: Role of volumetric energy density on the microstructure, texture and mechanical properties*. Additive Manufacturing, 2020. **32**: p. 101011.
102. Hooper, P.A., *Melt pool temperature and cooling rates in laser powder bed fusion*. Additive Manufacturing, 2018. **22**: p. 548-559.
103. Lykov, P. *The Energy Density as a Reliable Parameter for Characterization of Selective Laser Melting of Various Alloys*. in *Materials Science Forum*. 2019. Trans Tech Publ.

104. Prashanth, K.G., et al., *Is the energy density a reliable parameter for materials synthesis by selective laser melting?* Materials Research Letters, 2017. **5**(6): p. 386-390.
105. Suzuki, A., et al., *Design of laser parameters for selectively laser melted maraging steel based on deposited energy density.* Additive Manufacturing, 2019. **28**: p. 160-168.
106. Promoppatum, P. and S.-C. Yao, *Influence of scanning length and energy input on residual stress reduction in metal additive manufacturing: Numerical and experimental studies.* Journal of Manufacturing Processes, 2020. **49**: p. 247-259.
107. Yusuf, S.M. and N. Gao, *Influence of energy density on metallurgy and properties in metal additive manufacturing.* Materials Science and Technology, 2017. **33**(11): p. 1269-1289.
108. AlFaify, A., J. Hughes, and K. Ridgway, *Controlling the porosity of 316L stainless steel parts manufactured via the powder bed fusion process.* Rapid Prototyping Journal, 2019.
109. Scipioni Bertoli, U., et al., *On the limitations of Volumetric Energy Density as a design parameter for Selective Laser Melting.* Materials & Design, 2017. **113**: p. 331-340.
110. Baumgartl, H., et al., *A deep learning-based model for defect detection in laser-powder bed fusion using in-situ thermographic monitoring.* Progress in Additive Manufacturing, 2020.

111. Chen, Y., et al., *In-situ Synchrotron imaging of keyhole mode multi-layer laser powder bed fusion additive manufacturing*. Applied Materials Today, 2020. **20**: p. 100650.
112. Le, K., C. Tang, and C. Wong, *On the study of keyhole-mode melting in selective laser melting process*. International Journal of Thermal Sciences, 2019. **145**: p. 105992.
113. Hojjatzadeh, S.M.H., et al., *Pore elimination mechanisms during 3D printing of metals*. Nature communications, 2019. **10**(1): p. 1-8.
114. Hojjatzadeh, S.M.H., et al., *Direct observation of pore formation mechanisms during LPBF additive manufacturing process and high energy density laser welding*. International Journal of Machine Tools and Manufacture, 2020. **153**: p. 103555.
115. du Plessis, A., I. Yadroitsava, and I. Yadroitsev, *Effects of defects on mechanical properties in metal additive manufacturing: A review focusing on X-ray tomography insights*. Materials & Design, 2020. **187**: p. 108385.
116. Donik, Č., et al., *Influence of the Energy Density for Selective Laser Melting on the Microstructure and Mechanical Properties of Stainless Steel*. Metals, 2020. **10**(7): p. 919.
117. King, W.E., et al., *Laser powder bed fusion additive manufacturing of metals; physics, computational, and materials challenges*. 2015. **2**(4): p. 041304.

118. Oliveira, J.P., T.G. Santos, and R.M. Miranda, *Revisiting fundamental welding concepts to improve additive manufacturing: From theory to practice*. Progress in Materials Science, 2020. **107**: p. 100590.
119. Ronneberg, T., C.M. Davies, and P.A. Hooper, *Revealing relationships between porosity, microstructure and mechanical properties of laser powder bed fusion 316L stainless steel through heat treatment*. Materials & Design, 2020. **189**: p. 108481.
120. Shahriari, A., et al., *Microstructure and corrosion behavior of a novel additively manufactured maraging stainless steel*. Electrochimica Acta, 2020. **339**: p. 135925.
121. Wang, D., et al., *Investigation of crystal growth mechanism during selective laser melting and mechanical property characterization of 316L stainless steel parts*. Materials & Design, 2016. **100**: p. 291-299.
122. King, W.E., et al., *Observation of keyhole-mode laser melting in laser powder-bed fusion additive manufacturing*. Journal of Materials Processing Technology, 2014. **214**(12): p. 2915-2925.
123. Panwisawas, C., et al., *Keyhole formation and thermal fluid flow-induced porosity during laser fusion welding in titanium alloys: Experimental and modelling*. Acta Materialia, 2017. **126**: p. 251-263.
124. Bertoli, U.S., et al., *On the limitations of volumetric energy density as a design parameter for selective laser melting*. Materials & Design, 2017. **113**: p. 331-340.

125. Ning, J., et al., *Analytical thermal modeling of metal additive manufacturing by heat sink solution*. *Materials*, 2019. **12**(16): p. 2568.
126. Heeling, T., M. Cloots, and K. Wegener, *Melt pool simulation for the evaluation of process parameters in selective laser melting*. *Additive Manufacturing*, 2017. **14**: p. 116-125.
127. Leung, C.L.A., et al., *In situ X-ray imaging of defect and molten pool dynamics in laser additive manufacturing*. *Nature Communications*, 2018. **9**(1): p. 1355.
128. Hussein, A., et al., *Finite element simulation of the temperature and stress fields in single layers built without-support in selective laser melting*. *Materials & Design (1980-2015)*, 2013. **52**: p. 638-647.
129. Biegler, M., B. Graf, and M. Rethmeier, *In-situ distortions in LMD additive manufacturing walls can be measured with digital image correlation and predicted using numerical simulations*. *Additive Manufacturing*, 2018. **20**: p. 101-110.
130. Panwisawas, C., Y.T. Tang, and R.C. Reed, *Metal 3D printing as a disruptive technology for superalloys*. *Nature communications*, 2020. **11**(1): p. 1-4.
131. Leach, R. and S. Carmignato, *Precision Metal Additive Manufacturing*. 2020: CRC Press.
132. Tan, J., C. Tang, and C. Wong, *Study and modeling of melt pool evolution in selective laser melting process of SS316L*. *MRS Communications*, 2018. **8**(3): p. 1178-1183.



133. DebRoy, T., et al., *Metallurgy, mechanistic models and machine learning in metal printing*. Nature Reviews Materials, 2020: p. 1-21.
134. Johnson, N.S., et al., *Invited review: Machine learning for materials developments in metals additive manufacturing*. Additive Manufacturing, 2020: p. 101641.
135. Renken, V., et al., *Model assisted closed-loop control strategy for selective laser melting*. Procedia CIRP, 2018. **74**: p. 659-663.
136. Freeman, F.S., L. Chechik, and I. Todd, *Beat the machine (learning): metal additive manufacturing and closed loop control*. Physics Education, 2020. **55**(5): p. 055012.
137. Paulson, N.H., et al., *Correlations between thermal history and keyhole porosity in laser powder bed fusion*. Additive Manufacturing, 2020. **34**: p. 101213.
138. Khairallah, S.A., et al., *Controlling interdependent meso-nanosecond dynamics and defect generation in metal 3D printing*. Science, 2020. **368**(6491): p. 660-665.
139. Lott, P., et al., *Design of an optical system for the in situ process monitoring of selective laser melting (SLM)*. Physics Procedia, 2011. **12**: p. 683-690.
140. Loterie, D., P. Delrot, and C. Moser, *High-resolution tomographic volumetric additive manufacturing*. Nature Communications, 2020. **11**(1): p. 852.
141. Zhang, X., et al., *Correlation approach for quality assurance of additive manufactured parts based on optical metrology*. Journal of Manufacturing Processes, 2020. **53**: p. 310-317.

142. Boschetto, A., et al., *Post-processing of complex SLM parts by barrel finishing*. Applied Sciences, 2020. **10**(4): p. 1382.
143. Ni, J., et al., *Three-dimensional printing of metals for biomedical applications*. Materials Today Bio, 2019. **3**: p. 100024.
144. Wei, C., et al., *3D printing of multiple metallic materials via modified selective laser melting*. CIRP Annals, 2018. **67**(1): p. 245-248.
145. Lavery, N.P., et al., *Effects of hot isostatic pressing on the elastic modulus and tensile properties of 316L parts made by powder bed laser fusion*. Materials Science and Engineering: A, 2017. **693**: p. 186-213.
146. Srivastava, M., et al., *Additive Manufacturing: Fundamentals and Advancements*. 2019: CRC Press.
147. Tascioglu, E., Y. Karabulut, and Y. Kaynak, *Influence of heat treatment temperature on the microstructural, mechanical, and wear behavior of 316L stainless steel fabricated by laser powder bed additive manufacturing*. The International Journal of Advanced Manufacturing Technology, 2020: p. 1-10.
148. Snow, Z., A.R. Nassar, and E.W. Reutzel, *Invited Review Article: Review of the formation and impact of flaws in powder bed fusion additive manufacturing*. Additive Manufacturing, 2020. **36**: p. 101457.
149. (BDLI).<https://www.bdli.de/en>, G.A.I.A. [cited 2021].
150. Chandler, H., *Heat treater's guide: practices and procedures for irons and steels*. 1994: ASM international.

151. Lo, K.H., C.H. Shek, and J.K.L. Lai, *Recent developments in stainless steels*. Materials Science and Engineering: R: Reports, 2009. **65**(4): p. 39-104.
152. Totten, G.E., *Steel heat treatment: metallurgy and technologies*. 2006: CRC press.
153. Handbook, A.M., *Howard E. Boyer and Timothy L. Gall, Eds.*, American Society for Metals, Materials Park, OH, 1985.
154. Bhadeshia, H. and R. Honeycombe, *Steels: microstructure and properties*. 2017: Butterworth-Heinemann.
155. Bartolomeu, F., et al., *316L stainless steel mechanical and tribological behavior—A comparison between selective laser melting, hot pressing and conventional casting*. Additive Manufacturing, 2017. **16**: p. 81-89.
156. Tolosa, I., et al., *Study of mechanical properties of AISI 316 stainless steel processed by “selective laser melting”, following different manufacturing strategies*. The International Journal of Advanced Manufacturing Technology, 2010. **51**(5-8): p. 639-647.
157. Aircraft Systems and Manufacturing, I.h.a.n.i.h. 2021.
158. Fractography, P., *Oct 5-9 How to Organize and Run a Failure Investigation and Principles of Failure Analysis ASM World Headquarters*.
159. S., D., H. L., and S. N., *Effect of selective laser melting layout on the quality of stainless steel parts*. Rapid Prototyping Journal, 2012. **18**(3): p. 241-249.

160. Trubačová, P., et al., *Analysis of Selective Laser Melting Process Parameters Effect on Mechanical and Material Properties for Stainless Steel 316L*. Solid State Phenomena, 2016. **258**: p. 579-582.
161. Yakout, M., M.A. Elbestawi, and S.C. Veldhuis, *On the characterization of stainless steel 316L parts produced by selective laser melting*. The International Journal of Advanced Manufacturing Technology, 2018. **95**(5): p. 1953-1974.
162. Cao, Q., et al., *Removability of 316L stainless steel cone and block support structures fabricated by Selective Laser Melting (SLM)*. Materials & Design, 2020. **191**: p. 108691.
163. Chao, Q., et al., *On the enhanced corrosion resistance of a selective laser melted austenitic stainless steel*. Scripta materialia, 2017. **141**: p. 94-98.
164. Hardes, C., et al., *Cavitation erosion resistance of 316L austenitic steel processed by selective laser melting (SLM)*. Additive Manufacturing, 2019. **29**: p. 100786.
165. Li, R., et al., *316L Stainless Steel with Gradient Porosity Fabricated by Selective Laser Melting*. Journal of Materials Engineering and Performance, 2010. **19**(5): p. 666-671.
166. Kurzynowski, T., et al., *Correlation between process parameters, microstructure and properties of 316 L stainless steel processed by selective laser melting*. Materials Science and Engineering: A, 2018. **718**: p. 64-73.

167. Calta, N.P., et al., *Pressure dependence of the laser-metal interaction under laser powder bed fusion conditions probed by in situ X-ray imaging*. Additive Manufacturing, 2020. **32**: p. 101084.
168. Ni, X., et al., *Corrosion Behavior of 316L Stainless Steel Fabricated by Selective Laser Melting Under Different Scanning Speeds*. Journal of Materials Engineering and Performance, 2018.
169. Zhong, Y., et al., *Intragranular cellular segregation network structure strengthening 316L stainless steel prepared by selective laser melting*. Journal of Nuclear Materials, 2016. **470**: p. 170-178.
170. Krell, J., et al., *General investigations on processing tool steel X40CrMoV5-1 with selective laser melting*. Journal of Materials Processing Technology, 2018. **255**: p. 679-688.
171. Cherry, J., et al., *Investigation into the effect of process parameters on microstructural and physical properties of 316L stainless steel parts by selective laser melting*. 2015. **76**(5-8): p. 869-879.
172. Suryawanshi, J., K.G. Prashanth, and U. Ramamurty, *Mechanical behavior of selective laser melted 316L stainless steel*. Materials Science and Engineering: A, 2017. **696**: p. 113-121.
173. Choi, J.-P., et al., *Densification behavior of 316L stainless steel parts fabricated by selective laser melting by variation in laser energy density*. 2016. **57**(11): p. 1952-1959.

174. Saeidi, K., et al., *Transformation of austenite to duplex austenite-ferrite assembly in annealed stainless steel 316L consolidated by laser melting*. Journal of Alloys and Compounds, 2015. **633**: p. 463-469.
175. Ahmadi, A., et al., *Effect of manufacturing parameters on mechanical properties of 316L stainless steel parts fabricated by selective laser melting: A computational framework*. Materials & Design, 2016. **112**: p. 328-338.
176. Mäkinen, M., et al., *Preliminary Comparison of Properties between Ni-electroplated Stainless Steel Parts Fabricated with Laser Additive Manufacturing and Conventional Machining*. Physics Procedia, 2015. **78**: p. 337-346.
177. Zhao, S., et al., *Densification behavior and mechanical properties of nanocrystalline TiC reinforced 316L stainless steel composite parts fabricated by selective laser melting*. Optics & Laser Technology, 2018. **103**: p. 239-250.
178. Zhu, Y., et al., *Electrical energy consumption and mechanical properties of selective-laser-melting-produced 316L stainless steel samples using various processing parameters*. Journal of cleaner production, 2019. **208**: p. 77-85.
179. Bahl, S., et al., *Non-equilibrium microstructure, crystallographic texture and morphological texture synergistically result in unusual mechanical properties of 3D printed 316L stainless steel*. Additive Manufacturing, 2019. **28**: p. 65-77.
180. Basak, A. and S. Das, *Epitaxy and microstructure evolution in metal additive manufacturing*. Annual Review of Materials Research, 2016. **46**: p. 125-149.

181. Gäumann, M., et al., *Epitaxial laser metal forming: analysis of microstructure formation*. Materials Science and Engineering: A, 1999. **271**(1-2): p. 232-241.
182. Messler Jr, R.W., *Principles of welding: processes, physics, chemistry, and metallurgy*. 2008: John Wiley & Sons.
183. Chen, Z., M. Phan, and K. Darvish, *Grain growth during selective laser melting of a Co–Cr–Mo alloy*. Journal of Materials Science, 2017. **52**(12): p. 7415-7427.
184. Smallman, R.E. and A.H.W. Ngan, *Chapter 3 - Solidification*, in *Modern Physical Metallurgy (Eighth Edition)*, R.E. Smallman and A.H.W. Ngan, Editors. 2014, Butterworth-Heinemann: Oxford. p. 93-119.
185. Li, X. and W. Tan, *Numerical investigation of effects of nucleation mechanisms on grain structure in metal additive manufacturing*. Computational Materials Science, 2018. **153**: p. 159-169.
186. Kim, J., A. Wakai, and A. Moridi, *Materials and manufacturing renaissance: Additive manufacturing of high-entropy alloys*. Journal of Materials Research: p. 1-21.
187. Yang, Y., et al., *Densification, surface morphology, microstructure and mechanical properties of 316L fabricated by hybrid manufacturing*. The International Journal of Advanced Manufacturing Technology, 2018. **97**(5): p. 2687-2696.
188. Li, C., et al., *Residual Stress in Metal Additive Manufacturing*. Procedia CIRP, 2018. **71**: p. 348-353.

189. Bartlett, J.L., et al., *Revealing mechanisms of residual stress development in additive manufacturing via digital image correlation*. Additive Manufacturing, 2018. **22**: p. 1-12.
190. Rappaz, M., et al., *Analysis of solidification microstructures in Fe-Ni-Cr single-crystal welds*. Metallurgical transactions A, 1990. **21**(6): p. 1767-1782.
191. Kurz, W. and D.J. Fisher, *Fundamentals of solidification*. 1989.
192. Prashanth, K. and J. Eckert, *Formation of metastable cellular microstructures in selective laser melted alloys*. Journal of Alloys and Compounds, 2017. **707**: p. 27-34.
193. Godec, M., et al., *Effect of post-treated low-temperature plasma nitriding on the wear and corrosion resistance of 316L stainless steel manufactured by laser powder-bed fusion*. Additive Manufacturing, 2020. **32**: p. 101000.
194. Thijs, L., et al., *Fine-structured aluminium products with controllable texture by selective laser melting of pre-alloyed AlSi10Mg powder*. Acta Materialia, 2013. **61**(5): p. 1809-1819.
195. Li, R., et al., *Effects of processing parameters on the temperature field of selective laser melting metal powder*. Powder Metallurgy and Metal Ceramics, 2009. **48**(3): p. 186-195.
196. Romano, J., L. Ladani, and M. Sadowski, *Thermal Modeling of Laser Based Additive Manufacturing Processes within Common Materials*. Procedia Manufacturing, 2015. **1**: p. 238-250.



197. Pham, M.-S., et al., *The role of side-branching in microstructure development in laser powder-bed fusion*. Nature Communications, 2020. **11**(1): p. 1-12.
198. Choo, H., et al., *Effect of laser power on defect, texture, and microstructure of a laser powder bed fusion processed 316L stainless steel*. Materials & Design, 2019. **164**: p. 107534.
199. Sun, Z., et al., *Selective laser melting of stainless steel 316L with low porosity and high build rates*. Materials & Design, 2016. **104**: p. 197-204.
200. Saeidi, K., et al., *Hardened austenite steel with columnar sub-grain structure formed by laser melting*. Materials Science and Engineering: A, 2015. **625**: p. 221-229.
201. Petch, N., *The cleavage strength of polycrystals*. Journal of the Iron and Steel Institute, 1953. **174**: p. 25-28.
202. Popovich, V.A., et al., *Functionally graded Inconel 718 processed by additive manufacturing: Crystallographic texture, anisotropy of microstructure and mechanical properties*. Materials & Design, 2017. **114**: p. 441-449.
203. Yadollahi, A., et al., *Effects of process time interval and heat treatment on the mechanical and microstructural properties of direct laser deposited 316L stainless steel*. Materials Science and Engineering: A, 2015. **644**: p. 171-183.
204. Anstaett, C., C. Seidel, and G. Reinhart. *Fabrication of 3D multi-material parts using laser-based powder bed fusion*. in *Proceedings of the 28th Annual International Solid Freeform Fabrication Symposium*. 2017.

205. Mumtaz, K.A. and N. Hopkinson, *Laser melting functionally graded composition of Waspaloy® and Zirconia powders*. Journal of materials science, 2007. **42**(18): p. 7647-7656.
206. Niendorf, T., et al., *Functionally Graded Alloys Obtained by Additive Manufacturing*. Advanced Engineering Materials, 2014. **16**(7): p. 857-861.
207. Attard, B., et al., *Microstructural control during laser powder fusion to create graded microstructure Ni-superalloy components*. Additive Manufacturing, 2020. **36**: p. 101432.
208. Mahamood, R.M., et al., *Functionally graded material: an overview*. 2012.
209. Miyamoto, Y., et al., *Functionally graded materials: design, processing and applications*. Vol. 5. 2013: Springer Science & Business Media.
210. Mahmoud, D. and M.A. Elbestawi, *Lattice structures and functionally graded materials applications in additive manufacturing of orthopedic implants: a review*. Journal of Manufacturing and Materials Processing, 2017. **1**(2): p. 13.
211. El-Galy, I.M., B.I. Saleh, and M.H. Ahmed, *Functionally graded materials classifications and development trends from industrial point of view*. SN Applied Sciences, 2019. **1**(11): p. 1378.
212. Suresh, S., *Graded materials for resistance to contact deformation and damage*. Science, 2001. **292**(5526): p. 2447-2451.
213. Muller, P., J.Y. Hascoet, and P. Mognol. *A method for the manufacturing of functionally graded material parts*. in *Advanced Materials Research*. 2013. Trans Tech Publ.

214. Mahamood, R.M. and E.T. Akinlabi, *Types of functionally graded materials and their areas of application*, in *Functionally Graded Materials*. 2017, Springer. p. 9-21.
215. Muller, P., P. Mognol, and J.-Y. Hascoet. *Functionally graded material (FGM) parts: from design to the manufacturing simulation*. in *ASME 2012 11th Biennial Conference on Engineering Systems Design and Analysis*. 2012. American Society of Mechanical Engineers Digital Collection.
216. Pierre, M., H. Jean-Yves, and M. Pascal, *Toolpaths for additive manufacturing of functionally graded materials (FGM) parts*. *Rapid Prototyping Journal*, 2014. **20(6)**: p. 511-522.
217. Sarathchandra, D., S.K. Subbu, and N. Venkaiah, *Functionally graded materials and processing techniques: An art of review*. *Materials today: Proceedings*, 2018. **5(10)**: p. 21328-21334.
218. Singh, R. and J.P. Davim, *Additive Manufacturing: Applications and Innovations*. 2018: CRC Press.
219. Yang, L., et al., *Functionally graded ceramic based materials using additive manufacturing: review and progress*. *Additive Manufacturing and Strategic Technologies in Advanced Ceramics: Ceramic Transactions*, Volume 258, 2016. **258**: p. 43-55.
220. Steuben, J.C., A.P. Iliopoulos, and J.G. Michopoulos, *Implicit slicing for functionally tailored additive manufacturing*. *Computer-Aided Design*, 2016. **77**: p. 107-119.

221. Schneider-Maunoury, C., et al., *Functionally graded Ti6Al4V-Mo alloy manufactured with DED-CLAD® process*. Additive Manufacturing, 2017. **17**: p. 55-66.
222. Li, L., et al., *Composite Modeling and Analysis for Fabrication of FDM Prototypes with Locally Controlled Properties*. Journal of Manufacturing Processes, 2002. **4**(2): p. 129-141.
223. Chung, H. and S. Das, *Functionally graded Nylon-11/silica nanocomposites produced by selective laser sintering*. Materials Science and Engineering: A, 2008. **487**(1): p. 251-257.
224. Choy, S.Y., et al., *Compressive properties of functionally graded lattice structures manufactured by selective laser melting*. Materials & Design, 2017. **131**: p. 112-120.
225. Dehoff, R.R., et al., *Site specific control of crystallographic grain orientation through electron beam additive manufacturing*. Materials Science and Technology, 2015. **31**(8): p. 931-938.
226. Tammam-Williams, S. and I. Todd, *Design for additive manufacturing with site-specific properties in metals and alloys*. Scripta Materialia, 2017. **135**: p. 105-110.
227. Ilie, A., H. Ali, and K. Mumtaz, *In-built customised mechanical failure of 316L components fabricated using selective laser melting*. Technologies, 2017. **5**(1): p. 9.

228. Amine, T., J.W. Newkirk, and F. Liou, *An investigation of the effect of laser deposition parameters on characteristics of multilayered 316 L deposits*. The International Journal of Advanced Manufacturing Technology, 2014. **73**(9-12): p. 1739-1749.
229. Qu, H.P., et al., *Microstructure and mechanical property of laser melting deposition (LMD) Ti/TiAl structural gradient material*. Materials & Design, 2010. **31**(1): p. 574-582.
230. Hofmann, D.C., et al., *Compositionally graded metals: A new frontier of additive manufacturing*. Journal of Materials Research, 2014. **29**(17): p. 1899-1910.
231. Hofmann, D.C., et al., *Developing gradient metal alloys through radial deposition additive manufacturing*. Scientific reports, 2014. **4**: p. 5357.
232. Carroll, B.E., et al., *Functionally graded material of 304L stainless steel and inconel 625 fabricated by directed energy deposition: Characterization and thermodynamic modeling*. Acta Materialia, 2016. **108**: p. 46-54.
233. Wang, Z., et al., *Premature failure of an additively manufactured material*. NPG Asia Materials, 2020. **12**(1): p. 30.
234. Mukherjee, T. and T. DebRoy, *Printability of 316 stainless steel*. Science and Technology of Welding and Joining, 2019. **24**(5): p. 412-419.
235. Parimi, L.L., et al., *Microstructural and texture development in direct laser fabricated IN718*. Materials Characterization, 2014. **89**: p. 102-111.

236. Gray, G.T., et al., *Structure/property (constitutive and spallation response) of additively manufactured 316L stainless steel*. Acta Materialia, 2017. **138**: p. 140-149.
237. Renishaw Inc. Available from: <https://www.renishaw.com/en/metal-3d-printing--32084>.
238. Ready, J., *Effects of high-power laser radiation*. 2012: Elsevier.
239. Parry, L.A., *Investigation of Residual Stress in Selective Laser Melting*, in *Department of Engineering*. 2018, University of Nottingham. p. 289.
240. Karimi, P., et al., *Influence of laser exposure time and point distance on 75- $\mu$ m-thick layer of selective laser melted Alloy 718*. The International Journal of Advanced Manufacturing Technology, 2018. **94**(5): p. 2199-2207.
241. Renishaw, R. Systems, Editor. 2018.
242. ASTM, A., *A240/A240M-10–Standard Specification for Chromium and Chromium-Nickel Stainless Steel Plate, Sheet, and Strip for Pressure Vessels and for General Applications*.
243. Spierings, A.B. and G. Levy. *Comparison of density of stainless steel 316L parts produced with selective laser melting using different powder grades*. in *Proceedings of the Annual International Solid Freeform Fabrication Symposium*. 2009. Austin, TX.
244. Spierings, A.B., M. Schneider, and R. Eggenberger, *Comparison of density measurement techniques for additive manufactured metallic parts*. Rapid Prototyping Journal, 2011.

245. Products, A.S.f.T.a.M.C.B.o.M.P.a.M.P., *Standard Test Methods for Density of Compacted or Sintered Powder Metallurgy (PM) Products Using Archimedes' Principle*. 2009: ASTM International.
246. Norma, A., *E92-82 (1997) E3 Standard Test Method for Vickers Hardness of Metallic Materials*. Filadelfia (EE. UU.): American Society for Testing and Materials, 1997.
247. Oliver, W.C. and G.M. Pharr, *Measurement of hardness and elastic modulus by instrumented indentation: Advances in understanding and refinements to methodology*. Journal of Materials Research, 2004. **19**(1): p. 3-20.
248. International, A., *Standard test methods for tension testing of metallic materials*. 2016: ASTM international.
249. Crammond, G., et al., *Speckle pattern quality assessment for digital image correlation*. 2013. **51**(12): p. 1368-1378.
250. Haddadi, H., S.J.O. Belhabib, and L.i. Engineering, *Use of rigid-body motion for the investigation and estimation of the measurement errors related to digital image correlation technique*. 2008. **46**(2): p. 185-196.
251. International, A., *ASTM C1161-18, Standard Test Method for Flexural Strength of Advanced Ceramics at Ambient Temperature*. 2018.
252. E407-07, A., *Standard practice for microetching metals and alloys*. 2015, ASTM International West Conshohocken, PA.

253. Yang, Y., et al., *Accuracy and density optimization in directly fabricating customized orthodontic production by selective laser melting*. Rapid Prototyping Journal, 2012.
254. Tucho, W.M., et al., *Investigation of effects of process parameters on microstructure and hardness of SLM manufactured SS316L*. Journal of Alloys and Compounds, 2018. **740**: p. 910-925.
255. Frick, J.P., *Woldman's engineering alloys*. 2000: ASM international Materials Park, OH.
256. Hall, E., *The deformation and ageing of mild steel: III discussion of results*. Proceedings of the Physical Society. Section B, 1951. **64**(9): p. 747.
257. ASTM International, W.C., PA, *ASTM B962-17, Standard Test Methods for Density of Compacted or Sintered Powder Metallurgy (PM) Products Using Archimedes' Principle*. 2018. p. 1-7.
258. Hitzler, L., et al., *On the anisotropic mechanical properties of selective laser-melted stainless steel*. Materials, 2017. **10**(10): p. 1136.
259. Ramirez-Cedillo, E., et al., *Process planning of L-PBF of AISI 316L for improving surface quality and relating part integrity with microstructural characteristics*. Surface and Coatings Technology, 2020. **396**: p. 125956.
260. Cacace, S., A.G. Demir, and Q. Semeraro, *Densification Mechanism for Different Types of Stainless Steel Powders in Selective Laser Melting*. Procedia CIRP, 2017. **62**: p. 475-480.



261. International, A., *ASTM E112-13: Standard Test Methods for Determining Average Grain Size*. 2013. p. 1-28.
262. Kluczyński, J., et al., *The influence of exposure energy density on porosity and microhardness of the SLM additive manufactured elements*. *Materials*, 2018. **11**(11): p. 2304.
263. Jeon, J.M., et al., *Effects of microstructure and internal defects on mechanical anisotropy and asymmetry of selective laser-melted 316L austenitic stainless steel*. *Materials Science and Engineering: A*, 2019. **763**: p. 138152.
264. Vander Voort, G.F., et al., *ASM handbook. Metallography and microstructures*, 2004. **9**: p. 44073-0002.
265. Krauss, G., *Steels: processing, structure, and performance*. 2015: Asm International.
266. Zhang, S.Y., et al., *Investigation of martensite transformation in 316L stainless steel*. *Materials Today: Proceedings*, 2015. **2**: p. 251-260.
267. Krauss, G. and A. Marder, *The morphology of martensite in iron alloys*. *Metallurgical Transactions*, 1971. **2**(9): p. 2343.
268. Saeidi, K., *Stainless steels fabricated by laser melting : Scaled-down structural hierarchies and microstructural heterogeneities*. 2016, Department of Materials and Environmental Chemistry (MMK), Stockholm University: Stockholm. p. 115.

269. Murr, L.E., et al., *Metal Fabrication by Additive Manufacturing Using Laser and Electron Beam Melting Technologies*. Journal of Materials Science & Technology, 2012. **28**(1): p. 1-14.
270. Bajaj, P., et al., *Steels in additive manufacturing: A review of their microstructure and properties*. Materials Science and Engineering: A, 2019: p. 138633.
271. Boes, J., A. Röttger, and W. Theisen, *Microstructure and properties of high-strength C+ N austenitic stainless steel processed by laser powder bed fusion*. Additive Manufacturing, 2020. **32**: p. 101081.
272. Kou, S., *Welding metallurgy*. New Jersey, USA, 2003: p. 431-446.
273. Wang, Q., et al., *Microstructure evolution and EBSD analysis of a graded steel fabricated by laser additive manufacturing*. Vacuum, 2017. **141**: p. 68-81.
274. Casati, R., J. Lemke, and M. Vedani, *Microstructure and fracture behavior of 316L austenitic stainless steel produced by selective laser melting*. Journal of Materials Science & Technology, 2016. **32**(8): p. 738-744.
275. Kong, D., et al., *Anisotropy in the microstructure and mechanical property for the bulk and porous 316L stainless steel fabricated via selective laser melting*. Materials Letters, 2019. **235**: p. 1-5.
276. Niendorf, T., et al., *Highly anisotropic steel processed by selective laser melting*. Metallurgical and Materials Transactions B, 2013. **44**(4): p. 794-796.

277. Ono, Y. and S. Matsumoto, *Diffusion of chromium, manganese, and nickel in molten iron*. Transactions of the Japan Institute of Metals, 1975. **16**(7): p. 415-422.
278. Yasa, E. and J.P. Kruth, *Microstructural investigation of Selective Laser Melting 316L stainless steel parts exposed to laser re-melting*. Procedia Engineering, 2011. **19**: p. 389-395.
279. Wei, H., J. Mazumder, and T. DebRoy, *Evolution of solidification texture during additive manufacturing*. Scientific reports, 2015. **5**: p. 16446.
280. Salzbrenner, B.C., et al., *High-throughput stochastic tensile performance of additively manufactured stainless steel*. Journal of Materials Processing Technology, 2017. **241**: p. 1-12.
281. Kramer, S.L.B., et al., *The third Sandia fracture challenge: predictions of ductile fracture in additively manufactured metal*. International Journal of Fracture, 2019. **218**(1): p. 5-61.
282. Yoon, K.B., V.H. Dao, and J.M. Yu, *Effects of build direction on tensile and creep properties of 316L stainless steel produced by selective laser melting*. Fatigue & Fracture of Engineering Materials & Structures, 2020. **43**(11): p. 2623-2636.
283. Li, Z., et al., *Tensile properties, strain rate sensitivity, and activation volume of additively manufactured 316L stainless steels*. International Journal of Plasticity, 2019. **120**: p. 395-410.

284. Byun, T.S., et al., *Mechanical behavior of additively manufactured and wrought 316L stainless steels before and after neutron irradiation*. Journal of Nuclear Materials, 2021. **548**: p. 152849.
285. ASTM, E.J.S.T.M.f.T.T.o.M.M., ASTM International, West Conshohocken, PA, USA, 8.(2004). 2004.
286. Tucho, W.M., et al., *Microstructure and hardness studies of Inconel 718 manufactured by selective laser melting before and after solution heat treatment*. Materials Science and Engineering: A, 2017. **689**: p. 220-232.
287. Roach, A.M., et al., *Size-dependent stochastic tensile properties in additively manufactured 316L stainless steel*. Additive Manufacturing, 2020. **32**: p. 101090.
288. Zhang, B., L. Dembinski, and C. Coddet, *The study of the laser parameters and environment variables effect on mechanical properties of high compact parts elaborated by selective laser melting 316L powder*. Materials Science and Engineering: A, 2013. **584**: p. 21-31.
289. Chadha, K., et al., *Effect of Annealing Heat Treatment on the Microstructural Evolution and Mechanical Properties of Hot Isostatic Pressed 316L Stainless Steel Fabricated by Laser Powder Bed Fusion*. Metals, 2020. **10**(6): p. 753.
290. Ledbetter, H., W. Weston, and E. Naimon, *Low-temperature elastic properties of four austenitic stainless steels*. Journal of Applied Physics, 1975. **46**(9): p. 3855-3860.
291. Ledbetter, H., *Stainless-steel elastic constants at low temperatures*. Journal of Applied Physics, 1981. **52**(3): p. 1587-1589.

292. Harvey, P.D., *Engineering properties of steel*. 1982: Asm International.
293. Hutchinson, B., *Critical assessment 16: anisotropy in metals*. Materials Science and Technology, 2015. **31**(12): p. 1393-1401.
294. Li, X., et al., *Rate- and Temperature-Dependent Plasticity of Additively Manufactured Stainless Steel 316L: Characterization, Modeling and Application to Crushing of Shell-Lattices*. International Journal of Impact Engineering, 2020: p. 103671.
295. Andreau, O., et al., *A competition between the contour and hatching zones on the high cycle fatigue behaviour of a 316L stainless steel: Analyzed using X-ray computed tomography*. Materials Science and Engineering: A, 2019. **757**: p. 146-159.
296. Marattukalam, J.J., et al., *The effect of laser scanning strategies on texture, mechanical properties, and site-specific grain orientation in selective laser melted 316L SS*. Materials & Design, 2020. **193**: p. 108852.

## PUBLICATIONS

### **Journal Papers**

[J3] Das O., **Parikh, Y.**, Wang J., & Kuttolamadam, M. A. (2020). Manufacturability & Bending Behavior of Stiffness-Graded Steel Structures Fabricated by Selective Laser Melting. Journal of Manufacturing Systems, (in preparation).

[J2] **Parikh, Y.**, & Kuttolamadam, M. A. (2020). Property-Graded Single-Alloy Stainless Steel 316L by Selective Laser Melting: Interfaces & Performance Journal of Manufacturing Processes, (under review).

[J1] **Parikh, Y.**, & Kuttolamadam, M. A. (2020). Property-Graded Single-Alloy Stainless Steel 316L by Selective Laser Melting: Fabrication & Characterization Journal of Manufacturing Processes, (under review).

### **Refereed Conference Papers**

[C2] **Parikh, Y.** & Kuttolamadam, M. A. (2021). Selective Laser Melting of Stainless Steel 316L for Mechanical Property-gradation. Proceedings of the ASME 16th International Manufacturing Science & Engineering Conference (MSEC-2021), Cincinnati, OH., (June 2021).

[C1] **Parikh, Y.**, Carter, J., & Kuttolamadam, M. A. (2020). Investigation of Porosity & Microstructure-Induced Property Variations in Additive Manufactured Stainless Steel 316L. Proceedings of the ASME 15th International Manufacturing Science & Engineering Conference (MSEC-2020), Cincinnati, OH., (June 2020).

### **Conference Presentations**

[CP5] **Parikh, Y., & Kuttolamadom, M. A.** (2019). Investigation of Additively Manufactured Functionally-Graded Steel Structures. Additive Manufacturing with Powder Metallurgy (AMPM-2019) Conference, Phoenix, Arizona, USA, Jun. 23-26, 2019.

[CP4] **Parikh, Y., & Kuttolamadom, M. A.** (2019). Investigation of Additively Manufactured Functionally-Graded Steel Structures. 2019 Student Research Week, Texas A&M University, Texas, USA, Mar. 19, 2019.

[CP3] **Parikh, Y., & Kuttolamadom, M. A.** (2019). Investigation of a Mechanical Engineering Design Self-efficacy Scale for Undergraduates. 2019 Student Research Week, Texas A&M University, College Station, Texas, USA, Mar. 19, 2019.

[CP2] **Parikh, Y., & Kuttolamadom, M. A.** (2018). Effect of Energy Density Parameters on Mechanical Property Gradients in Additive Manufacturing. Additive Manufacturing with Powder Metallurgy (AMPM-2018) Conference, San Antonio, Texas, USA, Jun. 17-20, 2018.

[CP1] **Parikh, Y., & Kuttolamadom, M. A.** (2018). Effect of Energy Density Parameters on Mechanical Property Gradients in Additive Manufacturing. 2018 ASME South Texas Section University Technical Competition, Texas A&M University, College Station, Texas, USA, Apr. 7, 2018.

### **Poster Presentations**

[P7] **Parikh, Y.,** & Kuttolamadom, M. A. (2019). Investigation of Additively Manufactured Functionally-Graded Steel Structures. Additive Manufacturing with Powder Metallurgy (AMPM-2019) Conference, Phoenix, Arizona, USA, Jun. 23-26, 2019.

[P6] **Parikh, Y.,** & Kuttolamadom, M. A. (2018). Effect of Energy Density Parameters on Mechanical Property Gradients in Additive Manufacturing. Additive Manufacturing with Powder Metallurgy (AMPM-2018) Conference, San Antonio, Texas, USA, Jun. 17-20, 2018.

[P5] **Parikh, Y.,** & Kuttolamadom, M. A. (2018). Effect of Energy Density Parameters on Mechanical Property Gradients in Additive Manufacturing. Research Lab Poster Session, Mechanical Engineering Graduate Student Organization (MEGSO), Texas A&M University, College Station, Texas, USA, Mar. 9, 2018.

[P4] **Parikh, Y.,** Carter, J., Sheldon, C., Sai Prasad Yallasiri, L., Bercich, K., & Kuttolamadom, M. A. (2017). Additive Manufacturing of Bio-Inspired Gradient Materials & Surfaces. 2017 College of Engineering National Labs Day, Texas A&M University, College Station, Texas, USA, Nov. 3, 2017.

[P3] **Parikh, Y.,** & Kuttolamadom, M. A. (2017). Effect of Energy Density Parameters on Mechanical Property Gradients in Additive Manufacturing. 2017 College of Engineering National Labs Day, Texas A&M University, College Station, Texas, USA, Nov. 3, 2017.



[P2] Carter, J., **Parikh, Y.**, Sheldon, C., Bercich, K., & Kuttolamadam, M. A. (2017). Additive Manufacturing of Bio-Inspired Gradient Materials & Surfaces. 2017 National Science Foundation (NSF) Engineering Education & Centers (EEC) Grantees Conference, Hosted by American Society for Engineering Education (ASEE), Arlington, Virginia, USA, Oct. 29-31, 2017.

[P1] Carter, J., **Parikh, Y.**, & Kuttolamadam, M. A. (2017). Effect of Energy Density Parameters on Mechanical Property Gradients in Additive Manufacturing. 2017 Engineering Undergraduate Summer Research Grant (USRG) & Research Experiences for Undergraduates (REU) Research Poster Symposium, Texas A&M University, College Station, Texas, USA, Aug. 4, 2017.

## APPENDIX A

### Powder Size Distribution

Detailed particle size distribution (with counts and volume) analysis was carried out for the virgin SS 316L powder as-received with assistance from Nanoscience Instruments. A total of 2200 powder particles were analyzed for the D10, D50, and D90 distributions as shown in Table 24.

**Table 24. Results from SS 316L PSD analysis.**

#### Stainless Steel Particle Size Distribution Analysis

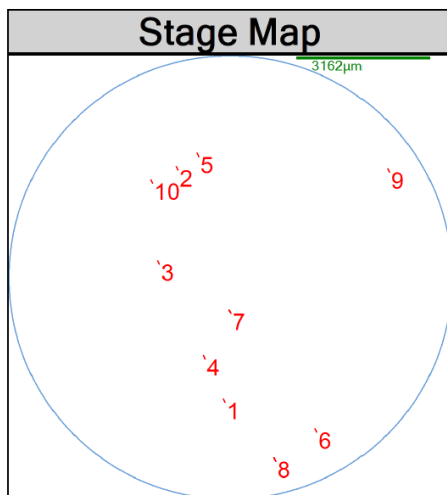
DAvg Distribution			
Based on Davg	10%	50%	90%
Agglomerates SS	21.49 $\mu\text{m}$	34.75 $\mu\text{m}$	51.93 $\mu\text{m}$
Spherical SS	19.17 $\mu\text{m}$	26.35 $\mu\text{m}$	34.96 $\mu\text{m}$
Satellite SS	5.08 $\mu\text{m}$	45.40 $\mu\text{m}$	45.68 $\mu\text{m}$

#### Average Diameter of Stainless Steel Particles Identified\_By Count

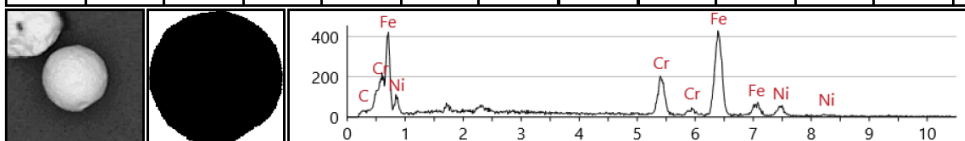
DAve Distribution					
Bin ( $\mu\text{m}$ )	Count	Bin ( $\mu\text{m}$ )	Count	Bin ( $\mu\text{m}$ )	Count
[4-6)	11	[20-22)	196	[36-38)	93
[6-8)	3	[22-24)	239	[38-40)	55
[8-10)	4	[24-26)	244	[40-42)	42
[10-12)	10	[26-28)	269	[42-44)	34
[12-14)	16	[28-30)	217	[44-46)	24
[14-16)	37	[30-32)	184	[46-48)	26
[16-18)	73	[32-34)	165	[48-50)	12
[18-20)	117	[34-36)	128	[50-94)	66

**Table 25. Results from spherical SS particle examples.**

Individual Particle Parameters													
Selected particles based on							ROUNDNESS, ASPECT, Descending						



Rank	ID	Size (μm)	Width (μm)	Class	X	Y	Aspect	Area	Roundness	Form Factor	EdgeRoughness	ECD	Fe
1	2038	24.408	24.176	Spherical SS	-15.363	-2.470	1.018	455.727	0.974	0.849	0.677	24.088	69.700



Rank	ID	Size (μm)	Width (μm)	Class	X	Y	Aspect	Area	Roundness	Form Factor	EdgeRoughness	ECD	Fe
2	493	24.633	24.422	Spherical SS	-16.484	3.052	1.011	464.047	0.974	0.850	0.631	24.307	67.700

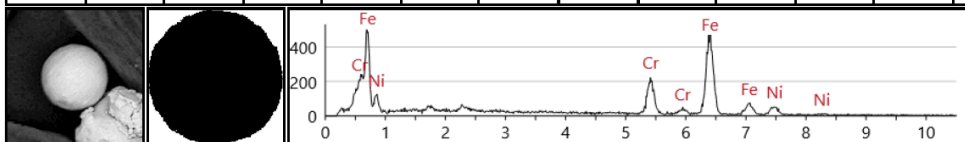
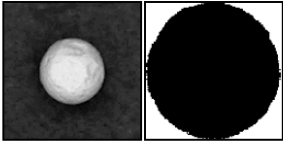
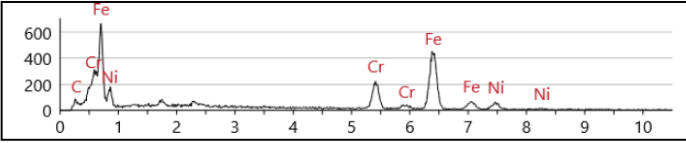
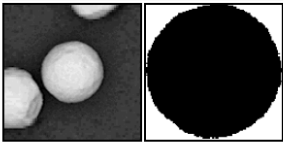
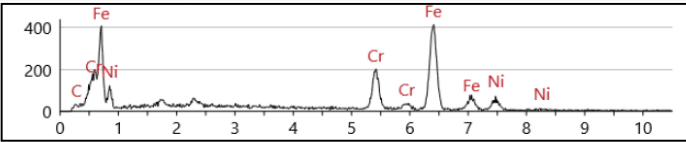
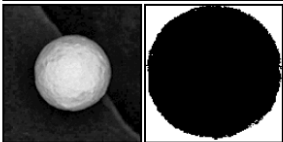
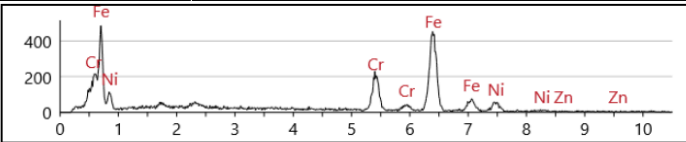
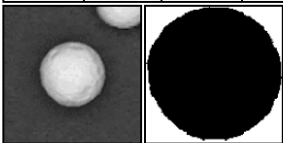
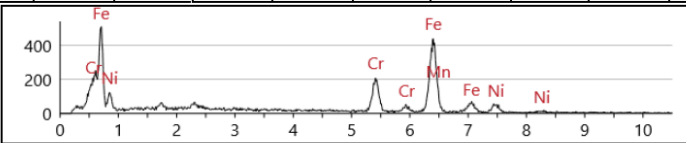
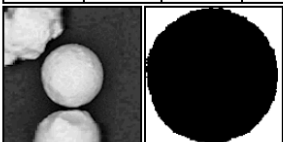
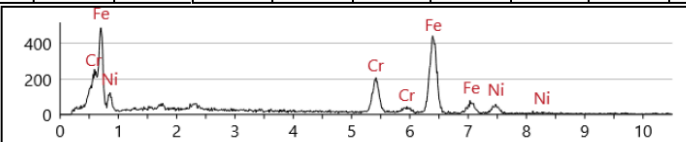


Table 25. Continued.

Rank	ID	Size (µm)	Width (µm)	Class	X	Y	Aspect	Area	Roundness	Form Factor	EdgeRoughness	ECD	Fe
3	1100	23.963	23.566	Spherical SS	-16.933	0.812	1.027	438.922	0.973	0.828	0.760	23.640	66.200
													
4	1674	21.627	21.512	Spherical SS	-15.833	-1.439	1.009	356.759	0.971	0.861	0.542	21.313	67.300
													
5	404	32.640	32.585	Spherical SS	-15.995	3.365	1.002	811.906	0.970	0.699	0.941	32.152	66.200
													
6	2261	23.974	23.640	Spherical SS	-13.177	-3.178	1.019	437.639	0.970	0.869	0.586	23.605	67.800
													
7	1484	22.560	22.061	Spherical SS	-15.233	-0.361	1.023	387.347	0.969	0.873	0.672	22.208	67.900
													

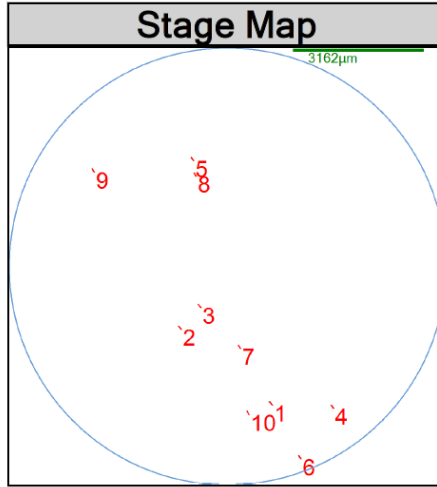
**Table 25. Continued.**

Rank	ID	Size (μm)	Width (μm)	Class	X	Y	Aspect	Area	Roundness	Form Factor	EdgeRoughness	ECD	Fe
8	2317	30.718	30.165	Spherical SS	-14.159	-3.866	1.019	717.450	0.968	0.833	0.626	30.224	66.900
Rank	ID	Size (μm)	Width (μm)	Class	X	Y	Aspect	Area	Roundness	Form Factor	EdgeRoughness	ECD	Fe
9	543	18.416	17.942	Spherical SS	-11.477	2.993	1.036	257.832	0.968	0.814	0.832	18.119	67.200
Rank	ID	Size (μm)	Width (μm)	Class	X	Y	Aspect	Area	Roundness	Form Factor	EdgeRoughness	ECD	Fe
10	483	14.411	14.135	Spherical SS	-17.089	2.743	1.020	157.787	0.967	0.837	0.574	14.174	66.700

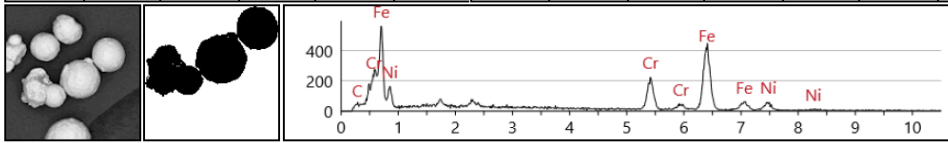
**Table 26. Results from agglomerates SS particle examples.**

**Agglomerates SS Particle Examples**

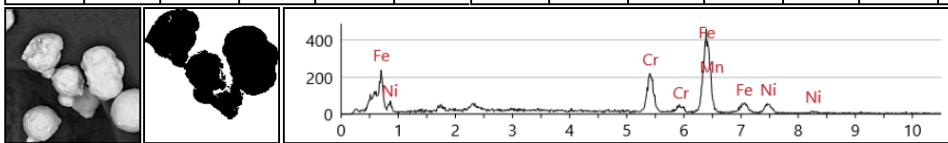
Individual Particle Parameters													
Selected particles based on							DMAX, ROUNDNESS, Descending						



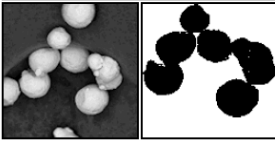
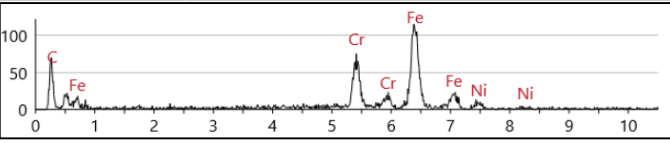
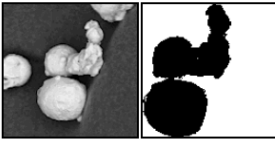
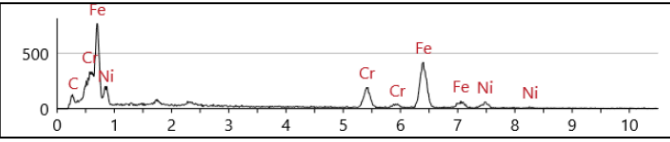
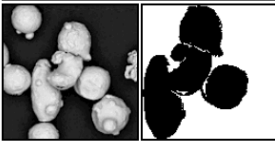
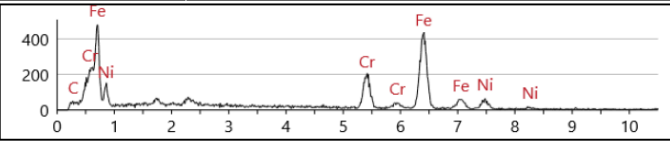
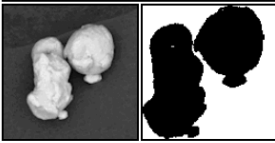
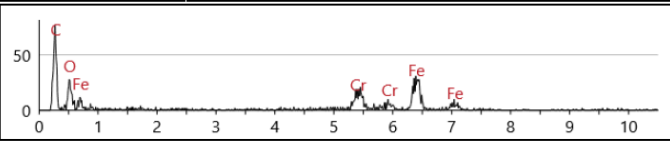
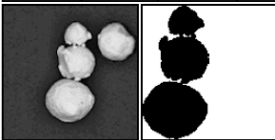
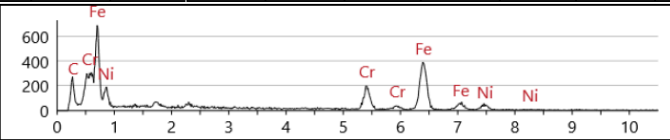
Rank	ID	Size (μm)	Width (μm)	Class	X	Y	Aspect	Area	Roundness	Form Factor	EdgeRoughness	ECD	Fe
1	2162	101.434	45.356	Agglomerates SS	-14.182	-2.863	2.236	2626.247	0.325	0.255	0.508	57.826	66.300



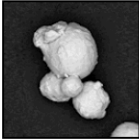

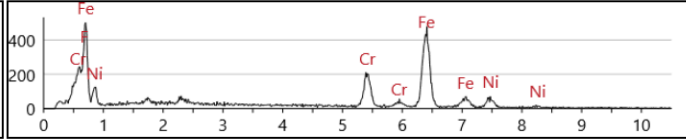

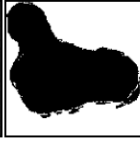
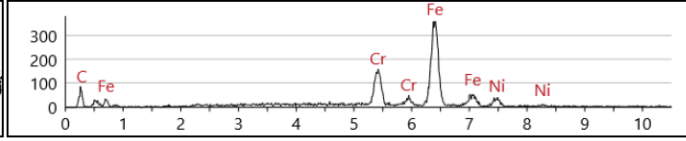


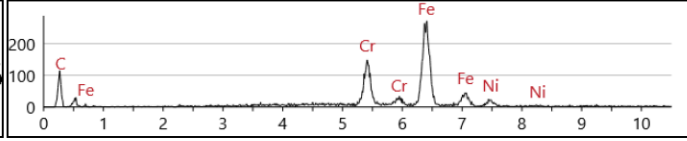
Rank	ID	Size (μm)	Width (μm)	Class	X	Y	Aspect	Area	Roundness	Form Factor	EdgeRoughness	ECD	Fe
2	1554	90.724	63.671	Agglomerates SS	-16.377	-1.033	1.430	3165.876	0.490	0.136	0.843	63.490	67.700



**Table 26. Continued.**

Rank	ID	Size (µm)	Width (µm)	Class	X	Y	Aspect	Area	Roundness	Form Factor	EdgeRoughness	ECD	Fe
3	1465	87.727	75.306	Agglomerates SS	-15.903	-0.512	1.165	2786.765	0.461	0.142	0.834	59.567	60.700
													
4	2180	84.206	44.681	Agglomerates SS	-12.702	-2.938	1.885	2227.310	0.400	0.250	0.618	53.253	63.200
													
5	506	82.512	59.656	Agglomerates SS	-16.075	3.039	1.383	2471.275	0.462	0.195	0.759	56.094	67.400
													
6	2362	78.608	51.230	Agglomerates SS	-13.481	-4.155	1.534	2334.101	0.481	0.281	0.914	54.515	48.600
													
7	1723	77.093	37.600	Agglomerates SS	-14.939	-1.498	2.050	1828.952	0.392	0.304	0.648	48.257	62.800
													

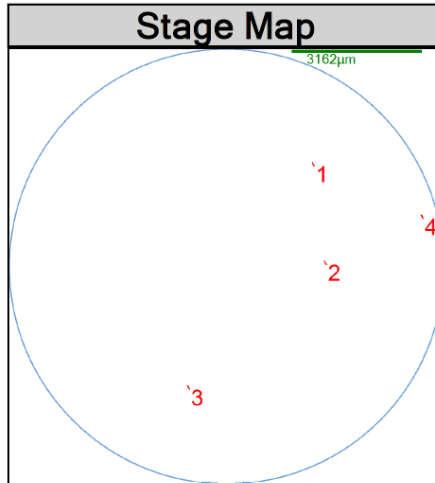
**Table 26. Continued.**

Rank	ID	Size (µm)	Width (µm)	Class	X	Y	Aspect	Area	Roundness	Form Factor	EdgeRoughness	ECD	Fe
8	614	76.511	52.366	Agglomerates SS	-16.003	2.662	1.567	2222.177	0.483	0.312	0.877	53.192	67.900
 													
9	454	74.204	47.677	Agglomerates SS	-18.476	2.767	1.892	2048.827	0.474	0.287	0.883	51.075	70.300
 													
10	2149	73.434	33.705	Agglomerates SS	-14.733	-3.081	2.502	1655.064	0.391	0.392	0.979	45.905	68.100
 													

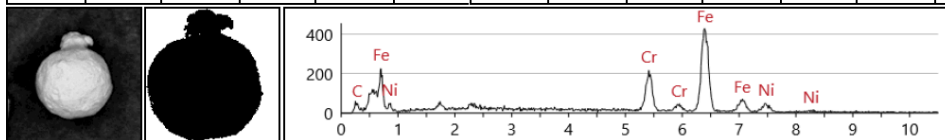


**Table 27. Results from satellite SS particle examples.**  
**Satellite SS Particle Examples**

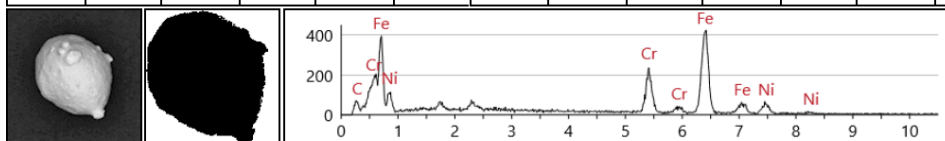
Individual Particle Parameters													
Selected particles based on							AREA, Descending						



Rank	ID	Size (μm)	Width (μm)	Class	X	Y	Aspect	Area	Roundness	Form Factor	EdgeRoughness	ECD	Fe
1	537	48.427	42.991	Satellite SS	-13.114	2.933	1.126	1441.356	0.783	0.539	0.970	42.839	67.800

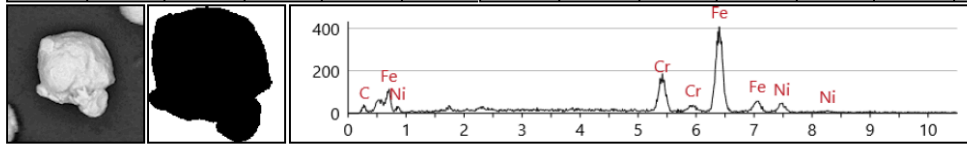


Rank	ID	Size (μm)	Width (μm)	Class	X	Y	Aspect	Area	Roundness	Form Factor	EdgeRoughness	ECD	Fe
2	1285	51.135	42.555	Satellite SS	-12.827	0.547	1.236	1434.237	0.698	0.665	0.837	42.733	64.300

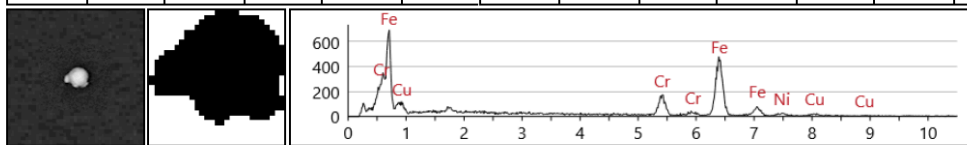


**Table 27. Continued.**

Rank	ID	Size (μm)	Width (μm)	Class	X	Y	Aspect	Area	Roundness	Form Factor	EdgeRoughness	ECD	Fe
3	2010	50.338	43.255	Satellite SS	-16.140	-2.481	1.165	1376.660	0.692	0.689	0.508	41.867	69.100



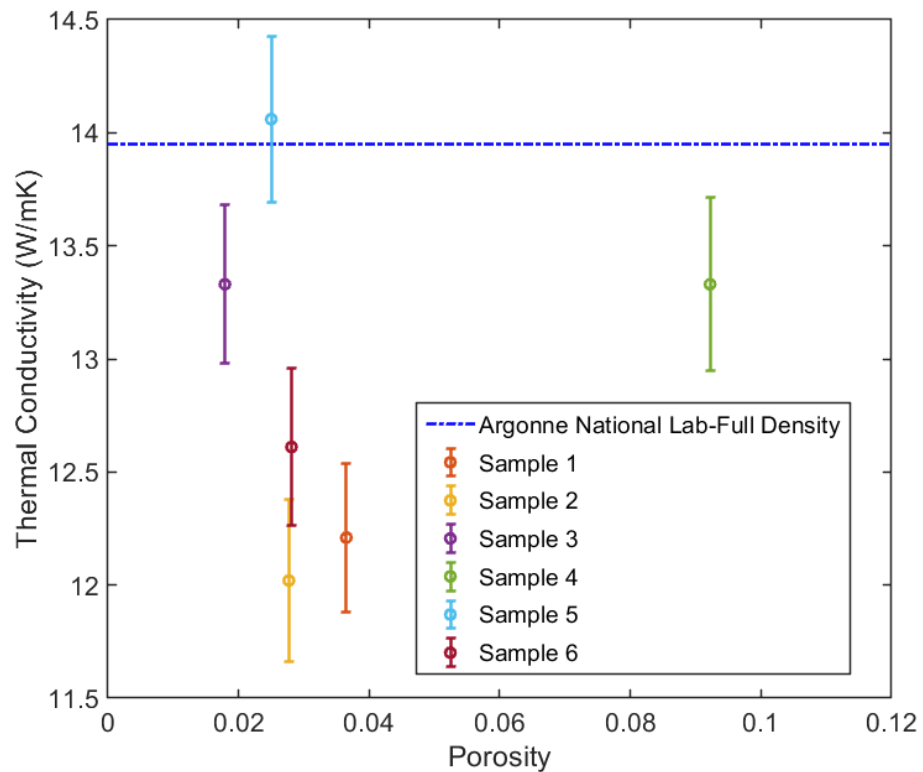
Rank	ID	Size (μm)	Width (μm)	Class	X	Y	Aspect	Area	Roundness	Form Factor	EdgeRoughness	ECD	Fe
4	922	5.478	4.654	Satellite SS	-10.479	1.656	1.177	17.923	0.760	0.790	0.535	4.777	70.900



## APPENDIX B

### Thermal Conductivity

Thermal conductivity study was performed in collaboration with the UT Arlington. Six cylindrical samples were fabricated based on the same processing conditions as that of graded samples to understand their thermal conductivity range. A significant change in thermal conductivity,  $K$  (W/mK) of  $\sim 2$  W/mK, was observed across the six samples in Figure 167.



**Figure 167. Difference in thermal conductivity amongst samples with varying porosity.**